



UiT The Arctic University of Norway

Faculty of Science and Technology
Department of Physics and Technology

**Numerical simulations and stochastic modeling of intermittent
fluctuations in magnetized plasmas**

Gregor Decristoforo

A dissertation for the degree of Philosophiae Doctor, March 2021



Abstract

The exhaust of particles and heat in the boundary of contemporary magnetic confinement experiments remains to this day a major obstacle on the road to commercially viable fusion energy production. It is recognized, that coherent structures of hot and dense plasma, called blobs or filaments, are the dominant mechanism for cross-field particle transport. These filaments are created by plasma turbulence at the outboard midplane and move radially outwards driven by interchange motions. This leads to high average particle densities and relative fluctuation levels in the scrape-off layer, which increases plasma-wall interactions.

Time series of the plasma density measured at a fixed point using either Langmuir probes or gas puff imaging have shown highly intermittent fluctuations across a variety of devices, plasma parameters and confinement modes. Recent statistical analysis of measurement data time series has revealed that the fluctuations are well described as a superposition of uncorrelated exponential pulses with fixed duration and exponentially distributed pulse amplitudes, arriving according to a Poisson process.

Due to the complexity of the physics involved in the boundary of fusion devices, numerical simulations are utilized to gain an accurate description of scrape-off layer plasmas. This approach requires a validation metric for simulations of plasma turbulence such as the statistical framework based on filtered Poisson processes. In this thesis, well-established models for scrape-off layer plasmas are analyzed. These models use two-fluid equations simulating plasma evolution in the two-dimensional plane perpendicular to the magnetic field. Time series of the plasma density are measured at a fixed point and their fluctuation statistics are compared to experimental measurements utilizing the statistical framework. This includes probability density functions, power spectral densities and conditionally averaged waveforms. In addition, simulations of a population of seeded blobs are performed in order to study the effects of blob interactions. It is shown that the fluctuation statistics of single-point measurements in simple numerical models stand in excellent agreement with their experimental counterparts. This work thereby sets a new standard and methodology for validating scrape-off layer turbulence simulations.

Acknowledgements

After three and a half years as a PhD student, I would like to thank a number of people who have supported me on this journey. First, I would like to thank my main supervisor, Odd Erik Garcia. In addition to his guidance and support, Odd Erik also gave me the opportunity to participate at summer schools at CCFE and MIT, visit DTU for two weeks during my first year and spend a whole year at CCFE. Visiting different research facilities and meeting many gifted scientists was one of the highlights during this time.

I would also like to thank Fulvio Militello for hosting me at CCFE and proofreading parts of this thesis. Our weekly catch-ups in the last year and a half were extremely insightful and productive. I am grateful to him reserving time for me even though I am not directly supervised by him.

I am very grateful for being part of such friendly and supportive research groups. These include Audun Theodorsen, Ralph Kube, Juan Manuel Losada and Magdalena Korzeniowska at UiT. From CCFE these include John Omotani, Tom Nicholas, Fabio Riva, Sarah Newton and Nick Walkden as well as Matthias Wiesenberger at DTU. Further thanks go to my office mates, Patrick Stoll, Sindre Fritzner, Tuomas Heiskanen, Tom Farley, Daljeet Singh Gahle, Enrique Miralles and Joe Allcock. Raheesty Nishta Nem deserves my gratitude for proof-reading my thesis and giving me valuable comments. I am also grateful to the University of Tromsø – The Arctic University of Norway for funding my PhD.

On a less academic note, I would like to thank my landlord in Oxford, Michael Butcher, for letting Sajidah and me stay in his flat during the UK-wide lockdown due to the COVID-19 pandemic. Being able to stay together with Sajidah made this challenging time much easier. Thanks also to my friends in Tromsø and Oxford, I have always been looking forward to spending time with you during band practice and other occasions.

Vielen Dank an meine Familie für eure Unterstützung und euer Verständnis für die örtliche Distanz. Auch wenn ich euch pandemiebedingt schon lange nicht mehr persönlich sehen konnte, bleibt ihr in meinem Herzen.

Finally, I would like to thank Sajidah for her patience, laughter and support. This PhD would not have been as joyful without you.

Contents

1	Fluctuations in magnetized plasmas	1
1.1	Nuclear fusion	2
1.2	Magnetic confinement	2
1.3	Radial transport in the SOL	4
1.4	Intermittent fluctuations in the SOL	6
1.5	Plasma filaments	11
1.6	Numerical modeling of SOL plasmas	16
2	Reduced fluid models for SOL plasmas	21
2.1	Braginskii fluid equations	21
2.2	Drift reduction	23
2.3	Further approximations and simplifications	25
2.4	Reduced two-fluid model	29
2.5	Idealized interchange model	32
3	Stochastic modeling	35
3.1	Filtered Poisson Process	35
3.2	Moments and PDFs	38
3.3	Second order statistics	39
3.4	Excess time statistics	41
3.5	Density profiles	42
3.6	Deconvolution method	44
4	Summary of Papers	47
5	Conclusion and future work	51
	Bibliography	53

Paper I:	
Intermittent fluctuations due to Lorentzian pulses in turbulent thermal convection	73
Paper II:	
Dirac comb and exponential frequency spectra in chaotic dynamics	87
Paper III:	
Numerical turbulence simulations of intermittent fluctuations in the scrape-off layer of magnetized plasmas	111
Paper IV:	
Blob interactions in 2D scrape-off layer simulations	143

1 | Fluctuations in magnetized plasmas

Nuclear fusion is the process by which light atomic nuclei fuse together to form heavier nuclei and smaller by-products, releasing large amounts of energy. Since the middle of the last century, different strategies to harness fusion energy have been investigated. At present magnetic confinement is considered the most promising approach to deliver fusion power in the foreseeable future. To this day, however, controlling and harnessing nuclear fusion remains one of the greatest engineering challenges. Magnetically confined fusion requires the fuel to have enormously high temperatures while the vessel walls must be at room temperature or lower. The heat exhaust problem has therefore famously been referred to as “probably the main challenge towards the realization of magnetic confinement fusion” [1]. A detailed understanding of the intricate physics involved in the boundary of fusion devices therefore remains crucial in order to provide fusion energy as a sustainable and CO₂ emission free option for the future energy grid.

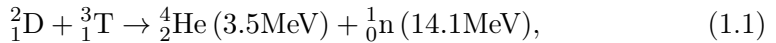
This thesis project is concerned with numerical simulations of boundary plasmas and a statistical analysis of plasma fluctuations. These simulations require a method of validation with experimental observations. In this thesis, a recently developed stochastic model for fluctuation statistics is utilized to identify suitable numerical models for boundary plasmas.

This thesis is structured as follows: This chapter delivers a brief overview of the current state of knowledge on the boundary of fusion plasmas. The main emphasis will lie on plasma fluctuations for reasons that will become clear over the course of this chapter. Chapter 2 is dedicated to the derivation of reduced fluid models for the boundary plasma, which are used for the numerical simulations presented in this thesis. Chapter 3 introduces the Filtered Poisson Process, a phenomenological model which is able to describe all relevant statistical properties of plasma fluctuations in the boundary region. Chapter 4 delivers a summary of the publications and unpublished manuscripts included

in this thesis and Chapter 5 provides the conclusion and outlook. The published papers and unpublished manuscripts are attached at the end of this thesis, representing the main contribution of this work.

1.1 Nuclear fusion

Although a multitude of nuclear reactions produces fusion energy, only the reaction of the hydrogen isotopes Deuterium ${}^2_1\text{D}$ and Tritium ${}^3_1\text{T}$,



is feasible with the prevailing technology. This reaction produces a helium particle ${}^4_2\text{He}$ and a neutron ${}^1_0\text{n}$ together with 17 MeV of kinetic energy. This exothermic, single-step reaction has the largest fusion cross section at the lowest temperatures of all potential reactions. In addition, the low atomic number results in a lower electrostatic potential that must be overcome, making this the most promising candidate for fusion power plants. With one in 6420 hydrogen atoms in sea water, Deuterium can be considered abundant, while the radioactive Tritium must be obtained from breeding of the lithium isotope ${}^6\text{Li}$, which can be found in minerals from the Earth's crust. Due to the high temperature of approximately 10^8 K for D-T fusion, no solid vessel could achieve steady-state confinement at these temperatures. The fuel would instantaneously lose its heat when colliding with the vessel walls. In order to achieve long enough energy confinement times, required for producing fusion power in a steady-state, a different approach has to be adopted. Since all hydrogen particles are fully ionized at these temperatures, i.e., in a plasma state, the particles can be confined with magnetic fields [2].

1.2 Magnetic confinement

Magnetic Confinement Fusion (MCF) chooses the approach to use the gyromotion of charged particles in a magnetic field to confine the plasma. An array of cylindrical solenoidal coils creating a uniform magnetic field can confine the plasma in the radial direction, however charged particles moving along these field lines can intersect material surfaces at both ends. The simplest method to mitigate these end losses is to bend the magnetic field to connect the ends, which results in a torus shape. The resulting inhomogeneity of the magnetic field due to its curvature and radial gradient, however, complicates plasma confinement. Since a gyrating particle experiences a stronger magnetic field on one side of its orbit than the other, it will experience a change in its gyration

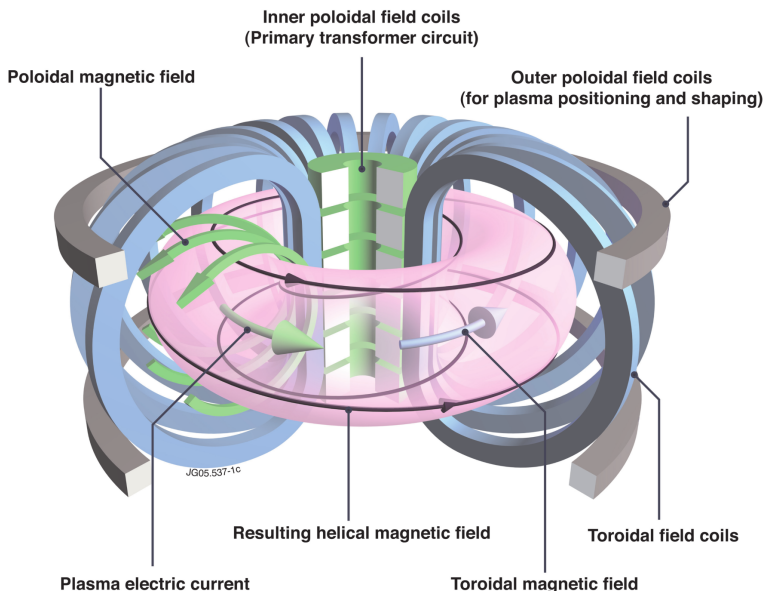


Figure 1.1: Schematic illustration of a tokamak device [3].

radius, resulting in a net drift which is in opposite direction for ions and electrons. These “guiding-center drifts” which are perpendicular to the magnetic field \mathbf{B} and its variation ∇B , create a vertical electric field \mathbf{E} . The resulting fields give rise to another guiding-center drift, the electric or $\mathbf{E} \times \mathbf{B}$ drift, which moves both negatively and positively charged particles radially outwards. A toroidal plasma current, induced by a central transformer, creates a poloidal magnetic field. Introducing this poloidal field results in helical magnetic field lines, which mitigates this problem since the guiding-center drifts cancel out as the particles rotate poloidally while following the magnetic field lines. Outer poloidal field coils are used in addition to shape and position the plasma column. This concept is known as a tokamak, invented in the 1950s in the Soviet Union and to this day considered to be the most promising route for plasma confinement and nuclear fusion. A schematic illustration of the tokamak concept is shown in Fig. 1.1.

Despite the advanced magnetic geometry of tokamak devices which establish a perfect equilibrium, experimental measurements indicate that large amounts of particles and heat are still transported across the magnetic flux surfaces. This transport is caused by plasma turbulence, which is particularly strong at the boundary of the device. All modern tokamak experiments adopted the “divertor configuration”, which is illustrated in Fig. 1.2. This configuration is achieved by creating a magnetic null point (X-point) in the

poloidal plane with a divertor coil carrying a current parallel to the plasma current. Within this point, the magnetic field lines are closed with the last closed flux surface (LCFS), often referred to as the separatrix. The outward region is called the Scrape-Off Layer (SOL), in which the magnetic field lines intersect the divertor plates. Ideally, all plasma leaking from the core through the separatrix into the SOL flows down to the divertor plates where it interacts with the material surfaces, with little to no influence on the fusion process in the core. The poloidal flux expansion near the X-point increases the distance of the magnetic field lines to the divertor plates, letting the plasma cool down before it reaches the material surfaces. Additional precautions, such as tilted target plates, buffers of neutralized gas in front of the target (divertor detachment) or installing a second divertor above the plasma column (double-null configuration) are applied in some experiments to reduce the heat flux on the divertor plates further. Despite all these efforts, plasma turbulence leads to highly intermittent bursts of particles and heat propagating through the SOL to the main chamber walls, leading to erosion, damages of sensitive equipment and the release of impurities into the core plasma, where they may degrade confinement and create radiative instabilities. An accurate description for the cross-field transport in the SOL is therefore required in order to predict and handle plasma and heat exhaust in future devices [2].

1.3 Radial transport in the SOL

Historically, the first attempts to describe cross-field transport in tokamak plasmas used a simple diffusive model in the SOL [4]. In this case the transport follows Fick's law

$$\Gamma_{\perp} = -D_{\perp} \frac{\partial n}{\partial r}, \quad (1.2)$$

where Γ_{\perp} stands for the cross-field particle flux, D_{\perp} is the diffusion coefficient estimated from the plasma parameters [5], n stands for the plasma density and r for the radial/cross field dimension. This model, however, fails to account for experimental observations, requiring significantly higher diffusion coefficients than expected from classical or Bohm diffusion [6, 7]. Experimental radial profiles in the SOL could only be reproduced by numerical simulations by assuming large cross field drifts or high effective diffusion coefficients D_{\perp}^{eff} , often referred to as ‘‘anomalous’’ diffusion [8]. It was expected that the SOL is dominated by strong flows parallel to the magnetic field, transporting most of the plasma to the divertor targets, resulting in exponential profiles with constant D_{\perp}^{eff} . These assumptions were refuted by experimental measurements such as presented for the TCV tokamak in Fig. 1.3. Here, the variable ρ stands for the distance to the separatrix and the dashed line indicates the beginning

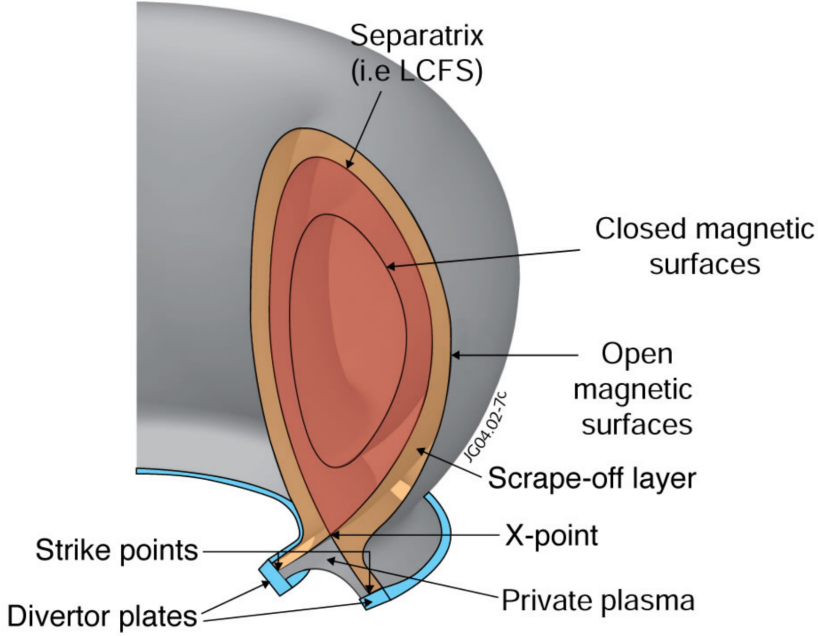


Figure 1.2: Schematic illustration of the boundary region of a tokamak in a divertor configuration [3].

of the wall shadow, the region in which the magnetic field lines interact with the vessel walls. For the lowest line-averaged densities \bar{n} a sharp decay in the density profile is observed close to the separatrix, with a much slower decay radially outwards. These regions are referred to as the near-SOL for the region of steep profiles and far-SOL, respectively [10]. For increasing \bar{n} the breakpoint between these two regions moves radially inwards, resulting in a long decay length in the whole SOL, called broadening [11]. This radial variation is also observed in other tokamak experiments such as Alcator C-Mod, MAST, NSTX, ASDEX, JET and DIII-D [12–18], and in numerical simulations with SOL turbulence codes such as ESEL [19]. For a purely diffusive transport this effect requires a significant radial increase of the effective diffusion coefficient as indicated in Fig. 1.4 for Alcator C-Mod plasmas, questioning the concept of purely diffusive transport. In the case of the DIII-D experiment, UEDGE transport simulations were unable to find any matching diffusion coefficient [21]. This motivates the introduction of an effective anomalous velocity v_{\perp}^{eff} to the diffusion model,

$$\Gamma_{\perp} = -D_{\perp}^{\text{eff}} \frac{\partial n}{\partial r} + v_{\perp}^{\text{eff}} n. \quad (1.3)$$

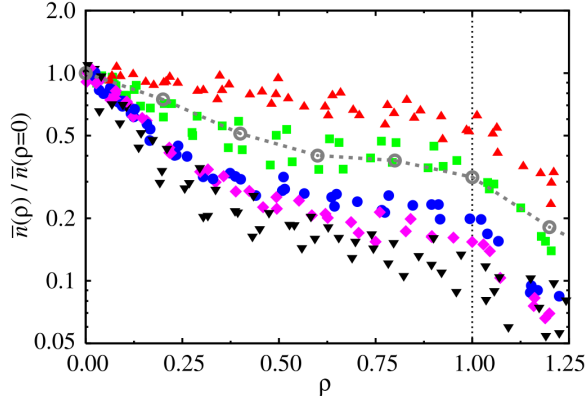


Figure 1.3: Time-averaged, radial profile of the particle density normalized to the separatrix value in the TCV tokamak. The different colored symbols refer to different line-averaged core plasma densities with the black triangles referring to the lowest and the red triangles to the highest value. Reprinted from [9], with permission from IAEA.

For an advective-diffusive transport, however, the particle flux would follow a linear relationship with the inverse density scale length λ_n [22] as

$$\frac{\Gamma_{\perp}}{n} = v_{\perp}^{\text{eff}} - \frac{D_{\perp}^{\text{eff}}}{n} \frac{\partial n}{\partial r} = v_{\perp}^{\text{eff}} + \frac{D_{\perp}^{\text{eff}}}{\lambda_n}. \quad (1.4)$$

In experimental measurements, such as for TCV shown in Fig. 1.5, no linear relationship can be found. Similar studies on the flux-gradient relation in a simple ESEL interchange model of the SOL at constant temperatures, shown in Fig. 1.6, draw an equivalent conclusion [19].

These findings clearly indicate that a different model is needed in order to describe turbulence and cross-field transport in the SOL adequately.

1.4 Intermittent fluctuations in the SOL

In the process of finding a better model describing plasma transport in the SOL of tokamak experiments, measurements of the relative fluctuation levels provide additional insight. Among the first experiments investigating this is the Caltech tokamak where fluctuation levels of 10-90% of the mean were measured in ion saturation current measurements in the edge [23, 24]. Similar observations were made in other experimental devices where these include the TEXT device, shown in Fig. 1.7, and in TCV, Fig. 1.8. The fluctuation profiles

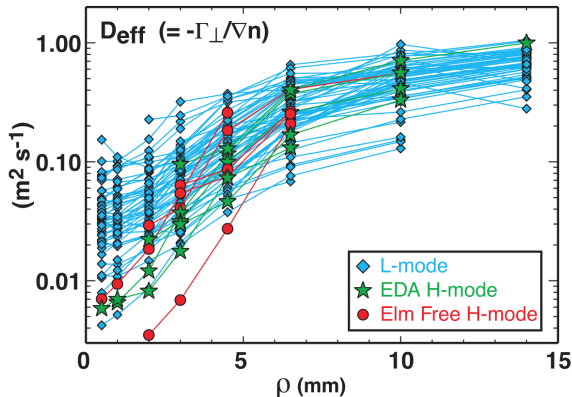


Figure 1.4: Effective diffusivity profiles for different operational modes of the Alcator C-Mod experiment. The effective diffusion coefficient must vary by several orders of magnitude in order to match purely diffusive transport models. Reprinted from [20], with the permission of IAEA.

of the TCV experiment correspond to the time averaged profiles shown in Fig. 1.3. In the low-density case the relative fluctuation levels increase radially in the near SOL and stay approximately constant in the far SOL. Note that the fluctuation levels in the far SOL are independent of the line-averaged core density. For all densities the relative fluctuation levels in the far SOL range between 0.5 and 1, indicating that the broad profiles are dominated by large fluctuations. These findings differ drastically from the plasma core, where fluctuation levels are only around 1% [25].

A more detailed picture of SOL fluctuations can be obtained by analyzing time series of the plasma parameters. These time series are typically obtained by Langmuir probes, consisting of a conducting element which is inserted into the plasma and draws a measurable current [27, 28]. Another well-known method is Gas puff imaging (GPI), where a puff of neutral gas is injected into the plasma edge, so that excitation radiation can be measured [29]. Examples for time series measured at the outboard mid-plane in the far SOL of TCV, Alcator C-Mod and KSTAR are shown in Fig. 1.9. Here, $\tilde{\Phi}$ stands for the time series $\Phi(t)$ normalized to have zero mean and unit standard deviation. In all three devices, the time series show strongly intermittent positive bursts, which suggests an explanation for the large relative fluctuation levels in the SOL. A stochastic model describing these fluctuations as a superposition of uncorrelated pulses was introduced in 2012 [30]. This phenomenological model, known in the context of stochastic processes as the Filtered Poisson Process

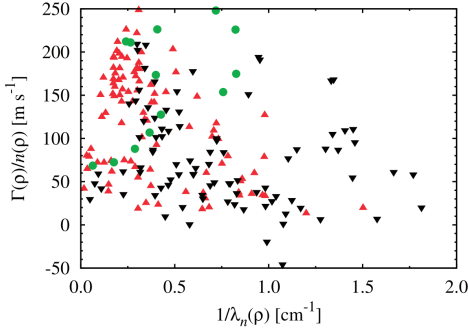


Figure 1.5: The relationship between the normalized radial particle flux and the inverse density scale length for a range of TCV experiments. Reprinted from [22], with the permission from Elsevier.

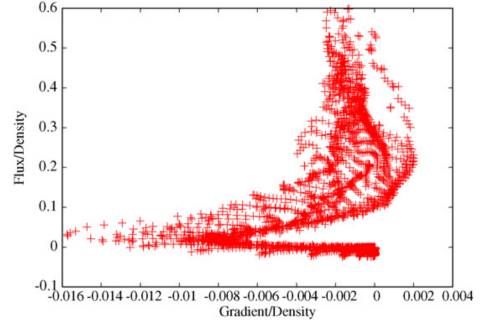


Figure 1.6: The flux–gradient relation in a simple ESEL interchange model of the SOL at constant temperatures. Reprinted from [19], with the permission from Elsevier.

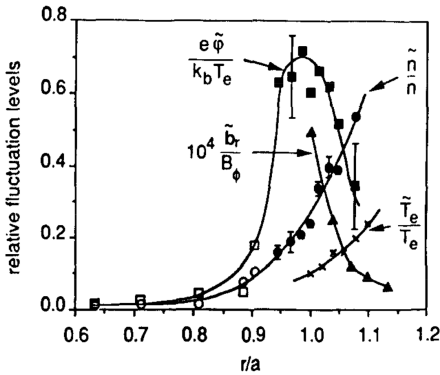


Figure 1.7: Radial dependencies of fluctuation levels of different plasma parameters in the TEXT tokamak experiment. Reprinted from [26], with the permission from Elsevier.

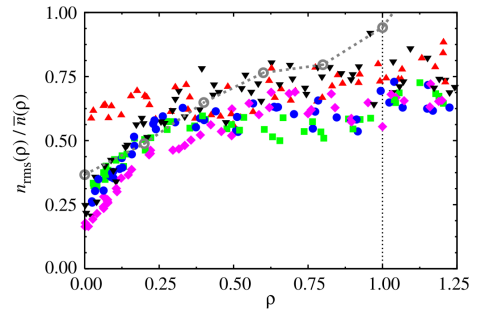


Figure 1.8: Radial profile of the relative fluctuation level of the particle density in the TCV SOL. Reprinted from [9], with permission from IAEA.

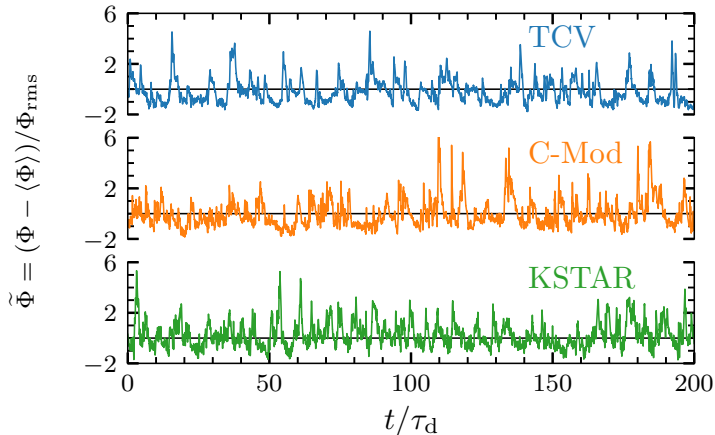


Figure 1.9: Fluctuation time series measured from different tokamak experiments. The time is normalized by the characteristic duration time of the underlying bursts. The black line indicates the mean value of the signal. Image courtesy of A. Theodorsen [39].

(FPP), remains to the day of writing this thesis the most accurate statistical description of SOL fluctuations, as all of its major assumptions and predictions agree with the statistical properties of experimental measurements [31–38]. A detailed discussion of the FPP model is provided in Chapter 3 of this thesis.

The statistical properties of the fluctuations appear to be remarkably universal across numerous tokamak experiments, confinement modes and plasma parameters. Since positive fluctuations dominate over negative ones, the probability density functions (PDFs) are positively skewed and flattened. Fig. 1.10 shows the PDFs of the ion saturation current measured in the boundary of four different devices, exhibiting almost identical results. Time series obtained at different radial positions in the boundary region of Alcator C-Mod exhibit close to normal distributions near the separatrix, whereas in the far SOL show increasingly skewed PDFs with an exponential tail towards positive values, as shown in Fig. 1.11. Collectively, all of these PDFs are well described by a Gamma distribution with a shape parameter depending on the intermittency of the time series [40]. PDFs with exponential tails towards positive events have also been observed in multiple other devices such as TCV, Tore Supra and KSTAR [9, 35, 41–45]. The skewness and kurtosis of these time series are exceeding 0 and 3 respectively, as they would be for a normal distribution. A parabolic relationship between skewness and kurtosis has been demonstrated in [46–48] which remains consistent with predictions of the FPP model [49].

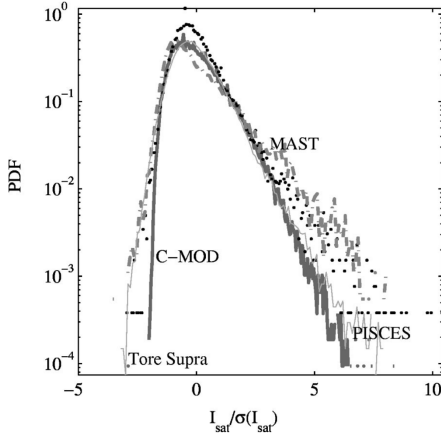


Figure 1.10: PDF of the ion saturation current in the boundary of Tora Supra, Alcator C-Mod, MAST and PISCES. Reprinted from [42], with permission from AIP Publishing.

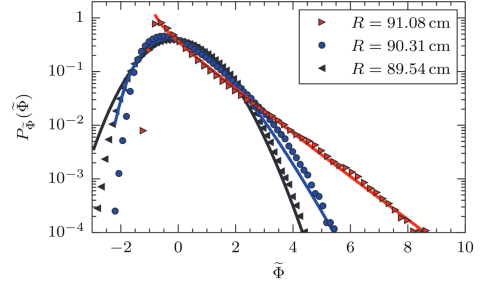


Figure 1.11: PDFs of gas puff imaging data time series at different radial positions in the boundary of Alcator C-Mod. The full lines represent the predictions of the FPP model. Reprinted from [40], with permission from IAEA.

The universality of plasma fluctuations in the SOL is also observed in the power spectral densities (PSDs) of the measured time series [36–38, 40, 50, 51]. The PSDs of time series for the ion saturation current in a variety of devices are shown in Fig. 1.12. For a given scaling factor for the frequency axis all PSDs collapse to a single curve. In contrast to the PDFs, the radial position does not seem to have any influence on the PSDs as shown for Alcator C-Mod in Fig. 1.13. In all experimental measurements the PSD remains flat for low frequencies and shows a power law decay for high frequencies. The analysis of these fluctuations utilizing the FPP framework has shown that the shape of the PSD can be attributed to the shape of the underlying pulses from the time series [52], providing further support for the stochastic model.

Apart from stochastic modeling, conditional averaging can be applied in order to reveal the shape of these large-amplitude fluctuations. Hereby all events above a certain threshold, typically 2.5 times the rms-value above the signal mean, are considered and their peak is stored within a time window. The average over all windows is referred to as the conditionally averaged waveform, showing a sharp peak with a short rise and longer decay [9, 31, 33, 35–37, 42, 44, 53]. The conditionally averaged waveform of time series acquired from the boundary of TCV are shown in Fig. 1.14. The shape of these large-amplitude fluctuations remain similar for all line-averaged core densities of the experiment and are reproducible by numerical simulations of the two-dimensional ESEL

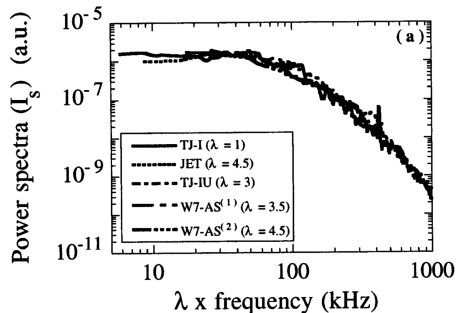


Figure 1.12: PSDs of fluctuation time series of the ion saturation current in various devices. Reprinted figure with permission from [50]. Copyright (1999) by the American Physical Society.

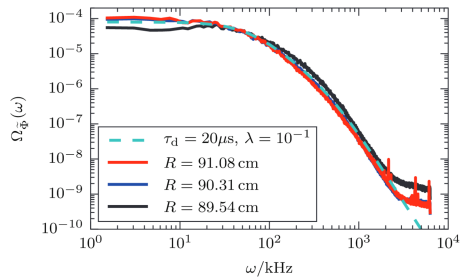


Figure 1.13: PSDs for gas puff imaging time series at different radial positions in the edge of Alcator C-Mod. The broken line shows the FPP predictions. Reprinted from [40], with permission from IAEA.

model. Fig. 1.15 shows the agreement of conditionally averaged waveforms for time series measured in different tokamak experiments and compared to an asymmetric, two-sided exponential function. Both the distribution of the maximal amplitude of the conditional structures and the waiting times between two consecutive peaks are found to be exponentially distributed [33, 35–37, 54].

In conclusion, the statistical properties of time series measured at the mid-plane boundary of tokamak devices indicate that the SOL is dominated by intermittent structures. In order to investigate the shape of these objects and to gain more information about the physical mechanisms responsible for their transport, stochastic modeling alone, however, does not suffice.

1.5 Plasma filaments

2D imaging diagnostics such as GPI and wide angle visible imaging reveal that edge transport in the SOL can be attributed to coherent structures. These objects have historically been featured under a variety of names, such as intermittent plasma objects (IPOs), avaloids, solitary vortices and streamers, but are most commonly referred to as filaments or blobs in recent literature. First observations of plasma filaments were made with fast cameras at the Caltech tokamak in the mid 1980's [55–57] and with 2D probe arrays in the 1990's [58, 59]. The importance of filaments for edge transport, however, has only been considered at the discovery of the main chamber recycling regime at Al-

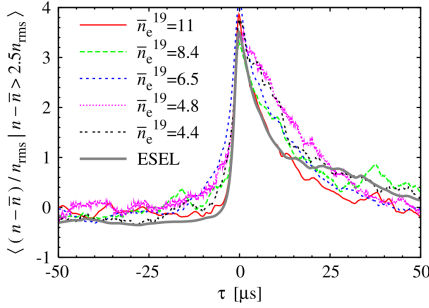


Figure 1.14: Conditionally averaged waveform of particle density time series from TCV and ESEL simulations. Reprinted from [9], with permission from IAEA.

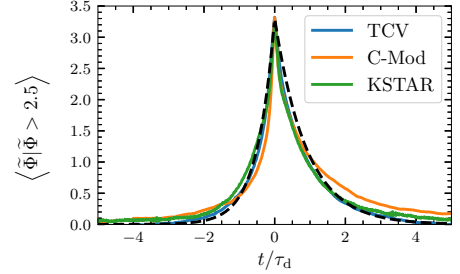


Figure 1.15: Conditionally averaged waveform for time series measured in the edge of TCV, Alcator C-Mod and KSTAR. The broken line shows a two-sided exponential fit. Image courtesy of A. Theodorsen [39].

cator C-Mod in 1998 [60]. Since then, plasma filaments have been observed in over 40 devices, including all major tokamak experiments, with a variety of diagnostics [61]. Filaments typically have a significantly higher density than the surrounding plasma and are aligned to the local magnetic field with their scale lengths much larger in the direction parallel to the magnetic field compared to the perpendicular direction. Filaments have a cross-field size between 2 mm and 10 cm, radial velocity of 0.2 to 2 km/s and a lifetime in the range of tens of μs [62–70]. Examples of plasma filaments for different confinement modes in the MAST device are shown in Fig. 1.16. The elongation of the filaments along the magnetic field, stretching from the upper to the lower divertor is clearly visible. Filaments propagate through the SOL due to interchange motion, illustrated in Fig. 1.17. A simplified model ignoring parallel dynamics explains filament motion as follows: Due to the magnetic geometry at the outboard mid-plane, magnetic gradient and curvature drifts result in a charge polarization, perpendicular to the magnetic field \mathbf{B} . This results in an electric field \mathbf{E} , transporting the filament in the radial direction with the $\mathbf{E} \times \mathbf{B}$ velocity \mathbf{u}_E . While the filaments propagate outwards they carry particles and heat much faster than purely diffusive transport would allow, explaining the broad profiles in the SOL. Fig. 1.18 shows an example of a filament propagating through the SOL of NSTX. Here, the filament is visualized in the plane perpendicular to the field lines. Due to their appearance in the two-dimensional plane, filaments are often referred to as blobs in this context.

Measurements using Langmuir probes and GPI simultaneously confirmed that propagating filaments are the same structures that cause intermittent

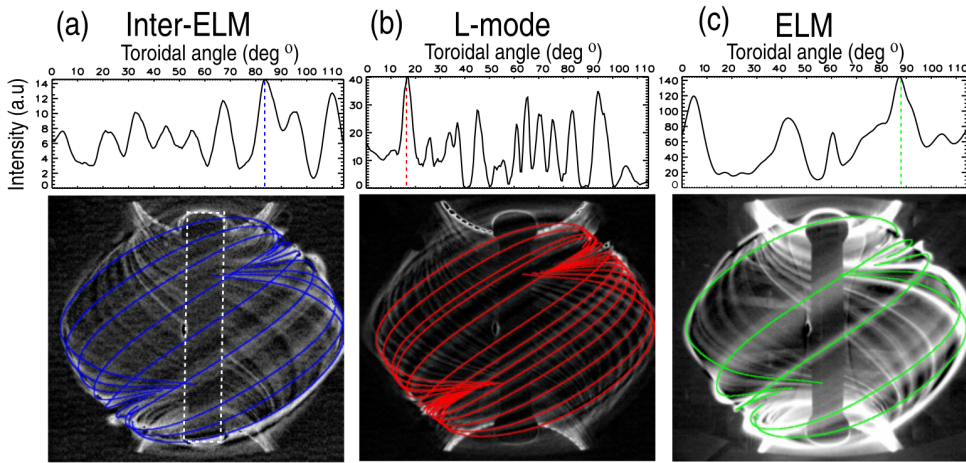


Figure 1.16: Wide angle fast visible imaging of inter-ELM, L-mode and ELM filaments in the MAST device. The panels above show the toroidal variation in emission across the center column, the peaks are used to label the filaments. Reprinted from [71], © IOP Publishing. Reproduced with permission. All rights reserved.

bursts in the time series [74, 75]. The intermittency of the time series and the length and amplitude of individual bursts are therefore given by the filament parameters.

Even though radial blob propagation can be qualitatively understood with the presented two-dimensional model, parallel dynamics must be considered for a more accurate picture [7]. Since the filament plasma is neutral, the current due to magnetic gradient and curvature drifts must be closed. The charged particles stream along the magnetic field lines until they reach the target plates where the resulting parallel current can close in the plasma Debye sheath. The parallel resistivity of the plasma and the sheath resistivity limits the magnitude of the parallel current. Alternatively, the current can be closed by polarization currents in the cross-field plane, thereby creating the dipolar electric potential. A schematic illustration of the current paths are shown in Fig. 1.19. The ratio of the current closed through the parallel and perpendicular path determines the strength of the electric field in the filament and therefore its $\mathbf{E} \times \mathbf{B}$ velocity. If the parallel currents are dominant and close mainly in the plasma sheath the filament is said to be in the “sheath limited” regime, while in the case where the currents are closed in the cross-field plane, the filament is in the “inertial” regime. Analytical velocity scaling laws show that the radial velocity of a filament v_{\perp} is strongly dependent on its perpendicular size a of a filament

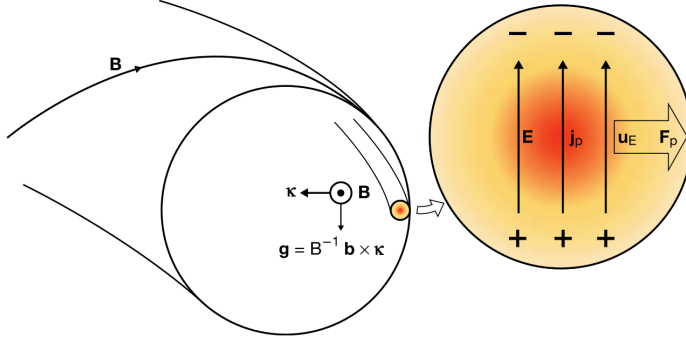


Figure 1.17: Illustration of charge separation in the filament and the resulting $\mathbf{E} \times \mathbf{B}$ drift, transporting the filament in the radial direction. Reprinted from [72], with the permission from AIP Publishing.

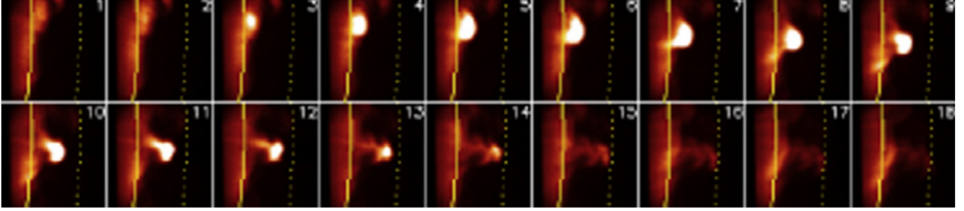


Figure 1.18: Propagation of a blob from the main plasma through the SOL in the NSTX device. Each box shows a 24×24 cm portion of the edge at the outer mid-plane and the frame rate is $7\mu\text{s}$. The position of the separatrix is given by the full line and the the wall shadow by the broken line. Reprinted from [73], with the permission from Elsevier.

[76, 77], as

$$v_{\perp}(a) \propto \begin{cases} \sqrt{2a} & \text{for } a \gg a^* \\ 1/a^2 & \text{for } a \ll a^* \end{cases} \quad (1.5)$$

where a^* is defined as

$$a^* = \left(\frac{4L^2}{\rho_s R} \right)^{1/5} \rho_s. \quad (1.6)$$

In this expression L stands for the connection length to the divertor targets, R is the major radius of the tokamak and ρ_s the ratio between the acoustic speed and the ion gyration radius. These velocity scaling laws are reproduced with numerical simulations [78–80]. However, it is found difficult to match these laws to experimental observations in both asymptotic limits, as small

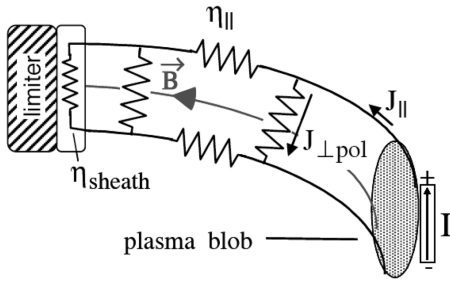


Figure 1.19: Schematic illustration of current paths within a filament. Reprinted from [7]. Copyright © Cambridge University Press 2008.

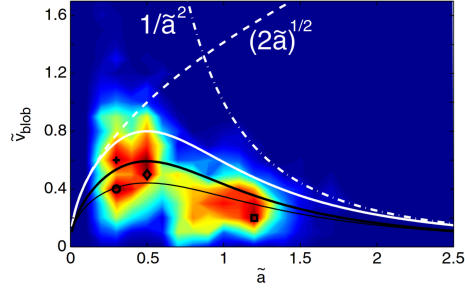


Figure 1.20: Joint probability of the normalized filament velocity and cross field size in the TORPEX device. Reprinted figure with permission from [76]. Copyright (2009) by the American Physical Society.

filaments are difficult to identify and filaments cannot become larger than the SOL width [65, 66]. Relatively good agreement has been found in the toroidal plasma device TORPEX shown in Fig. 1.20, showing the joint probability of the filament velocity and cross-field size [76]. Here, the perpendicular width of the filaments is normalized by a^* and the filament velocity by

$$v^* = \left(\frac{2L\rho_s^2}{R^3} \right)^{1/5} c_s \quad (1.7)$$

with c_s standing for the ion sound speed. The dashed and dotted lines show the ideal scaling laws for the inertial and sheath connected regimes. It is found that the cross-field size of filaments is in between the scale length of the plasma pressure gradient and the particle gyration radius, hence, filaments are often referred to as mesoscale structures.

Even though filament generation has been extensively studied in tokamak plasmas [81, 82], simple toroidal plasmas [83–86] and numerical simulations [87–90], to this day no quantitatively accurate analytical model of filament generation has been developed [61, 91, 92]. A number of linear instabilities have been identified that are attributed to cause filament generation, namely the interchange, drift-wave, Kelvin-Helmholtz, Rayleigh–Taylor, resistive-ballooning and conducting-wall instabilities [61, 93]. Due to the limited understanding of the intricate physics responsible for filament generation in tokamak plasmas, this topic remains a field of active research.

1.6 Numerical modeling of SOL plasmas

As experimental measurements and analytical models for SOL turbulence and plasma filaments face intrinsic limitations, numerical simulations of first principle based models have provided further insight. Due to the complexity of the involved physics, it remains a delicate task to derive models with appropriate approximations that still capture the most relevant physical mechanisms of SOL turbulence. Attempts to model the SOL with gyrokinetic particle-in-cell codes are limited by their enormous computational costs and their dependence on poorly understood boundary conditions [94, 95]. Electromagnetic gyrofluid models have been derived [96] and applied for studying temperature dynamics and finite Larmor radius effects on filaments [97, 98], as well as turbulence in open and closed magnetic field lines [99, 100]. At present, most numerical models for SOL turbulence and filament dynamics originate from the standard plasma fluid transport equations derived by Braginskii [101]. The derivations of the fluid models used in the papers and manuscripts included in this thesis are discussed in Chapter 2.

Numerical simulations of SOL plasmas can be categorized into models of saturated turbulence where filament-like structures are created due to non-linear dynamics, and simulations of explicitly seeded, isolated filaments. The first self-consistent evolution of a seeded plasma blob in two dimensions has been studied in 2003 [102], shown in Fig. 1.21. Here, the blob is initialized as a symmetrical 2D-Gaussian on a constant plasma background. The radial propagation and the evolution of the blob into a mushroom-shaped object with a steep front has been observed. The radial variation of the density of the blob and its according $\mathbf{E} \times \mathbf{B}$ velocity is shown in Fig. 1.22. The peak of the radial velocity is trailing the density peak, resulting in a steepening of the blob front. The according temporal evolution is shown in Fig. 1.23, where the observed pulses have a short rise and long fall time; an observation consistent with the underlying pulses of time series in experiments such as in Fig. 1.9. Studies of isolated filaments have been extended to three dimensions, considering dynamics parallel to the magnetic field [103–108] and have been used to investigate specific physical effects such as electromagnetic effects or finite ion Larmor radius effects [103, 109–111]. Models for radial blob velocity dependencies on filament amplitudes and sizes have been developed [78, 80, 112, 113]. Simulations of multiple simultaneously seeded filaments discovered that filaments in close proximity interact through the electric potential they generate [114, 115]. A systematical analysis of blob interaction in dependence of the intermittency, defined as the level of blob overlap, is presented in Paper IV.

First attempts of modeling plasma turbulence typically use two-dimensional slab geometries, where curvature effects are modeled by effective gravity terms.

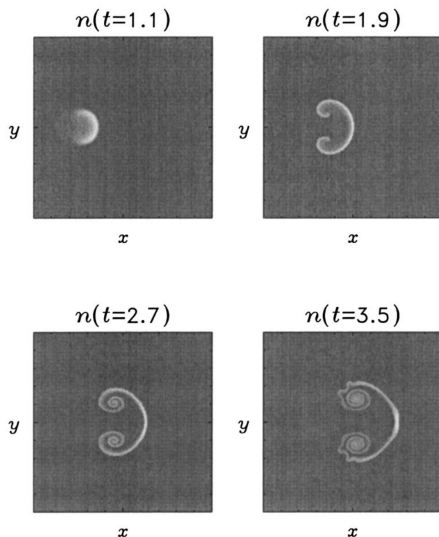


Figure 1.21: Contour plot of the evolution of a 2D density blob. Reprinted from [102], with the permission from AIP Publishing.

Rayleigh–Bénard convection models have been used as a simplified description of the non-linear interchange dynamics in the SOL [116–123]. These models have been further extended by including sheath dissipation due to losses along magnetic field lines and drift wave dynamics in the edge region [87, 124–133]. One example for a turbulence simulation in a 2D slab geometry of a model including sheath dissipation is presented in Fig. 1.24. Plasma streaming from the core into the SOL is modeled as a density source term in the left hand side of the simulation domain. Small perturbations in the plasma density become unstable and result in coherent structures that propagate radially outwards due to the interchange mechanism. The transition from closed to open magnetic field lines is simulated by applying different closures for the parallel dynamics. These 2D turbulence simulations have contributed to the understanding of the stability of filaments in the SOL and were able to reproduce the characteristic PDFs of plasma fluctuations and their radial variations [131, 134]. Further investigations on the statistical properties in turbulence simulations can be performed by analyzing time series [9, 123, 135–137] and blob tracking methods in order to investigate filament properties [138–141].

Advances in computing power enabled three-dimensional turbulence simulations in the last decade, taking into account the parallel dynamics in SOL plasmas [106, 142–147]. Three-dimensional simulations enable implementing realistic geometries and can therefore be used to explore X-point effects and dif-

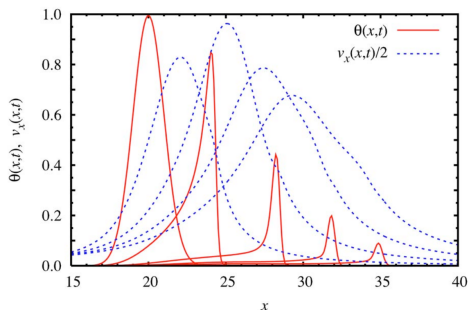


Figure 1.22: Radial variation of the plasma density (full line) and the radial velocity (broken line) at the symmetry axis of a seeded blob. Reprinted from [112], with the permission from AIP Publishing.

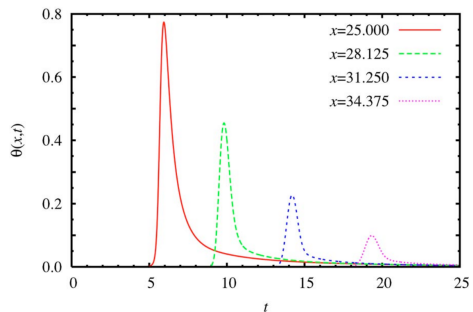


Figure 1.23: Temporal evolution of the plasma density recorded at the symmetry axis at different radial positions. Reprinted from [112], with the permission from AIP Publishing.

ferent divertor configurations [139, 148]. Due to their immense computational costs, three-dimensional turbulence simulations have relatively short runs, limiting the amount of statistical analysis that can be performed.

A variety of comparisons between the output from numerical simulation codes and experiments have been performed in order to validate simulation codes. These studies mainly focused on the dynamics of individual blob structures or on specific physical effects on turbulence and transport. Surprisingly little attention has been attributed to comparisons of fluctuation statistics, considering their universal nature in experiments. The published papers and yet unpublished manuscripts included in this thesis attempt to fill this gap. Here, the main focus lies on utilizing the FPP model, which predicts all major statistical properties of experimental measurements at the outboard mid-plane. By comparing time series from numerical simulations to the predictions of the FPP model one can identify which parameters and assumptions conform to experimental observations. We can thereby gain additional insight and a better understanding of the intricate physics of the boundary of present and future fusion devices.

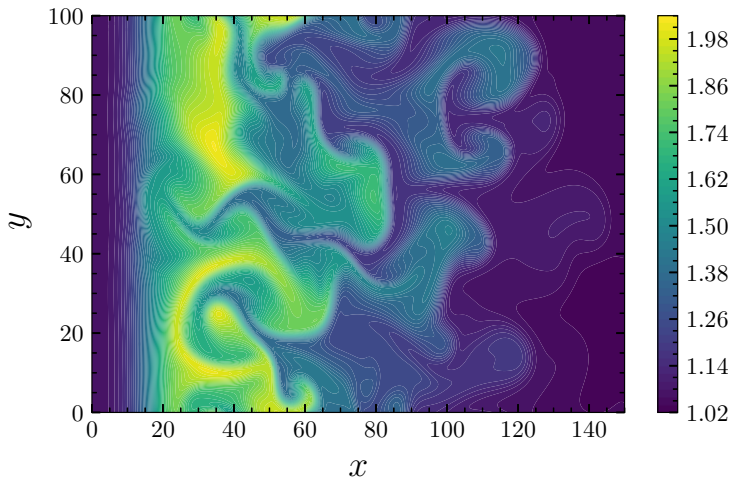


Figure 1.24: Snapshot of plasma density of a two-dimensional turbulence simulation. Plasma is injected into the simulation domain at a constant rate and generates blob-like structures due to turbulence. Reprinted from [141], with the permission from AIP Publishing.

2 | Reduced fluid models for SOL plasmas

In this chapter, a brief derivation of the reduced fluid models used in the included publications is presented. The derivations start from the Braginskii fluid equations whose assumptions and validity for SOL plasmas are discussed. Applying drift reduction, Bohm-normalization and a number of approximations, results in the reduced two-fluid model, equivalent to the two-dimensional fluid models used in Paper III and IV. By applying interchange normalization this model will be further modified to the idealized interchange model, used in Paper I.

2.1 Braginskii fluid equations

The Braginskii fluid model is derived by taking successive velocity moments of the kinetic Boltzmann equation and applying a collisional closure. Each moment depends on the next higher order and therefore require additional assumptions to obtain a closure for the model. The Braginskii equations describe the evolution of the three lowest order fluid moments. The assumptions and the formulation of this closure are presented in [101]. The standard Braginskii fluid equations describing the evolution of the particle density n_α , fluid velocity \mathbf{u}_α and temperature T_α for particle species α are given by

$$\frac{\partial n_\alpha}{\partial t} + \nabla \cdot (n_\alpha \mathbf{u}_\alpha) = 0, \quad (2.1)$$

$$m_\alpha n_\alpha \left(\frac{\partial}{\partial t} + \mathbf{u}_\alpha \cdot \nabla \right) \mathbf{u}_\alpha = -\nabla p_\alpha - \nabla \cdot \Pi_\alpha + Z_\alpha e n_\alpha (\mathbf{E} + \mathbf{u}_\alpha \times \mathbf{B}) + \mathbf{R}_\alpha, \quad (2.2)$$

$$\frac{3}{2} n_\alpha \left(\frac{\partial}{\partial t} + \mathbf{u}_\alpha \cdot \nabla \right) T_\alpha + p_\alpha \nabla \cdot \mathbf{u}_\alpha = -\nabla \cdot \mathbf{q}_\alpha - \Pi_\alpha : \nabla \mathbf{u}_\alpha + Q_\alpha. \quad (2.3)$$

Here, α determines the particle species, i.e., electrons and ions, m the particle mass, p the pressure, $Z_\alpha e$ the particle charge, \mathbf{R} the friction force, Π the viscous stress tensor, \mathbf{q} the heat flux, $:$ the tensor inner product and Q the frictional interspecies heating and energy exchange.

The Braginskii equations are only applicable if certain assumptions for the modeled system are valid. Applying fluid equations requires that the distribution of particle velocities is close to Maxwellian, i.e., the time scale of relaxation back to a Maxwellian must be shorter than the characteristic time scales of the modeled system. If this condition is fulfilled, the system is referred to as collisional. In addition to being collisional, a plasma must be strongly magnetized to be adequately described by the Braginskii equations. This implies that the particles complete many gyrations between collisions, setting an upper limit for the collisionality of the plasma.

In summary, the phenomenon we want to model needs to satisfy the following conditions in order to be well described by the Braginskii equations:

$$L_\perp \gg \rho_\alpha, \quad (2.4)$$

$$L_\parallel \gg \lambda, \quad (2.5)$$

$$\tau \gg \tau_c \gg \Omega_\alpha^{-1}. \quad (2.6)$$

In these expressions L_\perp stands for the characteristic size of the modeled phenomena perpendicular to the magnetic field, ρ_α is the gyration radius for species α , L_\parallel the parallel size of the system, λ the collisional mean free path, τ the characteristic time of the problem, τ_c the collision time and Ω_α the gyration frequency of the referred particle species [149].

For the further derivation using drift reduction it will be useful to quantify the magnetization. We thereby define the magnetization parameter δ as

$$\delta = \frac{\rho_\alpha}{L_\perp}. \quad (2.7)$$

The magnetization can be equivalently expressed in the temporal domain by

$$\delta = \frac{\nu_{ie}}{\Omega_i} \quad (2.8)$$

where ν_{ie} stands for the collisional frequency between ions and electrons.

For both electrons and ions the magnetization parameter is $\delta \ll 1$ for a fully magnetized plasma.

2.2 Drift reduction

The Braginskii model given by Eqs. (2.1) - (2.3) is very general, making modeling of SOL plasmas with the presented equations relatively inefficient. A more suitable description of plasma phenomena in the SOL can be derived by simplifying the presented model with an approach called drift ordering. Since turbulence and filaments in the SOL, evolve with velocities much lower than the plasma sound speed $c_s = \sqrt{(T_e + T_i)/m_i}$ we apply the ordering

$$\mathbf{u}_\perp \sim \frac{\rho_\alpha}{L_\perp} c_s \sim \delta c_s. \quad (2.9)$$

This ordering assumes that the transverse electric fields are small, resulting in the perpendicular electric field being substantially electrostatic. This is a direct consequence of the $\mathbf{E} \times \mathbf{B}$ velocity being a factor δ smaller than sound speed and Faraday's law [149]. We can now determine the perpendicular part of the momentum equation, given by Eq. (2.2), by taking the cross product with \mathbf{B} resulting in

$$\mathbf{u}_{\alpha,\perp} = \frac{\mathbf{E} \times \mathbf{B}}{B^2} - \frac{\nabla p_\alpha \times \mathbf{B}}{e_\alpha n_\alpha B^2} - \frac{m_\alpha d\mathbf{u}_\alpha/dt \times \mathbf{B}}{e_\alpha B^2} - \frac{\nabla \cdot \Pi_\alpha \times \mathbf{B}}{e_\alpha n_\alpha B^2} + \frac{\mathbf{R}_\alpha \times \mathbf{B}}{e_\alpha n_\alpha B^2}, \quad (2.10)$$

where we used $d/dt = \partial/\partial t + (\mathbf{u}_\alpha \cdot \nabla)$ and assumed single charge particle species, i.e., $Z_\alpha e = e_\alpha$. The terms in this expression display the fluid drifts occurring in the system, namely from left to right: the $\mathbf{E} \times \mathbf{B}$ drift; the diamagnetic drift; the polarization drift; the viscous drift and the collisional drift. From this expression we can determine the dominant drifts and thereby simplify the model.

As mentioned previously, the electric drift velocity is of $\mathcal{O}(\delta)$ compared to the plasma sound speed:

$$\mathbf{u}_E = \frac{\mathbf{E} \times \mathbf{B}}{B^2} \sim \delta c_s. \quad (2.11)$$

Similarly, the diamagnetic drift is also of $\mathcal{O}(\delta)$ since

$$\mathbf{u}_{\text{dia}} = -\frac{\nabla p_\alpha \times \mathbf{B}}{e_\alpha n_\alpha B^2} \sim \frac{n_\alpha T_\alpha B}{L_\perp e_\alpha n_\alpha B^2} \sim \frac{T_\alpha}{L_\perp \Omega_\alpha m_\alpha} \sim \delta c_s. \quad (2.12)$$

The polarization drifts for both ions and electrons are smaller in comparison, as can be shown by

$$\mathbf{u}_{\text{pol},i} = \frac{m_i d\mathbf{u}_i/dt \times \mathbf{B}}{e_i B^2} \sim \delta^3 c_s, \quad (2.13)$$

and

$$\mathbf{u}_{\text{pol},e} \sim \frac{m_e}{m_i} \delta^3 c_s. \quad (2.14)$$

For the viscous drift we use Bragniskii's approximation for the perpendicular component of the viscous stress tensor $\Pi_\alpha \sim (p_\alpha/\Omega_\alpha)\nabla v_\alpha$ which shows that this term is of $\mathcal{O}(\delta^3)$ since

$$\mathbf{u}_{\text{vis},i} = \frac{\nabla \cdot \Pi_\alpha \times \mathbf{B}}{e_\alpha n_\alpha B^2} \sim \frac{nT\delta c_s}{e_i n_i B L_\perp^2 \Omega} \sim \delta^3 c_s, \quad (2.15)$$

and

$$\mathbf{u}_{\text{vis},e} \sim \frac{m_e}{m_i} \delta^3 c_s, \quad (2.16)$$

respectively. Lastly, we need to find an approximation for the collisional drift. For this we use $\mathbf{R}_\perp = en\mathbf{J}_\perp/\sigma_\perp$ for the perpendicular momentum transfer from electron-ion friction and $\sigma_\perp = ne^2\nu_{ei}/m_e$. From the ordering follows $\mathbf{J}_\perp \sim en\delta c_s$ which leads to the approximation of the frictional drift

$$\mathbf{u}_{\text{fri}} = \frac{\mathbf{R}_\alpha \times \mathbf{B}}{e_\alpha n_\alpha B^2} \sim \frac{ne\delta c_s}{B\sigma_\perp} \sim \frac{m_e}{m_i} \frac{\nu_{ei}}{\Omega} \delta c_s. \quad (2.17)$$

For SOL conditions we can typically assume that $\nu_{ei}/\Omega \sim \delta$ so that the collisional drift is of $\mathcal{O}(\delta^2)$.

This ordering reveals that the dominant perpendicular drifts are the electric and the diamagnetic drifts as all other drifts are at least one order of magnitude smaller. By substituting the remaining drifts into the Bragniskii equation we can rewrite the electron density equation in a simpler form,

$$\frac{\partial n_e}{\partial t} + \nabla \cdot [n_e (\mathbf{u}_E + \mathbf{u}_{\text{dia},e} + \mathbf{u}_{e\parallel})] = 0. \quad (2.18)$$

Since the plasma is quasi-neutral, i.e. $n_e \simeq n_i \simeq n$, this equation is used to describe the evolution of the total plasma density n . Eq. (2.18) is usually manipulated to

$$\frac{\partial n}{\partial t} + \mathbf{u}_E \cdot \nabla n = -\nabla \cdot (n\mathbf{u}_{\parallel,e}) + \left(\frac{1}{e} \nabla p_e - n \nabla \phi \right) \cdot \nabla \times \left(\frac{\mathbf{b}}{B} \right). \quad (2.19)$$

Instead of explicitly deriving separate continuity equations for electrons and ions, we can utilize quasi-neutrality and charge conservation to derive an equation for the fluid velocity, which will prove to be very handy. For this we use $\nabla \cdot \mathbf{J} = 0$ with $\mathbf{J} = en(\mathbf{u}_i - \mathbf{u}_e)$. Inserting all drifts that give rise to a net current results in

$$\nabla \cdot (\mathbf{J}_{\text{dia}} + \mathbf{J}_{\text{pol}} + \mathbf{J}_{\text{vis}} + \mathbf{J}_{\parallel}) = 0. \quad (2.20)$$

In the following we only include the leading order drifts in the ion polarization velocity and neglect the electron polarization drift entirely due to the small electron mass. The sum of the ion polarization and viscous drifts using the lowest order solution of the perpendicular momentum equation and the parallel velocity $\mathbf{u}_0 = \mathbf{u}_{0\perp} + \mathbf{u}_{i\parallel}$ is then given by

$$\mathbf{u}_{\text{pol},i} + \mathbf{u}_{\text{vis},i} = \mathbf{b} \times \frac{1}{enB} \left[m_i n \left(\frac{\partial}{\partial t} + \mathbf{u}_{i0} \cdot \nabla \right) \mathbf{u}_{i0} + \nabla \cdot \Pi_{i0} \right], \quad (2.21)$$

where Π_{i0} is the viscous stress tensor calculated with \mathbf{u}_{i0} and

$$\mathbf{u}_{0\perp} = \mathbf{b} \times \frac{1}{B} \left(\nabla \phi + \frac{1}{en} \nabla p_i \right). \quad (2.22)$$

Inserting this into Eq. (2.20) leads to the drift-reduced charge conservation equation [149]

$$-\nabla \cdot \left\{ \mathbf{b} \times \frac{1}{B} \left[m_i n \left(\frac{\partial}{\partial t} + \mathbf{u}_{i0} \cdot \nabla \right) \mathbf{u}_{i0} + \nabla \cdot \Pi_{i0} \right] \right\} = \nabla \cdot \mathbf{J}_{\parallel} + \nabla \cdot (p_i + p_e) \cdot \nabla \times \left(\frac{\mathbf{b}}{B} \right), \quad (2.23)$$

which will be further simplified in the following.

2.3 Further approximations and simplifications

A number of additional approximations are applied to simplify the model and make it efficiently numerically solvable.

First of all, we apply the electrostatic approximation, and thereby neglect all time derivatives of \mathbf{B} and calculate the electric field \mathbf{E} directly from the electric potential. Under this approximation, Eq. (2.23) can be expressed in the more readable form

$$m_i \nabla \cdot \left[\frac{n}{B} \frac{d_0}{dt} \left(\frac{\nabla_{\perp} \phi}{B} + \frac{\nabla_{\perp} p_i}{enB} \right) \right] - \nabla \cdot (\mathbf{b} \times \nabla \cdot \Pi_0) = \nabla \cdot \mathbf{J}_{\parallel} + \nabla \cdot (p_i + p_e) \cdot \nabla \times \left(\frac{\mathbf{b}}{B} \right), \quad (2.24)$$

where we used $d_0/dt = \partial/\partial t + (\mathbf{u}_{i0} \cdot \nabla)$. In addition, we neglected spatial non-uniformity of \mathbf{B} , which will be discussed in further detail later. Studies of electromagnetic effects on plasma blob-filament transport showed that these effects in high temperature or high beta plasmas suppress the resistive

drift wave turbulence in filaments [109, 150] but will not be considered in the following.

We can further simplify Eq. (2.24) by applying scale separation for the plasma density, so that $\nabla n \sim \nabla n_0 + \nabla \tilde{n} \sim 1/L_n + k\tilde{n}$, where the particle density has been separated into a background n_0 and a fluctuation \tilde{n} . L_n stands for the characteristic scale length for the background density and k for the wave number for the particle density fluctuations. Dividing by n_0 leads to $\nabla \ln n \sim 1/L_n + k\tilde{n}/n_0$. We now assume that $1/kL_n \ll 1$ and $\tilde{n}/n_0 \ll 1$. The latter assumption is the so called thin layer or Boussinesq approximation where we assume that the density perturbations are small compared to the equilibrium. This assumption is hardly justified since relative fluctuations in the SOL can be of order unity as discussed in the previous chapter. This approximation is, however, commonly used since it makes the numerical integration of Eq. (2.24) significantly more efficient. By introducing a generalized vorticity,

$$\varpi = \nabla \cdot \left(\nabla_{\perp} \phi + \frac{\nabla_{\perp} p_i}{en} \right), \quad (2.25)$$

we can now simplify the first term in Eq. (2.24) to

$$m_i \nabla \cdot \left[\frac{n}{B} \frac{d_0}{dt} \left(\frac{\nabla_{\perp} \phi}{B} + \frac{\nabla_{\perp} p_i}{enB} \right) \right] \approx \frac{m_i n}{B^2} \frac{d_0 \varpi}{dt}. \quad (2.26)$$

From this expression, ϖ can be relatively easily inverted, especially when assuming that ions are cold, leading us to the next approximation.

For the remaining derivation we will assume small ion temperature, $T_i \ll T_e$, simplifying the equations significantly. This is a restrictive assumption, as experimental measurements indicate that the ion temperature is higher than the electron temperature in the SOL [151, 152]. Numerical simulations incorporating finite ion temperature have shown that the coherency of filaments is increased [153]. However, since the simplified model still captures the fundamental dynamics in the SOL, this approximation is commonly used to reduce the model complexity.

As for the electrons, all models in the included publications and manuscripts assume isothermal electrons. This assumption simplifies the model drastically, as it makes Eq. (2.3) obsolete. Numerical simulations of isolated filaments with dynamic electron temperature have shown that thermal effects lead to a strong increase in the filament propagation in the poloidal direction and reduce the net radial propagation. These effects arise from the electron temperature dependence of the sheath currents, which will be discussed later in this chapter [154].

Next, we will define the geometry of the magnetic field. For the whole simulation domain, we assume straight magnetic field lines with constant field

strength. We need to make one exception to this assumption, as no curvature term would remain in a completely homogeneous field. As there would be no drive for filament motion without this term, it is required to capture some effects of curvature in the model. With the use of vector algebra presented in [149] we can write the curvature term from Eqs. (2.19) and (2.24) as

$$\nabla \times \left(\frac{\mathbf{b}}{B} \right) = 2 \frac{\mathbf{b} \times \boldsymbol{\kappa}}{B} + \frac{\mu_0 (\mathbf{J}_{\parallel} - \mathbf{J}_{\perp})}{B^2}, \quad (2.27)$$

where we introduced the curvature vector $\boldsymbol{\kappa} = (\mathbf{b} \cdot \nabla)\mathbf{b}$. Note that one unit of the term $\mathbf{b} \times \boldsymbol{\kappa}/B$ originates from the magnetic gradient and one from the curvature. The second term on the right hand side can be neglected due to charge conservation [149]. The magnetic field in a tokamak can be approximated to lowest order to be purely toroidal and falling radially with $1/R$. In a cylindrical coordinate system (R, Φ, Z) the toroidal magnetic field is therefore

$$\mathbf{B} = \frac{B_0 R_0}{R} \hat{\boldsymbol{\Phi}}. \quad (2.28)$$

In a slab geometry with Z being replaced with the binormal direction y which is perpendicular to $\hat{\mathbf{R}}$ and $\hat{\boldsymbol{\Phi}}$ this motivates the definition of the curvature operator

$$\mathcal{K}(u) = \nabla \times \left(\frac{\mathbf{b}}{B} \right) \cdot \nabla u \approx -\frac{2}{B_0 R_0} \frac{\partial u}{\partial y}. \quad (2.29)$$

Despite arguing that the frictional drift is negligible in Eq. (2.30) one typically retains an approximation of this term due to numerical reasons. We therefore add this term to Eq. (2.19) as

$$\nabla \cdot (n_e \mathbf{u}_{\text{fri}}) \approx -\nabla \cdot (D_n \nabla_{\perp} n_e) \approx -D_n \nabla_{\perp}^2 n_e, \quad (2.30)$$

where we introduced the density diffusion coefficient D_n which we assumed to be spatially constant. Similarly, one can derive the diffusion term for Eq. (2.24) from its ion viscosity term, since we can use the approximation

$$\nabla \cdot \Pi_i = -m_i n_i \mu_{\omega} \nabla_{\perp}^2 \mathbf{u}_E, \quad (2.31)$$

where μ_{ω} stands for the effective cross-field kinematic viscosity of the ions. Inserting the electric drift and taking the divergence results in the diffusion term for $\nabla_{\perp}^2 \phi$ as

$$\nabla \cdot \left(\frac{m_i \mu_{\omega}}{e B^2} \nabla_{\perp} \nabla_{\perp}^2 \phi \right). \quad (2.32)$$

The diffusion coefficients can be approximated from classical or neo-classical diffusion such as presented in [155], or are chosen for numerical accuracy and stability.

Arguably the starkest simplification of the presented models in this thesis is the restriction to only two dimensions, the plane perpendicular to \mathbf{B} . The parallel closure of the model equations is different for closed and open field lines, i.e., whether the simulation domain is located in the SOL or in the edge region. Since the parallel direction plays an important role in the SOL for particle and current dissipation as plasma flows along the magnetic field lines towards the divertor plates, a suitable approximation for the parallel losses is required. This closure is achieved by integrating over the parallel direction where the so-called sheath boundary conditions come into play. In the initial transient period where the plasma vessel is filled and the cold wall surface electrically neutral, electrons will strike the surface at a higher rate than the ions due to their higher speed. This charges the vessel walls negatively which impedes further electron flow towards the surface and results in a thin sheath at material surfaces. Here, the ions shield the electric potential of the surface and the sheath extends a few Debye lengths, $\lambda_D = \sqrt{\epsilon_0 T_e / n_e e^2}$, outwards from the surface into the plasma. In this region quasi neutrality is violated since the ion density is higher than the electron density, $n_i > n_e$. The electric current density drawn by the vessel walls is governed by the influx of electrons and ions at the sheath surface. It depends on the potential ϕ at the sheath entrance and can be written as

$$\mathbf{J}_{\parallel}|_{\text{sheath}} = en_{se}c_s \left[1 - e^{\Lambda - e\phi/T_e} \right], \quad (2.33)$$

with the plasma density at the sheath edge n_{se} , the acoustic speed c_s and the floating potential $\Lambda = \ln \sqrt{m_i / 2\pi m_e}$. The first term in the parenthesis is due to the ion flux and the second due to the electron flux [17]. We can now take the average of the parallel dimension in a slab geometry with $\mathbf{B} = B\hat{\mathbf{z}}$,

$$\frac{1}{L_{\parallel}} \int_{-L_{\parallel}/2}^{L_{\parallel}/2} \nabla_{\parallel} \cdot \mathbf{J}_{\parallel} dz, \quad (2.34)$$

and use Eq. (2.33) as the boundary conditions. The first term on the right hand side of Eq. (2.19) can be handled analogously for the parallel electron velocity.

Paper III includes a core region in the simulation domain, requiring a different closure for the parallel dynamics. In this model we include resistivity in the parallel component of the electron momentum equation neglecting inertia, i.e.,

$$en \frac{\partial \phi}{\partial z} - T_e \frac{\partial n}{\partial z} + \chi en J_{\parallel} = 0, \quad (2.35)$$

where the resistivity is given by $\chi = m\nu_{ei}/n_e e^2$. Rearranging Eq. (2.35) for J_{\parallel}

and taking the parallel derivative results in [156, 157]

$$\nabla_{\parallel} \cdot \mathbf{J}_{\parallel} = \frac{T_e}{e\chi} \frac{\partial^2}{\partial z^2} \left(\ln n_e - \frac{e\phi}{T_e} \right). \quad (2.36)$$

From this we can take the average of the parallel dimension by integrating over z , resulting in the desired 2D model equations. A systematic analysis of the dimensionality of scrape-off layer turbulence is presented in [147, 158].

2.4 Reduced two-fluid model

Since the Braginskii fluid model is only valid in a specific range of time and length scales it seems natural to normalize all physical variables to values that are characteristic for the modeled system. We will first discuss the so-called Bohm normalization where we normalize the spatial and temporal units by ρ_s and Ω_i , respectively, i.e.,

$$\nabla \rightarrow \nabla' = \rho_s \nabla, \quad \frac{\partial}{\partial t} \rightarrow \frac{\partial}{\partial t'} = \frac{1}{\Omega_i} \frac{\partial}{\partial t}. \quad (2.37)$$

Here, ρ_s stands for the ion sound Larmor radius defined as $\rho_s = \sqrt{T_e m_i} / eB$. We normalize the remaining variables with their characteristic values for SOL conditions N and T_0 as

$$n \rightarrow n' = \frac{n}{N}, \quad T_e \rightarrow T' = \frac{T_e}{T_0}, \quad \phi \rightarrow \phi' = \frac{e\phi}{T_0}. \quad (2.38)$$

From these expressions we can define the characteristic magnitude for the density source, diffusion coefficients and effective gravity drive as

$$S \rightarrow S' = SN\Omega_i, \quad D_n \rightarrow D'_n = D_{\text{Bohm}} D_n, \quad \mu_{\omega} \rightarrow D'_{\Omega} = D_{\text{Bohm}} \mu_{\omega}, \quad g = \frac{2\rho_s}{R}, \quad (2.39)$$

where the collisional diffusion is defined as $D_{\text{Bohm}} = \rho_s^2 \Omega_i$. Applying this normalization to Eq. (2.19) and dropping the dash sign, inserting the curvature operator from Eq. (2.29) and adding the diffusion term of Eq. (2.30) results in the electron density equation

$$\frac{dn}{dt} + g \left(\frac{\partial n}{\partial y} - n \frac{\partial \phi}{\partial y} \right) = D_n \nabla_{\perp}^2 n + S_n + \left\langle \nabla_{\parallel} (n u_{e\parallel}) \right\rangle_{\parallel}, \quad (2.40)$$

where the advective derivative is given by $d/dt = \partial/\partial t + \mathbf{u}_E \cdot \nabla_{\perp}$ and $\mathbf{u}_E = -\nabla_{\perp} \phi \times \mathbf{B} / B^2$ is the $\mathbf{E} \times \mathbf{B}$ drift. Here, $\langle \cdot \rangle_{\parallel}$ refers to the average over the parallel dimension. We also added the density source term S_n . Performing the same

kind of operations on Eq. (2.24) after applying the Boussinesq approximation results in the vorticity equation

$$\frac{d\nabla_{\perp}^2\phi}{dt} + \frac{g}{n} \frac{\partial n}{\partial y} = D_{\Omega} \nabla_{\perp}^4 \phi + \left\langle \frac{1}{n} \nabla_{\parallel} J_{\parallel} \right\rangle_{\parallel}, \quad (2.41)$$

where we introduced D_{Ω} as the collisional dissipation term representing viscosity. Averaging over the parallel direction after inserting Eq. (2.34) and Eq. (2.36) can be expressed as

$$\left\langle \nabla_{\parallel} (nu_{e\parallel}) \right\rangle_{\parallel} = -\eta(x)n \exp(\Lambda - \phi) + \chi(x)(\widehat{\phi} - \widehat{n}), \quad (2.42a)$$

$$\left\langle \frac{1}{n} \nabla_{\parallel} J_{\parallel} \right\rangle_{\parallel} = \eta(x) [1 - \exp(\Lambda - \phi)] + \chi(x)(\widehat{\phi} - \widehat{n}), \quad (2.42b)$$

where the spatially fluctuating electron density \widehat{n} and plasma potential $\widehat{\phi}$ are defined as $\widehat{n} = n - \langle n \rangle_y$ and $\widehat{\phi} = \phi - \langle \phi \rangle_y$ and $\langle \cdot \rangle_y$ refers to the flux surface average. Note, that we neglect $1/n$ in the plasma conductivity term for the vorticity equation, since we assume the plasma density to have small relative fluctuation levels in the edge region and $n \sim 1$. We redefined $\chi = (\rho_s/L_{\parallel})^2 (m_i/m_e)(\Omega_s/\nu_{ei})$ as the normalized parallel plasma conductivity where we used $\nabla_{\parallel}^2 \rightarrow -k_{\parallel}^2 \simeq -L_{\parallel}^{-2}$ and introduced $\eta = \rho_s/L_{\parallel}$ as the normalized sheath dissipation coefficient. ν_{ei} stands for the collision frequency between electrons and ions given by

$$\nu_{ei} = \frac{\log \Lambda_c e^4 Z^2 n_i}{6\sqrt{2}\pi^{3/2} \epsilon_0^2 \sqrt{m_e} T_e^{3/2}}, \quad (2.43)$$

and the Coulomb logarithm is approximately [149]

$$\log \Lambda_c \approx 18 - \log \left[\left(\frac{n_e}{10^{19}} \right)^{1/2} \left(\frac{T_e}{10^3 e} \right)^{-3/2} \right]. \quad (2.44)$$

These parameters depend on the radial position, the sheath dissipation term only occurs in the SOL and the plasma conductivity term is finite in the plasma edge region. A schematic illustration of these two regions in the simulation domain is shown in Fig. 2.1.

This model is equivalent to the one used in Paper III. Paper IV utilizes a slightly simpler model placing the whole domain in the SOL by choosing $\eta = \text{constant}$ and $\chi = 0$, and discarding Λ in the sheath dissipation term. A list of

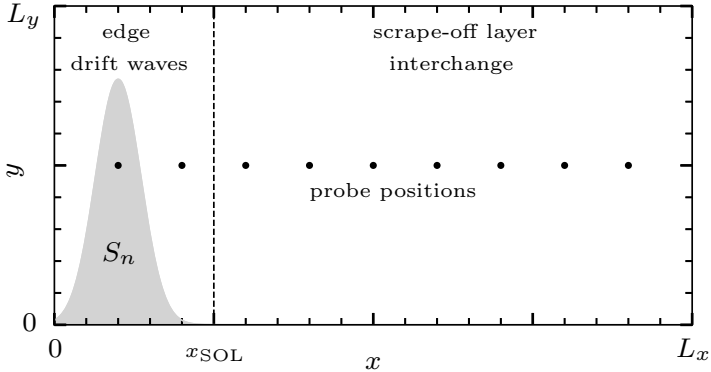


Figure 2.1: Schematic illustration of the edge and scrape-off layer region in the simulation domain. The position of the plasma source term (gray shaded) and the border between edge and SOL (dashed vertical line) are indicated [137].

representative machine parameters relevant for the reduced two-fluid models is presented in Table 2.1. Since each device performs a range of experiments with slightly different configurations, these parameters might vary. The presented parameters are consistent with those used in the numerical simulations in the included references. The radial position of the SOL is indicated by the sum of the major and minor radius and the parallel connection length is estimated as $L_{\parallel} = \pi q_{95} R$, with q_{95} as the safety factor at the 95% poloidal magnetic flux surface, if not explicitly stated in the references. It should also be noted, that the definition of the connection length varies from source to source as it may refer to the whole poloidal length or only to the length between the outboard midplane to the outer divertor plates.

Table 2.1: Machine parameters.

	$n_e[\text{m}^{-3}]$	$T_e[\text{eV}]$	$B[\text{T}]$	$L_{\parallel}[\text{m}]$	$R + r[\text{m}]$	reference
MAST	8×10^{18}	40	0.5	30	1.5	[106]
C-Mod	1.4×10^{19}	23	4.5	20	0.9	[159]
TCV	5×10^{18}	25	1.45	15	1.13	[138, 160]
KSTAR	7×10^{17}	35	2.0	26	2.3	[161]
AUG	8×10^{18}	40	2.5	25	2.15	[162]
JET	2×10^{19}	45	3.45	25	4.21	[155]
NSTX	6×10^{18}	13	0.25	20	1.53	[159]

The plasma parameters calculated for these device parameters are pre-

sented in Table 2.2. Based on these values, we can estimate the input pa-

Table 2.2: Physical parameters.

	ρ_s [m]	Ω_i [s ⁻¹]	c_s [ms ⁻¹]
MAST	1.8×10^{-3}	2.4×10^7	4.4×10^4
C-Mod	1.5×10^{-4}	2.2×10^8	3.3×10^4
TCV	5.0×10^{-4}	6.9×10^7	3.5×10^4
KSTAR	4.3×10^{-4}	9.6×10^7	4.1×10^4
AUG	3.7×10^{-4}	1.2×10^8	4.4×10^4
JET	2.8×10^{-4}	1.7×10^8	4.6×10^4
NSTX	2.1×10^{-3}	1.2×10^7	2.5×10^4

rameters for the reduced two-fluid model shown in Table 2.3. Note that the diffusion and viscosity coefficients for the model are not presented as they are chosen arbitrarily high for numerical stability in the included publications.

Table 2.3: Input parameters.

	g	η	χ
MAST	2.4×10^{-3}	6.1×10^{-5}	2.7×10^{-4}
C-Mod	3.4×10^{-4}	7.7×10^{-6}	1.0×10^{-5}
TCV	8.8×10^{-4}	3.3×10^{-5}	1.9×10^{-4}
KSTAR	3.7×10^{-4}	1.6×10^{-5}	6.8×10^{-4}
AUG	3.4×10^{-4}	1.5×10^{-5}	7.7×10^{-5}
JET	1.3×10^{-4}	1.1×10^{-5}	3.1×10^{-5}
NSTX	2.7×10^{-3}	1.0×10^{-4}	1.1×10^{-4}

2.5 Idealized interchange model

A minimal model for SOL plasma dynamics in the cross-field plane can be obtained by ignoring parallel dynamics entirely and applying the so called interchange normalization. We start again with Eq. (2.19) and Eq. (2.24), use the curvature operator given by Eq. (2.29), and include the diffusion terms.

The perpendicular components then take the form

$$\left(\frac{\partial}{\partial t} + \frac{1}{B}\hat{\mathbf{z}} \times \nabla\phi \cdot \nabla\right)n - \frac{2n}{B_0 R_0} \frac{\partial\phi}{\partial y} + \frac{2T_e}{eB_0 R_0} \frac{\partial n}{\partial y} = D_n \nabla_{\perp}^2 n, \quad (2.45a)$$

$$\left(\frac{\partial}{\partial t} + \frac{1}{B}\hat{\mathbf{z}} \times \nabla\phi \cdot \nabla\right)\nabla_{\perp}^2\phi + \frac{2c_s^2}{R_0 n} \frac{\partial n}{\partial y} = D_{\Omega} \nabla_{\perp}^4\phi. \quad (2.45b)$$

Under the interchange normalization, length scales are normalized by the characteristic length l of the system, time scales by the ideal interchange rate $\gamma = \sqrt{g/l}$ with $g = 2c_s^2/R_0$ and the plasma density and electrostatic potential accordingly, i.e.,

$$\nabla \rightarrow \nabla' = l\nabla, \quad \frac{\partial}{\partial t} \rightarrow \frac{\partial}{\partial t'} = \frac{1}{\gamma} \frac{\partial}{\partial t'}, \quad n \rightarrow n' = \frac{n}{N}, \quad \phi \rightarrow \phi' = \frac{\phi}{\gamma B_0 l^2}. \quad (2.46)$$

Inserting these expressions into the equations for plasma density and vorticity results in

$$\left(\frac{\partial}{\partial t'} + \hat{\mathbf{z}} \times \nabla'\phi' \cdot \nabla'\right)n' - 2n' \frac{l}{R_0} \frac{\partial\phi'}{\partial y'} + \frac{\gamma}{\Omega_i} \frac{\partial n'}{\partial y'} = \frac{D_n}{\gamma l^2} \nabla_{\perp}^2 n', \quad (2.47a)$$

$$\left(\frac{\partial}{\partial t'} + \hat{\mathbf{z}} \times \nabla'\phi' \cdot \nabla'\right)\nabla_{\perp}^2\phi' + \frac{1}{n'} \frac{\partial n'}{\partial y'} = \frac{D_{\Omega}}{\gamma l^2} \nabla_{\perp}^4\phi'. \quad (2.47b)$$

We neglect the term resulting from the compression of the electric drift since its prefactor is $l/R_0 \ll 1$. The term resulting from the compression of the diamagnetic drift will also be neglected in the continuity equation as previous work has shown that it has a negligible contribution to the cross-field dynamics and since $\gamma/\Omega_i \ll 1$ [163]. In addition we introduce the normalized particle diffusion and viscosity coefficients

$$\kappa = D_n/\gamma l^2 \quad \text{and} \quad \mu = D_{\phi}/\gamma l^2, \quad (2.48)$$

neglect $1/n$ in front of the interchange term as we apply the Boussinesq approximation and drop the dash notation to receive the minimal model for plasma convection

$$\left(\frac{\partial}{\partial t} + \hat{\mathbf{z}} \times \nabla\phi \cdot \nabla\right)n = \kappa \nabla_{\perp}^2 n, \quad (2.49a)$$

$$\left(\frac{\partial}{\partial t} + \hat{\mathbf{z}} \times \nabla\phi \cdot \nabla\right)\nabla_{\perp}^2\phi + \frac{\partial n}{\partial y} = \mu \nabla_{\perp}^4\phi. \quad (2.49b)$$

The emphasis of this model lies on reducing the complexity and the number of free parameters as drastically as possible without losing the capability of modeling plasma advection self-consistently. This model has also been used in

the past to describe buoyancy-driven convection in a fluid confined between two horizontal plates and heated from below. The model, named the Rayleigh-Bénard convection model after the original experimental work of Henri Bénard [164] and the first analytical work on this model of Lord Rayleigh [165], has become a paradigm to investigate nonlinear phenomena due to its rich dynamics [123, 166–170]. The normalized particle diffusion and viscosity coefficients in the presented formulation are related to the Rayleigh and Prandtl numbers as $R = 1/\kappa\mu$ and $R = \mu/\kappa$, which are typically used as model parameters for the Rayleigh-Bénard model. We use this model in Paper I.

3 | Stochastic modeling

This chapter is dedicated to describing the Filtered Poisson Process (FPP), a stochastic model used for describing the intermittent fluctuations in single point measurements obtained in the boundary of fusion experiments. The basis of this model was already developed in 1909 [171] and was further extended in the 1940s to describe noise in vacuum tubes [172, 173]. Since then, the model has been extended and used to describe fluctuations in numerous academic fields, including neuroscience, fluid dynamics and nuclear fission [174–180]. The FPP has first been introduced as a model describing SOL fluctuations in 2012 [30] and has since then shown excellent agreement with the statistical properties of fluctuations in various fusion experiments [31–38].

3.1 Filtered Poisson Process

The FPP is a stochastic process, given by a superposition of uncorrelated pulses which are distributed according to a Poisson process. For a given time $t \in [0, T]$ the process $\Phi_k(t)$ can be written as [30, 49]

$$\Phi_k(t) = \sum_{k=1}^{K(T)} A_k \phi \left(\frac{t - t_k}{\tau_d} \right). \quad (3.1)$$

Here, the random variables are defined as follows: $K(T)$ stands for the number of pulses arriving in the time interval $[0, T]$, A_k is the pulse amplitude and t_k the pulse arrival time. It is further assumed that all pulses have the same pulse shape ϕ and duration time τ_d .

Alternatively, the process can be expressed as a convolution of the pulse shape and a delta pulse train

$$\Phi_k(t) = [\phi * f_K] \left(\frac{t}{\tau_d} \right), \quad (3.2)$$

where f_K is the forcing defined as a train of delta pulses

$$f_K(\theta) = \sum_{k=1}^{K(T)} A_k \delta\left(\theta - \frac{t_k}{\tau_d}\right). \quad (3.3)$$

As the process can be expressed as a train of delta pulses filtered through the pulse shape, it is called a *Filtered Poisson Process*.

For a given time interval $[0, T]$, the number of pulses $K(T)$ follows a Poisson distribution

$$P_K(K|T) = \frac{1}{K!} \left(\frac{T}{\tau_w}\right)^K \exp\left(-\frac{T}{\tau_w}\right), \quad (3.4)$$

with intensity T/τ_w . The waiting times between two consecutive pulses are independent and exponentially distributed with mean value τ_w and the arrival times t_k are independent and uniformly distributed in the interval $[0, T]$. These properties of the process are consistent with experimental measurements, showing exponentially distributed waiting times [33, 35–37]. Time series with quasi-periodic arrival times are observed in SOL simulations utilizing Rayleigh–Bénard like convection models [123] and are discussed in Paper II in further detail. The amplitudes are chosen to be exponentially distributed, as this is observed in experimental measurements [35–37].

In the following, we will discuss two pulse shapes that are most relevant for SOL fluctuation measurements and corresponding numerical simulations. Firstly, the pulse shape of an asymmetric, two-sided exponential pulse is defined as

$$\phi(\theta, \lambda) = \begin{cases} \exp\left(-\frac{\theta}{1-\lambda}\right), & \theta \geq 0, \\ \exp\left(\frac{\theta}{\lambda}\right), & \theta < 0. \end{cases} \quad (3.5)$$

Here, θ is a dimensionless variable and λ stands for the asymmetry parameter with $\lambda \in (0, 1)$. In some cases, a one-sided exponential pulse is applied with $\lambda = 0$, which refers to the limit $\lim_{\lambda \rightarrow 0} \phi(\theta, \lambda)$. Exponential pulses stand in good agreement with experimental measurements [9, 31, 33, 35–37, 42, 44, 53] and numerical SOL simulations [9, 137]. Secondly, Lorentzian pulses are considered which are defined as

$$\psi(\theta) = \frac{1}{\pi} \frac{1}{1 + \theta^2}. \quad (3.6)$$

These can also be generalized to a skewed Lorentzian, however no closed analytical form is known and require a definition via the inverse Fourier transform [181]. Indications for Lorentzian pulses in time series in the edge region [182–185] and corresponding numerical simulations [123] have been reported. Exponential pulses consist of a discontinuous peak and exponential tails, whereas

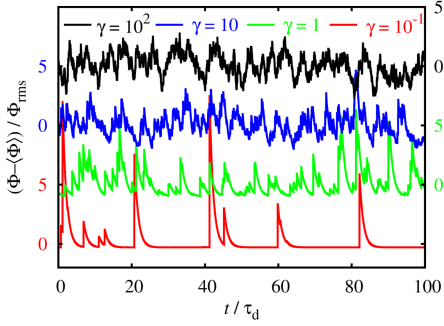


Figure 3.1: Realizations of the FPP with one-sided exponential pulses and different intermittency parameters. Reprinted from [49], with the permission from AIP Publishing.

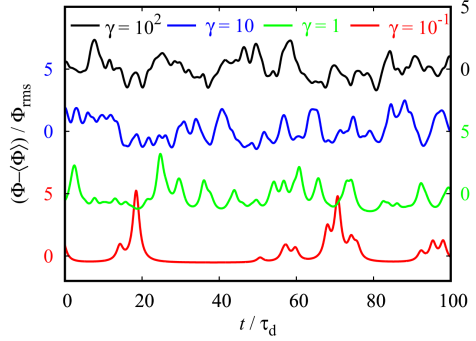


Figure 3.2: Realizations of the FPP with Lorentzian pulses and different intermittency parameters. Reprinted from [186], with the permission from AIP Publishing.

Lorentzian pulses have a smooth peak and algebraic tails. The consequences of these properties will be apparent in the following discussions.

Calculating moments of distributions of the process requires the integrals of the pulse shapes, defined as

$$I_n = \int_{-\infty}^{\infty} d\theta [\phi(\theta)]^n. \quad (3.7)$$

For exponential pulses this results in $I_{\phi,n} = 1/n$, independent of the pulse asymmetry λ . For Lorentzian pulses the first four integrals are given by $I_{\psi,1} = 1$, $I_{\psi,2} = 1/2\pi$, $I_{\psi,3} = 3/8\pi^2$ and $I_{\psi,4} = 5/16\pi^3$.

The main property of the FPP is given by the ratio of the pulse duration and average waiting time,

$$\gamma = \frac{\tau_d}{\tau_w}, \quad (3.8)$$

which is referred to as the intermittency parameter. For short waiting times and long duration times, $\gamma \gg 1$, the level of pulse overlap is high, resulting in a large mean value and small relative variation around the mean. In the opposite limit, $\gamma \ll 1$, the signal is dominated by individual, isolated pulses, resulting in a small mean value and large relative fluctuations. Numerical realizations of the FPP with different intermittency parameters are shown for one-sided exponential pulses in Fig. 3.1 and for symmetric Lorentzian pulses in Fig. 3.2 displaying the features of these processes.

3.2 Moments and PDFs

The four lowest order central moments of the FPP take the form

$$\langle \Phi \rangle = \gamma \langle A \rangle I_1, \quad (3.9a)$$

$$\Phi_{\text{rms}}^2 = \gamma \langle A^2 \rangle I_2, \quad (3.9b)$$

$$S_\Phi = \frac{1}{\gamma^{1/2}} \frac{\langle A^3 \rangle I_3}{\langle A^2 \rangle^{3/2} I_2^{3/2}}, \quad (3.9c)$$

$$F_\Phi = 3 + \frac{1}{\gamma} \frac{\langle A^4 \rangle I_4}{\langle A^2 \rangle^2 I_2^2}, \quad (3.9d)$$

where S_Φ stands for the skewness of the process and F_Φ is the kurtosis or flatness [30]. The last two moments exhibit the parabolic relationship

$$F_\Phi = 3 + \frac{\langle A^2 \rangle \langle A^4 \rangle}{\langle A^3 \rangle^2} \frac{I_2 I_4}{I_3^2} S_\Phi^2. \quad (3.10)$$

Inserting the expressions for the integrals of the pulse shapes for two-sided exponential and Lorentzian pulses and assuming exponentially distributed amplitudes simplifies these expressions further. For exponential pulses the expression for the relative fluctuation level becomes

$$\frac{\Phi_{\text{rms}}}{\langle \Phi \rangle} = \gamma^{-1/2}, \quad (3.11)$$

and the universal parabolic relationship of Eq. (3.10) reduces to

$$F_\Phi = 3 + \frac{3}{2} S_\Phi^2, \quad (3.12)$$

which stands in good agreement with experimental measurements [46–48]. Notably, these expressions do not depend on the pulse asymmetry parameter, λ .

The PDF of the process with exponential pulses is given by a Gamma distribution with shape parameter γ and scale parameter $\langle A \rangle$ [187],

$$P_{\Phi, \phi}(\Phi) = \frac{\Phi^{\gamma-1}}{\langle A \rangle^\gamma \Gamma(\gamma)} \exp\left(-\frac{\Phi}{\langle A \rangle}\right). \quad (3.13)$$

Typically, the realization of the process is normalized to have zero mean and unit standard deviation,

$$\tilde{\Phi} = \frac{\Phi - \langle \Phi \rangle}{\Phi_{\text{rms}}}, \quad (3.14)$$

with the according PDF [187],

$$P_{\tilde{\Phi}, \phi}(\tilde{\Phi}) = \frac{\gamma^{\gamma/2}}{\Gamma(\gamma)} \left(\tilde{\Phi} + \gamma^{1/2}\right)^{\gamma-1} \exp\left(-\gamma^{1/2} \tilde{\Phi} - \gamma\right). \quad (3.15)$$

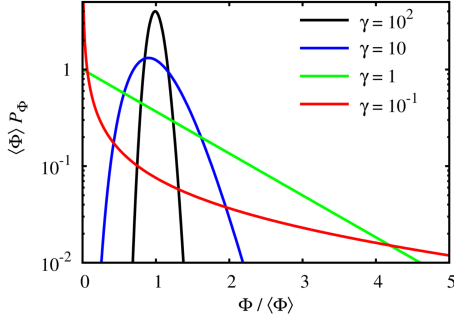


Figure 3.3: PDFs of a FPP with exponential pulses with different intermimency parameters γ . Reprinted from [49], with the permission from AIP Publishing.

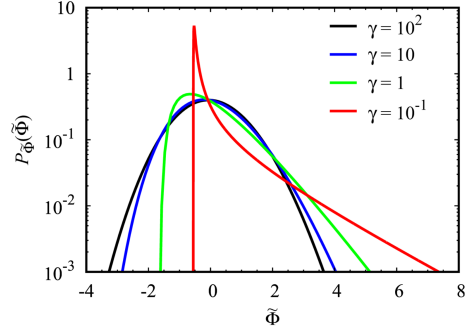


Figure 3.4: PDFs of a normalized FPP with Lorentzian pulses with different intermimency parameters γ . Reprinted from [188], with the permission from AIP Publishing.

This expression is used as a fit in Fig. 1.11. For an FPP of Lorentzian pulses no closed expressions for its PDF is known. However, it can be derived by taking the inverse Fourier transform of its corresponding characteristic function resulting in [188]

$$P_{\tilde{\Phi},\psi}(\tilde{\Phi}) = \left(\frac{\pi}{\gamma}\right)^{1/2} \int_0^\infty dw \exp\left(-\frac{\gamma\pi w \sin(1/2 \arctan w)}{(1+w^2)^{1/4}}\right) \times \cos\left(\pi\gamma w + \sqrt{\pi\gamma}\tilde{\Phi}w - \frac{\gamma\pi w \cos(1/2 \arctan w)}{(1+w^2)^{1/4}}\right). \quad (3.16)$$

For both exponential and Lorentzian pulses the PDF of the processes are characterized by the intermimency parameter. The PDFs are shown for a range of different γ in Fig. 3.3 and Fig. 3.4. The PDFs are unimodal for all values of γ and have an exponential tail towards large fluctuation amplitudes for small values of γ . In the opposite limit, the PDFs approach a normal distribution with vanishing mean and unit standard deviation for $\tilde{\Phi}$.

3.3 Second order statistics

In order to calculate the second order moments, namely the power spectral density (PSD) and the Auto-correlation function (ACF), we consider the FPP as a convolution of a pulse train f_K and a pulse shape ϕ . The Fourier transform of the FPP is given by the product of the Fourier transform of f_K and ϕ . The power spectrum of Φ can therefore be expressed as the product of the power

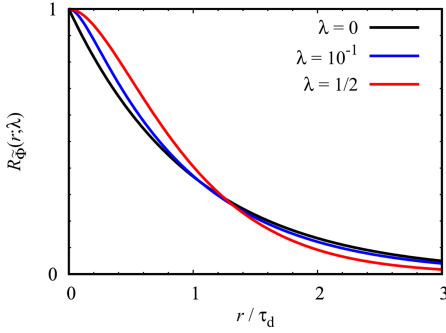


Figure 3.5: Auto-correlation function of a normalized FPP consisting of two-sided exponential pulses with different asymmetry parameters λ . Reprinted from [52], with the permission from AIP Publishing.

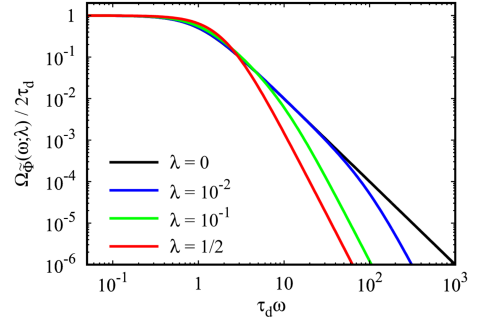


Figure 3.6: Power spectral density of a normalized FPP consisting of two-sided exponential pulses with different asymmetry parameters λ . Reprinted from [52], with the permission from AIP Publishing.

spectrum of f_K and ϕ . The power spectrum of f_K is flat due to the uncorrelated delta pulses, so that the frequency dependence of the spectrum of Φ is only dependent on ϕ . The ACF is given by the Fourier transform of the PSD. For two-sided exponential pulses the PSD of an FPP normalized according to Eq. (3.14), takes the form [52]

$$\Omega_{\tilde{\Phi},\phi}(\omega; \lambda) = \frac{2\tau_d}{[1 + (1 - \lambda)^2 \tau_d^2 \omega^2][1 + \lambda^2 \tau_d^2 \omega^2]}, \quad (3.17)$$

with the according ACF

$$R_{\tilde{\Phi},\phi}(r; \lambda) = \frac{1}{1 - 2\lambda} \left[(1 - \lambda) \exp\left(-\frac{|r|}{(1 - \lambda)\tau_d}\right) - \lambda \exp\left(-\frac{|r|}{\lambda\tau_d}\right) \right]. \quad (3.18)$$

The ACF and PSD are displayed for a range of γ -values in Figs. 3.5 and 3.6. In contrast to the PDFs, the second order statistics are independent of γ but change for different λ . In the limits of a one-sided exponential pulse, the ACF is purely exponential and the PSD is Lorentzian shaped. For λ close to zero or 1, the spectrum has an intermediate range where the spectrum falls with ω^{-2} before it falls with ω^{-4} in the high frequency limit. This expression is in excellent agreement with the experimental measurements shown in Fig. 1.13 with $\lambda = 0.1$.

For Lorentzian pulses the PSD of a normalized FPP takes an exponential form [181]

$$\Omega_{\tilde{\Phi},\psi}(\omega) = 2\pi\tau_d \exp(-2\tau_d|\omega|), \quad (3.19)$$

and the ACF is Lorentzian shaped,

$$R_{\tilde{\Phi},\psi}(r) = \frac{4}{4 + (r/\tau_d)^2}. \quad (3.20)$$

These expressions can be generalized to skewed Lorentzian pulses, however no closed expressions are known. An alternative formulation is presented in [181].

3.4 Excess time statistics

Expressions for excess time statistics, specifically the rate of level crossings above a given threshold and the average time spent above this threshold, can be derived for an FPP. In the context of fluctuations in the SOL of fusion experiments, these quantities are crucial considering the energy of incoming particles to the vessel walls and the energy threshold of physical sputtering. The number of sputtered particles per incoming particle is specified by the modified Bohdanský yield function [189]. The mean yield as a function of energy of an incoming deuterium particle on a tungsten wall is plotted for a range of relative fluctuation levels in Fig. 3.7. For constant energy, no sputtering occurs beneath 200 eV. For realistic scenarios of $E_{\text{rms}}/\langle E \rangle > 0$ sputtering already occurs at significantly lower mean energies. An accurate description of excess time statistics is therefore of importance for fusion experiments.

For an FPP the number of level crossings is given by Rice's formula [173]

$$X(\Phi) = T \int_0^\infty d\dot{\Phi} \dot{\Phi} P_{\Phi, \dot{\Phi}}(\Phi, \dot{\Phi}). \quad (3.21)$$

Here $\dot{\Phi}$ stands for the derivative of the process Φ and $P_{\Phi, \dot{\Phi}}(\Phi, \dot{\Phi})$ for the joint PDF between Φ and $\dot{\Phi}$. This formulation requires the process to be differentiable, hence an FPP consisting of one-sided exponential pulses cannot be considered this way. For two-sided exponential pulses with $\lambda \in (0, 1)$ the rate of up-crossings is given by [190]

$$\frac{\tau_d}{T} X(\Phi) = \frac{\lambda^{\gamma\lambda-1} (1-\lambda)^{\gamma(1-\lambda)-1}}{\gamma \Gamma(\gamma\lambda) \Gamma(\gamma(1-\lambda))} \left(\frac{\gamma\Phi}{\langle \Phi \rangle} \right)^\gamma \exp\left(-\frac{\gamma\Phi}{\langle \Phi \rangle}\right). \quad (3.22)$$

For this expression, the limit $\lambda \rightarrow 0$ exists. Eq. (3.22) is plotted for exponential pulses with $\lambda = 0$ and $\lambda = 1/2$ and a range of γ -values in Fig. 3.8. From this, the PDF of time as well as mass above a given threshold can be determined analytically for the limits $\gamma \rightarrow 0$ and $\gamma \rightarrow \infty$ and numerically with Monte Carlo simulations for general γ [190].

At the time of writing this thesis, excess time statistics of an FPP consisting of Lorentzian pulses have not been investigated.

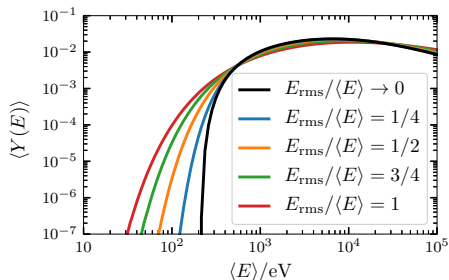


Figure 3.7: Mean yield function for a range of relative fluctuation levels. Image courtesy of A. Theodorsen [39].

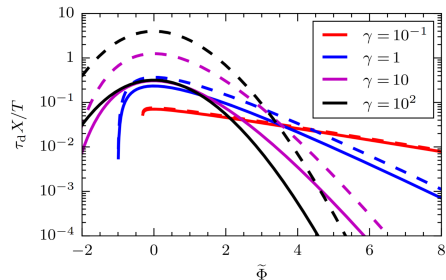


Figure 3.8: Rate of up-crossings for a FPP consisting of exponential pulses with $\lambda = 0$ (dashed line) and $\lambda = 1/2$ (full line) for various γ -values. Reprinted figure with permission from [190]. Copyright (2018) by the American Physical Society.

3.5 Density profiles

The FPP can be extended to include a spatial variable x , resulting in a model of advecting single pulses and corresponding profiles. In the following, this model is discussed in the context of filament motion in SOL plasmas. The presented notation is consistent with [49]. Alternative formulations based on a Lagrangian approach to filament dynamics result in equivalent expressions [11, 191–193].

The model is given by a superposition of pulses

$$\Phi_K(x, t) = \sum_{k=1}^K \phi_k(x, t). \quad (3.23)$$

In contrast to previous sections ϕ_k is compounded by both amplitude and pulse shape. For simplicity, we keep K constant in the following derivation. The evolution of individual pulses, neglecting pulse interaction, is given by the modified advection equation,

$$\frac{\partial \phi_k}{\partial t} + v_{\perp} \frac{\partial \phi_k}{\partial x} + \frac{\phi_k}{\tau_{\parallel}} = 0, \quad (3.24)$$

with v_{\perp} as the radial velocity and τ_{\parallel} representing the parallel transit time, describing parallel losses along the magnetic field. Note, that we assume v_{\perp} and τ_{\parallel} to be constant for all filaments. Following Eq. (3.24), individual pulses can be written as the product of their amplitude and pulse shape, $\phi_k(x, t) =$

$A_k(t)\varphi_k(x - x_k - v_k t)$ with x_k as the position of the pulse at $t = 0$. The individual amplitudes are assumed to satisfy the expression

$$\frac{dA_k}{dt} = -\frac{A_k}{\tau_{\parallel}}. \quad (3.25)$$

The solution for this amplitude equation can be expressed by introducing the initial amplitude A_{0k} resulting in

$$A_k(t) = A_{0k} \exp\left(-\frac{t + x_k/v_{\perp}}{\tau_{\parallel}}\right), \quad (3.26)$$

with the pulse k being located at $x = 0$ at time $-x_k/v_{\perp}$. We further assume the pulse shape to take the form of an exponential function,

$$\varphi_k(x) = \Theta\left(-\frac{x}{l_{\perp}}\right) \exp\left(\frac{x}{l_{\perp}}\right), \quad (3.27)$$

where Θ is the Heaviside function and l_{\perp} is the radial size of the pulse. Note, that this pulse shape is consistent with the findings shown in Fig. 1.22. We now consider the signal at a reference position ξ . At the reference time $t_k = (\xi - x_k)/v_{\perp}$ for pulse k at position ξ , the process takes the form

$$\Phi_K(\xi, t) = \sum_{k=1}^K A_{0k} \exp\left(-\frac{\xi}{v_{\perp}\tau_{\parallel}}\right) \Theta\left(\frac{t - t_k}{\tau_{\perp}}\right) \exp\left(-\frac{t - t_k}{\tau_d}\right), \quad (3.28)$$

with $\tau_{\perp} = l_{\perp}/v_{\perp}$ and the pulse duration given by the harmonic mean of the perpendicular and parallel transit time $\tau_d = \tau_{\parallel}\tau_{\perp}/(\tau_{\parallel} + \tau_{\perp})$. By averaging over uniformly distributed pulse arrivals, the resulting radial profile takes the exponential form

$$\langle\Phi\rangle(\xi) = \frac{\tau_d}{\tau_w} \langle A_0 \rangle \exp\left(-\frac{\xi}{v_{\perp}\tau_{\parallel}}\right). \quad (3.29)$$

The resulting scale length of the profile is governed by the radial velocity of the filaments and the parallel transit time. Multiple realizations at individual points in time and the corresponding mean profile are shown in Fig. 3.9.

The application of this model exhibits numerous limitations. The assumption of constant radial velocities and pulse size is an overly simplified description for filament transport in the SOL. In addition, the assumption of radially constant τ_w and therefore radially constant γ does not hold in experimental observations. Interactions between individual filaments and two-dimensional motion are also not considered. However, this mathematical model still provides valuable insight in the relation between individual filaments and radial profiles in the SOL and can serve as a framework to relate isolated blob and filament studies to turbulence simulations and experimental measurements.

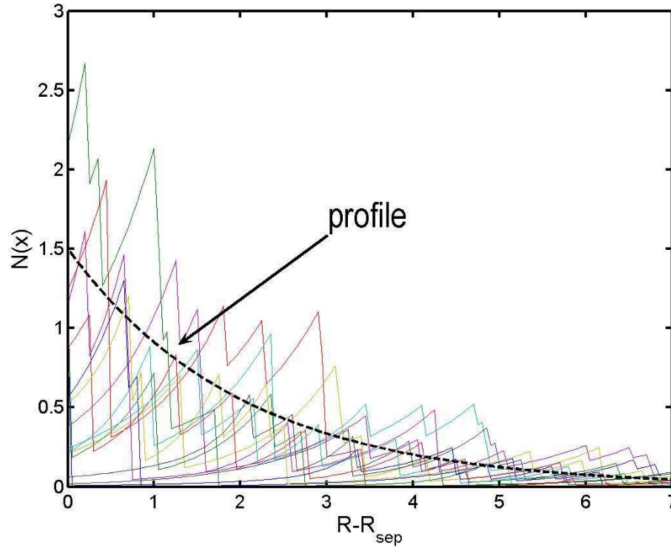


Figure 3.9: Radial exponential density profile (black dashed line) illustrated as the mean of individual density realizations (colored lines) given by a superposition of individual exponentially shaped pulses. Image courtesy of F. Militello [194].

3.6 Deconvolution method

Since the FPP can be expressed as a convolution of a pulse function ϕ and a forcing, consisting of delta-function pulses f_K , shown in Eq. (3.2), one can attempt to estimate the forcing if the pulse shape is known [38, 123, 195]. For a given forcing, one can determine the pulse amplitudes $\{A_k\}_{k=1}^K$ and arrival times $\{t_k\}_{k=1}^K$ directly. This method has the advantage of capturing pulses of all sizes, not only events above a certain threshold as is the case for conditional averaging. Additionally, the problem of pulse overlap is less severe. In order to estimate the forcing, a modified Richardson-Lucy deconvolution algorithm can be used [196, 197]. The algorithm is initialized with a first guess for the forcing $f_K^{(1)}$. This value is iteratively updated with the n -th iteration given by

$$f_K^{(n+1)} = f_K^{(n)} \frac{D * \hat{\phi}}{f_K^{(n)} * \phi * \hat{\phi}}. \quad (3.30)$$

Here, $\hat{\phi}(t) = \phi(-t)$ and D denotes the investigated time series. This algorithm converges to the least squares solution [198]. The initial guess for the forcing matters little as it only determines the number of iterations required until the

algorithm converges.

This deconvolution algorithm thereby provides a versatile tool to analyze time series of SOL fluctuations in experiments and simulations, as it can provide clear results even for relatively short time series.

4 | Summary of Papers

The main focus of this thesis is on investigating the statistical properties of fluctuations in numerical simulations of SOL plasmas. Papers I and III study time series of single point measurements of established fluid models utilizing the FPP framework. Paper II provides additional theoretical insight to the results obtained in Paper I. Lastly, Paper IV investigates the interaction of filaments in SOL simulations and thereby discusses to what degree filaments can be considered uncorrelated, which is a basic assumption for the FPP model. The papers are ordered thematically.

In order to investigate the statistical properties of fluctuations described by different SOL models, we start with the idealized interchange model discussed in Paper I, arguably the simplest self-consistent description of SOL turbulence. Fluctuation time series at different radial positions are obtained and analyzed by stochastic modeling. We observe that the PDFs for the temperature fluctuations change from a normal distribution in the center of the simulation domain to a distribution with an exponential tail at the boundary of the simulation domain, a result consistent with experimental measurements of SOL plasmas. The PSDs have an exponential shape, which can be attributed to the underlying Lorentzian pulses, identified by a deconvolution method. The time series of the temperature show periods of strongly intermittent fluctuations with large bursts, interrupted by quiescent periods with quasi-periodic oscillations. These alternating periods can be attributed to the generation of a sheared mean flow through the fluid layer resulting in predator-prey-like dynamics of the kinetic energy integrals. Since this behavior has not been observed in time series of experimental measurements, it becomes clear that the utilized Rayleigh-Bénard-like model is insufficient to reproduce all statistical properties of SOL fluctuations.

Paper II provides additional theoretical insight as the shot noise process with periodic arrivals is investigated. It is shown analytically that the PSD of a shot noise process with periodic arrivals, Lorentzian pulses and exponentially distributed amplitudes has an exponentially modulated Dirac comb of

decaying amplitudes. In addition, we provide numerical realizations of a shot noise process with quasi-periodic arrival times by using a narrow, uniform distribution for each arrival around the strictly periodic arrival time. We find that moderate deviations from perfect periodicity destroys the Dirac comb as it leads to a broadening of its peaks and the decrease of the peak amplitudes for higher harmonics. The resulting PSD resembles the findings of Paper I, thereby confirming that the statistical properties of the fluctuation time series of the idealized interchange model are due to the presence of quasi-periodic Lorentzian pulses.

In Paper III we study the statistical properties of reduced two-fluid models and thereby increase the model complexity and number of considered physical effects compared to the idealized interchange equations. Again, we observe that the PDFs of fluctuation time series of the plasma density show an exponential tail in the far SOL. In contrast to the model discussed in Paper I, we find that the average burst or pulse shape is well described by a two-sided exponential function. The PSD of the particle density is that of the average pulse shape and does not change with radial position. The amplitudes and the waiting times between two consecutive arrivals are exponentially distributed. The profiles have an exponential form with radially constant scale length. As for the moments, we find that the fluctuation level increases with radial position and a nearly parabolic relationship between skewness and flatness moments. All of these results stand in perfect agreement with the predictions of the FPP model. In contrast to experimental measurements, we can choose an arbitrarily high sampling frequency for the single point measurements in these simulations. For frequencies higher than what is experimentally feasible, we observe an exponential spectrum in the PSD and a continuous, Lorentzian-like peak in the averaged pulse shape. These results cannot be compared directly to experimental counterparts due to the poor sampling rate by the diagnostics.

The last paper included in this thesis investigates the interaction of single filaments with each other and thereby addresses the question to what extent filaments can be considered isolated. As the FPP model assumes all pulses in a time series to be uncorrelated, this study remains highly relevant for the work presented in Papers I-III. A reduced two-fluid model is used for this investigation. In order to track filaments and determine filament parameters, a blob tracking algorithm based on an amplitude threshold method is presented. The velocity estimates of the algorithm are validated by a conventional center of mass approach. We introduce a model of multiple seeded filaments where the filament parameters, i.e. size, initial position, amplitude and arrival time, are sampled from appropriate distribution functions. A model-specific intermittency parameter is introduced which quantifies the level of filament interac-

tions as a function of their average size, velocity and waiting time. This model is then studied for different levels of complexity and filament interaction compared to theoretical size-velocity scaling laws of perfectly isolated filaments. We observe an increase in the average radial velocity for strongly interacting filaments. This is found to be caused by the interaction of filaments with the electrostatic potential of one another. The blob tracking approach is then applied on full plasma turbulence simulations where a strong correlation is found between filament amplitudes, sizes and velocities. Despite the observed increase in the radial velocities for strongly interacting filaments, we observe a systematic size-velocity relationship consistent with theoretical predictions. We therefore conclude that filaments can be regarded to lowest order as isolated structures, i.e., that the corresponding pulses in the FPP model can be assumed to be uncorrelated.

5 | Conclusion and future work

The exhaust of particles and heat in the boundary of contemporary magnetic confinement experiments remains to this day one of the biggest challenges on the road to commercially viable fusion energy production. Due to the complexity of the physics involved in the boundary of fusion devices, the scientific community relies increasingly on numerical simulations. This approach requires a validation metric for boundary turbulence simulations such as the Filtered Poisson Process (FPP), a model which is capable to predict all relevant statistical properties of fluctuations in the scrape-off layer (SOL). In this thesis, two models for boundary plasmas are analyzed in detail. The idealized interchange model, one of the simplest models used in the past, has shown to only reproduce some of the statistical properties observed in experimental measurements. The reduced two-fluid model has proven to reproduce all relevant properties of the FPP model and experimental measurements. These results are especially encouraging when considering the assumptions and simplifications of this model, such as the reduction to two dimensions, cold ions and isothermal electrons. In addition, this thesis provides a systematical study of plasma filament interaction, concluding that studies of isolated filaments adequately describe filament motion in turbulent SOL plasmas. This thesis thereby displays the relevance and importance of numerical simulations of reduced two-fluid models for gaining a better understanding of the intricate physics of boundary plasmas.

Based on the presented results, a number of ideas for future work can be proposed. One next step would be the analysis of three-dimensional turbulence simulations utilizing the FPP model, as the restriction to two dimensions remains arguably the strongest simplification of the presented simulations. Recent work studying the dimensionality of SOL turbulence utilizing the STORM code, the same code basis as used in Paper III and IV, provides a useful starting point for this investigation [147, 158]. The short time durations of 3D codes due to their computational costs remain a limitation for this project. However, this limitation could be compensated by placing several measurement probes

at different binormal/poloidal positions, where we expect the statistical properties of the fluctuation time series to be statistically identical. Including additional physical parameters such as evolving electron and ion temperature, using non-Boussinesq models or a more realistic magnetic geometry may also provide additional insight.

Hitherto, we have only considered models derived from the Braginskii fluid equations, leaving out codes utilizing different models that are commonly used for SOL plasmas. An obvious next candidate for stochastic validation would be fully self-consistent global gyrofluid models [96–98, 199, 200]. These models incorporate high fluctuation amplitude levels and finite Larmor radius effects and are considered to be a more complete description of the physical mechanisms in the SOL.

As for the reduced two-fluid model, a systematical parameter scan should be performed in order to identify the model variables relevant for the moments and fluctuation statistics. Unpublished work on this topic has found a non-trivial relationship between the sheath dissipation coefficient and the scale length of the radial profile. The blob tracking algorithm presented in Paper IV might provide further insight as the blob parameters could be compared to the FPP framework for density profiles discussed in chapter 3.5.

The role of neutral particles in the SOL has been studied in various turbulence codes [201–204]. To this day however, no attempt has been made to analyze the effects of local ionization and recombination on the fluctuation statistics. Applying the FPP framework on one of the existing models incorporating plasma-neutral interactions would be another interesting extension of the presented work.

Lastly, the stochastic model of multiple seeded filaments discussed in Paper IV opens the door to a number of applications. Since it enables to define all filament parameters it provides a perfect tool to bridge the gap between isolated filaments and turbulence simulations. One example would be the evaluation of the FPP framework for density profiles in a controlled environment if turbulence simulations prove to be too demanding.

Bibliography

- [1] F. Romanelli, P. Barabaschi, D. Borba, G. Federici, L. Horton, R. Neu, D. Stork, and H. Zohm. *EU-EFDA report: Fusion Electricity - A roadmap to the realisation of fusion energy*. 2012.
- [2] J. P. Freidberg. *Plasma Physics and Fusion Energy*. Cambridge University Press, 2008.
- [3] “EUROfusion”. <https://www.euro-fusion.org>.
- [4] J. W. Connor, G. F. Counsell, S. K. Erents, S. J. Fielding, B. LaBombard, and K. Morel. Comparison of theoretical models for scrape-off layer widths with data from COMPASS-D, JET and Alcator C-Mod. *Nuclear Fusion*, 39:169, 1999.
- [5] D. Bohm. *The Characteristics of Electrical Discharges in Magnetic Fields*. New York: McGraw-Hill, 1949.
- [6] B. Lipschultz, B. LaBombard, C. S. Pitcher, and R. Boivin. Investigation of the origin of neutrals in the main chamber of Alcator C-Mod. *Plasma Physics and Controlled Fusion*, 44:733, 2002.
- [7] S. I. Krasheninnikov, D. A. D’ippolito, and J. R. Myra. Recent theoretical progress in understanding coherent structures in edge and SOL turbulence. *Journal of Plasma Physics*, 74:679, 2008.
- [8] J. Wesson and D. J. Campbell. *Tokamaks*. Oxford University Press, 2011.
- [9] O. E. Garcia, J. Horacek, R. A. Pitts, A. H. Nielsen, W. Fundamenski, V. Naulin, and J. Juul Rasmussen. Fluctuations and transport in the TCV scrape-off layer. *Nuclear Fusion*, 47:667, 2007.
- [10] B. LaBombard, R. L. Boivin, M. Greenwald, J. Hughes, B. Lipschultz, D. Mossessian, C. S. Pitcher, J. L. Terry, S. J. Zweben, and Alcator

- Group. Particle transport in the scrape-off layer and its relationship to discharge density limit in Alcator C-Mod. *Physics of Plasmas*, 8:2107, 2001.
- [11] F. Militello and J. T. Omotani. Scrape off layer profiles interpreted with filament dynamics. *Nuclear Fusion*, 56:104004, 2016.
- [12] M. V. Umansky, S. I. Krasheninnikov, B. LaBombard, B. Lipschultz, and J. L. Terry. Modeling of particle and energy transport in the edge plasma of Alcator C-Mod. *Physics of Plasmas*, 6:2791, 1999.
- [13] D. L. Rudakov, J. A. Boedo, R. A. Moyer, P. C. Stangeby, J. G. Watkins, D. G. Whyte, L. Zeng, N. H. Brooks, R. P. Doerner, T. E. Evans, M. E. Fenstermacher, M. Groth, E. M. Hollmann, S. I. Krasheninnikov, C. J. Lasnier, A. W. Leonard, M. A. Mahdavi, G. R. McKee, A. G. McLean, A. Y. Pigarov, W. R. Wampler, G. Wang, W. P. West, and C. P. C. Wong. Far SOL transport and main wall plasma interaction in DIII-D. *Nuclear Fusion*, 45:1589, 2005.
- [14] F. Militello, P. Tamain, W. Fundamenski, A. Kirk, V. Naulin, A. H. Nielsen, and the MAST team. Experimental and numerical characterization of the turbulence in the scrape-off layer of MAST. *Plasma Physics and Controlled Fusion*, 55:025005, 2013.
- [15] J. A. Boedo, J. R. Myra, S. Zweben, R. Maingi, R. J. Maqueda, V. A. Soukhanovskii, J. W. Ahn, J. Canik, N. Crocker, D. A. D'Ippolito, R. Bell, H. Kugel, B. Leblanc, L. A. Roquemore, D. L. Rudakov, and NSTX Team. Edge transport studies in the edge and scrape-off layer of the National Spherical Torus Experiment with Langmuir probes. *Physics of Plasmas*, 21:042309, 2014.
- [16] D. Carralero, G. Birkenmeier, H. W. Müller, P. Manz, P. DeMarne, S. H. Müller, F. Reimold, U. Stroth, M. Wischmeier, E. Wolfrum, and The ASDEX Upgrade Team. An experimental investigation of the high density transition of the scrape-off layer transport in ASDEX Upgrade. *Nuclear Fusion*, 54:123005, 2014.
- [17] P. C. Stangeby. *The Plasma Boundary of Magnetic Fusion Devices*. Institute of Physics Publishing, 2000.
- [18] B. Lipschultz, D. Whyte, and B. LaBombard. Comparison of particle transport in the scrape-off layer plasmas of Alcator C-Mod and DIII-D. *Plasma Physics and Controlled Fusion*, 47:1559, 2005.

- [19] V. Naulin. Turbulent transport and the plasma edge. *Journal of Nuclear Materials*, 363:24, 2007.
- [20] B. LaBombard, M. V. Umansky, R. L. Boivin, J. A. Goetz, J. Hughes, B. Lipschultz, D. Mossessian, C. S. Pitcher, J. L. Terry, and Alcator Group. Cross-field plasma transport and main-chamber recycling in diverted plasmas on Alcator C-Mod. *Nuclear Fusion*, 40:2041, 2000.
- [21] A. Y. Pigarov, S. I. Krasheninnikov, T. D. Rognlien, M. J. Schaffer, and W. P. West. Tokamak edge plasma simulation including anomalous cross-field convective transport. *Physics of Plasmas*, 9:1287, 2002.
- [22] O. E. Garcia, R. A. Pitts, J. Horacek, A. H. Nielsen, W. Fundamenski, J. P. Graves, V. Naulin, and J. Juul Rasmussen. Turbulent transport in the TCV SOL. *Journal of Nuclear Materials*, 363:575, 2007.
- [23] S. Zweben, P. C. Liewer, and R. W. Gould. Edge plasma transport experiments in the Caltech tokamak. *Journal of Nuclear Materials*, 111:39, 1982.
- [24] S. J. Zweben and R. W. Gould. Scaling of edge-plasma turbulence in the Caltech tokamak. *Nuclear Fusion*, 23:1625, 1983.
- [25] G. R. McKEE, R. J. Fonck, D. K. Gupta, D. J. Schlossberg, M. W. Shafer, R. L. Boivin, and W. Solomon. Plasma turbulence imaging via beam emission spectroscopy in the core of the DIII-D tokamak. *Plasma and Fusion Research*, 2:S1025, 2007.
- [26] A. J. Wootton. Edge turbulence. *Journal of Nuclear Materials*, 176:77, 1990.
- [27] I. Langmuir. Positive ion currents from the positive column of mercury arcs. *Science*, 58:290, 1923.
- [28] H. M. Mott-Smith and I. Langmuir. The theory of collectors in gaseous discharges. *Physical Review*, 28:727, 1926.
- [29] S. J. Zweben, J. L. Terry, D. P. Stotler, and R. J. Maqueda. Invited Review Article: Gas puff imaging diagnostics of edge plasma turbulence in magnetic fusion devices. *Review of Scientific Instruments*, 88:041101, 2017.
- [30] O. E. Garcia. Stochastic modeling of intermittent scrape-off layer plasma fluctuations. *Physical Review Letters*, 108:265001, 2012.

- [31] O.E. Garcia, S. M. Fritzner, R. Kube, I. Cziegler, B. LaBombard, and J. L. Terry. Intermittent fluctuations in the Alcator C-Mod scrape-off layer. *Physics of Plasmas*, 20:055901, 2013.
- [32] O. E. Garcia, I. Cziegler, R. Kube, B. LaBombard, and J. L. Terry. Burst statistics in Alcator C-Mod SOL turbulence. *Journal of Nuclear Materials*, 438:S180, 2013.
- [33] O. E. Garcia, J. Horacek, and R. A. Pitts. Intermittent fluctuations in the TCV scrape-off layer. *Nuclear Fusion*, 55:062002, 2015.
- [34] R. Kube, A. Theodorsen, O. E. Garcia, B. LaBombard, and J. L. Terry. Fluctuation statistics in the scrape-off layer of Alcator C-Mod. *Plasma Physics and Controlled Fusion*, 58:054001, 2016.
- [35] O. E. Garcia, R. Kube, A. Theodorsen, J. G. Bak, S. H. Hong, H. S. Kim, the KSTAR Project Team, and R. A. Pitts. SOL width and intermittent fluctuations in KSTAR. *Nuclear Materials and Energy*, 12:36, 2017.
- [36] R. Kube, O. E. Garcia, A. Theodorsen, D. Brunner, A. Q. Kuang, B. LaBombard, and J. L. Terry. Intermittent electron density and temperature fluctuations and associated fluxes in the Alcator C-Mod scrape-off layer. *Plasma Physics and Controlled Fusion*, 60:065002, 2018.
- [37] O. E. Garcia, R. Kube, A. Theodorsen, B. LaBombard, and J. L. Terry. Intermittent fluctuations in the Alcator C-Mod scrape-off layer for ohmic and high confinement mode plasmas. *Physics of Plasmas*, 25:056103, 2018.
- [38] A. Theodorsen, O. E. Garcia, R. Kube, B. LaBombard, and J. L. Terry. Universality of Poisson-driven plasma fluctuations in the Alcator C-Mod scrape-off layer. *Physics of Plasmas*, 25:122309, 2018.
- [39] A. Theodorsen. Statistical properties of intermittent fluctuations in the boundary of fusion plasmas. *PhD thesis, University of Tromsø*, 2018.
- [40] A. Theodorsen, O. E. Garcia, R. Kube, B. LaBombard, and J. L. Terry. Relationship between frequency power spectra and intermittent, large-amplitude bursts in the Alcator C-Mod scrape-off layer. *Nuclear Fusion*, 57:114004, 2017.
- [41] G. Y. Antar, P. Devynck, X. Garbet, and S. C. Luckhardt. Turbulence intermittency and burst properties in tokamak scrape-off layer. *Physics of Plasmas*, 8:1612, 2001.

- [42] G. Y. Antar, G. Counsell, Y. Yu, B. Labombard, and P. Devynck. Universality of intermittent convective transport in the scrape-off layer of magnetically confined devices. *Physics of Plasmas*, 10:419, 2003.
- [43] J. P. Graves, J. Horacek, R. A. Pitts, and K. I. Hopcraft. Self-similar density turbulence in the TCV tokamak scrape-off layer. *Plasma Physics and Controlled Fusion*, 47:L1, 2005.
- [44] O. E. Garcia, R. A. Pitts, J. Horacek, J. Madsen, V. Naulin, A. H. Nielsen, and J. Juul Rasmussen. Collisionality dependent transport in TCV SOL plasmas. *Plasma Physics and Controlled Fusion*, 49:B47, 2007.
- [45] O. E. Garcia. Blob transport in the plasma edge: a review. *Plasma and Fusion Research*, 4:019, 2009.
- [46] B. Labit, I. Furno, A. Fasoli, A. Diallo, S. H. Müller, G. Plyushchev, M. Podestà, and F. M. Poli. Universal statistical properties of drift-interchange turbulence in TORPEX plasmas. *Physical Review Letters*, 98:255002, 2007.
- [47] F. Sattin, M. Agostini, P. Scarin, N. Vianello, R. Cavazzana, L. Marrelli, G. Serianni, S. J. Zweben, R. J. Maqueda, Y. Yagi, et al. On the statistics of edge fluctuations: comparative study between various fusion devices. *Plasma Physics and Controlled Fusion*, 51:055013, 2009.
- [48] F. Sattin, M. Agostini, R. Cavazzana, G. Serianni, P. Scarin, and N. Vianello. About the parabolic relation existing between the skewness and the kurtosis in time series of experimental data. *Physica Scripta*, 79:045006, 2009.
- [49] O. E. Garcia, R. Kube, A. Theodorsen, and H. L. Pécseli. Stochastic modelling of intermittent fluctuations in the scrape-off layer: Correlations, distributions, level crossings, and moment estimation. *Physics of Plasmas*, 23:052308, 2016.
- [50] M. A. Pedrosa, C. Hidalgo, B. A. Carreras, R. Balbin, I. García-Cortés, D. Newman, B. Van Milligen, E. Sánchez, J. Bleuel, M. Endler, S. Davies, and G. F. Matthews. Empirical similarity of frequency spectra of the edge-plasma fluctuations in toroidal magnetic-confinement systems. *Physical Review Letters*, 82:3621, 1999.
- [51] B. A. Carreras, R. Balbin, B. Van Milligen, M. A. Pedrosa, I. Garcia-Cortes, E. Sanchez, C. Hidalgo, J. Bleuel, M. Endler, H. Thomsen,

- A. Chankin, S. Davies, K. Erents, and G. F. Matthews. Characterization of the frequency ranges of the plasma edge fluctuation spectra. *Physics of Plasmas*, 6:4615, 1999.
- [52] O. E. Garcia and A. Theodorsen. Auto-correlation function and frequency spectrum due to a super-position of uncorrelated exponential pulses. *Physics of Plasmas*, 24:032309, 2017.
- [53] J. A. Boedo, D. L. Rudakov, E. Hollmann, D. S. Gray, K. H. Burrell, R. A. Moyer, G. R. McKee, R. Fonck, P. C. Stangeby, T. E. Evans, P. B. Snyder, A. W. Leonard, M. A. Mahdavi, M. J. Schaffer, W. P. West, M. E. Fenstermacher, M. Grothd, S. L. Allend, C. Lasnierd, G. D. Porter, N. S. Wolf, R. J. Colchine, G. Zengf, L. Wangf, J. G. Watkinsg, T. Takahashih, and The DIII-D Team. Edge-localized mode dynamics and transport in the scrape-off layer of the DIII-D tokamak. *Physics of Plasmas*, 12:072516, 2005.
- [54] G. Y. Antar, G. Counsell, and J. W. Ahn. On the scaling of avaloids and turbulence with the average density approaching the density limit. *Physics of Plasmas*, 12:082503, 2005.
- [55] S. J. Zweben. Search for coherent structure within tokamak plasma turbulence. *The Physics of Fluids*, 28:974, 1985.
- [56] S. J. Zweben and R. W. Gould. Structure of edge-plasma turbulence in the Caltech tokamak. *Nuclear Fusion*, 25:171, 1985.
- [57] S. J. Zweben, D. Manos, R. V. Budny, P. Efthimion, E. Fredrickson, H. Greenside, K. W. Hill, S. Hiroe, S. Kilpatrick, K. McGuire, S. S. Medley, H. K. Park, A. T. Ramsey, and J. Wilgen. EDGE TURBULENCE MEASUREMENTS IN TFTR. *Journal of Nuclear Materials*, 145:250, 1987.
- [58] M. Endler, H. Niedermeyer, L. Giannone, E. Kolzhauer, A. Rudyj, G. Theimer, and N. Tsois. Measurements and modelling of electrostatic fluctuations in the scrape-off layer of ASDEX. *Nuclear Fusion*, 35:1307, 1995.
- [59] M. Endler. Turbulent SOL transport in stellarators and tokamaks. *Journal of Nuclear Materials*, 266:84, 1999.
- [60] M. V. Umansky, S. I. Krasheninnikov, B. LaBombard, and J. L. Terry. Comments on particle and energy balance in the edge plasma of Alcator C-Mod. *Physics of Plasmas*, 5:3373, 1998.

- [61] D. A. D’ippolito, J. R. Myra, and S. J. Zweben. Convective transport by intermittent blob-filaments: Comparison of theory and experiment. *Physics of Plasmas*, 18:060501, 2011.
- [62] A. Kirk, A. J. Thornton, J. R. Harrison, F. Militello, and N. R. Walkden. L-mode filament characteristics on MAST as a function of plasma current measured using visible imaging. *Plasma Physics and Controlled Fusion*, 58:085008, 2016.
- [63] B. D. Dudson, N. B. Ayed, A. Kirk, H. R. Wilson, G. Counsell, X. Xu, M. Umansky, P. B. Snyder, B. LLoyd, and the MAST team. Experiments and simulation of edge turbulence and filaments in MAST. *Plasma Physics and Controlled Fusion*, 50:124012, 2008.
- [64] S. J. Zweben, D. P. Stotler, J. L. Terry, B. LaBombard, M. Greenwald, M. Muterspaugh, C. S. Pitcher, Alcator C-Mod Group, K. Hallatschek, R. J. Maqueda, et al. Edge turbulence imaging in the Alcator C-Mod tokamak. *Physics of Plasmas*, 9:1981, 2002.
- [65] R. Kube, O. E. Garcia, B. LaBombard, J. L. Terry, and S. J. Zweben. Blob sizes and velocities in the Alcator C-Mod scrape-off layer. *Journal of Nuclear Materials*, 438:S505, 2013.
- [66] J. R. Myra, D. A. D’Ippolito, D. P. Stotler, S. J. Zweben, B. P. LeBlanc, J. E. Menard, R. J. Maqueda, and J. Boedo. Blob birth and transport in the tokamak edge plasma: Analysis of imaging data. *Physics of Plasmas*, 13:092509, 2006.
- [67] J. A. Boedo, D. Rudakov, R. Moyer, S. Krasheninnikov, D. Whyte, G. McKee, G. Tynan, M. Schaffer, P. Stangeby, P. West, et al. Transport by intermittent convection in the boundary of the DIII-D tokamak. *Physics of Plasmas*, 8:4826, 2001.
- [68] C. Silva, B. Goncalves, C. Hidalgo, M. A. Pedrosa, K. Erents, G. Matthews, and R. A. Pitts. Fluctuation measurements using a five-pin triple probe in the Joint European Torus boundary plasma. *Review of Scientific Instruments*, 75:4314, 2004.
- [69] D. Carralero, P. Manz, L. Aho-Mantila, G. Birkenmeier, M. Brix, M. Groth, H. W. Müller, U. Stroth, N. Vianello, E. Wolfrum, and AS-DEX Upgrade team. Experimental validation of a filament transport model in turbulent magnetized plasmas. *Physical Review Letters*, 115:215002, 2015.

- [70] S. H. Müller, C. Theiler, A. Fasoli, I. Furno, B. Labit, G. R. Tynan, M. Xu, Z. Yan, and J. H. Yu. Studies of blob formation, propagation and transport mechanisms in basic experimental plasmas (TORPEX and CSDX). *Plasma Physics and Controlled Fusion*, 51:055020, 2009.
- [71] N. B. Ayed, A. Kirk, B. Dudson, S. Tallents, R. G. L. Vann, H. R. Wilson, and the MAST team. Inter-ELM filaments and turbulent transport in the Mega-Amp Spherical Tokamak. *Plasma Physics and Controlled Fusion*, 51:035016, 2009.
- [72] G. S. Xu, V. Naulin, W. Fundamenski, J. Juul Rasmussen, A. H. Nielsen, and B. N. Wan. Intermittent convective transport carried by propagating electromagnetic filamentary structures in nonuniformly magnetized plasma. *Physics of Plasmas*, 17:022501, 2010.
- [73] R. J. Maqueda, D. P. Stotler, S. J. Zweben, and NSTX team. Intermittency in the scrape-off layer of the National Spherical Torus Experiment during H-mode confinement. *Journal of Nuclear Materials*, 415:S459, 2011.
- [74] O. Grulke, J. L. Terry, I. Cziegler, B. LaBombard, and O. E. Garcia. Experimental investigation of the parallel structure of fluctuations in the scrape-off layer of Alcator C-Mod. *Nuclear Fusion*, 54:043012, 2014.
- [75] S. J. Zweben, W. M. Davis, S. M. Kaye, J. R. Myra, R. E. Bell, B. P. LeBlanc, R. J. Maqueda, T. Munsat, S. A. Sabbagh, Y. Sechrest, D. P. Stotler, and the NSTX Team. Edge and SOL turbulence and blob variations over a large database in NSTX. *Nuclear Fusion*, 55:093035, 2015.
- [76] C. Theiler, I. Furno, P. Ricci, A. Fasoli, B. Labit, S. H. Müller, and G. Plyushchev. Cross-field motion of plasma blobs in an open magnetic field line configuration. *Physical Review Letters*, 103:065001, 2009.
- [77] J. R. Angus, S. I. Krasheninnikov, and M. V. Umansky. Effects of parallel electron dynamics on plasma blob transport. *Physics of Plasmas*, 19:082312, 2012.
- [78] O. E. Garcia, N. H. Bian, and W. Fundamenski. Radial interchange motions of plasma filaments. *Physics of Plasmas*, 13:082309, 2006.
- [79] R. Kube and O. E. Garcia. Effect of dynamical friction on interchange motion of plasma filaments. *Physics of Plasmas*, 19:042305, 2012.

- [80] R. Kube, O. E. Garcia, and M. Wiesenberger. Amplitude and size scaling for interchange motions of plasma filaments. *Physics of Plasmas*, 23:122302, 2016.
- [81] J. L. Terry, N. P. Basse, I. Cziegler, M. Greenwald, O. Grulke, B. LaBombard, S. J. Zweben, E. M. Edlund, J. W. Hughes, L. Lin, M. Porkolab, M. Sampsell, B. Veto, and S. J. Wukitch. Transport phenomena in the edge of Alcator C-Mod plasmas. *Nuclear Fusion*, 45:1321, 2005.
- [82] M. Agostini, S. J. Zweben, R. Cavazzana, P. Scarin, G. Serianni, R. J. Maqueda, and D. P. Stotler. Study of statistical properties of edge turbulence in the National Spherical Torus Experiment with the gas puff imaging diagnostic. *Physics of Plasmas*, 14:102305, 2007.
- [83] C. Theiler, A. Diallo, A. Fasoli, I. Furno, B. Labit, M. Podestà, F. M. Poli, and P. Ricci. The role of the density gradient on intermittent cross-field transport events in a simple magnetized toroidal plasma. *Physics of Plasmas*, 15:042303, 2008.
- [84] S. H. Müller, A. Diallo, A. Fasoli, I. Furno, B. Labit, and M. Podesta. Plasma blobs in a basic toroidal experiment: Origin, dynamics, and induced transport. *Physics of Plasmas*, 14:110704, 2007.
- [85] I. Furno, B. Labit, M. Podestà, A. Fasoli, S. H. Müller, F. M. Poli, P. Ricci, C. Theiler, S. Brunner, A. Diallo, and J. Graves. Experimental observation of the blob-generation mechanism from interchange waves in a plasma. *Physical Review Letters*, 100:055004, 2008.
- [86] I. Furno, B. Labit, A. Fasoli, F. M. Poli, P. Ricci, C. Theiler, S. Brunner, A. Diallo, J. P. Graves, M. Podestà, and S. H. Müller. Mechanism for blob generation in the TORPEX toroidal plasma. *Physics of Plasmas*, 15:055903, 2008.
- [87] O. E. Garcia, V. Naulin, A. H. Nielsen, and J. Juul Rasmussen. Computations of intermittent transport in scrape-off layer plasmas. *Physical Review Letters*, 92:165003, 2004.
- [88] N. Bisai, A. Das, S. Deshpande, R. Jha, P. Kaw, A. Sen, and R. Singh. Edge and scrape-off layer tokamak plasma turbulence simulation using two-field fluid model. *Physics of Plasmas*, 12:072520, 2005.
- [89] D. A. Russell, J. R. Myra, and D. A. D'Ippolito. Collisionality and magnetic geometry effects on tokamak edge turbulent transport. II. Many-blob turbulence in the two-region model. *Physics of Plasmas*, 14:102307, 2007.

- [90] D. A. Russell, J. R. Myra, and D. A. D'Ippolito. Saturation mechanisms for edge turbulence. *Physics of Plasmas*, 16:122304, 2009.
- [91] S. I. Krasheninnikov and A. I. Smolyakov. Generation of mesoscale convective structures in tokamak edge plasma. *Physics of Plasmas*, 14:102503, 2007.
- [92] S. I. Krasheninnikov and A. I. Smolyakov. Dynamics and generation mechanisms of mesoscale structures in tokamak edge plasmas. *Physics of Plasmas*, 15:055909, 2008.
- [93] P. Manz, T. T. Ribeiro, B. D. Scott, G. Birkenmeier, D. Carralero, G. Fuchert, S. H. Müller, H. W. Müller, U. Stroth, and E. Wolfrum. Origin and turbulence spreading of plasma blobs. *Physics of Plasmas*, 22:022308, 2015.
- [94] C. S. Chang and S. Ku. Spontaneous rotation sources in a quiescent tokamak edge plasma. *Physics of Plasmas*, 15:062510, 2008.
- [95] R. M. Churchill, C. S. Chang, S. Ku, and J. Dominski. Pedestal and edge electrostatic turbulence characteristics from an XGC1 gyrokinetic simulation. *Plasma Physics and Controlled Fusion*, 59:105014, 2017.
- [96] J. Madsen. Full-F gyrofluid model. *Physics of Plasmas*, 20:072301, 2013.
- [97] M. Wiesenberger, J. Madsen, and A. Kendl. Radial convection of finite ion temperature, high amplitude plasma blobs. *Physics of Plasmas*, 21:092301, 2014.
- [98] M. Held, M. Wiesenberger, J. Madsen, and A. Kendl. The influence of temperature dynamics and dynamic finite ion Larmor radius effects on seeded high amplitude plasma blobs. *Nuclear Fusion*, 56:126005, 2016.
- [99] T. T. Ribeiro and B. Scott. Tokamak turbulence computations on closed and open magnetic flux surfaces. *Plasma Physics and Controlled Fusion*, 47:1657, 2005.
- [100] T. T. Ribeiro and B. Scott. Gyrofluid turbulence studies of the effect of the poloidal position of an axisymmetric Debye sheath. *Plasma Physics and Controlled Fusion*, 50:055007, 2008.
- [101] S. I. Braginskii. Transport processes in a plasma. *Reviews of Plasma Physics*, 1965.

- [102] N. Bian, S. Benkadda, J. V. Paulsen, and O. E. Garcia. Blobs and front propagation in the scrape-off layer of magnetic confinement devices. *Physics of Plasmas*, 10:671, 2003.
- [103] J. R. Angus, M. V. Umansky, and S. I. Krasheninnikov. Effect of drift waves on plasma blob dynamics. *Physical Review Letters*, 108:215002, 2012.
- [104] N. R. Walkden, B. D. Dudson, and G. Fishpool. Characterization of 3D filament dynamics in a MAST SOL flux tube geometry. *Plasma Physics and Controlled Fusion*, 55:105005, 2013.
- [105] L. Easy, F. Militello, J. Omotani, B. Dudson, E. Havlíčková, P. Tamain, V. Naulin, and A. H. Nielsen. Three dimensional simulations of plasma filaments in the scrape off layer: A comparison with models of reduced dimensionality. *Physics of Plasmas*, 21:122515, 2014.
- [106] L. Easy, F. Militello, J. Omotani, N. R. Walkden, and B. Dudson. Investigation of the effect of resistivity on scrape off layer filaments using three-dimensional simulations. *Physics of Plasmas*, 23:012512, 2016.
- [107] F. Militello, N. R. Walkden, T. Farley, W. A. Gracias, J. Olsen, F. Riva, L. Easy, N. Fedorczak, I. Lupelli, J. Madsen, A. H. Nielsen, P. Ricci, P. Tamain, and J. Young. Multi-code analysis of scrape-off layer filament dynamics in MAST. *Plasma Physics and Controlled Fusion*, 58:105002, 2016.
- [108] F. Riva, C. Colin, J. Denis, L. Easy, I. Furno, J. Madsen, F. Militello, V. Naulin, A. H. Nielsen, J. M. B. Olsen, J. T. Omotani, J. Juul Rasmussen, P. Ricci, E. Serre, P. Tamain, and C. Theiler. Blob dynamics in the TORPEX experiment: a multi-code validation. *Plasma Physics and Controlled Fusion*, 58:044005, 2016.
- [109] W. Lee, J. R. Angus, M. V. Umansky, and S. I. Krasheninnikov. Electromagnetic effects on plasma blob-filament transport. *Journal of Nuclear Materials*, 463:765, 2015.
- [110] P. W. Gingell, S. C. Chapman, R. O. Dendy, and C. S. Brady. Transport and evolution of ion gyro-scale plasma blobs in perpendicular magnetic fields. *Plasma Physics and Controlled Fusion*, 54:065005, 2012.
- [111] P. W. Gingell, S. C. Chapman, and R. O. Dendy. Plasma blob formation by ion kinetic Kelvin-Helmholtz and interchange instabilities. *Plasma Physics and Controlled Fusion*, 56:035012, 2014.

- [112] O. E. Garcia, N. H. Bian, V. Naulin, A. H. Nielsen, and J. Juul Rasmussen. Mechanism and scaling for convection of isolated structures in nonuniformly magnetized plasmas. *Physics of Plasmas*, 12:090701, 2005.
- [113] R. Kube and O. E. Garcia. Velocity scaling for filament motion in scrape-off layer plasmas. *Physics of Plasmas*, 18:102314, 2011.
- [114] F. Militello, B. Dudson, L. Easy, A. Kirk, and P. Naylor. On the interaction of scrape off layer filaments. *Plasma Physics and Controlled Fusion*, 59:125013, 2017.
- [115] A. Kendl. Gyrofluid vortex interaction. *Plasma Physics and Controlled Fusion*, 60:025017, 2018.
- [116] O. Pogutse, W. Kerner, V. Gribkov, S. Bazdenkov, and M. Osipenko. The resistive interchange convection in the edge of tokamak plasmas. *Plasma Physics and Controlled Fusion*, 36:1963, 1994.
- [117] P. Beyer and K. H. Spatschek. Center manifold theory for the dynamics of the L-H-transition. *Physics of Plasmas*, 3:995, 1996.
- [118] W. Horton, G. Hu, and G. Laval. Turbulent transport in mixed states of convective cells and sheared flows. *Physics of Plasmas*, 3:2912, 1996.
- [119] M. Berning and K. H. Spatschek. Bifurcations and transport barriers in the resistive-g paradigm. *Physical Review E*, 62:1162, 2000.
- [120] O. E. Garcia, N. H. Bian, J. V. Paulsen, S. Benkadda, and K. Rypdal. Confinement and bursty transport in a flux-driven convection model with sheared flows. *Plasma Physics and Controlled Fusion*, 45:919, 2003.
- [121] O. E. Garcia and N. H. Bian. Bursting and large-scale intermittency in turbulent convection with differential rotation. *Physical Review E*, 68:047301, 2003.
- [122] O. E. Garcia, N. H. Bian, V. Naulin, A. H. Nielsen, and J. Juul Rasmussen. Two-dimensional convection and interchange motions in fluids and magnetized plasmas. *Physica Scripta*, 2006:104, 2006.
- [123] G. Decristoforo, A. Theodorsen, and O. E. Garcia. Intermittent fluctuations due to Lorentzian pulses in turbulent thermal convection. *Physics of Fluids*, 32:085102, 2020.
- [124] S. Benkadda, X. Garbet, and A. Verga. Interchange instability turbulence model in edge tokamak plasma. *Contributions to Plasma Physics*, 34:247, 1994.

- [125] Y. Sarazin and P. Ghendrih. Intermittent particle transport in two-dimensional edge turbulence. *Physics of Plasmas*, 5:4214, 1998.
- [126] V. Naulin, A. H. Nielsen, and J. Juul Rasmussen. Dispersion of ideal particles in a two-dimensional model of electrostatic turbulence. *Physics of Plasmas*, 6:4575, 1999.
- [127] O. E. Garcia. Two-field transport models for magnetized plasmas. *Journal of Plasma Physics*, 65:81, 2001.
- [128] P. Ghendrih, Y. Sarazin, G. Attuel, S. Benkadda, P. Beyer, G. Falchetto, C. Figarella, X. Garbet, V. Grandgirard, and M. Ottaviani. Theoretical analysis of the influence of external biasing on long range turbulent transport in the scrape-off layer. *Nuclear Fusion*, 43:1013, 2003.
- [129] Y Sarazin, Ph Ghendrih, G Attuel, C Clément, X Garbet, V Grandgirard, M Ottaviani, S Benkadda, P Beyer, N Bian, et al. Theoretical understanding of turbulent transport in the SOL. *Journal of Nuclear Materials*, 313:796, 2003.
- [130] N. Bisai, A. Das, S. Deshpande, R. Jha, P. Kaw, A. Sen, and R. Singh. Simulation of plasma transport by coherent structures in scrape-off-layer tokamak plasmas. *Physics of Plasmas*, 11:4018, 2004.
- [131] O. E. Garcia, V. Naulin, A. H. Nielsen, and J. Juul Rasmussen. Turbulence and intermittent transport at the boundary of magnetized plasmas. *Physics of Plasmas*, 12:062309, 2005.
- [132] N. Bisai, A. Das, S. Deshpande, R. Jha, P. Kaw, A. Sen, and R. Singh. Formation of a density blob and its dynamics in the edge and the scrape-off layer of a tokamak plasma. *Physics of Plasmas*, 12:102515, 2005.
- [133] O. E. Garcia, V. Naulin, A. H. Nielsen, and J. Juul Rasmussen. Turbulence simulations of blob formation and radial propagation in toroidally magnetized plasmas. *Physica Scripta*, 2006:89, 2006.
- [134] F. Militello, W. Fundamenski, V. Naulin, and A. H. Nielsen. Simulations of edge and scrape off layer turbulence in mega ampere spherical tokamak plasmas. *Plasma Physics and Controlled Fusion*, 54:095011, 2012.
- [135] V. Naulin. Electromagnetic transport components and sheared flows in drift-alfvén turbulence. *Physics of Plasmas*, 10:4016, 2003.
- [136] V. Naulin, O. E. Garcia, A. H. Nielsen, and J. Juul Rasmussen. Statistical properties of transport in plasma turbulence. *Physics Letters A*, 321:355, 2004.

- [137] G. Decristoforo, A. Theodorsen, J. Omotani, T. Nicholas, and O. E. Garcia. Numerical turbulence simulations of intermittent fluctuations in the scrape-off layer of magnetized plasmas. *arXiv:2102.04723*, 2021.
- [138] F. Nespoli, I. Furno, B. Labit, P. Ricci, F. Avino, F. D. Halpern, F. Musil, and F. Riva. Blob properties in full-turbulence simulations of the TCV scrape-off layer. *Plasma Physics and Controlled Fusion*, 59:055009, 2017.
- [139] F. Nespoli, P. Tamain, N. Fedorczak, G. Ciraolo, D. Galassi, R. Tatali, E. Serre, Y. Marandet, H. Bufferand, and P. Ghendrih. 3D structure and dynamics of filaments in turbulence simulations of WEST diverted plasmas. *Nuclear Fusion*, 59:096006, 2019.
- [140] P. Paruta, C. Beadle, P. Ricci, and C. Theiler. Blob velocity scaling in diverted tokamaks: A comparison between theory and simulation. *Physics of Plasmas*, 26:032302, 2019.
- [141] G. Decristoforo, F. Militello, T. Nicholas, J. Omotani, C. Marsden, N. Walkden, and O. E. Garcia. Blob interactions in 2D scrape-off layer simulations. *Physics of Plasmas*, 27:122301, 2020.
- [142] V. Naulin, A. Kendl, O. E. Garcia, A. H. Nielsen, and J. Juul Rasmussen. Shear flow generation and energetics in electromagnetic turbulence. *Physics of Plasmas*, 12:052515, 2005.
- [143] P. Ricci, F. D. Halpern, S. Jolliet, J. Loizu, A. Masetto, A. Fasoli, I. Furno, and C. Theiler. Simulation of plasma turbulence in scrape-off layer conditions: the GBS code, simulation results and code validation. *Plasma Physics and Controlled Fusion*, 54:124047, 2012.
- [144] P. Tamain, H. Bufferand, G. Ciraolo, C. Colin, P. Ghendrih, F. Schwander, and E. Serre. 3D Properties of Edge Turbulent Transport in Full-Torus Simulations and their Impact on Poloidal Asymmetries. *Contributions to Plasma Physics*, 54:555, 2014.
- [145] B. D. Dudson and J. Leddy. Hermes: global plasma edge fluid turbulence simulations. *Plasma Physics and Controlled Fusion*, 59:054010, 2017.
- [146] A. Stegmeir, D. Coster, A. Ross, O. Maj, K. Lackner, and E. Poli. GRILLIX: a 3D turbulence code based on the flux-coordinate independent approach. *Plasma Physics and Controlled Fusion*, 60:035005, 2018.
- [147] T. E. G. Nicholas, J. Omotani, F. Riva, F. Militello, and B. Dudson. Comparing Two- and Three-Dimensional Models of Scrape-Off-Layer Turbulent Transport. *arXiv:2103.09727*, 2021.

- [148] F. Riva, F. Militello, S. Elmore, J. T. Omotani, B. Dudson, N. R. Walkden, and the MAST team. Three-dimensional plasma edge turbulence simulations of the Mega Ampere Spherical Tokamak and comparison with experimental measurements. *Plasma Physics and Controlled Fusion*, 61:095013, 2019.
- [149] F. Militello. *Boundary plasma physics - An accessible guide to transport, detachment and divertor design*. To be published in Springer Nature, 2021.
- [150] D. Hoare, F. Militello, J. T. Omotani, F. Riva, S. Newton, T. Nicholas, D. Ryan, and N. R. Walkden. Dynamics of scrape-off layer filaments in high β plasmas. *Plasma Physics and Controlled Fusion*, 61:105013, 2019.
- [151] M. Kočan, R. Pánek, J. Stöckel, M. Hron, J. P. Gunn, and R. Dejarnac. Ion temperature measurements in the tokamak scrape-off layer. *Journal of Nuclear Materials*, 363:1436, 2007.
- [152] M. Kočan, F. P. Genrich, A. Kendl, H. W. Müller, and ASDEX Upgrade Team. Ion temperature fluctuations in the ASDEX Upgrade scrape-off layer. *Plasma Physics and Controlled Fusion*, 54, 2012.
- [153] S. Ahmed. Effects of ion temperature on Scrape-off layer filaments. *Master thesis, University of Bath*, 2020.
- [154] N. R. Walkden, L. Easy, F. Militello, and J. T. Omotani. Dynamics of 3D isolated thermal filaments. *Plasma Physics and Controlled Fusion*, 58:115010, 2016.
- [155] W. Fundamenski, O. E. Garcia, V. Naulin, R. A. Pitts, A. H. Nielsen, J. Juul Rasmussen, J. Horacek, J. P. Graves, and JET EFDA contributors. Dissipative processes in interchange driven scrape-off layer turbulence. *Nuclear Fusion*, 47:417, 2007.
- [156] P. M. Bellan. *Fundamentals of plasma physics*. Cambridge University Press, 2008.
- [157] O. Meyer. Drift wave turbulence and zonal flows. *Master thesis, University of Tromsø*, 2012.
- [158] T. Nicholas. Reduced Simulations of Scrape-Off-Layer Turbulence. *PhD thesis, University of York*, 2021.
- [159] J. L. Terry, S. J. Zweben, K. Hallatschek, B. LaBombard, R. J. Maqueda, B. Bai, C. J. Boswell, M. Greenwald, D. Kopon, W. M. Nevins, C. S.

- Pitcher, B. N. Rogers, D. P. Stotler, and X. Q. Xu. Observations of the turbulence in the scrape-off-layer of Alcator C-Mod and comparisons with simulation. *Physics of Plasmas*, 10:1739, 2003.
- [160] M. Wensing, B. P. Duval, O. Février, A. Fil, D. Galassi, E. Havlickova, A. Perek, H. Reimerdes, C. Theiler, K. Verhaegh, M. Wischmeier, the EUROfusion MST1 team, and the TCV team. SOLPS-ITER simulations of the TCV divertor upgrade. *Plasma Physics and Controlled Fusion*, 61:085029, 2019.
- [161] J. G. Bak, H. S. Kim, M. K. Bae, J. W. Juhn, D. C. Seo, E. N. Bang, S. B. Shim, K. S. Chung, H. J. Lee, and S. H. Hong. Investigation of SOL parameters and divertor particle flux from electric probe measurements in KSTAR. *Journal of Nuclear Materials*, 463:424, 2015.
- [162] F. Militello and W. Fundamenski. Multi-machine comparison of drift fluid dimensionless parameters. *Plasma Physics and Controlled Fusion*, 53:095002, 2011.
- [163] O. E. Garcia. Convective Transport and Shear Flows in Fluids and Magnetized Plasmas. *PhD thesis, University of Tromsø*, 2002.
- [164] H. Bénard. Les tourbillons cellulaires dans une nappe liquide.-Méthodes optiques d'observation et d'enregistrement. *Journal de Physique Théorique et Appliquée*, 10:254, 1901.
- [165] Lord Rayleigh. On convection currents in a horizontal layer of fluid, when the higher temperature is on the under side. *The London, Edinburgh, and Dublin Philosophical Magazine and Journal of Science*, 32:529, 1916.
- [166] F. H. Busse. Non-linear properties of thermal convection. *Reports on Progress in Physics*, 41:1929, 1978.
- [167] E. D. Siggia. High Rayleigh number convection. *Annual Review of Fluid Mechanics*, 26:137, 1994.
- [168] E. Bodenschatz, W. Pesch, and G. Ahlers. Recent developments in Rayleigh-Bénard convection. *Annual Review of Fluid Mechanics*, 32:709, 2000.
- [169] L. P. Kadanoff. Turbulent heat flow: structures and scaling. *Physics Today*, 54:34, 2001.
- [170] G. Ahlers and D. Grossmann, S. Lohse. Heat transfer and large scale dynamics in turbulent Rayleigh-Bénard convection. *Reviews of Modern Physics*, 81:503, 2009.

- [171] N. Campbell. The study of discontinuous phenomena. In *Proceedings of the Cambridge Philosophical Society*, volume 15, page 117, 1909.
- [172] S. O. Rice. Mathematical analysis of random noise. *The Bell System Technical Journal*, 23:282, 1944.
- [173] S. O. Rice. Mathematical analysis of random noise. *The Bell System Technical Journal*, 24:46, 1945.
- [174] J. R. Segal, B. Ceccarelli, R. Fesce, and W. P. Hurlbut. Miniature end-plate potential frequency and amplitude determined by an extension of Campbell's theorem. *Biophysical Journal*, 47:183, 1985.
- [175] R. Fesce, J. R. Segal, and W. P. Hurlbut. Fluctuation analysis of nonideal shot noise. Application to the neuromuscular junction. *The Journal of General Physiology*, 88:25, 1986.
- [176] J. W. Jang. Martingale approach for moments of discounted aggregate claims. *Journal of Risk and Insurance*, 71:201, 2004.
- [177] P. Claps, A. Giordano, and F. Laio. Advances in shot noise modeling of daily streamflows. *Advances in Water Resources*, 28:992, 2005.
- [178] M. Lefebvre. Generalized filtered Poisson processes and application in hydrology. *Statistics & Probability Letters*, 78:3274, 2008.
- [179] E. Daly and A. Porporato. Effect of different jump distributions on the dynamics of jump processes. *Physical Review E*, 81:061133, 2010.
- [180] Z. Elter, C. Jammes, I. Pázsit, L. Pál, and P. Filliatre. Performance investigation of the pulse and Campbelling modes of a fission chamber using a Poisson pulse train simulation code. *Nuclear Instruments and Methods in Physics Research Section A: Accelerators, Spectrometers, Detectors and Associated Equipment*, 774:60, 2015.
- [181] O. E. Garcia and A. Theodorsen. Skewed Lorentzian pulses and exponential frequency power spectra. *Physics of Plasmas*, 25:014503, 2018.
- [182] J. E. Maggs and G. J. Morales. Generality of deterministic chaos, exponential spectra, and Lorentzian pulses in magnetically confined plasmas. *Physical Review Letters*, 107:185003, 2011.
- [183] B. P. Van Milligen, R. Sánchez, and C. Hidalgo. Relevance of Uncorrelated Lorentzian Pulses for the Interpretation of Turbulence in the Edge of Magnetically Confined Toroidal Plasmas. *Physical Review Letters*, 109:105001, 2012.

- [184] J. E. Maggs, T. L. Rhodes, and G. J. Morales. Chaotic density fluctuations in L-mode plasmas of the DIII-D tokamak. *Plasma Physics and Controlled Fusion*, 57:045004, 2015.
- [185] Z. Zhu, A. E. White, T. A. Carter, S. G. Baek, and J. L. Terry. Chaotic edge density fluctuations in the Alcator C-Mod tokamak. *Physics of Plasmas*, 24:042301, 2017.
- [186] O. E. Garcia and A. Theodorsen. Power law spectra and intermittent fluctuations due to uncorrelated Lorentzian pulses. *Physics of Plasmas*, 24:020704, 2017.
- [187] A. Theodorsen and O. E. Garcia. Probability distribution functions for intermittent scrape-off layer plasma fluctuations. *Plasma Physics and Controlled Fusion*, 60:034006, 2018.
- [188] O. E. Garcia and A. Theodorsen. Intermittent fluctuations due to uncorrelated Lorentzian pulses. *Physics of Plasmas*, 25:014506, 2018.
- [189] Y. Marandet, N. Nace, M. Valentinuzzi, P. Tamain, H. Bufferand, G. Ciraolo, P. Genesio, and N. Mellet. Assessment of the effects of scrape-off layer fluctuations on first wall sputtering with the TOKAM-2D turbulence code. *Plasma Physics and Controlled Fusion*, 58:114001, 2016.
- [190] A. Theodorsen and O. E. Garcia. Level crossings and excess times due to a superposition of uncorrelated exponential pulses. *Physical Review E*, 97:012110, 2018.
- [191] F. Militello and J. T. Omotani. On the relation between non-exponential scrape off layer profiles and the dynamics of filaments. *Plasma Physics and Controlled Fusion*, 58:125004, 2016.
- [192] N. R. Walkden, A. Wynn, F. Militello, B. Lipschultz, G. Matthews, C. Guillemaut, J. Harrison, D. Moulton, and JET Contributors. Interpretation of scrape-off layer profile evolution and first-wall ion flux statistics on JET using a stochastic framework based on filamentary motion. *Plasma Physics and Controlled Fusion*, 59:085009, 2017.
- [193] F. Militello, T. Farley, K. Mukhi, N. Walkden, and J. T. Omotani. A two-dimensional statistical framework connecting thermodynamic profiles with filaments in the scrape off layer and application to experiments. *Physics of Plasmas*, 25:056112, 2018.

- [194] F. Militello. Understanding density decay lengths and particle exhaust in tokamaks. *16th European Fusion Theory Conference*, 2015.
- [195] R. Kube, A. Theodorsen, O. E. Garcia, D. Brunner, B. LaBombard, and J. L. Terry. Comparison between mirror Langmuir probe and gas puff imaging measurements of intermittent fluctuations in the Alcator C-Mod scrape-off layer. *arXiv:2005.02145*, 2020.
- [196] W. H. Richardson. Bayesian-based iterative method of image restoration. *Journal of the Optical Society of America*, 62:55, 1972.
- [197] L. B. Lucy. An iterative technique for the rectification of observed distributions. *The Astronomical Journal*, 79:745, 1974.
- [198] F. Dell’Acqua, G. Rizzo, P. Scifo, R. A. Clarke, G. Scotti, and F. Fazio. A model-based deconvolution approach to solve fiber crossing in diffusion-weighted MR imaging. *IEEE Transactions on Biomedical Engineering*, 54:462, 2007.
- [199] M. Wiesenberger. Gyrofluid computations of filament dynamics in tokamak scrape-off layers. *PhD thesis, University of Innsbruck*, 2014.
- [200] M. Held, M. Wiesenberger, R. Kube, and A. Kendl. Non-Oberbeck–Boussinesq zonal flow generation. *Nuclear Fusion*, 58:104001, 2018.
- [201] D. A. Russell, J. R. Myra, D. A. D’Ippolito, T. L. Munsat, Y. Sechrest, R. J. Maqueda, D. P. Stotler, S. J. Zweben, and NSTX Team. Comparison of scrape-off layer turbulence simulations with experiments using a synthetic gas puff imaging diagnostic. *Physics of Plasmas*, 18:022306, 2011.
- [202] Y. Marandet, P. Tamain, R. Futtersack, P. Ghendrih, H. Bufferand, P. Genesio, and A. Mekkaoui. Influence of neutral particles on scrape-off layer turbulence with application to the interpretation of fast camera data. *Journal of Nuclear Materials*, 438:S518, 2013.
- [203] A. S. Thryssøe, M. Løiten, J. Madsen, V. Naulin, A. H. Nielsen, and J. Juul Rasmussen. Plasma particle sources due to interactions with neutrals in a turbulent scrape-off layer of a toroidally confined plasma. *Physics of Plasmas*, 25:032307, 2018.
- [204] N. Bisai and P. K. Kaw. Influence of hot and cold neutrals on scrape-off layer tokamak plasma turbulence. *Physics of Plasmas*, 25:012503, 2018.

Paper I: Intermittent fluctuations due to Lorentzian pulses in turbulent thermal convection

G. Decristoforo, A. Theodorsen and O. E. Garcia,
Physics of Fluids **32**, 085102 (2020),
doi:10.1063/5.0012017

Intermittent fluctuations due to Lorentzian pulses in turbulent thermal convection

Cite as: Phys. Fluids **32**, 085102 (2020); <https://doi.org/10.1063/5.0012017>

Submitted: 30 April 2020 . Accepted: 14 July 2020 . Published Online: 03 August 2020

G. Decristoforo , A. Theodorsen , and O. E. Garcia 



View Online



Export Citation



CrossMark

ARTICLES YOU MAY BE INTERESTED IN

[Analysis of combustion acoustic phenomena in compression-ignition engines using large eddy simulation](#)

Physics of Fluids **32**, 085101 (2020); <https://doi.org/10.1063/5.0011929>

[Smoothed particle hydrodynamics simulation of converging Richtmyer–Meshkov instability](#)

Physics of Fluids **32**, 086102 (2020); <https://doi.org/10.1063/5.0015589>

[Visualizing the effectiveness of face masks in obstructing respiratory jets](#)

Physics of Fluids **32**, 061708 (2020); <https://doi.org/10.1063/5.0016018>



NEW!

Sign up for topic alerts
New articles delivered to your inbox



Intermittent fluctuations due to Lorentzian pulses in turbulent thermal convection

Cite as: Phys. Fluids **32**, 085102 (2020); doi: 10.1063/5.0012017

Submitted: 30 April 2020 • Accepted: 14 July 2020 •

Published Online: 3 August 2020



G. Decristoforo,^{a)}  A. Theodorsen,^{b)}  and O. E. Garcia^{c)} 

AFFILIATIONS

Department of Physics and Technology, UiT The Arctic University of Norway, NO-9037 Tromsø, Norway

^{a)} Author to whom correspondence should be addressed: gregor.decristoforo@uit.no

^{b)} audun.theodorsen@uit.no

^{c)} odd.erik.garcia@uit.no

ABSTRACT

Turbulent motions due to flux-driven thermal convection are investigated by numerical simulations and stochastic modeling. Tilting of convection cells leads to the formation of sheared flows and quasi-periodic relaxation oscillations for the energy integrals far from the threshold for linear instability. The probability density function for the temperature and radial velocity fluctuations in the fluid layer changes from a normal distribution at the onset of turbulence to a distribution with an exponential tail for large fluctuation amplitudes for strongly driven systems. The frequency power spectral density has an exponential shape, which is a signature of deterministic chaos. By use of a novel deconvolution method, this is shown to result from the presence of Lorentzian pulses in the underlying time series, demonstrating that exponential frequency spectra can also persist in turbulent flow regimes.

Published under license by AIP Publishing. <https://doi.org/10.1063/5.0012017>

I. INTRODUCTION

Buoyancy-driven motion of a fluid confined between horizontal plates is a cornerstone of fluid mechanics and has many areas of application, including astrophysics, industry, laboratory fluid dynamics, meteorology, oceanography, and plasma physics. Due to its rich dynamics, the Rayleigh–Bénard convection model has become a paradigm to investigate pattern formation, nonlinear phenomena, and scaling relationships.^{1–6}

For sufficiently strong forcing, oscillating fluid motion, and chaotic behavior results. An intrinsic property of deterministic chaos is an exponential frequency power spectral density for the fluctuations. This has been observed in numerous experiments and model simulations of fluids and magnetized plasmas.^{7–27} Recently, the exponential spectrum has been attributed to the presence of uncorrelated Lorentzian pulses in the temporal dynamics.^{29–43} This includes the Lorenz model, which describes chaotic dynamics in Rayleigh–Bénard convection.^{23–30}

In two-dimensional thermal convection, it is well known that the convection rolls in a horizontally periodic domain can give rise to the spontaneous formation of strong mean flows through a tilting instability.^{14–63} For strongly driven thermal convection,

turbulent states develop where the sheared mean flows transiently suppress the fluctuating motions, resulting in quasi-periodic relaxation oscillations.^{57–74} Similar relaxation oscillations have also been identified in turbulent plasmas.^{75–86} This dynamics has been described in terms of a predator–prey system, with a conservative transfer of kinetic energy from the fluctuating to the mean motions and a viscous dissipation of the latter.^{60–63,87–90} The velocity and temperature fluctuations throughout the fluid layer are strongly intermittent with positive skewness and flatness moments. The probability density functions have exponential tails, resembling the state of hard turbulence in Rayleigh–Bénard convection.^{91–100}

In this contribution, it is for the first time demonstrated that these properties of irregular fluid motion can be present simultaneously. The fluctuation statistics in a state of turbulent convection are investigated by numerical simulations of a fluid layer driven by a fixed heat flux.^{60,101–103} Time-series analysis and stochastic modeling of the temperature field are presented. It is demonstrated that the frequency power spectral density of the fluctuations has an exponential tail. A novel deconvolution algorithm is applied, showing that the temperature signal can be described as a superposition of Lorentzian pulses. Hence, the well-known properties of deterministic chaos can persist even in turbulent flow regimes.

The outline of this paper is as follows: In Sec. II, we present the model equations and briefly discuss the shear flow generation mechanism. In Sec. III, the basic results from the numerical simulations are presented. The fluctuation statistics are presented in Sec. IV and in Sec. V; it is demonstrated that the exponential frequency power spectral density is due to the presence of Lorentzian pulses in the time series. The conclusions and a summary of the results are presented in Sec. VI. The Appendix presents a derivation of the frequency power spectral density due to a periodic train of pulses with fixed shape and duration.

II. MODEL EQUATIONS

Considering two-dimensional fluid motions in a gravitational field opposite to the x -axis, the model equations describing thermal convection are given by

$$\left(\frac{\partial}{\partial t} + \bar{\mathbf{z}} \times \nabla \psi \cdot \nabla\right) \Theta = \kappa \nabla^2 \Theta, \tag{1a}$$

$$\left(\frac{\partial}{\partial t} + \bar{\mathbf{z}} \times \nabla \psi \cdot \nabla\right) \Omega + \frac{\partial \Theta}{\partial y} = \mu \nabla^2 \Omega, \tag{1b}$$

where Θ describes the temperature, ψ is the stream function for the two-dimensional fluid velocity field $\mathbf{v} = \bar{\mathbf{z}} \times \nabla \psi$, and $\Omega = \bar{\mathbf{z}} \cdot \nabla \times \mathbf{v} = \nabla^2 \psi$ is the associated fluid vorticity. The temperature perturbations are normalized by the temperature difference ΔT over the fluid layer in hydrostatic equilibrium, length scales are normalized by the fluid layer depth d , and time is normalized by the ideal interchange rate.^{101–103} The normalized heat diffusivity κ and viscosity μ are related to the Rayleigh and Prandtl numbers by $R = 1/\kappa\mu$ and $P = \mu/\kappa$, respectively. The temperature in hydrostatic equilibrium is given by $\Theta = 1 - x$. A similar mathematical model also describes fluctuations in non-uniformly magnetized plasmas where the symmetry axis z corresponds to the direction of the magnetic field and the effective gravity is due to magnetic field curvature.^{50–54,57–63}

In many cases, the fluid is confined in a geometry where x corresponds to the radial coordinate and y the azimuthal direction. In the following, we therefore refer to the x - and y -direction as radial and azimuthal, respectively. All dependent variables are accordingly assumed to be periodic in the azimuthal direction, for example, $\Theta(y) = \Theta(y + L)$. In the radial direction, the boundary conditions are taken to be

$$\psi(x = 0) = \psi(x = 1) = 0, \tag{2a}$$

$$\Omega(x = 0) = \Omega(x = 1) = 0, \tag{2b}$$

$$\frac{\partial \Theta}{\partial x}(x = 0) = -1, \quad \Theta(x = 1) = 0. \tag{2c}$$

The latter condition corresponds to a fixed conductive heat flux through the fluid layer.^{60,101–103} It should be noted that the free-slip boundary conditions imply that there is no convective heat transport through the radial boundaries since $v_x = -\partial\psi/\partial y = 0$ for $x = 0, 1$.

For the azimuthally periodic system, it is convenient to define the profile of any dependent variable as its azimuthal average and denote this by a zero subscript. For the temperature field Θ , this is given by

$$\Theta_0(x, t) = \frac{1}{L} \int_0^L dy \Theta(\mathbf{x}, t). \tag{3}$$

The motivation for separating profiles and spatial fluctuations is simply that the latter are the components mediating the radial convective heat flux, while the former describes the modifications of the equilibrium state profiles.

Similar to the temperature profile, an average azimuthal flow is also defined by

$$v_0(x, t) = \frac{1}{L} \int_0^L dy \frac{\partial \psi}{\partial x} = \frac{\partial \psi_0}{\partial x}. \tag{4}$$

Due to the conservation of net circulation of the fluid layer, the mean azimuthal flow is intrinsically sheared and corresponds to differential rotation of the fluid layer. Such flows develop due to a tilting instability of the convective cells.^{44–63} Since the symmetric flow v_0 is intrinsically incapable of mediating radial convective transport, it is natural to separate the kinetic energy into two components comprised by the fluctuating motions and the sheared mean flows, defined, respectively, by

$$K(t) = \int dx \frac{1}{2} [\nabla(\psi - \psi_0)]^2, \quad U(t) = \int dx \frac{1}{2} v_0^2. \tag{5}$$

The evolution of these energy integrals are readily derived from the mean vorticity equation,^{60–63}

$$\frac{dK}{dt} = \int dx v_x \Theta - \Pi - \mu \int dx (\Omega - \Omega_0)^2, \tag{6}$$

$$\frac{dU}{dt} = \Pi - \mu \int dx \Omega_0^2, \tag{7}$$

where the kinetic energy transfer rate from the fluctuating motions to the sheared mean flows is defined by

$$\Pi = \int dx v_0 \frac{\partial}{\partial x} (v_x v_y). \tag{8}$$

As expected, the convective transport drive for the kinetic energy integral in Eq. (6) appears only for the fluctuating motions, while viscous dissipation damps kinetic energy in either form. The radial convective transport of azimuthal momentum evidently yields a conservative transfer of kinetic energy between the fluctuating motions and the azimuthally mean flows.

Numerical simulations have shown that turbulent convection can display predator–prey-like relaxation oscillations for the energy integrals,^{57–62} which can be interpreted as follows: Initially, the convective energy grows exponentially due to the primary instability. When the fluctuation level becomes sufficiently large to sustain the sheared mean flows against viscous dissipation, this flow energy grows at the expense of the convective motions. The spatial fluctuations are effectively stabilized at a sufficiently strong shear flow. Kinetic energy is, however, continuously transferred to the mean flows, leading to an almost complete suppression of the fluctuation energy and, thus, the radial convective transport. Subsequently, there are no fluctuating motions to sustain the sheared flows, which hence decay on a viscous time scale. Finally, as the mean flows become sufficiently weak, the convective energy again starts to grow and the cycle repeats. As will be seen from the numerical simulations presented in Sec. III, this leads to a strong modulation of the fluctuations.

III. TURBULENT CONVECTION

The temperature and vorticity equations are solved numerically by combining a finite difference and a Fourier-Galerkin method for spatial discretization using an Arakawa scheme for the exact conservation of energy and enstrophy. The resolution of the simulation domain is set to 128×128 grid points. For time discretization, a third order stiffly stable integrator is used^{83,104,105} with a time step of $\Delta t = 5 \times 10^{-3}$. Time series of the dependent variables are recorded at radially equidistant points in the simulation domain and analyzed in the following.

For sufficiently high Rayleigh numbers, numerical simulations of the two-dimensional thermal convection model result in turbulent states.⁶⁰⁻⁶² Previously, it has been shown that close to the onset of turbulent convection, for $R = 4 \times 10^5$ and $P = 1$, the radial velocity fluctuations in the center of the domain are normally distributed.⁶⁰ Increasing the Rayleigh number to $R = 2 \times 10^6$ results in a probability distribution function for the radial velocity fluctuations with exponential tails.⁶⁰⁻⁶² Previous investigations have shown that the large-amplitude fluctuations are associated with coherent structures propagating through the fluid layer. Here, we present a detailed analysis of the fluctuation statistics in the latter parameter regime (with $R = 2 \times 10^6$, $P = 1$, corresponding to $\kappa = \mu = 7.07 \times 10^{-4}$ and $L = L_x = L_y = 1$), resembling the state of hard turbulence in thermal convection experiments.⁹¹⁻¹⁰⁰

The time-averaged profile of the temperature and the relative fluctuation level are presented in Fig. 1. Here and in the following, angular brackets indicate a time average. The turbulent motions significantly reduce the heat confinement in the fluid layer, reducing the temperature on the left boundary from unity in the case of only heat conduction to less than 0.343 on average in the turbulent state. There is a significant profile gradient in the center of the fluid layer. The relative fluctuation level increases drastically from the center of the domain and radially outward, reaching more than 0.5 close to the outer boundary.

The intermittency of the fluctuations is quantified by the skewness moment, defined by $S_\Theta = \langle (\Theta - \langle \Theta \rangle)^3 \rangle / \Theta_{\text{rms}}^3$, and the flatness moment, defined by $F_\Theta = \langle (\Theta - \langle \Theta \rangle)^4 \rangle / \Theta_{\text{rms}}^4 - 3$, where the variance is given by $\Theta_{\text{rms}}^2 = \langle (\Theta - \langle \Theta \rangle)^2 \rangle$. Both the skewness and flatness moments vanish for a normally distributed random variable. The profile of these moments for the temperature fluctuations is presented in Fig. 2. This shows that the probability density for the fluctuations is positively skewed and flattened in the outer part

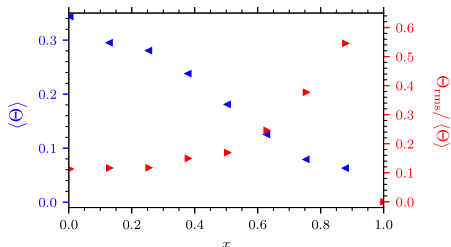


FIG. 1. Time-averaged profile of the temperature and the relative fluctuation level.

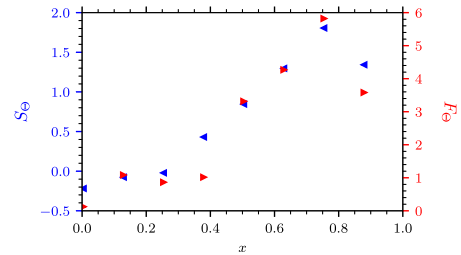


FIG. 2. Time-averaged profile of the skewness and flatness moments for the temperature fluctuations.

of the simulation domain, suggesting frequent appearance of large-amplitude bursts in the time series at a fixed point in the fluid layer. The moments are largest at $x = 3/4$, where the skewness is 1.81, while the flatness moment is 5.82. This demonstrates a strong departure from a normal distribution of the fluctuations.

The time-averaged profile of the stream function is presented in Fig. 3 together with the root mean square fluctuation level of the radial velocity. The time-averaged stream function has a near half-period sinusoidal variation over the fluid layer and vanishes at the boundaries. This implies an average counter-streaming mean flow in the fluid layer, which vanishes in the center of the domain and is strongest close to the boundaries. However, the radial velocity fluctuation vanishes at the boundaries due to the stress-free boundary conditions. The velocity fluctuation level has a local minimum in the center of the domain. At $x = 3/4$, the mean flow is 0.155, resulting in a vertical transit time of ~ 6.46 in non-dimensional units. There are some changes in this transit time since the mean flow velocity changes in time, as discussed later.

The evolution of the kinetic energy in the fluctuating and mean motions for a short part of the simulation run is presented in Fig. 4. This shows the quasi-periodic relaxation oscillations resembling predator-prey type dynamics, where kinetic energy is transferred from the fluctuating motions to the sheared flows and subsequently dissipated by viscosity. The auto-correlation function for the energy integrals is presented in Fig. 5. The mean flow energy

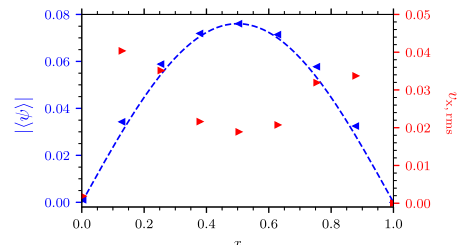


FIG. 3. Time-averaged profile of the stream function and the root mean square value of the radial velocity. The dashed line shows a half-period sine function fit to the stream function profile.

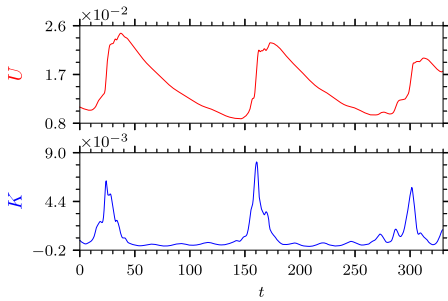


FIG. 4. Evolution of the kinetic energy in fluctuating, K , and mean flows, U , showing predator–prey-like relaxation oscillations.

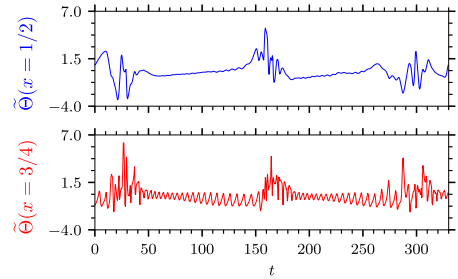


FIG. 6. Time series of the temperature fluctuations at $x = 1/2$ and $x = 3/4$.

auto-correlation function has a damped oscillatory behavior with a period of ~ 125 , corresponding to the characteristic separation between bursts in the energy integrals. The auto-correlation function for the energy in the fluctuating motions has a decay time of ~ 25 , which is attributed to the characteristic duration of the bursts in the kinetic energy seen in Fig. 4. This has been confirmed by conditional averaging of large-amplitude events in the energy integral time series.

In Fig. 6, the normalized temperature fluctuations $\tilde{\Theta} = (\Theta - \langle \Theta \rangle) / \Theta_{\text{rms}}$ recorded in the center of the fluid layer, at $x = 1/2$, and in the outer part, at $x = 3/4$, are presented. The evolution of the temperature during the onset of a turbulent period is shown in Fig. 7. This shows the presence of a structure moving radially through the fluid layer as well as azimuthally due to a sheared mean flow. Throughout the fluid layer, the fluctuations are strongly intermittent with large bursts during the time of strong activity in the energy of the fluctuating motions presented in Fig. 4. In the outer part of the fluid layer, the fluctuations have a nearly periodic oscillation in the periods between the bursts in the energy integrals. This is due to the sheared mean flow with a transit time of ~ 6.46 . In the following, the statistical properties of these fluctuations will be elucidated.

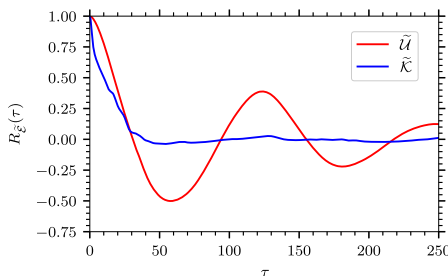


FIG. 5. Auto-correlation function for the kinetic energy in fluctuating and mean flows.

IV. FLUCTUATION STATISTICS

The probability density function for the temperature fluctuations measured at $x = 1/2$ and $x = 3/4$ is presented in Fig. 8. As expected from the radial variation of the skewness and kurtosis moments, the distributions have elevated tails compared to a normal distribution. For $x = 3/4$, the distribution is strongly skewed and has a nearly exponential tail toward large values. This is demonstrated by the solid line in Fig. 8, which is the best fit of a convolution of a normal distribution and a Gamma distribution. Similarly, the probability distribution functions for the radial velocity fluctuations are presented in Fig. 9 together with the best fit of a convolution between a Laplace and a normal distribution. This clearly demonstrates the presence of exponential tails in the probability densities.

The frequency power spectral densities for the temperature signals measured at $x = 1/2$ and $x = 3/4$ are presented in semi-logarithmic plots in Figs. 10 and 11. From Fig. 10, with logarithmic scaling of the frequency, it is clear that the frequency spectrum has a pronounced maximum at the linear frequency $f = 8 \times 10^{-3}$, which corresponds to the characteristic time between bursts in the energy integrals discussed above. Some higher harmonics of this frequency peak are also readily identified. The frequency spectrum for $x = 3/4$ also has a peak at $\sim f = 0.2$, corresponding to the vertical transit time by the average mean flow.

When the spectra are plotted with a logarithmic scaling for the power as presented in Fig. 11, it is clearly seen that frequency power spectral density has an exponential decay on the form $\exp(-4\pi\tau_d|f|)$, with the characteristic time $\tau_d = 0.637$ for $x = 1/2$ and $\tau_d = 0.382$ for $x = 3/4$. In Sec. V, it will be demonstrated that the exponential spectrum is due to the presence of Lorentzian pulses in the time series and that the slope corresponds to the duration time of these pulses. Similar exponential frequency spectra are also found for the stream function, radial velocity, and vorticity field. However, the slope, and therefore the duration time of the underlying pulses, varies for the different quantities.

V. LORENTZIAN PULSES

An exponential frequency power spectrum is a signature of deterministic chaos and has been attributed to Lorentzian-shaped pulses in the underlying time series. In order to demonstrate this, consider the stochastic process that gives a superposition of pulses

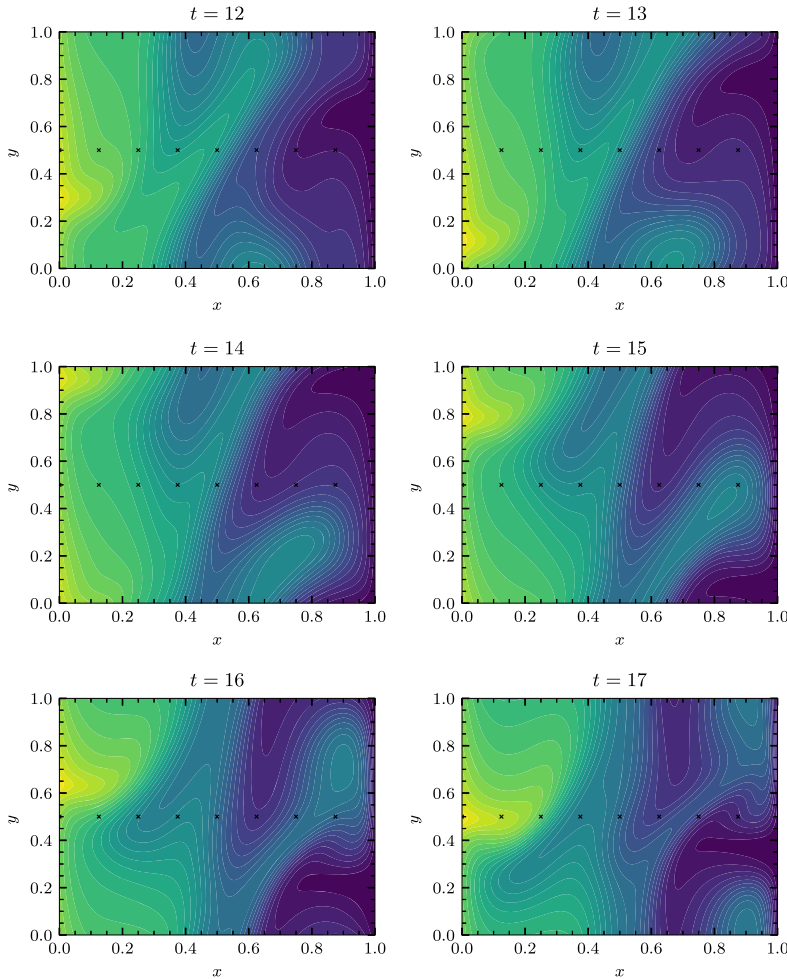


FIG. 7. Exemplary snapshots of the temperature field Θ , showing the evolution at the onset of a turbulent period. The black crosses show the radially equidistant positions where time series are recorded.

with fixed shape ϕ and duration τ_d ,^{106–117}

$$\Phi_K(t) = \sum_{k=1}^{K(T)} A_k \phi\left(\frac{t - t_k}{\tau_d}\right), \quad (9)$$

where A_k and t_k are pulse amplitude and arrival time for the pulse labeled k , respectively, and $K(T)$ is the number of pulses present in a time interval of duration T . In the case of Lorentzian pulses, the function ϕ is given by^{39–41}

$$\phi(\theta) = \frac{1}{\pi} \frac{1}{1 + \theta^2}. \quad (10)$$

In the case of uncorrelated Lorentzian pulses, it was recently shown that the frequency power spectral density is exponential, and for the normalized variable $\tilde{\Phi} = (\Phi - \langle \Phi \rangle) / \Phi_{\text{rms}}$, it is given by^{39,40}

$$\mathcal{S}_{\tilde{\Phi}}(f) = 2\pi\tau_d \exp(-4\pi\tau_d|f|).$$

In the [Appendix](#), it is shown that for a periodic sequence of Lorentzian pulses with fixed duration, the frequency power spectrum is a product of the exponential spectrum and a uniform delta pulse train at frequencies corresponding to multiples of the inverse periodicity time. In the case of a slight irregularity in the period between the pulses, the delta peaks in the frequency spectrum with broaden and have finite amplitude.

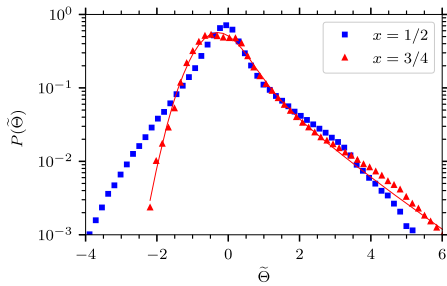


FIG. 8. Probability density function for the normalized temperature fluctuations at $x = 1/2$ and $x = 3/4$. The solid line shows the best fit of a convolution between a Gamma and a normal distribution.

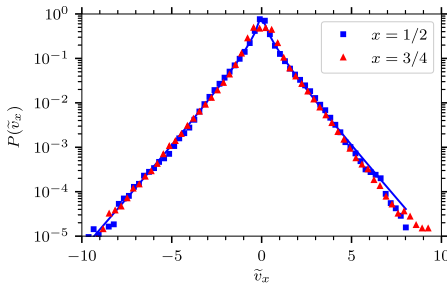


FIG. 9. Probability density function for the normalized radial velocity fluctuations at $x = 1/2$ and $x = 3/4$. The solid line shows the best fit of a convolution between a Laplace and a normal distribution.

As shown in Fig. 6, the temperature time series at $x = 3/4$ can be separated into parts with nearly periodic oscillations and turbulent parts with chaotic, large-amplitude fluctuations. An example of separating these periods is shown in Fig. 12. In Fig. 13, the frequency power spectral density of the quasi-periodic and turbulent parts is

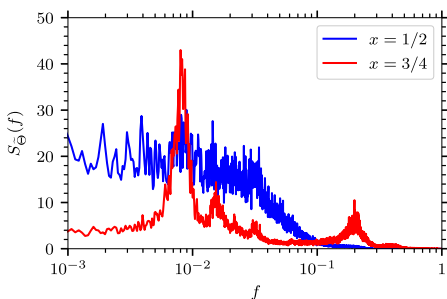


FIG. 10. Logarithm of the frequency power spectral density for temperature fluctuations at $x = 1/2$ and $x = 3/4$.

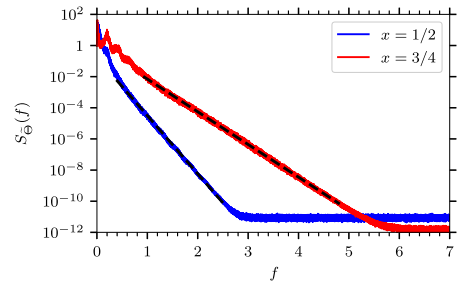


FIG. 11. Frequency power spectral density for temperature fluctuations at $x = 1/2$ and $x = 3/4$. The dashed lines show the best fit of an exponential function.

shown together with the power spectral density of the entire signal. It is clear that the power spectrum of the entire signal is well described by the power spectrum of the turbulent parts and that they have the same time scale, $\tau_d = 0.382$. The black dashed line gives an exponential spectrum with 4 times the duration time of the whole spectrum, which closely resembles the power spectrum of the quasi-periodic parts of the signal. In the following, this is used as an estimated duration time of the periodic part.

In order to demonstrate that the temperature time series can be described as a superposition of Lorentzian pulses, a deconvolution algorithm using a Lorentzian pulse with fixed duration time estimated from the power spectral density is applied. This gives the pulse amplitudes and arrival times, which can be used to reconstruct the original signal. The superposition of pulses with fixed duration given by Eq. (9) can be written as a convolution between the pulse function and a train of delta pulses,^{114,118}

$$\Phi_K(t) = [\phi * F_K] \left(\frac{t}{\tau_d} \right), \quad (11)$$

where

$$F_K(t) = \sum_{k=1}^{K(T)} A_k \delta \left(\frac{t - t_k}{\tau_d} \right). \quad (12)$$

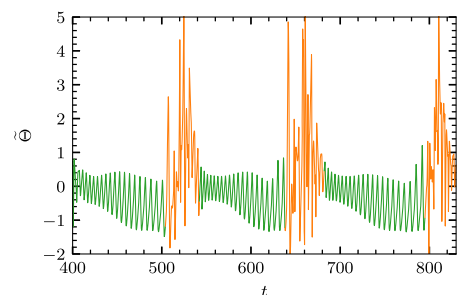


FIG. 12. Example of splitting of temperature fluctuations into quasi-periodic (green) and turbulent (orange) parts at $x = 3/4$.

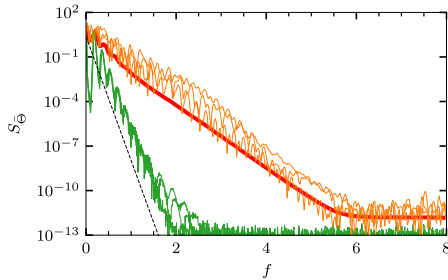


FIG. 13. Power spectral density of the temperature fluctuations at $x = 3/4$. The red line gives the spectrum of the entire time series as shown in Fig. 10, the orange lines give the spectra of the turbulent parts from Fig. 12, while the green lines give the spectra of the quasi-periodic parts. The black dashed line gives the prediction for an exponential spectrum with the periodicity time seen in the raw time series.

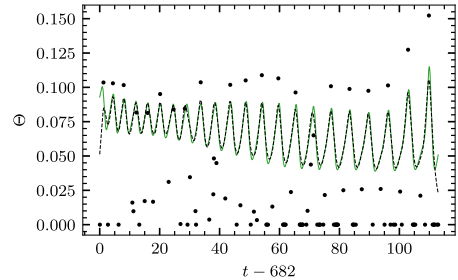


FIG. 15. Excerpt of quasi-periodic part (green solid line) and reconstructed signal from the deconvolution (black dashed line). The dots indicate arrival times and amplitudes of Lorentzian pulses with duration time $\tau_d = 1.528$. The circular dots give half the true amplitude value for better comparison with the time series.

The goal is to find the forcing $F_K(t)$ and to estimate the pulse amplitudes $\{A_k\}_{k=1}^K$ and arrival times $\{t_k\}_{k=1}^K$ as accurately as possible. In order to do this, a modified version of the Richardson–Lucy deconvolution algorithm will be used.^{118–123} Following this scheme, an initial guess for F_K is made, denoted by $F_K^{(1)}$. The numerical value of this initial forcing matters little and can be set as some positive constant or the signal itself. The initial value is updated iteratively, with the n th iteration given by

$$F_K^{(n+1)} = F_K^{(n)} \frac{D * \widehat{\phi}}{F_K^{(n)} * \phi * \widehat{\phi}}, \tag{13}$$

where $\widehat{\phi}(t) = \phi(-t)$. Here and in the following, D denotes any of the simulation data time series discussed above.

The result from the deconvolution algorithm is presented in Figs. 14 and 15 for representative turbulent and the quasi-periodic parts, respectively. It is clear that most of the signals are well reconstructed by a superposition of Lorentzian pulses. As an example,

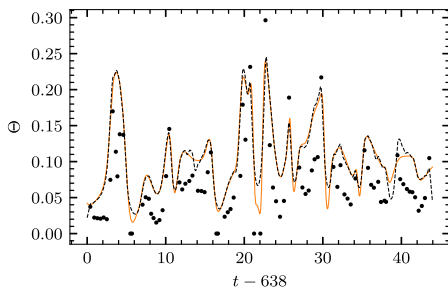


FIG. 14. Excerpt of turbulent part (orange solid line) and reconstructed signal from the deconvolution (black dashed line). The dots indicate arrival times and amplitudes of Lorentzian pulses with duration time $\tau_d = 0.382$. The circular dots give half the true amplitude value for better comparison with the time series.

the first peak in Fig. 14 results from a structure of high temperature moving radially through the fluid layer similar to the structures shown in Fig. 7. The lift-time of the two-dimensional structure in Fig. 7 exceeds the duration of the Lorentzian-shaped peak in Fig. 14, but the single-point recording can be modeled as a compound of several Lorentzian pulses. The frequency power spectral density of the reconstructed time series accurately reproduces that from the numerical simulations as expected. This analysis clearly demonstrates that the exponential frequency spectra for the temperature fluctuations in the thermal convection simulations are due to the presence of Lorentzian pulses in the time series.

VI. DISCUSSION AND CONCLUSIONS

In this contribution, the statistical properties of the temperature fluctuations in numerical simulations of turbulent thermal convection have been investigated by time-series analysis and stochastic modeling. The generation of a sheared mean flow through the fluid layer results in predator–prey-like dynamics of the energy integrals and leads to multiple temporal scales in the dynamics. For sufficiently large Rayleigh numbers, a regime corresponding to hard turbulence results with exponential tails in the probability distribution function for the temperature and velocity fluctuations.

The frequency power spectral density for the fluctuations has local maxima at frequencies corresponding to bursting in the energy integral as well as transit time for the mean flow through the fluid layer. However, when presented in a semi-logarithmic plot, it is clear that the frequency spectrum has an exponential tail for power densities all the way down to round off errors. A novel deconvolution method has been used to show that the exponential spectrum is due to the presence of Lorentzian pulses in the temperature time series. The time scale for the structures is consistent with the slope of the exponential frequency spectra.

ACKNOWLEDGMENTS

This work was supported by the UiT Aurora Centre Program, UiT The Arctic University of Norway (2020). Audun Theodorsen was supported by a Tromsø Science Foundation Starting Grant.

APPENDIX: PERIODIC ARRIVALS

In this appendix, the frequency power spectral density for a superposition of pulses with periodic arrivals is calculated. A superposition of K pulses with fixed shape and duration, as given by Eq. (9), can be written as a convolution between the pulse function ϕ and a train of delta pulses,

$$\Phi_K(t) = \int_{-\infty}^{\infty} d\theta \phi\left(\frac{t}{\tau_d} - \theta\right) F_K(\theta), \tag{A1}$$

where the forcing F_K due to the delta pulse train is given by

$$F_K(\theta) = \sum_{k=1}^K A_k \delta\left(\theta - \frac{t_k}{\tau_d}\right). \tag{A2}$$

The pulse duration time τ_d is taken to be the same for all pulses, and the pulse amplitudes A_k are taken to be randomly distributed with mean value $\langle A \rangle$ and variance $A_{rms}^2 = \langle (A - \langle A \rangle)^2 \rangle$. The pulse function is assumed to be localized and normalized such that^{112,115}

$$\int_{-\infty}^{\infty} d\theta |\phi(\theta)| = 1.$$

The frequency power spectral density of a random process $\Phi_K(t)$ is defined as

$$\mathcal{S}_\omega(\omega) = \lim_{T \rightarrow \infty} \langle |\mathcal{F}_T[\Phi_K](\omega)|^2 \rangle, \tag{A3}$$

where the Fourier transform of the random variable over the domain $[0, T]$ is defined by

$$\mathcal{F}_T[\Phi_K](\omega) = \frac{1}{\sqrt{T}} \int_0^T dt \exp(-i\omega t) \Phi_K(t). \tag{A4}$$

Here, $\omega = 2\pi f$ is the angular frequency. Analytical functions that fall sufficiently rapid to zero, such as the pulse function ϕ , have the Fourier transform

$$\mathcal{F}[\phi](\vartheta) = \int_{-\infty}^{\infty} d\theta \exp(-i\theta\vartheta) \phi(\theta) \tag{A5}$$

and the inverse transform

$$\phi(\theta) = \mathcal{F}^{-1}[\mathcal{F}[\phi](\vartheta)](\theta) = \frac{1}{2\pi} \int_{-\infty}^{\infty} d\vartheta \exp(i\theta\vartheta) \mathcal{F}[\phi](\vartheta). \tag{A6}$$

Note that, here, θ and ϑ are non-dimensional variables, as opposed to t and ω .

Neglecting end effects in by assuming $T/\tau_d \gg 1$, the frequency power spectral density of the stationary process Φ_K is found to be the product of the power of the pulse function and the power of the forcing,¹¹⁴

$$\mathcal{S}_\omega(\omega) = |\mathcal{F}[\phi](\tau_d\omega)|^2 \lim_{T \rightarrow \infty} \left\langle \left| \mathcal{F}_T \left[F_K \left(\frac{t}{\tau_d} \right) \right] (\omega) \right|^2 \right\rangle, \tag{A7}$$

which is independent of K since the average is over all random variables. The frequency power spectrum for the forcing F_K will now be calculated for the case of periodic pulses.

The marginal probability density function for the pulse arrival times when these are periodic with period τ_p and starting point s , assuming that the starting time s is known, is

$$P_k(t_k|s) = \delta(t_k - \tau_p k - s). \tag{A8}$$

Since each arrival is deterministic, the joint distribution of all arrivals with known starting point is the product of the marginal distributions,

$$P_{t_1, \dots, t_K}(t_1, \dots, t_K|s) = \prod_{k=1}^K \delta(t_k - \tau_p k - s). \tag{A9}$$

To account for the fact that the periodicity but not the actual arrival time is known, the starting point is randomly and uniformly chosen in the interval $[0, \tau_p]$,

$$P_s(s) = \begin{cases} \tau_p^{-1}, & 0 < s < \tau_p \\ 0, & \text{else.} \end{cases} \tag{A10}$$

The Fourier transform of the forcing is

$$\mathcal{F}_T \left[F_K \left(\frac{t}{\tau_d} \right) \right] (\omega) = \frac{\tau_d}{\sqrt{T}} \sum_{k=1}^K A_k \exp(-i\omega t_k). \tag{A11}$$

Multiplying this expression with its complex conjugate and averaging over all random variables give after some calculations, the frequency power spectrum of the forcing,

$$\lim_{T \rightarrow \infty} \langle |\mathcal{F}_T[F_K](\omega)|^2 \rangle = \frac{\tau_d^2}{\tau_p} A_{rms}^2 + \frac{\tau_d^2}{\tau_p} \langle A \rangle^2 2\pi \sum_{n=-\infty}^{\infty} \delta(\tau_p \omega - 2\pi n). \tag{A12}$$

According to Eq. (A7), this is to be multiplied by the spectrum of the pulse function. Thus, the frequency power spectral density for a superposition of periodic pulses with fixed shape and duration is given by the sum of the spectrum of the pulse function (due to a random distribution of pulse amplitudes and represented by the term proportional to A_{rms}^2 in the above equation) and the spectrum of the pulse function multiplied by a uniform delta pulse train, also known as a Dirac comb (represented by the last term in the above equation proportional to $\langle A \rangle^2$, which vanishes for a symmetric amplitude distribution).

DATA AVAILABILITY

The data that support the findings of this study are available from the corresponding author upon reasonable request.

REFERENCES

- ¹F. H. Busse, "Non-linear properties of thermal convection," *Rep. Prog. Phys.* **41**, 1929 (1978).
- ²E. D. Siggia, "High Rayleigh number convection," *Annu. Rev. Fluid Mech.* **26**, 137 (1994).
- ³E. Bodenschatz, W. Pesch, and G. Ahlers, "Recent developments in Rayleigh-Bénard convection," *Annu. Rev. Fluid Mech.* **32**, 709 (2000).
- ⁴L. P. Kadanoff, "Turbulent heat flow: Structures and scaling," *Phys. Today* **54**(8), 34 (2001).
- ⁵G. Ahlers, S. Grossmann, and D. Lohse, "Heat transfer and large scale dynamics in turbulent Rayleigh-Bénard convection," *Rev. Mod. Phys.* **81**, 503 (2009).
- ⁶M. K. Verma, *Physics of Buoyant Flows: From Instabilities to Turbulence* (World Scientific, 2018).
- ⁷P. Atten, J. C. Lacroix, and B. Malraison, "Chaotic motion in a Coulomb force driven instability: Large aspect ratio experiments," *Phys. Lett. A* **79**, 255 (1980).
- ⁸D. Farmer, J. Crutchfield, H. Froehling, N. Packard, and R. Shaw, "Power spectra and mixing properties of strange attractors," *Ann. New York Acad. Sci.* **357**, 453 (1980).
- ⁹U. Frisch and R. Morf, "Intermittency in nonlinear dynamics and singularities at complex times," *Phys. Rev. A* **23**, 2673 (1981).

- ¹⁰H. S. Greenside, G. Ahlers, P. C. Hohenberg, and R. W. Walden, "A simple stochastic model for the onset of turbulence in Rayleigh-Bénard convection," *Physica D* **5**, 322 (1982).
- ¹¹J. D. Farmer, "Chaotic attractors of an infinite-dimensional dynamical system," *Physica D* **4**, 366 (1982).
- ¹²A. Libchaber, S. Fauve, and C. Laroche, "Two-parameter study of the routes to chaos," *Physica D* **7**, 73 (1983).
- ¹³A. Brandstater and H. L. Swinney, "Strange attractors in weakly turbulent Couette-Taylor flow," *Phys. Rev. A* **35**, 2207 (1987).
- ¹⁴D. Sigeti and W. Horsthemke, "High-frequency power spectra for systems subject to noise," *Phys. Rev. A* **35**, 2276 (1987).
- ¹⁵E. F. Stone, "Power spectra of the stochastically forced Duffing oscillator," *Phys. Lett. A* **148**, 434 (1990).
- ¹⁶C. L. Streett and M. Y. Hussaini, "A numerical simulation of the appearance of chaos in finite-length Taylor-Couette flow," *Appl. Numer. Math.* **7**, 41 (1991).
- ¹⁷B. Mensour and A. Longtin, "Power spectra and dynamical invariants for delay-differential and difference equations," *Physica D* **113**, 1 (1998).
- ¹⁸M. R. Paul, M. C. Cross, P. F. Fischer, and H. S. Greenside, "Power-law behavior of power spectra in low Prandtl number Rayleigh-Bénard convection," *Phys. Rev. Lett.* **87**, 154501 (2001).
- ¹⁹L. A. Safonov, E. Tomer, V. V. Strygin, Y. Ashkenazy, and S. Havlin, "Multifractal chaotic attractors in a system of delay-differential equations modeling road traffic," *Chaos* **12**, 1006 (2002).
- ²⁰V. Schenzinger and S. M. Osprey, "Interpreting the nature of Northern and Southern Annular Mode variability in CMIP5 Models," *J. Geophys. Res. Atmos.* **120**, 11203, <https://doi.org/10.1002/2014jd022989> (2015).
- ²¹A. M. Reynolds, F. Bartumeus, A. Kölsch, and J. van de Koppel, "Signatures of chaos in animal search patterns," *Sci. Rep.* **6**, 23492 (2015).
- ²²S. Paul, P. K. Mishra, M. K. Verma and K. Kumar, "Order and chaos in two-dimensional Rayleigh-Bénard convection," [arXiv:0904.2917](https://arxiv.org/abs/0904.2917) [physics.flu-dyn].
- ²³D. E. Sigeti, "Exponential decay of power spectra at high frequency and positive Lyapunov exponents," *Physica D* **82**, 136 (1995).
- ²⁴D. E. Sigeti, "Survival of deterministic dynamics in the presence of noise and the exponential decay of power spectra at high frequency," *Phys. Rev. E* **52**, 2443 (1995).
- ²⁵D. S. Broomhead and G. P. King, "Extracting qualitative dynamics from experimental data," *Physica D* **20**, 2017 (1986).
- ²⁶S. M. Osprey and M. H. P. Ambaum, "Evidence for the chaotic origin of northern annular mode variability," *Geophys. Res. Lett.* **38**, L15702, <https://doi.org/10.1029/2011gl048181> (2011).
- ²⁷C. L. E. Franzke, S. M. Osprey, P. Davini, and N. W. Watkins, "A dynamical systems explanation of the Hurst effect and atmospheric low-frequency variability," *Sci. Rep.* **5**, 9068 (2015).
- ²⁸S. Paul, P. Wahi, and M. K. Verma, "Bifurcations and chaos in large-Prandtl number Rayleigh-Bénard convection," *Int. J. Nonlinear Mech.* **46**, 772 (2011).
- ²⁹N. Ohtomo, K. Tokiwano, Y. Tanaka, A. Sumi, S. Terachi, and H. Konno, "Exponential characteristics of power spectral densities caused by chaotic phenomena," *J. Phys. Soc. Jpn.* **64**, 1104 (1995).
- ³⁰J. E. Maggs and G. J. Morales, "Origin of Lorentzian pulses in deterministic chaos," *Phys. Rev. E* **86**, 015401 (2012).
- ³¹D. C. Pace, M. Shi, J. E. Maggs, G. J. Morales, and T. A. Carter, "Exponential frequency spectrum and Lorentzian pulses in magnetized plasmas," *Phys. Plasmas* **15**, 122304 (2008).
- ³²D. C. Pace, M. Shi, J. E. Maggs, G. J. Morales, and T. A. Carter, "Exponential frequency spectrum in magnetized plasmas," *Phys. Rev. Lett.* **101**, 085001 (2008).
- ³³G. Hornung, B. Nold, J. E. Maggs, G. J. Morales, M. Ramisch, and U. Stroth, "Observation of exponential spectra and Lorentzian pulses in the TJ-K stellarator," *Phys. Plasmas* **18**, 082303 (2011).
- ³⁴J. E. Maggs and G. J. Morales, "Generality of deterministic chaos, exponential spectra, and Lorentzian pulses in magnetically confined plasmas," *Phys. Rev. Lett.* **107**, 185003 (2011).
- ³⁵J. E. Maggs and G. J. Morales, "Exponential power spectra, deterministic chaos and Lorentzian pulses in plasma edge dynamics," *Plasma Phys. Contr. Fusion* **54**, 124041 (2012).
- ³⁶B. Ph. van Milligen, R. Sánchez, and C. Hidalgo, "Relevance of uncorrelated Lorentzian pulses for the interpretation of turbulence in the edge of magnetically confined toroidal plasmas," *Phys. Rev. Lett.* **109**, 105001 (2012).
- ³⁷J. E. Maggs and G. J. Morales, "Permutation entropy analysis of temperature fluctuations from a basic electron heat transport experiment," *Plasma Phys. Controlled Fusion* **55**, 085015 (2013).
- ³⁸Z. Zhu, A. E. White, T. A. Carter, S. G. Baek, and J. L. Terry, "Chaotic edge density fluctuations in the Alcator C-Mod tokamak," *Phys. Plasmas* **24**, 042301 (2017).
- ³⁹O. E. Garcia and A. Theodorsen, "Power law spectra and intermittent fluctuations due to uncorrelated Lorentzian pulses," *Phys. Plasmas* **24**, 020704 (2018).
- ⁴⁰O. E. Garcia and A. Theodorsen, "Skewed Lorentzian pulses and exponential frequency power spectra," *Phys. Plasmas* **25**, 014503 (2018).
- ⁴¹O. E. Garcia and A. Theodorsen, "Intermittent fluctuations due to uncorrelated Lorentzian pulses," *Phys. Plasmas* **25**, 014506 (2018).
- ⁴²G. J. Morales, "Investigation of a chaotic thermostat," *Phys. Rev. E* **97**, 032203 (2018).
- ⁴³G. J. Morales, "Two-dimensional chaotic thermostat and behavior of a thermalized charge in a weak magnetic field," *Phys. Rev. E* **99**, 062218 (2019).
- ⁴⁴F. H. Busse, "Generation of mean flows by thermal convection," *Physica D* **9**, 287 (1983).
- ⁴⁵L. N. Howard and R. Krishnamurti, "Large-scale flow in turbulent convection: A mathematical model," *J. Fluid Mech.* **170**, 385 (1986).
- ⁴⁶J. F. Drake, J. M. Finn, P. Guzdar, V. Shapiro, V. Shevchenko, F. Waelbroeck, A. B. Hassam, C. S. Liu, and R. Sagdeev, "Peeling of convection cells and the generation of sheared flow," *Phys. Fluids B* **4**, 488 (1992).
- ⁴⁷J. M. Finn, J. F. Drake, and P. N. Guzdar, "Instability of fluid vortices and generation of sheared flow," *Phys. Fluids B* **4**, 2758 (1992).
- ⁴⁸A. M. Rucklidge and P. C. Matthews, "Analysis of the shearing instability in nonlinear convection and magnetoconvection," *Nonlinearity* **9**, 311 (1996).
- ⁴⁹J. G. Fitzgerald and B. F. Farrell, "Mechanisms of mean flow formation and suppression in two-dimensional Rayleigh-Bénard convection," *Phys. Fluids* **26**, 054104 (2014).
- ⁵⁰O. Pogutse, W. Kerner, V. Gribkov, S. Bazdenkov, and M. Osipenko, "The resistive interchange convection in the edge of tokamak plasmas," *Plasma Phys. Controlled Fusion* **36**, 1963 (1994).
- ⁵¹H. Sugama and W. Horton, "L-H confinement mode dynamics in three-dimensional state space," *Plasma Phys. Controlled Fusion* **37**, 345 (1995).
- ⁵²P. Beyer and K. H. Spatschek, "Center manifold theory for the dynamics of the L-H-transition," *Phys. Plasmas* **3**, 995 (1996).
- ⁵³W. Horton, G. Hu, and G. Laval, "Turbulent transport in mixed states of convective cells and sheared flows," *Phys. Plasmas* **3**, 2912 (1996).
- ⁵⁴M. Berning and K. H. Spatschek, "Bifurcations and transport barriers in the resistive-g paradigm," *Phys. Rev. E* **62**, 1162 (2000).
- ⁵⁵K. B. Hermiz, P. N. Guzdar, and J. M. Finn, "Improved low-order model for shear flow driven by Rayleigh-Bénard convection," *Phys. Rev. E* **51**, 325 (1995).
- ⁵⁶J. Prat, J. M. Massaguer, and I. Mercader, "Large-scale flows and resonances in 2-D thermal convection," *Phys. Fluids* **7**, 121 (1995).
- ⁵⁷J. M. Finn, "Nonlinear interaction of Rayleigh-Taylor and shear instabilities," *Phys. Fluids B* **5**, 415 (1993).
- ⁵⁸J. M. Finn and K. Hermiz, "The role of self-consistent Lagrangian chaos in Bénard convection in an annulus," *Phys. Fluids B* **5**, 3897 (1993).
- ⁵⁹A. Takayama, T. Unemura, and M. Wakatani, "Comparison of Lorenz type and plasma fluid models for nonlinear-interchange-mode generation of shear flow," *Plasma Phys. Controlled Fusion* **40**, 775 (1998).
- ⁶⁰O. E. Garcia, N. H. Bian, J.-V. Paulsen, S. Benkadda, and K. Rypdal, "Confinement and bursty transport in a flux-driven convection model with sheared flows," *Plasma Phys. Controlled Fusion* **45**, 919 (2003).
- ⁶¹O. E. Garcia and N. H. Bian, "Bursting and large-scale intermittency in turbulent convection with differential rotation," *Phys. Rev. E* **68**, 047301 (2003).
- ⁶²O. E. Garcia, N. H. Bian, V. Naulin, A. H. Nielsen, and J. J. Rasmussen, "Two-dimensional convection and interchange motions in fluids and magnetized plasmas," *Phys. Scr.* **T122**, 104 (2006).

- ⁶³N. Bian, S. Benkadda, O. E. Garcia, J.-V. Paulsen, and X. Garbet, "The quasilinear behavior of convective turbulence with sheared flows," *Phys. Plasmas* **10**, 1382 (2003).
- ⁶⁴N. H. Brummell and J. E. Hart, "High Rayleigh number β -convection," *Geophys. Astrophys. Fluid Dyn.* **68**, 85 (1993).
- ⁶⁵F. H. Busse and R. M. Clever, "Bursts in inclined layer convection," *Phys. Fluids* **12**, 2137 (2000).
- ⁶⁶E. Grote, F. H. Busse, and A. Tilgner, "Regular and chaotic spherical dynamos," *Phys. Earth Planet. Inter.* **117**, 259 (2000).
- ⁶⁷U. R. Christensen, "Zonal flow driven by deep convection in the major planets," *Geophys. Res. Lett.* **28**, 2553, <https://doi.org/10.1029/2000gl012643> (2001).
- ⁶⁸J. M. Aurnou and P. L. Olson, "Strong zonal winds from thermal convection in a rotating spherical shell," *Geophys. Res. Lett.* **28**, 2557, <https://doi.org/10.1029/2000gl012474> (2001).
- ⁶⁹F. H. Busse, "Convective flows in rapidly rotating spheres and their dynamo action," *Phys. Fluids* **14**, 1301 (2002).
- ⁷⁰U. R. Christensen, "Zonal flow driven by strongly supercritical convection in rotating spherical shells," *J. Fluid Mech.* **470**, 115 (2002).
- ⁷¹E. Grote and F. H. Busse, "Dynamics of convection and dynamos in rotating spherical fluid shells," *Fluid Dyn. Res.* **28**, 349 (2001).
- ⁷²V. Morin and E. Dormy, "Time dependent β -convection in rapidly rotating spherical shells," *Phys. Fluids* **16**, 1603 (2004).
- ⁷³J.-J. Tau and W.-C. Tan, "Relaxation oscillation of thermal convection in rotating cylindrical annulus," *Chin. Phys. Lett.* **28**, 034706 (2010).
- ⁷⁴R. J. Teed, C. A. Jones, and R. Hollerbach, "On the necessary conditions for bursts of convection within the rapidly rotating cylindrical annulus," *Phys. Fluids* **24**, 066604 (2012).
- ⁷⁵A. Takayama, M. Wakatani, and H. Sugama, "Suppression of nonlinear interchange mode by zonal counterstreaming flow generation," *Phys. Plasmas* **3**, 3 (1996).
- ⁷⁶P. N. Guzdar and A. B. Hassam, "A self-consistent model for low-high transitions in tokamaks," *Phys. Plasmas* **3**, 3701 (1996).
- ⁷⁷Z. Lin, T. S. Hamm, W. W. Lee, W. M. Tang, and P. H. Diamond, "Effects of collisional zonal flow damping on turbulent transport," *Phys. Rev. Lett.* **83**, 3645 (1999).
- ⁷⁸Z. Lin, T. S. Hamm, W. W. Lee, W. M. Tang, and R. B. White, "Gyrokinetic simulations in general geometry and applications to collisional damping of zonal flows," *Phys. Plasmas* **7**, 1857 (2000).
- ⁷⁹M. A. Malkov, P. H. Diamond, and M. N. Rosenbluth, "On the nature of bursting in transport and turbulence in drift wave-zonal flow systems," *Phys. Plasmas* **8**, 5073 (2001).
- ⁸⁰K. Takeda, S. Hamaguchi, and M. Wakatani, "ELM-like behaviour generated by nonlinear ion-temperature-gradient-driven mode," *Plasma Phys. Controlled Fusion* **44**, A487 (2002).
- ⁸¹V. Naulin, J. Nycander, and J. J. Rasmussen, "Transport barriers and edge localized modes-like bursts in a plasma model with turbulent equipartition profiles," *Phys. Plasmas* **10**, 1075 (2003).
- ⁸²G. Manfredi and C. M. Roach, "Bursting events in zonal flow-drift wave turbulence," *Phys. Plasmas* **10**, 2824 (2003).
- ⁸³O. E. Garcia, V. Naulin, A. H. Nielsen, and J. Juul Rasmussen, "Turbulence and intermittent transport at the boundary of magnetized plasmas," *Phys. Plasmas* **12**, 062309 (2005).
- ⁸⁴P. Beyer, S. Benkadda, G. Fuhr-Chaudier, X. Garbet, Ph. Ghendrih, and Y. Sarazin, "Nonlinear dynamics of transport barrier relaxations in Tokamak edge plasmas," *Phys. Rev. Lett.* **94**, 105001 (2005).
- ⁸⁵O. E. Garcia, V. Naulin, A. H. Nielsen, and J. J. Rasmussen, "Turbulence simulations of blob formation and radial propagation in toroidally magnetized plasmas," *Phys. Scr.* **T122**, 89 (2006).
- ⁸⁶R. G. Kleva and P. N. Guzdar, "Zonal flow sawteeth and the time period between edge-localized transport bursts in tokamaks," *Phys. Plasmas* **14**, 012303 (2007).
- ⁸⁷N. H. Bian and O. E. Garcia, "Confinement and dynamical regulation in two-dimensional convective turbulence," *Phys. Plasmas* **10**, 4696 (2003).
- ⁸⁸O. E. Garcia and N. H. Bian, "Shear dispersion and turbulence decorrelation by differential rotation," *Phys. Plasmas* **12**, 014503 (2005).
- ⁸⁹N. H. Bian, "On-off intermittent regulation of plasma turbulence," *Phys. Plasmas* **17**, 044501 (2010).
- ⁹⁰H. Zhu, S. C. Chapman, and R. O. Dendy, "Robustness of predator-prey models for confinement regime transitions in fusion plasmas," *Phys. Plasmas* **20**, 042302 (2013).
- ⁹¹F. Heslot, B. Castaing, and A. Libchaber, "Transitions to turbulence in helium gas," *Phys. Lett. A* **36**, 5870 (1987).
- ⁹²B. Castaing, G. Gunaratne, F. Heslot, L. Kadanoff, A. Libchaber, S. Thomae, X.-Z. Wu, S. Zaleski, and G. Zanetti, "Scaling of hard thermal turbulence in Rayleigh-Bénard convection," *J. Fluid Mech.* **204**, 1 (1989).
- ⁹³M. Sano, X. Z. Wu, and A. Libchaber, "Turbulence in helium-gas free convection," *Phys. Lett. A* **40**, 6421 (1989).
- ⁹⁴E. DeLuca, J. Werne, R. Rosner, and F. Cattaneo, "Numerical simulations of soft and hard turbulence: Preliminary results for two-dimensional convection," *Phys. Rev. Lett.* **64**, 2370 (1990).
- ⁹⁵F. Massaioli, R. Benzi, and S. Succi, "Exponential tails in two-dimensional Rayleigh-Bénard convection," *Europhys. Lett.* **21**, 305 (1993).
- ⁹⁶J. Werne, "Structure of hard-turbulent convection in two dimensions: Numerical evidence," *Phys. Rev. E* **48**, 1020 (1993).
- ⁹⁷K. Julien, S. Legg, J. McWilliams, and J. Werne, "Hard turbulence in rotating Rayleigh-Bénard convection," *Phys. Rev. E* **53**, R5557 (1996).
- ⁹⁸B. I. Shraiman and E. D. Siggia, "Heat transport in high-Rayleigh-number convection," *Phys. Rev. A* **42**, 3650 (1990).
- ⁹⁹S. Cioni, S. Ciliberto, and J. Sommeria, "Strongly turbulent Rayleigh-Bénard convection in mercury: Comparison with results at moderate Prandtl number," *J. Fluid Mech.* **335**, 111 (1997).
- ¹⁰⁰J. Niemela, L. Skrbek, K. R. Sreenivasan, and R. J. Donnelly, "Turbulent convection at very high Rayleigh numbers," *Nature* **404**, 837 (2000).
- ¹⁰¹R. Verzicco and K. R. Sreenivasan, "A comparison of turbulent thermal convection between conditions of constant temperature and constant heat flux," *J. Fluid Mech.* **595**, 203 (2008).
- ¹⁰²H. Johnston and C. R. Doering, "Comparison of turbulent thermal convection between conditions of constant temperature and constant flux," *Phys. Rev. Lett.* **102**, 064501 (2009).
- ¹⁰³S.-D. Huang, F. Wang, H.-D. Xi, and K.-Q. Xia, "Comparative experimental study of fixed temperature and fixed heat flux boundary conditions in turbulent thermal convection," *Phys. Rev. Lett.* **115**, 154502 (2015).
- ¹⁰⁴V. Naulin and A. H. Nielsen, "Accuracy of spectral and finite difference schemes in 2D advection problems," *SIAM J. Sci. Comput. U. S. A.* **25**, 104 (2003).
- ¹⁰⁵O. E. Garcia, V. Naulin, A. H. Nielsen, and J. Juul Rasmussen, "Computations of intermittent transport in scrape-off layer plasmas," *Phys. Rev. Lett.* **92**, 165003 (2004).
- ¹⁰⁶S. O. Rice, "Mathematical analysis of random noise," *Bell Syst. Tech. J.* **23**, 282 (1944).
- ¹⁰⁷E. Daly and A. Porporato, "Effect of different jump distributions on the dynamics of jump processes," *Phys. Rev. E* **81**, 061133 (2010).
- ¹⁰⁸O. E. Garcia, "Stochastic modeling of intermittent scrape-off layer plasma fluctuations," *Phys. Rev. Lett.* **108**, 265001 (2012).
- ¹⁰⁹R. Kube and O. E. Garcia, "Convergence of statistical moments of particle density time series in scrape-off layer plasmas," *Phys. Plasmas* **22**, 012502 (2015).
- ¹¹⁰A. S. Bergsaker, Å. Fredriksen, H. L. Pécseli, and J. K. Trulsen, "Models for the probability densities of the turbulent plasma flux in magnetized plasmas," *Phys. Scr.* **90**, 108005 (2015).
- ¹¹¹A. Theodorsen and O. E. Garcia, "Level crossings, excess times, and transient plasma-wall interactions in fusion plasmas," *Phys. Plasmas* **23**, 040702 (2016).
- ¹¹²O. E. Garcia, R. Kube, A. Theodorsen, and H. L. Pécseli, "Stochastic modelling of intermittent fluctuations in the scrape-off layer: Correlations, distributions, level crossings, and moment estimation," *Phys. Plasmas* **23**, 052308 (2016).
- ¹¹³F. Militello and J. T. Omotani, "Scrape off layer profiles interpreted with filament dynamics," *Nucl. Fusion* **56**, 104004 (2016).

- ¹¹⁴A. Theodorsen, O. E. Garcia, and M. Rypdal, "Statistical properties of a filtered Poisson process with additive random noise: Distributions, correlations and moment estimation," *Phys. Scr.* **92**, 054002 (2017).
- ¹¹⁵O. E. Garcia and A. Theodorsen, "Auto-correlation function and frequency spectrum due to a super-position of uncorrelated exponential pulses," *Phys. Plasmas* **24**, 032309 (2017).
- ¹¹⁶A. Theodorsen and O. E. Garcia, "Probability distribution functions for intermittent scrape-off layer plasma fluctuations," *Plasma Phys. Controlled Fusion* **60**, 034006 (2018).
- ¹¹⁷A. Theodorsen and O. E. Garcia, "Level crossings and excess times due to a superposition of uncorrelated exponential pulses," *Phys. Rev. E* **97**, 012110 (2018).
- ¹¹⁸A. Theodorsen, O. E. Garcia, R. Kube, B. LaBombard, and J. L. Terry, "Universality of Poisson-driven plasma fluctuations in the Alcator C-Mod scrape-off layer," *Phys. Plasmas* **25**, 122309 (2018).
- ¹¹⁹W. H. Richardson, "Bayesian-based iterative method of image restoration," *J. Opt. Soc. Am.* **62**, 55 (1972).
- ¹²⁰L. B. Lucy, "An iterative technique for the rectification of observed distributions," *Astron. J.* **79**, 745 (1974).
- ¹²¹M. E. Daube-Witherspoon and G. Muehlechner, "An iterative image space reconstruction algorithm suitable for volume ECT," *IEEE Trans. Med. Imaging* **5**, 61 (1986).
- ¹²²F. Dell'Acqua, G. Rizzo, P. Scifo, R. A. Clarke, G. Scotti, and F. Fazio, "A model-based deconvolution approach to solve fiber crossing in diffusion-weighted MR imaging," *IEEE Trans. Biomed. Eng.* **54**, 462 (2007).
- ¹²³Y.-W. Tai, P. Tan, and M. S. Brown, "Richardson-Lucy deblurring for scenes under a projective motion path," *IEEE Trans. Pattern Anal. Mach. Intell.* **33**, 1603 (2011).

Paper II:
Dirac comb and exponential frequency spectra in chaotic dynamics

A. Theodorsen, G. Decristoforo and O. E. Garcia,
To be submitted to *Chaos: An Interdisciplinary Journal of Nonlinear Science*

Dirac comb and exponential frequency spectra in chaotic dynamics

A. Theodorsen, G. Decristoforo and O. E. Garcia

*Department of Physics and Technology, UiT The Arctic University of Norway,
N-9037 Tromsø, Norway*

An exponential frequency power spectral density is a well known property of many continuous time chaotic systems and has been attributed to the presence of Lorentzian-shaped pulses. Here a stochastic modelling of such fluctuations are presented, describing these as a super-position of pulses with fixed shape and constant duration. Closed form expressions are derived for the lowest order moments, auto-correlation function and frequency power spectral density in the case of periodic pulse arrivals and a random distribution of pulse amplitudes. In general, the spectrum is a Dirac comb located at multiples of the periodicity time and modulated by the pulse spectrum. Randomness in the pulse arrival times is investigated by numerical realizations of the process and the results are discussed in the context of some well-known chaos models.

I. INTRODUCTION

An intrinsic property of deterministic chaos in continuous time systems is an exponential frequency power spectral density (PSD) for the fluctuations.¹⁻¹⁰ This has been observed in numerous experiments and model simulations of fluids and magnetized plasmas. Recently, the exponential spectrum has been attributed to the presence of Lorentzian pulses in the temporal dynamics.¹¹⁻²¹ Weakly non-linear systems are often characterized by a quasi-periodic oscillations, resulting in a frequency power spectral density resembling a Dirac comb.¹⁹⁻²⁷ Far from the linear instability threshold the spectral peaks broaden and in many cases an exponential spectrum results.¹⁻²⁷

Many chaotic systems, including the Lorenz and the Rössler models, display quasi-periodic orbits with Lorentzian-shaped pulses close to the primary instability threshold. The associated PSD has sharp peaks at frequencies corresponding to the periodicity of the oscillations, resembling a Dirac comb. The Lorentzian-shaped pulses lead to an exponential modulation of the amplitude of the spectral peaks. With period-doubling the density of spectral peaks increases and in the chaotic state the spectral peaks broadens and the PSD is eventually an exponential function of frequency.

In this contribution, we present a stochastic model that describes a super-position of Lorentzian pulses and the resulting frequency spectra.²⁸⁻³⁰ The model is based on the process known as shot noise or filtered Poisson process.³¹⁻⁴¹ This model has recently been used to describe intermittent fluctuations in turbulent fluids and plasmas.^{17,18}

For a super-position of pulses with fixed shape and constant duration closed form expressions are here derived for the lowest order moments, auto-correlation function and frequency power spectral density in the case of periodic pulse arrivals and a random distribution of pulse amplitudes. In general, the spectrum is a Dirac comb located at multiples of the periodicity time and modulated by the pulse spectrum. Randomness in the pulse arrival times is investigated by numerical realizations of the process and the results are discussed in the context of some well-known chaos models.

The contribution is structured as follows. In Sec. II, a motivating example for studying periodic pulse trains in connection to chaotic motion is presented. In Sec. III the stochastic model for a super-position of pulses is presented and its PSD for general arrival times is derived. In Sec. IV the case of periodic pulse arrivals is analyzed in detail with a particular

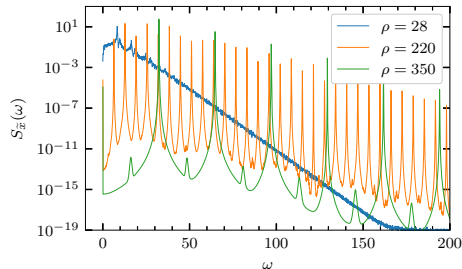


FIG. 1. Power spectral density of the x -variable in the Lorenz system for $\sigma = 10$, $\beta = 8/3$ and various values of ρ .

focus on Lorentzian pulses. Finally, in Sec. VI it is demonstrated that the stochastic model describes the chaotic dynamics of the Lorenz system.

II. THE LORENZ SYSTEM

A canonical chaos system is given by the Lorenz equations describing weakly non-linear thermal convection in an inversely stratified fluid

$$\frac{dx}{dt} = \sigma(y - x), \quad (1)$$

$$\frac{dy}{dt} = x(\rho - z) - y, \quad (2)$$

$$\frac{dz}{dt} = xy - \beta z. \quad (3)$$

Here x , y and z are the variables and σ , ρ and β are the model parameters. Time series of the x -variable and the associated frequency PSD are presented in Figs. 2 and 1 for $\sigma = 10$, $\beta = 8/3$ and three different values of the model parameter ρ .

For $\rho = 350$ the solutions consists of periodic oscillations and the frequency PSD resemble a Dirac comb with an exponential modulation of the peak amplitudes. As shown in Fig. 2, the oscillations are well described by Lorentzian-shaped pulses. Following a period doubling bifurcation, the solution for $\rho = 220$ is still regular and the PSD is again dominated by a Dirac-like comb. For $\rho = 28$ the solution is chaotic and the PSD has an exponential shape for high frequencies and some narrow peaks for low frequencies. In the following, these features of the chaotic dynamics will be analyzed by describing the fluctuations as a super-position

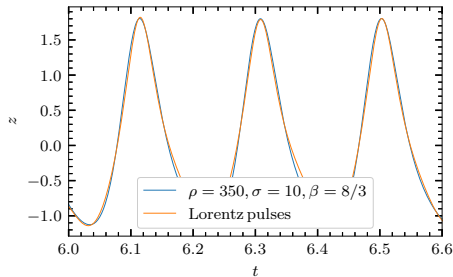


FIG. 2. Excerpt of the time series of the z -variable in the Lorenz system for $\sigma = 10$, $\beta = 8/3$ and $\rho = 350$ compared to a superposition of Lorentz pulses.

of Lorentzian-shaped pulses.

III. THE POWER SPECTRAL DENSITY OF A SUM OF PULSES

In this section, we develop an expression for the power spectral density of the a shot noise process for general arrival times. This is based on the formalism developed for filtered Poisson processes, also called shot noise processes.

We consider a train of $K(T)$ pulses arriving in the interval $[0, T]$ with randomly distributed arrival times $\{t_k\}_{k=1}^{K(T)}$ and randomly distributed amplitudes $\{A_k\}_{k=1}^{K(T)}$. The pulses have a characteristic shape φ and a characteristic duration time τ_d .

Following these remarks, the process is written as a convolution between a pulse train f_K and a pulse shape φ :

$$\Phi_K(t) = \int_{-\infty}^{\infty} ds \varphi\left(\frac{t}{\tau_d} - s\right) f_K(s), \quad (4)$$

where

$$f_K(s) = \sum_{k=1}^{K(T)} A_k \delta\left(s - \frac{t_k}{\tau_d}\right) \quad (5)$$

and δ denotes the Dirac delta function. This can be viewed as a point process f_K passed through a filter with response function ϕ , hence the name. Note that for i.i.d. uniform pulse arrivals, $K(T)$ is a Poisson process.

We normalize the pulse shape such that

$$\int_{-\infty}^{\infty} |\varphi(s)| ds = 1. \quad (6)$$

We also introduce the notation

$$\rho_\varphi(s) = \frac{1}{I_2} \int_{-\infty}^{\infty} du \varphi(u) \varphi(u+s) \quad (7)$$

and

$$\varrho_\varphi(\theta) = \frac{1}{I_2} |\mathcal{F}[\varphi](\theta)|^2 \quad (8)$$

for the auto-correlation and the power spectral density of the pulse shape, respectively. Here,

$$I_n = \int_{-\infty}^{\infty} \varphi(s)^n ds. \quad (9)$$

Note that the functions ρ_φ and ϱ_φ form a Fourier transform pair, where the definition of the Fourier transform is given in Appendix A. Throughout this contribution, we will use Lorentzian pulses, which are detailed in Appendix D.

To find the PSD, we start from Eq. (4), and take the Fourier transform as defined in Appendix A:

$$\mathcal{F}_T[\Phi_K](\omega) = \int_0^T dt \exp(-i\omega t) \Phi_K(t) = \int_0^T dt \exp(-i\omega t) \int_{-\infty}^{\infty} ds \varphi(s) f_K\left(\frac{t}{\tau_d} - s\right) \quad (10)$$

where we have exchanged the functions in the convolution given by Eq. (4). A change of variables $u(t) = t - \tau_d s$ gives

$$\mathcal{F}_T[\Phi_K](\omega) = \int_{-\infty}^{\infty} ds \varphi(s) \exp(-i\tau_d \omega s) \int_{-\tau_d s}^{T-\tau_d s} du f_K\left(\frac{u}{\tau_d}\right) \exp(-i\omega u). \quad (11)$$

We assume that $\varphi(s)$ is negligible after a few τ_d . Moreover, since no pulses arrive for negative times, $f_K(u) = 0$ for $u < 0$. Assuming $T/\tau_d \gg 1$, we can therefore approximate the limits of the second integral in Eq. (11) as $u \in [0, T]$, and the two integrals become independent.

This gives

$$\mathcal{F}_T[\Phi_K](\omega) = \mathcal{F}[\varphi](\tau_d \omega) \mathcal{F}_T[f_K](\omega). \quad (12)$$

The power spectral density (PSD) of the stationary process Φ is therefore

$$\mathcal{S}_\Phi(\omega) = \lim_{T \rightarrow \infty} \frac{1}{T} \langle |\mathcal{F}_T[\Phi_K](\omega)|^2 \rangle = |\mathcal{F}[\varphi](\tau_d \omega)|^2 \lim_{T \rightarrow \infty} \frac{1}{T} \langle |\mathcal{F}_T[f_K](\omega)|^2 \rangle, \quad (13)$$

where $\mathcal{S}_\Phi(\omega)$ is independent of K , since the average is over all random variables. The power spectrum is thus the product of the power spectrum of the pulse shape and the power

spectrum of the point process. Non-uniform arrivals only affect the point process, so this will be isolated in the analysis in Sec. III A.

Using Eq. (8), the full power spectral density of Φ can be written as

$$\mathcal{S}_\Phi(\omega) = I_2 \varrho_\varphi(\tau_d \omega) \lim_{T \rightarrow \infty} \frac{1}{T} \langle |\mathcal{F}_T[f_K](\omega)^2| \rangle. \quad (14)$$

A. The power spectral density for general arrival times

The Fourier transform of the point process is

$$\mathcal{F}_T[f_K](\omega) = \tau_d \sum_{k=1}^K A_k \exp(-i\omega t_k). \quad (15)$$

Multiplying this expression with its complex conjugate and averaging over all random variables gives (for a general distribution of arrivals $P_{t_1, t_2, \dots, t_K}(t_1, t_2, \dots, t_K)$, assuming amplitudes are i.i.d. and independent of the arrival times):

$$\begin{aligned} & \frac{1}{T} \langle |\mathcal{F}_T[f_K](\omega)^2| \rangle \\ &= \sum_{K=0}^{\infty} P_K(K; T, \tau_w) \frac{\tau_d^2}{T} \sum_{k=1}^K \sum_{l=1}^K \int_{-\infty}^{\infty} dt_1 \cdots \int_{-\infty}^{\infty} dt_K P_{t_1, \dots, t_K}(t_1, \dots, t_K) \\ & \quad \times \int_0^{\infty} dA_1 P_A(A_1) \cdots \int_0^{\infty} dA_K P_A(A_K) A_k A_l \exp(i\omega(t_l - t_k)). \\ &= \sum_{K=0}^{\infty} P_K(K; T, \tau_w) \frac{\tau_d^2}{T} \sum_{k, l=1}^K \langle A_k A_l \rangle \langle \exp(i\omega(t_l - t_k)) \rangle. \end{aligned} \quad (16)$$

In this equation, there are K terms where $k = l$ and $K(K - 1)$ terms where $k \neq l$. Summing over all these terms, we have

$$\begin{aligned} \frac{1}{T} \langle |\mathcal{F}_T[f_K](\omega)^2| \rangle &= \tau_d^2 \sum_{K=0}^{\infty} P_K(K; T, \tau_w) \\ & \quad \left\{ \frac{K}{T} \langle A^2 \rangle + \frac{1}{T} \langle A \rangle^2 \sum_{k=1}^K \sum_{l \neq k}^K \langle \exp(i\omega(t_l - t_k)) \rangle \right\}. \end{aligned} \quad (17)$$

The average inside the exponential sum is the joint characteristic function of t_l and t_k . Exchanging the order of k and l in the double sum is the same as taking the complex

conjugate of this characteristic function, so we get

$$\frac{1}{T} \langle |\mathcal{F}_T[f_K](\omega)^2| \rangle = \frac{\tau_d^2 \langle K \rangle}{T} \langle A^2 \rangle + \frac{\tau_d^2}{T} \langle A \rangle^2 \sum_{K=0}^{\infty} P_K(K; T, \tau_w) \sum_{k=2}^K \sum_{l=1}^{k-1} 2\text{Re}[\langle \exp(i\omega(t_l - t_k)) \rangle]. \quad (18)$$

1. Uniformly distributed i.i.d arrivals

As an example, we show that the expression in Eq. (18) is consistent with the established result for $K(T)$ a pure Poisson point process.

Now t_l, t_k are i.i.d. uniformly distributed arrivals on $[0, T]$. We therefore have that

$$\langle \exp(i\omega(t_l - t_k)) \rangle = \langle \exp(i\omega t_l) \rangle \langle \exp(-i\omega t_k) \rangle = 2 \frac{1 - \cos(\omega T)}{\omega^2 T^2}. \quad (19)$$

All terms in the double sum are equal, and we get

$$\frac{1}{T} \langle |\mathcal{F}_T[f_K](\omega)^2| \rangle = \frac{\tau_d^2 \langle K \rangle}{T} \langle A^2 \rangle + 2 \frac{\tau_d^2}{T} \langle A \rangle^2 \langle K(K-1) \rangle \frac{1 - \cos(\omega T)}{\omega^2 T^2}. \quad (20)$$

In this case, K is Poisson distributed with mean and variance equal to T/τ_w and we get

$$\frac{1}{T} \langle |\mathcal{F}_T[f_K](\omega)^2| \rangle = \frac{\tau_d^2}{\tau_w} \langle A^2 \rangle + \frac{2\tau_d^2}{\tau_w^2} \langle A \rangle^2 \frac{1 - \cos(\omega T)}{\omega^2 T^2}, \quad (21)$$

which gives, using $\gamma = \tau_d/\tau_w$,

$$\lim_{T \rightarrow \infty} \frac{1}{T} \langle |\mathcal{F}_T[f_K](\omega)^2| \rangle = \tau_d \gamma \langle A^2 \rangle + 2\pi \tau_d \gamma^2 \langle A \rangle^2 \delta(\tau_d \omega), \quad (22)$$

which is the standard expression for the Poisson process.³⁹ Identifying the last term as containing a Dirac delta in the limit $T \rightarrow \infty$ makes sense in the theory of distributions⁴⁶. A Poisson process gives a flat spectrum, so the only frequency variation in the full spectrum will be due to the pulse function.

2. Periodic arrival times

We consider the situation where the periodicity is known, but the exact arrivals are not. This corresponds to uncertainty in where the measurement starts in relation to the first arrival time. If the arrivals are periodic, the marginal PDF of arrival k given that the starting time is s , is

$$P_{t_k|s}(t_k|s) = \delta(t_k - \tau_p k - s). \quad (23)$$

Since each arrival is deterministic, the joint PDF with known starting point is the product of the marginal PDFs, and we have

$$\langle \exp(i\omega(t_l - t_k)) \rangle = \exp(i\omega\tau_p(l - k)). \quad (24)$$

Note that this is independent of s for all starting points, so for now we need not consider s further. We have from Eq. (18)

$$\begin{aligned} \sum_{k=2}^K \sum_{l=1}^{k-1} 2\text{Re}[\langle \exp(i\omega(t_l - t_k)) \rangle] &= \sum_{k=2}^K \sum_{l=1}^{k-1} 2 \cos(\tau_p\omega(l - k)) \\ &= \frac{K - 1 + \cos(\tau_p\omega K) - K \cos(\tau_p\omega)}{\cos(\tau_p\omega) - 1} = \frac{\cos(\tau_p\omega K) - 1}{\cos(\tau_p\omega) - 1} - K. \end{aligned} \quad (25)$$

Due to the periodicity, there are $\lfloor T/\tau_p \rfloor$ events in a time series of length T . We use $P_K(K; T, \tau_p) = \delta(K - \lfloor T/\tau_p \rfloor)$. Inserting this and Eq. (25) into Eq. (18) gives

$$\frac{1}{T} \langle |\mathcal{F}_T[f_K](\omega)^2| \rangle = \frac{\tau_d^2}{T} \lfloor T/\tau_p \rfloor \langle A^2 \rangle + \frac{\tau_d^2}{T} \lfloor T/\tau_p \rfloor \langle A \rangle^2 \left[\lfloor T/\tau_p \rfloor^{-1} \frac{\cos(\tau_p\omega \lfloor T/\tau_p \rfloor) - 1}{\cos(\tau_p\omega) - 1} - 1 \right]. \quad (26)$$

For $T/\tau_p \gg 1$, $\lfloor T/\tau_p \rfloor/T \approx 1/\tau_p$, and we have (writing $K = \lfloor T/\tau_p \rfloor$)

$$\lim_{K \rightarrow \infty} \frac{1}{T} \langle |\mathcal{F}_T[f_K](\omega)^2| \rangle = \frac{\tau_d^2}{\tau_p} \langle A^2 \rangle - \frac{\tau_d^2}{\tau_p} \langle A \rangle^2 + \frac{\tau_d^2}{\tau_p} \langle A \rangle^2 \lim_{K \rightarrow \infty} \frac{1}{K} \frac{\cos(\tau_p\omega K) - 1}{\cos(\tau_p\omega) - 1}. \quad (27)$$

Let us consider the last part of the last term,

$$\lim_{K \rightarrow \infty} \frac{1}{K} \frac{\cos(\tau_p\omega K) - 1}{\cos(\tau_p\omega) - 1}. \quad (28)$$

For integer n and $\tau_p\omega \neq 2\pi n$, this limit is zero. For $\tau_p\omega \rightarrow 2\pi n$, this limit tends to ∞ . We might therefore consider Eq. (28) proportional to a train of δ -pulses located at $\tau_p\omega = 2\pi n$.

Setting $\tau_p\omega = 2\pi n + \epsilon$ where $\epsilon \ll 1$ and expanding the cosine in the denominator, we have

$$\lim_{K \rightarrow \infty} \frac{1}{K} \frac{\cos(\tau_p\omega K) - 1}{\cos(\tau_p\omega) - 1} \approx \lim_{K \rightarrow \infty} \frac{2}{K} \frac{1 - \cos(\epsilon K)}{\epsilon^2}. \quad (29)$$

This is on the same form as we had when deriving Eq. (22), so we conclude that

$$\lim_{K \rightarrow \infty} \frac{1}{K} \frac{\cos(\tau_p\omega K) - 1}{\cos(\tau_p\omega) - 1} \sim 2\pi \sum_{n=-\infty}^{\infty} \delta(\tau_p\omega - 2\pi n). \quad (30)$$

Inserting this into Eq. (26) gives the full expression for the PSD of a train of delta pulses with randomly distributed amplitudes:

$$\lim_{T \rightarrow \infty} \frac{1}{T} \langle |\mathcal{F}_T[f_K](\omega)^2| \rangle = \tau_d\gamma A_{\text{rms}}^2 + 2\pi\tau_d\gamma^2 \langle A \rangle^2 \sum_{n=-\infty}^{\infty} \delta(\tau_d\omega - 2\pi n\gamma). \quad (31)$$

This equation will be discussed in the following section.

IV. THE SHOT NOISE PROCESS WITH PERIODIC ARRIVALS

The full power spectral density of Φ is given by multiplying Eq. (31) by the power spectrum of the pulse functions, Eq. (8), as given by Eq. (14):

$$\mathcal{S}_\Phi(\omega) = \tau_d \gamma A_{\text{rms}}^2 I_2 \varrho_\varphi(\tau_d \omega) + 2\pi \tau_d \gamma^2 \langle A \rangle^2 I_2 \varrho_\varphi(\tau_d \omega) \sum_{n=-\infty}^{\infty} \delta(\tau_d \omega - 2\pi n \gamma). \quad (32)$$

There are two main differences from the uniformly distributed pulses, given by Eq. (22): A_{rms} enters into the first term instead of $\langle A^2 \rangle$, and there is a contribution of delta spikes at integer multiples of $2\pi/\tau_p$, with an envelope given by the pulse shape. We may view the first term as the average spectrum, due to the randomness of the amplitude distribution, while the second term containing the sum of delta pulses is due to the periodicity of the pulse arrivals. Accordingly, the first term vanishes for degenerately distributed amplitudes, $p_A(A) = \delta(A - \langle A \rangle)$. For a symmetric amplitude distribution around 0, $\langle A \rangle = 0$ and $A_{\text{rms}}^2 = \langle A^2 \rangle$. The periodicity is canceled out and only the first term remains.

In Fig. 3, the power spectral density of a synthetically generated shot noise is presented for exponentially distributed amplitudes (blue line) and symmetrically Laplace distributed amplitudes (orange line). The arrivals are periodic and the pulses have a Lorentzian shape. The analytic expression Eq. (32) for both cases is given by the black and green dashed lines respectively. The Dirac comb with decaying amplitudes is easily seen in the case with exponential amplitudes. We emphasize that the main effect of the periodicity, the Dirac comb, is completely cancelled out by the symmetrically distributed pulse amplitudes.

A. The correlation function

By the Wiener-Khinchin theorem,

$$R_\Phi(t) = \frac{1}{2\pi} \int_{-\infty}^{\infty} d\omega \mathcal{S}_\Phi(\omega) \exp(i\omega t) \quad (33)$$

$$= \gamma A_{\text{rms}}^2 I_2 \rho_\varphi(t/\tau_d) + \gamma^2 \langle A \rangle^2 I_2 \sum_{n=-\infty}^{\infty} \varrho_\varphi(2\pi n \gamma) \exp(i2\pi n \gamma t/\tau_d). \quad (34)$$

By using the Poisson summation formula and properties of the Fourier transform as detailed in Appendix C, we can write R_Φ as

$$R_\Phi(t) = \gamma A_{\text{rms}}^2 I_2 \rho_\varphi\left(\frac{t}{\tau_d}\right) + \gamma \langle A \rangle^2 I_2 \sum_{m=-\infty}^{\infty} \rho_\varphi\left(\frac{m}{\gamma} + \frac{t}{\tau_d}\right). \quad (35)$$

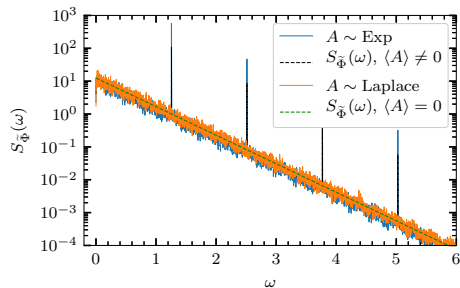


FIG. 3. The power spectral density of a shot noise process with periodic arrival times for exponentially (blue) and Laplace (orange) distributed amplitudes. The analytic expression is given by the black and green dashed lines, respectively.

Writing $m/\gamma + t/\tau_d = (m + t/\tau_p)/\gamma$, we see that the correlation function consists of a central peak with followed by periodic modulations at integer multiples of τ_p . Again, for degenerate amplitudes the correlation function only consists of the periodic train: there is no randomness left in the signal and so the correlation function does not decay for large times. For symmetric amplitudes, only the central peak remains.

In Fig. 4, the auto-correlation function of a synthetically generated shot noise is presented for exponentially distributed amplitudes (blue line) and symmetrically Laplace distributed amplitudes (orange line). The arrivals are periodic and the pulses have a Lorentzian shape. The analytic expression Eq. (32) for both cases is given by the black and green dashed lines respectively. For exponentially distributed amplitudes, the periodicity is clearly seen. This effect is again completely cancelled out by symmetrically distributed amplitudes.

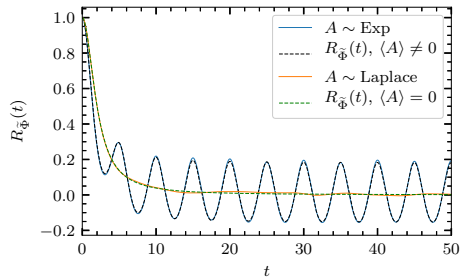


FIG. 4. The auto-correlation function of a shot noise process with periodic arrival times for exponentially (blue) and Laplace (orange) distributed amplitudes. The analytic expression is given by the black and green dashed lines, respectively.

B. The mean value and standard deviation

The mean value of the shot noise process with periodic pulses, assuming a uniform starting time distribution in $[0, \tau_p)$, is given by

$$\begin{aligned}
 \langle \Phi_K \rangle &= \sum_{k=1}^K \int dA P_A(A) \int ds P_s(s) A \varphi\left(\frac{t - \tau_p k - s}{\tau_d}\right) \\
 &= \frac{\langle A \rangle}{\tau_p} \sum_{k=1}^K \int_0^{\tau_p} ds \varphi\left(\frac{t - \tau_p k - s}{\tau_d}\right) \\
 &= \frac{\langle A \rangle}{\tau_p} \sum_{k=1}^K \int_{(t - \tau_p(k+1))/\tau_d}^{(t - \tau_p k)/\tau_d} \tau_d du \varphi(u) = \gamma \langle A \rangle \int_{(t - (K+1)\tau_p)/\tau_d}^{(t - \tau_p)/\tau_d} du \varphi(u) \\
 \langle \Phi \rangle &= \lim_{T \rightarrow \infty} \sum_{K=1}^{\infty} p_K(K; \tau_w, T) \langle \Phi_K \rangle = \gamma \langle A \rangle I_1.
 \end{aligned} \tag{36}$$

In the last step, we let $T \rightarrow \infty$ giving $K \rightarrow \infty$ and set the upper integration limit to ∞ to avoid the effect due to the signal starting at $t = 0$. This is the expected result from Campbell's theorem. This is also consistent with the fact that the square mean value is given by the zero-frequency delta function in the power spectrum, $\mathcal{S}_{\Phi}(\omega) = 2\pi \langle \Phi \rangle^2 \delta(\omega) + \dots$

The second moment is most conveniently found by noting that

$$\langle \Phi \rangle^2 = \langle \Phi(t) \Phi(t) \rangle = R_{\Phi}(0) = \gamma A_{\text{rms}}^2 I_2 + \gamma \langle A \rangle^2 I_2 \sum_{m=-\infty}^{\infty} \rho_{\varphi}\left(\frac{m}{\gamma}\right), \tag{37}$$

where we have used that $\rho_\varphi(0) = 1$. This can be verified by calculating the second moment directly as was done for the first. In Appendix B, it is shown that this is also equivalent to an extension of Campbell's theorem. We get the variance

$$\Phi_{\text{rms}}^2 = \gamma A_{\text{rms}}^2 I_2 + \gamma \langle A \rangle^2 I_2 \left(\sum_{m=-\infty}^{\infty} \rho_\varphi(m/\gamma) - \gamma \frac{I_1^2}{I_2} \right). \quad (38)$$

In the case $\gamma \ll 1$, only the $m = 0$ term in the sum gives a contribution, $\rho_\varphi(0) = 1$, giving

$$\lim_{\gamma \rightarrow 0} \Phi_{\text{rms}}^2 = \gamma \langle A^2 \rangle I_2, \quad (39)$$

where we neglect the γ^2 -contribution of the last term in the bracket. Thus, in the limit of no pulse overlap, the variance for the case of periodic pulses is equivalent to the case of Poisson distributed pulses.

In the case $\gamma \gg 1$, we can write $m/\gamma = m\Delta_t \rightarrow t$ and treat the sum as an integral, $\gamma \sum_m \rho(m/\gamma)(1/\gamma) \approx \gamma \int \rho(t)\Delta_t = \gamma I_1^2/I_2$, where the sum is over all integers and the integral is over all reals. The terms inside the bracket cancel, and we get

$$\lim_{\gamma \rightarrow \infty} \Phi_{\text{rms}}^2 = \gamma A_{\text{rms}}^2 I_2. \quad (40)$$

Since $A_{\text{rms}}^2 = \langle A^2 \rangle - \langle A \rangle^2 \leq \langle A^2 \rangle$, the periodic pulse overlap gives lower variance than the Poisson distributed pulses as there is less randomness in the signal. For exponential amplitudes, the variance in the periodic case is a factor 2 smaller. For amplitudes with zero mean value, it is equal to the Poisson case while for fixed amplitudes, the signal has no variance as pulses will accumulate until the rate of accumulation exactly matches the rate of decay, after which the signal will remain constant.

C. Quasi-periodic pulses

In this section, we present the effect of quasi-periodicity in the arrival time distribution on the second-order statistics of the shot noise process. Here, we model quasi-periodicity using a uniform distribution for each arrival around the periodic arrival time, so that the distribution of the k 'th arrival time given the starting time s is

$$P_{t_k}(t_k|s) = \begin{cases} \frac{1}{2\tau_p\kappa}, & -\tau_p\kappa \leq t_k - \tau_p k - s \leq \tau_p\kappa \\ 0, & \text{else} \end{cases}. \quad (41)$$

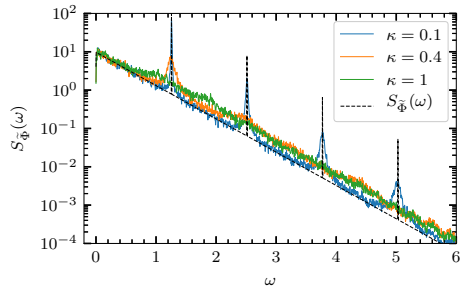


FIG. 5. The power spectral density of a shot noise process with quasi-periodic arrival times for different values of the κ -parameter. The analytic expression for purely periodic pulses is given by the black dashed line.

In the limit $\kappa \rightarrow 0$, we recover the periodic arrivals, while for $\kappa > 1$, the probability distributions of adjacent arrivals overlap. We emphasize that this is still a very restrictive formulation: even for $\kappa > 1$, each arrival is guaranteed to be centered on the time corresponding to the periodic arrival time, and the number of arrivals in a given interval is fixed up to end effects.

In Figs. 5 and 6, the effect of this quasi-periodicity is presented. The full lines give the power spectral densities and the auto-correlation functions of the shot noise process with quasi-periodic arrival times for different values of the κ -parameter, Lorentzian pulses and exponentially distributed amplitudes. The black dashed line gives the analytic prediction for purely periodic pulses. Even moderate deviations from pure periodicity quickly destroy the Dirac comb. For $\kappa = 1$, the spectrum and correlation function are already difficult to distinguish from the case of Poisson distributed arrivals. Thus, quasi-periodic phenomena in for example turbulent fluids cannot be expected to produce more than the first peak of the Dirac comb.

V. MULTIPLE PERIODICITIES: ROUTE TO CHAOS

We now consider a situation where we have multiple periodicities, each with their own amplitudes and possible offsets, such that we can write the Fourier transform of the point

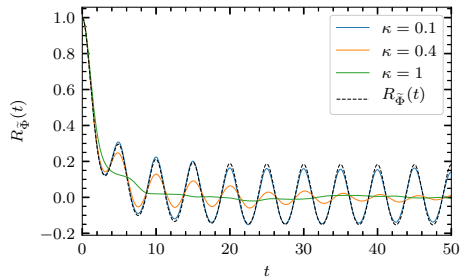


FIG. 6. The auto-correlation function of a shot noise process with quasi-periodic arrival times for different values of the κ -parameter. The analytic expression for purely periodic pulses is given by the black dashed line.

process as

$$\mathcal{F}_T[f_K](\omega) = \tau_d \sum_{p=1}^P \sum_{k=1}^{K^p} A_k^p \exp(-i\omega[\tau^p k + \alpha^p]), \quad (42)$$

where τ^p are the periods, $\{A_k^p\}_{k=1}^{K^p}$ are the arrivals connected to the p 'th periodicity, α^p are constant offsets for the first arrivals and $K^p = \lfloor (T - \alpha^p)/\tau^p \rfloor$. We assume that arrivals for different periodicities are independent. Further, we arrange the periods in decreasing order, $\tau^1 \geq \tau^2 \geq \tau^3 \geq \dots$. For large enough T that the offsets can be neglected, this leads to an increasing order in the number of events, $K^1 \leq K^2 \leq K^3 \leq \dots$. We get

$$\begin{aligned} & |\mathcal{F}_T[f_K](\omega)|^2 \\ &= \tau_d^2 \sum_{p,q=1}^P \sum_{k=1}^{K^p} \sum_{l=1}^{K^q} A_k^p A_l^q \exp(-i\omega[\tau^p k - \tau^q l + \alpha^p - \alpha^q]) \\ &= \tau_d^2 \sum_{p=1}^P \sum_{k=1}^{K^p} (A_k^p)^2 \\ &+ \tau_d^2 \sum_{p=1}^P \sum_{\substack{k,l=1 \\ k \neq l}}^{K^p} A_k^p A_l^p \exp(-i\omega\tau^p[k - l]) \\ &+ \tau_d^2 \sum_{\substack{p,q=1 \\ p \neq q}}^P \sum_{k=1}^{K^p} \sum_{l=1}^{K^q} A_k^p A_l^q \exp(-i\omega[\tau^p k - \tau^q l + \alpha^p - \alpha^q]). \end{aligned}$$

Taking the average over all amplitudes and gathering terms $(k, l) + (l, k)$ in the second double sum as well as terms $(p, q) + (q, p)$ in the triple sum, we get

$$\begin{aligned}
& \frac{1}{T} \langle |\mathcal{F}_T[f_K](\omega)^2| \rangle \\
&= \frac{\tau_d^2}{T} \sum_{p=1}^P K^p \langle (A^p)^2 \rangle + \frac{\tau_d^2}{T} \sum_{p=1}^P \sum_{k=2}^{K^p} \sum_{l=1}^{k-1} \langle A^p \rangle^2 2 \cos(\omega \tau^p [k-l]) \\
&\quad + \frac{\tau_d^2}{T} \sum_{p=2}^P \sum_{q=1}^{p-1} \sum_{k=1}^{K^p} \sum_{l=1}^{K^q} 2 \langle A^p \rangle \langle A^q \rangle \\
&\exp\left(i\omega \frac{(k-l)(\tau^p + \tau^q)}{2}\right) \cos\left(\omega \frac{(k+l)(\tau^p - \tau^q)}{2} + \omega(\alpha^p - \alpha^q)\right).
\end{aligned}$$

The first two terms just gives a sum of the result in (31) over all periods. To investigate the last term, we consider the special case where $\tau^p = \tau \forall p$ so $K^p = K \forall p$. Then we have that the last term is

$$\begin{aligned}
& \frac{\tau_d^2}{T} \sum_{p=2}^P \sum_{q=1}^{p-1} \langle A^p \rangle \langle A^q \rangle 2 \cos(\omega(\alpha^p - \alpha^q)) \sum_{k=1}^K \sum_{l=1}^K \exp(i\omega\tau(k-l)) \\
&= \frac{\tau_d^2}{T} \sum_{p=2}^P \sum_{q=1}^{p-1} \langle A^p \rangle \langle A^q \rangle 2 \cos(\omega(\alpha^p - \alpha^q)) \frac{\cos(K\omega\tau) - 1}{\cos(\omega\tau) - 1}. \quad (43)
\end{aligned}$$

This contains exactly the expression found in Eq. (29), so we have that

$$\begin{aligned}
& \lim_{T \rightarrow \infty} \frac{1}{T} \langle |\mathcal{F}_T[f_K](\omega)^2| \rangle \\
&= \sum_{p=1}^P \left\{ \tau_d \gamma (A_{\text{rms}}^p)^2 + 2\pi \tau_d \gamma^2 \langle A^p \rangle^2 \sum_{n=-\infty}^{\infty} \delta(\tau_d \omega - 2\pi n \gamma) \right\} \\
&+ \sum_{p=2}^P \sum_{q=1}^{p-1} \langle A^p \rangle \langle A^q \rangle 2 \cos(\omega(\alpha^p - \alpha^q)) 2\pi \tau_d \gamma \sum_{n=-\infty}^{\infty} \delta(\tau \omega - 2\pi n).
\end{aligned} \tag{44}$$

Here, $\gamma = \tau_d/\tau$. Seeing that we can exchange $2 \sum_{p=2}^P \sum_{q=1}^{p-1}$ with $\sum_{p=1}^P \sum_{q=1, q \neq p}^P$, we can write the full expression as

$$\begin{aligned} \lim_{T \rightarrow \infty} \frac{1}{T} \langle |\mathcal{F}_T[f_K](\omega)^2| \rangle &= \sum_{p=1}^P \tau_d \gamma (A_{\text{rms}}^p)^2 + \\ &\quad \sum_{p=1}^P 2\pi \tau_d \gamma^2 \langle A^p \rangle \left[\langle A^p \rangle + \sum_{q \neq p} \langle A^q \rangle \cos(\omega(\alpha^p - \alpha^q)) \right] \sum_{n=-\infty}^{\infty} \delta(\tau_d \omega - 2\pi n \gamma) \\ &= \sum_{p=1}^P \tau_d \gamma (A_{\text{rms}}^p)^2 + 2\pi \tau_d \gamma^2 \sum_{p=1}^P \sum_{q=1}^P \langle A^p \rangle \langle A^q \rangle \cos(\omega(\alpha^p - \alpha^q)) \sum_{n=-\infty}^{\infty} \delta(\tau_d \omega - 2\pi n \gamma). \end{aligned} \quad (45)$$

Thus, we get the same expression as for only one periodicity, except that we make the replacements

$$\begin{aligned} A_{\text{rms}}^2 &\rightarrow \sum_{p=1}^P (A_{\text{rms}}^p)^2, \\ \langle A \rangle^2 &\rightarrow \sum_{p=1}^P \sum_{q=1}^P \langle A^p \rangle \langle A^q \rangle \cos(\omega(\alpha^p - \alpha^q)). \end{aligned}$$

In this case, the correction to the second term in the expression for the PSD depends on the offset between the different pulse trains. In particular, if there is no offset, $\alpha^p - \alpha^q = 0$, we just get the double sum over all mean values of the amplitudes. In this model, this means that adding further pulses with the same periodicity does not affect the density of the spikes in the Dirac comb. As period doubling can be seen as both decreasing τ_p and adding more pulses, this result shows that only decreasing τ_p affects the density of the Dirac comb.

VI. APPLICATION TO THE LORENZ ATTRACTOR

The predictions for the PSD of the stochastic model can be compared to that from numerical simulations of Lorenz system. In Fig. 7 the low-frequency part of the spectrum is presented for $\rho = 350$ as well as the predicted Dirac comb for a super-position of Lorentzian pulses with duration $\tau_d = 0.039$ and periodicity $\tau_p = 0.194$. This is clearly a good description of the oscillations in the Lorenz system.

In the chaotic state for $\rho = 28$ the PSD presented in Fig. 8 has some low-frequency peaks with higher harmonics on top of a exponential spectrum. This spectrum can be reproduced by a super-position of quasi-periodic Lorentzian with duation $\tau_d = 0.135$, periodicity $\tau_p =$

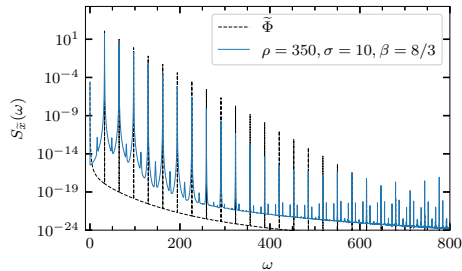


FIG. 7. The power spectral density of a Lorenz system with $\rho = 350$, $\sigma = 10$ and $\beta = 8/3$ compared to the frequency power spectral density of a synthetic shot noise process with periodic arrival times and exponentially distributed amplitudes.

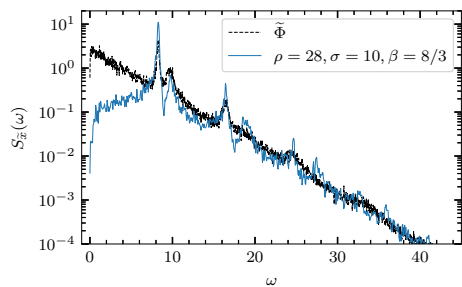


FIG. 8. The power spectral density of a Lorenz system with $\rho = 28$, $\sigma = 10$ and $\beta = 8/3$ compared to the power spectral density of a synthetic shot noise process with quasi-periodic arrival times, exponentially distributed amplitudes and $\kappa = 0.1$.

0.643 and $\kappa = 0.1$ for the distribution of pulse arrivals. This is an excellent description of the PSD for the Lorenz system except for the very lowest frequencies which is likely due to the chaotic nature of the fluctuations.

VII. ACKNOWLEDGEMENTS

This work was supported by the UiT Aurora Centre Program, UiT The Arctic University of Norway (2020) and the Tromsø Research Foundation under grant number 19_SG_AT. Discussions with M. Rypdal and M. Overholt are gratefully acknowledged.

Appendix A: Definitions of the Fourier transform and the Power spectral density

The PSD of a random process $\Phi(t)$ is defined as

$$\mathcal{S}_\Phi(\omega) = \lim_{T \rightarrow \infty} \frac{1}{T} \langle |\mathcal{F}_T[\Phi](\omega)|^2 \rangle, \quad (\text{A1})$$

where

$$\mathcal{F}_T[\Phi_K](\omega) = \int_0^T dt \exp(-i\omega t) \Phi(t) \quad (\text{A2})$$

is the Fourier transform of the random variable over the domain $[0, T]$.

Analytical functions which fall rapidly enough to zero (such as the pulse function) have the Fourier transform

$$\mathcal{F}[\varphi](\theta) = \int_{-\infty}^{\infty} ds \varphi(s) \exp(-i\theta s) \quad (\text{A3})$$

and the inverse transform

$$\varphi(s) = \mathcal{F}^{-1}[\mathcal{F}[\varphi](\theta)](s) = \frac{1}{2\pi} \int_{-\infty}^{\infty} d\theta \exp(i\theta s) \mathcal{F}[\varphi](\theta). \quad (\text{A4})$$

Note that here, θ and s are non-dimensional variables, as opposed to t and ω .

Appendix B: The extended Campbell's theorem

For a full discussion of Campbell's theorem for the mean value of a shot noise process as well as various extensions, we refer to [Rice, Campbell, Pecseli]. It can be shown that for i.i.d. waiting times W with distribution p_W and mean value τ_w , we have in our notation

$$\langle \Phi^2 \rangle = \gamma \langle A^2 \rangle I_2 + 2\gamma \langle A \rangle^2 I_2 \sum_{k=1}^{\infty} \int_0^{\infty} ds_1 \int_0^{\infty} ds_2 \cdots \int_0^{\infty} ds_k p_W(s_1) p_W(s_2) \cdots p_W(s_k) \rho_\varphi \left(\frac{1}{\tau_d} \sum_{n=1}^k s_n \right). \quad (\text{B1})$$

The k 'th order integral can be compactly written as $\langle \rho_\varphi(S_k/\tau_d) \rangle$, where $S_k = \sum_{n=1}^k s_n$. All s_n are i.i.d., with distribution p_W , and we denote the corresponding characteristic function as C_W . We get

$$\left\langle \rho_\varphi \left(\frac{1}{\tau_d} S_k \right) \right\rangle = \int_{-\infty}^{\infty} dS p_S(S; k) \rho_\varphi \left(\frac{1}{\tau_d} S \right) = \frac{1}{2\pi} \int_{-\infty}^{\infty} du \int_{-\infty}^{\infty} dS C_S(u; k) \exp(-iSu) \rho_\varphi \left(\frac{1}{\tau_d} S \right). \quad (\text{B2})$$

As C_S is the characteristic function of the sum of k i.i.d. random variables, we get $C_S(u; k) = C_W(u)^k$. Further, we see that this equation contains the Fourier transform of ρ_φ , so we have

$$\left\langle \rho_\varphi \left(\frac{1}{\tau_d} S_k \right) \right\rangle = \frac{\tau_d}{2\pi} \int_{-\infty}^{\infty} du C_W(u)^k \varrho_\varphi(\tau_d u), \quad (\text{B3})$$

which gives

$$\langle \Phi^2 \rangle = \gamma \langle A^2 \rangle I_2 + 2\gamma \langle A \rangle^2 I_2 \sum_{k=1}^{\infty} \frac{\tau_d}{2\pi} \int_{-\infty}^{\infty} du C_W(u)^k \varrho_\varphi(\tau_d u). \quad (\text{B4})$$

Note that in this equation, only C_W^k depends on k , so we may take the sum over k into the integral and investigate \sum_k . For periodic arrivals, $p_W(w) = \delta(w - \tau_w)$, giving $C_W(u) = \exp(iu\tau_w)$, and we get

$$\langle \Phi^2 \rangle = \gamma \langle A^2 \rangle I_2 + 2\gamma \langle A \rangle^2 I_2 \sum_{k=1}^{\infty} \rho_\varphi \left(\frac{1}{\tau_d} k \tau_w \right). \quad (\text{B5})$$

As $A_{\text{rms}}^2 I_2 = \langle A^2 \rangle I_2 - \langle A \rangle^2 I_2 = \langle A^2 \rangle I_2 - \langle A \rangle^2 I_2 \rho_\varphi(0)$ and $\rho_\varphi(s) = \rho_\varphi(-s)$, this is equivalent to Eq. (37).

Appendix C: The Poisson summation formula

Here, we briefly present the well-known Poisson summation formula, which is treated in a number of textbooks^{42–45}. For our purposes, the formulation used in Corollary VII.2.6 in⁴⁵ is the most useful. The statement in the book is for functions on general Euclidian spaces, but we repeat it here only for our special case (the real line):

The Poisson summation formula Suppose the Fourier transform of f and its inverse are defined as in Eq. (A3) and Eq. (A4) respectively. Further suppose that $|f(s)| \leq A(1 + |s|)^{-1-\delta}$ and $|\mathcal{F}[f](\theta)| \leq A(1 + |\theta/2\pi|)^{-1-\delta}$ with $A > 0$ and $\delta > 0$. Then

$$\sum_{m=-\infty}^{\infty} f(m) = \sum_{n=-\infty}^{\infty} \mathcal{F}[f](2\pi n), \quad (\text{C1})$$

where both series converge absolutely.

- Note that the inequality conditions guarantee that both $|f(s)|$ and $|\mathcal{F}[f](\theta)|$ are integrable, which again guarantees that both f and its Fourier transform are continuous and vanish at ∞ (Theorem I.1.2 in⁴⁵).

- Using properties of the Fourier transform, the summation formula can be cast to a number of different forms:

$$\sum_{n=-\infty}^{\infty} \mathcal{F}[f](2\pi n) = \sum_{m=-\infty}^{\infty} f(m) \quad (\text{C2})$$

$$\sum_{n=-\infty}^{\infty} \gamma \mathcal{F}[f](2\pi n \gamma) = \sum_{m=-\infty}^{\infty} f(m/\gamma) \quad (\text{C3})$$

$$\sum_{n=-\infty}^{\infty} \gamma \mathcal{F}[f](2\pi n \gamma) \exp(i2\pi n \gamma t/\tau_d) = \sum_{m=-\infty}^{\infty} f(m/\gamma + t/\tau_d). \quad (\text{C4})$$

- By using the definitions of ρ and ϱ given in Eq. (7) and Eq. (8) respectively, as well as the Fourier transform, we have that if Eq. (C1) holds for φ , then by Eq. (C4) we have

$$\begin{aligned} \sum_{m=-\infty}^{\infty} \varphi(m+s) &= \sum_{n=-\infty}^{\infty} \mathcal{F}[\varphi](2\pi n) \exp(i2\pi n s), \\ \int_{-\infty}^{\infty} du \varphi(u) \sum_{m=-\infty}^{\infty} \varphi(s+m) &= \int_{-\infty}^{\infty} du \varphi(u) \sum_{m=-\infty}^{\infty} \mathcal{F}[\varphi](2\pi n) \exp(i2\pi n s), \\ \sum_{m=-\infty}^{\infty} \rho_{\varphi}(m) &= \sum_{n=-\infty}^{\infty} \varrho_{\varphi}(2\pi n), \end{aligned}$$

which means that the summation formula holds for the correlation function and power spectrum of the pulse as well. This does not necessarily work in reverse - if one of the sums over φ or its Fourier transform diverges, we cannot exchange the summation and the integral in the second step. Consider as an example the one-sided exponential pulse (detailed in Appendix E). Here, the pulse function does not fulfill the Poisson summation formula as the Fourier transform goes as θ^{-1} , and so the sum diverges. Its correlation function and power spectrum do, however, fulfill the conditions and therefore the formula.

Appendix D: The Lorentz pulse

The Lorentz pulse is given by

$$\varphi(s) = (1 + s^2)^{-1}/\pi. \quad (\text{D1})$$

Its Fourier transform is

$$\mathcal{F}[\varphi](\theta) = \exp(-|\theta|), \quad (\text{D2})$$

the integrals are $I_n =$, and we have the correlation function

$$\rho_\varphi(s) = 4(4 + s^2)^{-1}, \quad (\text{D3})$$

and spectrum

$$\varrho_\varphi(\theta) = 2\pi \exp(-2|\theta|). \quad (\text{D4})$$

In general, the full sum of the correlation function is given by

$$\sum_{m=-\infty}^{\infty} \rho_\varphi\left(\frac{m}{\gamma} + \frac{t}{\tau_d}\right) = \gamma\pi[\coth(2\gamma\pi - i\gamma\pi t/\tau_d) + \coth(2\gamma\pi + i\gamma\pi t/\tau_d)]. \quad (\text{D5})$$

Two special cases of this are of interest in the current contribution. For $t = 0$, we get

$$\sum_{m=-\infty}^{\infty} \rho_\varphi\left(\frac{m}{\gamma}\right) = 2\gamma\pi \coth(2\gamma\pi), \quad (\text{D6})$$

while in the limit $\gamma \rightarrow 0$ we get the expected result

$$\lim_{\gamma \rightarrow 0} \sum_{m=-\infty}^{\infty} \rho_\varphi\left(\frac{m}{\gamma} + \frac{t}{\tau_d}\right) = \rho_\varphi(t/\tau_d). \quad (\text{D7})$$

Appendix E: Table of pulses

For reference, we here present some relations for other pulse functions.

Name	$\varphi(s)$	$\mathcal{F}[\varphi](\theta)$	$\rho_\varphi(s)$	$\varrho_\varphi(\theta)$
One-sided exponential	$\begin{cases} 0, & s < 0 \\ \exp(-s), & s \geq 0 \end{cases}$	$(1 + i\theta)^{-1}$	$\exp(- s)$	$2(1 + \theta^2)^{-1}$
Symmetric exponential	$\exp(- s)$	$2(1 + \theta^2)^{-1}$	$2\exp(- s)[1 + s]$	$8(1 + \theta^2)^{-2}$
Sech	$\text{sech}(s)/\pi$	$\text{sech}[\pi\theta/2]$	$s \text{csch}(s)$	$\pi^2 \text{sech}[\pi\theta/2]^2/2$
Gauss	$\exp(-s^2/2)/\sqrt{2\pi}$	$\exp(-\theta^2/2)$	$\exp(-s^2/4)$	$2\sqrt{\pi} \exp(-\theta^2)$

A few reasonable results for the infinite sums can be obtained:

Name	$\sum_{m=-\infty}^{\infty} \rho_\varphi(m/\gamma)$
One-sided exponential	$\coth\left(\frac{1}{2\gamma}\right)$
Symmetric exponential	$2\coth\left(\frac{1}{2\gamma}\right) + \frac{1}{\gamma}\text{csch}\left(\frac{1}{2\gamma}\right)^2$

Appendix F: Representation of delta functions under finite sampling

In this contribution, we frequently plot delta functions superposed on a waveform. A true representation of a continuous-time delta function would be a line extending out of the plot domain. Alternatively, we could indicate the delta spikes by arrows or stars on the ends. The first solution does not give an indication of the amplitude of the delta, while the second makes for very busy figures.

We have instead elected to represent the Dirac delta by its discrete analog, the Kronecker delta. For $t \rightarrow \Delta_t n$, we have $\omega = 2\pi f \rightarrow 2\pi m/\Delta_t$. A Dirac delta at a given angular frequency ω_* is then given by $\delta(\omega - \omega_*) = \delta(2\pi(m - k)/\Delta_t) = \frac{\Delta_t}{2\pi} \delta_{m-k}$ where k is the nearest integer to $\Delta_t \omega_*/2\pi$. That is, the Dirac delta is approximated as a boxcar of width equal to the sampling step and a height equal to the inverse of the sampling step. This indicates the amplitude of the delta spikes, separates them from any superposed functions and tends to better approximations for finer sampling.

REFERENCES

- ¹P. Atten, J. C. Lacroix, and B. Malraison, *Phys. Lett. A* **79**, 255 (1980).
- ²U. Frisch and R. Morf, *Phys. Rev. A* **23**, 2673 (1981).
- ³H. S. Greenside, G. Ahlers, P. C. Hohenberg, and R. W. Walden, *Physica D* **5**, 322 (1982).
- ⁴D. S. Broomhead and G. P. King, *Physica* **10D**, 217 (1986).
- ⁵A. Brandstater and H. L. Swinney, *Phys. Lett. A* **35**, 2207 (1987).
- ⁶C. L. Streett and M. Y. Hussaini, *Applied Numerical Mathematics* **7**, 41 (1991).
- ⁷D. E. Sigeti, *Physica D* **82**, 136 (1995).
- ⁸D. E. Sigeti, *Phys. Rev. E* **52**, 2443 (1995).
- ⁹M. R. Paul, M. C. Cross, P. F. Fischer, and H. S. Greenside, *Phys. Rev. Lett.* **87**, 154501 (2001).
- ¹⁰C. L. E. Franzke, S. M. Osprey, P. Davini and N. W. Watkins, *Sci. Rep.* **5**, 9068 (2015).
- ¹¹D. C. Pace, M. Shi, J. E. Maggs, G. J. Morales, and T. A. Carter, “Exponential frequency spectrum in magnetized plasmas” *Phys. Rev. Lett.* **101**, 085001 (2008).
- ¹²D. C. Pace, M. Shi, J. E. Maggs, G. J. Morales, and T. A. Carter, “Exponential frequency spectrum and Lorentzian pulses in magnetized plasmas” *Phys. Plasmas* **15**, 122304 (2008).

- ¹³G. Hornung, B. Nold, J. E. Maggs, G. J. Morales, M. Ramisch, and U. Stroth, “Observation of exponential spectra and Lorentzian pulses in the TJ-K stellarator” *Phys. Plasmas* **18**, 082303 (2011).
- ¹⁴J. E. Maggs and G. J. Morales, “Origin of Lorentzian pulses in deterministic chaos” *Phys. Rev. E* **86**, 015401 (2012).
- ¹⁵J. E. Maggs, T. L. Rhodes, and G. J. Morales, “Chaotic density fluctuations in L-mode plasmas of the DIII-D tokamak” *Plasma Phys. Contr. Fusion* **55**, 085014 (2013).
- ¹⁶Z. Zhu, A. E. White, T. A. Carter, S. G. Baek, and J. L. Terry, “Chaotic edge density fluctuations in the Alcator C-Mod tokamak” *Phys. Plasmas* **24**, 042301 (2017).
- ¹⁷G. Decristoforo, A. Theodorsen, and O. E. Garcia, “Intermittent fluctuations due to Lorentzian pulses in turbulent thermal convection” *Phys. Fluids* **32**, 085102 (2020).
- ¹⁸G. Decristoforo, A. Theodorsen, J. Omotani, T. Nicholas, and O. E. Garcia, “Intermittent fluctuations due to Lorentzian pulses in turbulent thermal convection” *Phys. Fluids* **32**, 085102 (2020).
- ¹⁹N. Ohtomo, K. Tokiwano, Y. Tanaka, A. Sumi, S. Terachi, and H. Konno, “Exponential characteristics of power spectral densities caused by chaotic phenomena” *J. Phys. Soc. Japan* **64**, 1104 (1995).
- ²⁰J. E. Maggs and G. J. Morales, “Generality of deterministic chaos, exponential spectra, and Lorentzian pulses in magnetically confined plasmas” *Phys. Rev. Lett.* **107**, 185003 (2011).
- ²¹J. E. Maggs and G. J. Morales, “Exponential power spectra, deterministic chaos and Lorentzian pulses in plasma edge dynamics” *Plasma Phys. Contr. Fusion* **54**, 124041 (2012).
- ²²J. D. Farmer, *Physica D* **4**, 366 (1982).
- ²³A. Libchaber, S. Fauve, and C. Laroche, *Physica D* **7**, 73 (1983).
- ²⁴E. F. Stone, *Phys. Lett. A* **148**, 434 (1990).
- ²⁵T. Klinger, A. Latten, A. Piel, G. Bonhomme, T. Pierre, and T. Dudok de Wit, *Phys. Rev. Lett.* **79**, 3913 (1997).
- ²⁶B. Mensour and A. Longtin, *Physica D* **113**, 1 (1998).
- ²⁷L. A. Safonov, E. Tomer, V. V. Strygin, Y. Ashkenazy, and S. Havlin, *Chaos* **12**, 1006 (2002).
- ²⁸O. E. Garcia and A. Theodorsen, “Power law spectra and intermittent fluctuations due to

- uncorrelated Lorentzian pulses” *Phys. Plasmas* **24**, 020704 (2017).
- ²⁹O. E. Garcia and A. Theodorsen, “Skewed Lorentzian pulses and exponential frequency power spectra” *Phys. Plasmas* **25**, 014503 (2018).
- ³⁰O. E. Garcia and A. Theodorsen, “Intermittent fluctuations due to uncorrelated Lorentzian pulses” *Phys. Plasmas* **25**, 014506 (2018).
- ³¹E. Parzen, *Stochastic processes* (Holden-Day, Oakland, CA, 1962).
- ³²H. L. Pécseli, *Fluctuations in Physical Systems* (Cambridge University Press, Cambridge, 2000).
- ³³S. O. Rice, “Mathematical analysis of random noise” *Bell Sys. Tech. J.* **23**, 282 (1944).
- ³⁴O. E. Garcia, “Stochastic modeling of intermittent scrape-off layer plasma fluctuations” *Phys. Rev. Lett.* **108**, 265001 (2012).
- ³⁵R. Kube and O. E. Garcia, “Convergence of statistical moments of particle density time series in scrape-off layer plasmas” *Phys. Plasmas* **22**, 012502 (2015).
- ³⁶A. Theodorsen and O. E. Garcia, “Level crossings, excess times, and transient plasma-wall interactions in fusion plasmas” *Phys. Plasmas* **23**, 040702 (2016).
- ³⁷O. E. Garcia, R. Kube, A. Theodorsen, and H. L. Pécseli, “Stochastic modelling of intermittent fluctuations in the scrape-off layer: Correlations, distributions, level crossings, and moment estimation” *Phys. Plasmas* **23**, 052308 (2016).
- ³⁸O. E. Garcia and A. Theodorsen, “Auto-correlation function and frequency spectrum due to a super-position of uncorrelated exponential pulses” *Phys. Plasmas* **24**, 032309 (2017).
- ³⁹A. Theodorsen, O. E. Garcia, and M. Rypdal, “Statistical properties of a filtered Poisson process with additive random noise: distributions, correlations and moment estimation” *Phys. Scripta* **92**, 054002 (2017).
- ⁴⁰A. Theodorsen and O. E. Garcia, “Level crossings and excess times due to a superposition of uncorrelated exponential pulses” *Phys. Rev. E* **97**, 012110 (2018).
- ⁴¹A. Theodorsen and O. E. Garcia, “Probability distribution functions for intermittent scrape-off layer plasma fluctuations” *Plasma Phys. Contr. Fusion* **60**, 034006 (2018)
- ⁴²M. Overholt, *A Course in Analytic Number Theory*. American Mathematical Society (AMS) 2014 ISBN 978-1-4704-1706-2.
- ⁴³S. Bochner, *Lectures on Fourier Integrals*, Annals of Math. Studies 42, Princeton University press, Princeton, NJ, 1959
- ⁴⁴L. Grafakos, “Classical Fourier Analysis”, <https://doi.org/10.1007/978-0-387-09432-8>

⁴⁵E. M. Stein and G. Weiss, “Introduction to Fourier Analysis on Euclidian Spaces”, Princeton University Press, Princeton, NJ, 1971

⁴⁶I. Richards and H. Youn, “Theory of Distributions”, Cambridge University Press, <https://doi.org/10.1017/CBO9780511623837>

Paper III: Numerical turbulence simulations of intermittent fluctuations in the scrape-off layer of magnetized plas- mas

G. Decristoforo, A. Theodorsen, J. Omotani, T. Nicholas, and O. E. Garcia,
Submitted to Physics of Plasmas on 15.2.2021,
Available online: [arXiv:2102.04723](https://arxiv.org/abs/2102.04723) [physics.plasm-ph]

Numerical turbulence simulations of intermittent fluctuations in the scrape-off layer of magnetized plasmas

G. Decristoforo,^{a)} A. Theodorsen,^{a)} J. Omotani,^{b)} T. Nicholas,^{c)} and O. E. Garcia^{a)}

(Dated: 8 March 2021)

Intermittent fluctuations in the boundary of magnetically confined plasmas are investigated by numerical turbulence simulations of a reduced fluid model describing the evolution of the plasma density and electric drift vorticity in the two-dimensional plane perpendicular to the magnetic field. Two different cases are considered, one describing resistive drift waves in the edge region and another including only the interchange instability due to unfavorable magnetic field curvature in the scrape-off layer. Analysis of long data time series obtained by single-point recordings are compared to predictions of a stochastic model describing the plasma fluctuations as a super-position of uncorrelated pulses. For both cases investigated, the radial particle density profile in the scrape-off layer is exponential with a radially constant scale length. The probability density function for the particle density fluctuations in the far scrape-off layer has an exponential tail. Radial motion of blob-like structures leads to large-amplitude bursts with an exponential distribution of peak amplitudes and the waiting times between them. The average burst shape is well described by a two-sided exponential function. The frequency power spectral density of the particle density is simply that of the average burst shape and is the same for all radial positions in the scrape-off layer. The fluctuation statistics obtained from the numerical simulations are in excellent agreement with recent experimental measurements on magnetically confined plasmas. The statistical framework defines a new validation metric for boundary turbulence simulations.

^{a)}Department of Physics and Technology, UiT The Arctic University of Norway, NO-9037 Tromsø, Norway

^{b)}United Kingdom Atomic Energy Authority, Culham Centre for Fusion Energy, Culham Science Centre, Abingdon, Oxon, OX14 3DB, UK

^{c)}York Plasma Institute, Department of Physics, University of York, Heslington, York YO10 5DD, UK

I. INTRODUCTION

At the boundary of magnetically confined plasma, turbulent transport of particles and heat in the outermost region enhances plasma interactions with the material surfaces. This can become a serious issue for future fusion experiments and reactors.¹⁻³ A complete description of the physical mechanisms underlying the cross-field plasma and heat transport in the scrape-off layer (SOL) and its effects on plasma-wall interactions is necessary if reliable predictions for reactor relevant devices are to be obtained. Unfortunately, such an understanding is at present still not fully achieved and predictions and extrapolations are often based on empirical scaling laws or highly simplified transport modelling with limited theoretical foundation.³⁻⁵

Fluctuations and turbulent motions in the boundary region of magnetized plasmas have been extensively investigated both experimentally and theoretically. It is recognized that in the SOL radial motion of blob-like filament structures is the dominant mechanism for cross-field transport of particles and heat.⁶⁻⁹ This leads to broadening and flattening of radial profiles and high average particle density in the SOL that increases plasma-wall interactions.¹⁰⁻²³ Experimental measurements using Langmuir probes and gas puff imaging have revealed highly intermittent fluctuations of the particle density in the far SOL. Interestingly, measurements across a variety of magnetic geometries, including conventional tokamaks, spherical tokamaks, reversed field pinches and stellarators have shown similar fluctuation characteristics.²⁴⁻²⁷ Recent statistical analysis of exceptionally long fluctuation data time series from several tokamak devices has shown that the fluctuations are well described as a super-position of uncorrelated exponential pulses with fixed duration, arriving according to a Poisson process and with exponentially distributed pulse amplitudes.²⁸⁻⁴² A statistical framework based on filtered Poisson processes has proven an accurate description of both average radial profiles and fluctuations in the boundary of magnetically confined plasma.⁴³⁻⁵³

So far, this stochastic model has not been utilized to analyze fluctuation data from numerical turbulence simulations of the boundary region of magnetized plasmas. In order to obtain statistically significant results, long simulation data time series or a large ensemble are required, equivalent to several hundred milliseconds in experiments with medium-sized magnetically confined plasma. Since most turbulence simulation studies have been focused on the dynamics of individual blob structures or on the effects of specific physical mechanisms on turbulence and transport, the simulations have likely not produced time series data of sufficient duration in order to analyze them in the same manner as the experimental measurements.²⁸⁻⁴² In this paper we present the first

results from applying the same statistical framework on numerical simulation data as has recently been done on experimental measurements. By using a simplified turbulence model describing the fluctuations in the two-dimensional plane perpendicular to the magnetic field, we have obtained data time series sufficiently long to allow unambiguous identification of the fluctuation statistics. The main goal of this study is to clarify these statistical properties and compare them with that found from experimental measurements. This is considered an essential step towards validation of turbulence simulation codes.^{54–56}

A recent analysis of fluctuation data time series obtained from numerical simulations of turbulent Rayleigh–Bénard-convection in two dimensions has given some illuminating results.⁵⁷ This model has frequently been used as a simplified description of the non-linear interchange dynamics in the SOL of magnetically confined plasmas.^{58–66} In Ref. 57 it was found that the fluctuation time series are well described as a super-position of Lorentzian pulses, resulting in an exponential frequency power spectral density. In the present study, more sophisticated models for SOL turbulence are investigated, including sheath dissipation due to losses along magnetic field lines intersecting material surfaces as well as drift wave dynamics in the edge region.^{67–83} The resulting far SOL data time series are shown to be dominated by large-amplitude bursts with a two-sided exponential pulse shape and fluctuation statistics that compare favorably with those found in experimental measurements.^{28–42}

In this contribution we present a detailed statistical analysis of fluctuation data time series from numerical simulations of a two-dimensional reduced fluid model describing the evolution of the electron density and electric drift vorticity. The paper is structured as follows. The reduced fluid model equations, normalization and parameters are discussed in Sec. II. A brief introduction to the stochastic model is also presented here. We present the results for the time-averaged profiles and probability densities in Sec. III and for the fluctuation statistics in Sec. IV. A discussion of the results and the conclusions are finally presented in Sec. V.

II. MODEL EQUATIONS

The reduced fluid model investigated here is motivated by previous simulation studies performed by Sarazin *et al.*,^{69–71} Garcia *et al.*,^{72–74}, Myra *et al.*,^{75–77}, Bisai *et al.*,^{78–80} and Nielsen *et al.*^{81–83} One particular case of the model is equivalent to that used in Ref. 71 and simulates SOL conditions in the entire simulation domain where a particle source is located close to the

inner boundary. The particle density profile results from a balance between the plasma source, the sheath dissipation and radial transport due to the interchange instability. Another case of the model is similar to that used in Ref. 79 and features a simulation domain separating an edge region corresponding to plasma dynamics on closed magnetic flux surfaces and a SOL region where sheath dissipation balances the interchange drive. The source term is located in the plasma edge region where parallel resistivity gives rise to unstable drift waves. Despite these two fundamentally different descriptions of the primary instability mechanism underlying the SOL turbulence, the resulting fluctuations are remarkably similar as will be shown in the following.

We use two-field fluid model equations describing the plasma evolution in the edge and SOL regions for a quasi-neutral plasma, neglecting electron inertia and assuming for simplicity isothermal electrons and negligibly small ion temperature. We make these simplifying assumptions in order to obtain long fluctuation data time series from the numerical simulations. We choose a slab geometry where x refers to the radial direction and y to the binormal or poloidal direction. The reduced electron continuity and electron drift vorticity equations are given by

$$\frac{dn}{dt} + g \left(\frac{\partial n}{\partial y} - n \frac{\partial \phi}{\partial y} \right) = S_n + D_{\perp} \nabla_{\perp}^2 n + \left\langle \frac{1}{L_{\parallel}} \nabla_{\parallel} J_{\parallel e} \right\rangle_{\parallel}, \quad (1a)$$

$$\frac{d\nabla_{\perp}^2 \phi}{dt} + \frac{g}{n} \frac{\partial n}{\partial y} = v_{\perp} \nabla_{\perp}^4 \phi + \left\langle \frac{1}{nL_{\parallel}} \nabla_{\parallel} J_{\parallel} \right\rangle_{\parallel}, \quad (1b)$$

where n represents the normalized electron density, ϕ is the normalized electric potential, g is normalized effective gravity (that is, drive from unfavorable magnetic curvature), S_n is the plasma source term, and D_{\perp} and v_{\perp} are the normalized particle and vorticity diffusion coefficients. We use the standard Bohm normalization as previously used and discussed in Refs. 67–80. In addition we have the advective derivative $d/dt = \partial/\partial t + \mathbf{V}_E \cdot \nabla_{\perp}$, where $\mathbf{V}_E = \hat{\mathbf{z}} \times \nabla \phi$ is the electric drift. The plasma source term is given by $S_n(x) = S_0 \exp(-(x - x_0)^2/\lambda_s^2)$, where S_0 is the maximum amplitude of the source, x_0 is the source location and λ_s is the e -folding length for the source.

Equations (1) are averaged along the magnetic field lines, with the contribution from the normalized parallel electron $J_{\parallel e}$ and total plasma currents J_{\parallel} in the sheath connected regime given

by

$$\left\langle \frac{1}{L_{\parallel}} \nabla_{\parallel} J_{\parallel e} \right\rangle_{\parallel} = -\sigma n \exp(\Lambda - \phi) + \chi(\widehat{\phi} - \widehat{n}), \quad (2a)$$

$$\left\langle \frac{1}{nL_{\parallel}} \nabla_{\parallel} J_{\parallel} \right\rangle_{\parallel} = \sigma [1 - \exp(\Lambda - \phi)] + \chi(\widehat{\phi} - \widehat{n}). \quad (2b)$$

Here Λ is the sheath potential, σ the normalized sheath dissipation and χ the normalized parallel plasma conductivity. Like in several previous investigations, these parameters are taken to be a function of the radial position in the boundary region.^{72–83} In particular, the sheath dissipation coefficient σ is finite in the SOL region ($x > x_{\text{SOL}}$) and vanishes in the edge ($x < x_{\text{SOL}}$), which corresponds to the region with closed magnetic flux surfaces,

$$\sigma(x) = \begin{cases} 0, & 0 \leq x < x_{\text{SOL}}, \\ \sigma_0, & x_{\text{SOL}} \leq x \leq L_x. \end{cases} \quad (3)$$

Similarly, the plasma conductivity χ is neglected in the SOL and is finite in the edge region,

$$\chi(x) = \begin{cases} \chi_0, & 0 \leq x < x_{\text{SOL}}, \\ 0, & x_{\text{SOL}} \leq x \leq L_x. \end{cases} \quad (4)$$

The simulation domain is sketched in Fig. 1, showing the location of the plasma source and the separation between the edge and SOL regions. Furthermore, the spatially fluctuating electron density \widehat{n} and plasma potential $\widehat{\phi}$ are defined as $\widehat{n} = n - \langle n \rangle_y$ and $\widehat{\phi} = \phi - \langle \phi \rangle_y$ where $\langle \cdot \rangle_y$ refers to the flux surface average. This leads to the final reduced electron continuity and electric drift vorticity equations,

$$\frac{dn}{dt} + g \left(\frac{\partial n}{\partial y} - n \frac{\partial \phi}{\partial y} \right) = S_n(x) + D_{\perp} \nabla_{\perp}^2 n - \sigma(x) n \exp(\Lambda - \phi) + \chi(x) (\widehat{\phi} - \widehat{n}), \quad (5a)$$

$$\frac{d\nabla_{\perp}^2 \phi}{dt} + \frac{g}{n} \frac{\partial n}{\partial y} = v_{\perp} \nabla_{\perp}^4 \phi + \sigma(x) [1 - \exp(\Lambda - \phi)] + \chi(x) (\widehat{\phi} - \widehat{n}). \quad (5b)$$

In the following we present results from numerical simulations of this model for two different cases. In the first case, the domain is split into two regions, effectively the edge and the SOL regions, by taking $x_{\text{SOL}} = 50$. In the second case, a pure SOL plasma is considered with $x_{\text{SOL}} = 0$, thus plasma conductivity χ is not present in the simulation domain.

The input parameters have been chosen to be similar to that used in previous publications based on this model.⁷⁹ For all runs presented here, the simulation domain lengths are chosen to

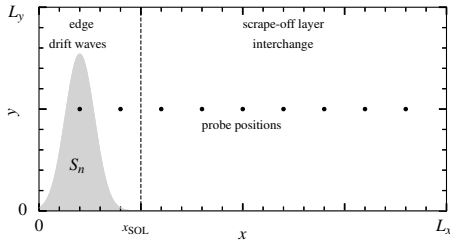


FIG. 1. Schematic illustration of the simulation domain for the $x_{\text{SOL}} = 50$ case. The position of the plasma source term (gray shaded) and the border between edge and SOL (dashed vertical line) are indicated.

be $L_x = 200$ and $L_y = 100$, with the border between the edge and the SOL at $x_{\text{SOL}} = 50$ for the two-region case. It has been verified that a change of the size of the simulation domain does not influence the fluctuation statistics. The simulation code is implemented in BOUT++⁸⁴ utilizing the STORM branch,⁸⁵ which uses a finite difference scheme in the x -direction and a spectral scheme in the y -direction. Time integration is performed with the PVODE solver.⁸⁶ We use a resolution of 512×256 grid points for all runs. We further take $D_{\perp} = \nu_{\perp} = 10^{-2}$, $g = 10^{-3}$, $\chi = 6 \times 10^{-4}$, $S_0 = 11/2000$, $\sigma_0 = 5 \times 10^{-4}$, $\Lambda = 0.5 \ln(2\pi m_i/m_e)$ with deuterium ions, $x_0 = 20$ and $\lambda_s = 10$. We apply periodic boundary conditions in the poloidal direction and zero gradient boundary conditions in the radial direction for both the electron density and vorticity fields. For the plasma potential we use zero gradient boundary conditions at the outer boundary and fixed boundary conditions $\phi(x=0) = 0$ at the inner boundary.

During the simulations, the plasma parameters at 9 different radial positions in the simulation domain are recorded with a sampling frequency of one in normalized time units. The location of these probes are presented in Fig. 1. This corresponds to single-point measurements in the experiments, and the simulation data will be analyzed in the same manner as has previously been done for experimental measurement data. The contour plots of the electron density in both simulation cases presented in Fig. 2 show several blob-like structures with the familiar mushroom-shape typical for strongly non-linear interchange motions.⁶⁵

Time series of the plasma parameters with a duration of 2×10^6 time units have been obtained under statistically stationary conditions, that is, excluding initial transients in the turbulence simulations. 10 simulation runs with this duration time are performed for the two-region model and 7 for the one region model. The fluctuation statistics to be presented in Sec. IV are based on these

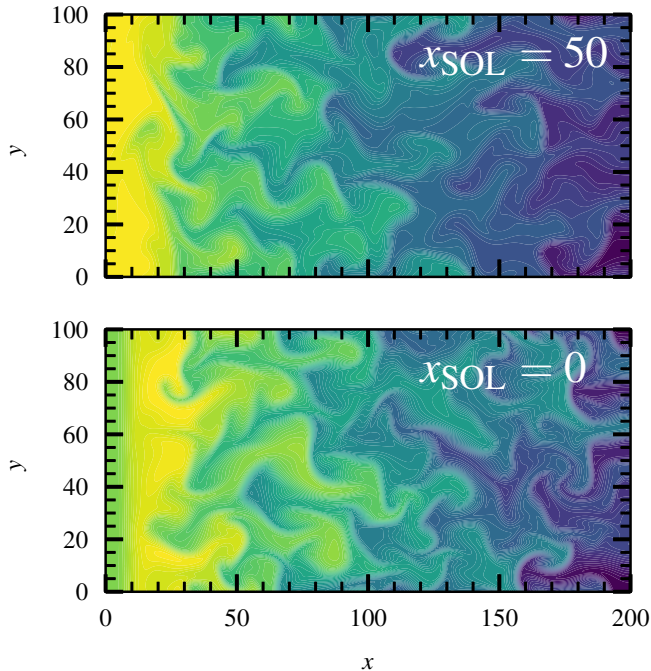


FIG. 2. Contour plots of $\log(n)$ in the turbulent state for the $x_{\text{SOL}} = 0$ and $x_{\text{SOL}} = 50$ cases showing the presence of mushroom-shaped blob-like structures in the SOL.

ensembles of simulation data. In the following analysis we will frequently consider plasma parameters normalized such as to have vanishing mean and unit standard deviation, for example. For the electron density we define

$$\tilde{n} = \frac{n - \langle n \rangle}{n_{\text{rms}}}, \quad (6)$$

where the angular brackets denote a time average and n_{rms} is the root mean square value calculated from the time series. A short part of the normalized electron density time series are presented in Fig. 3 for both simulation cases, showing frequent appearance of large-amplitude bursts due to the high density blob-like structures moving radially outwards. The radial variation of the lowest order moments of these fluctuations are presented and discussed in Sec. III.

In the following, the numerical simulation data will be compared to predictions of a stochastic model which describes the fluctuations as a super-position of uncorrelated pulses with fixed shape

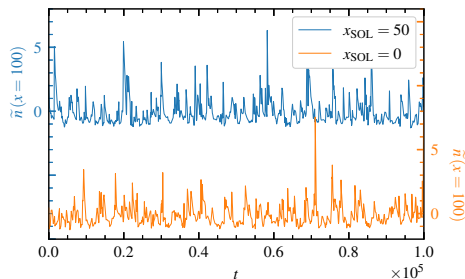


FIG. 3. A short part of the normalized electron density time series recorded at $x = 100$ for the $x_{\text{SOL}} = 0$ and $x_{\text{SOL}} = 50$ simulation cases.

and constant duration. This is written as^{43–53}

$$\Psi_K(t) = \sum_{k=1}^{K(T)} A_k \psi\left(\frac{t-t_k}{\tau_d}\right), \quad (7)$$

where ψ is the pulse function, τ_d is the pulse duration time, $K(T)$ is the number of pulses for a realization of duration T , and for the event labelled k the pulse amplitude is A_k and the arrival time t_k . The mean value of the random variable Ψ_K is $\langle\Psi\rangle = (\tau_d/\tau_w)\langle A\rangle$, where $\langle A\rangle$ is the average pulse amplitude and τ_w is the average pulse waiting time. We will assume pulses arriving according to a Poisson process, which implies independent and exponentially distributed waiting times and independent arrival times uniformly distributed on the realization. We further assume independently and exponentially distributed amplitudes, $P_A(A) = \exp(-A/\langle A\rangle)/\langle A\rangle$, and we will consider the case of a two-sided exponential pulse function,⁵⁰

$$\psi(\theta; \lambda) = \begin{cases} \exp(\theta/\lambda), & \theta < 0, \\ \exp(-\theta/(1-\lambda)), & \theta \geq 0, \end{cases} \quad (8)$$

where the pulse asymmetry parameter λ is restricted to the range $0 < \lambda < 1$. For $\lambda < 1/2$, the pulse rise time is faster than the decay time, while the pulse shape is symmetric in the case $\lambda = 1/2$. The frequency power spectral density for this process is just the spectrum of the pulse function,⁵⁰

$$\Omega_{\tilde{\Psi}}(\omega) = \frac{2\tau_d}{[1 + (1-\lambda)^2(\tau_d\omega)^2][1 + \lambda^2(\tau_d\omega)^2]}, \quad (9)$$

where ω is the angular frequency. Note that the power spectral density of $\tilde{\Psi}$ is independent of the amplitude distribution. From this it follows that the frequency power spectral density can be

used to estimate the pulse parameters τ_d and λ , which will be done in the following analysis of the numerical simulations.

The stationary probability density function (PDF) for the random variable Ψ_K can be shown to be a Gamma distribution,⁵³

$$\langle \Psi \rangle P_\Psi(\Psi) = \frac{\gamma}{\Gamma(\gamma)} \left(\frac{\gamma \Psi}{\langle \Psi \rangle} \right)^{\gamma-1} \exp \left(-\frac{\gamma \Psi}{\langle \Psi \rangle} \right), \quad (10)$$

with shape parameter $\gamma = \tau_d/\tau_w$, that is, the ratio of the pulse duration and the average pulse waiting time τ_w . This parameter describes the degree of pulse overlap, which determines the level of intermittency in the process. From the Gamma distribution it follows that the skewness moment is $S_\Psi = \langle (\Psi - \langle \Psi \rangle)^3 \rangle / \Psi_{\text{rms}}^3 = 2/\gamma^{1/2}$ and the flatness moment is $F_\Psi = \langle (\Psi - \langle \Psi \rangle)^4 \rangle / \Psi_{\text{rms}}^4 = 3 + 6/\gamma$. Accordingly, there is a parabolic relationship between these moments given by $F_\Psi = 3 + 3S_\Psi^2/2$. For strong pulse overlap and large γ , the probability density function approaches a normal distribution and the skewness S_Ψ and excess flatness $F_\Psi - 3$ moments vanish.

III. PROFILES AND DISTRIBUTIONS

The time-averaged electron density profiles in the turbulence simulations are presented in Fig. 4. Since the $x_{\text{SOL}} = 50$ case does not include any sheath dissipation in the edge region, the average density is higher here than for the $x_{\text{SOL}} = 0$ case. Throughout the entire SOL region, we observe that the electron density decreases exponentially with a radially constant scale length of 35.5. This is to be compared with the equilibrium SOL profile scale length in the absence of turbulence given by $(D_\perp/\sigma_0) = \sqrt{20}$ for the simulation parameters used here. Interestingly, both the scale length and the absolute density are very similar for the two simulation cases investigated. We further show the relative fluctuation level at different radial positions for both cases in Fig. 5. The normalized fluctuation level is very high, increases radially outwards and is roughly similar for the two simulation cases.

The radial variation of the skewness and flatness moments of the electron density fluctuations are presented in Figs. 6 and 7, respectively. From these figures it is clear that the intermittency of the fluctuations increases radially outwards in the SOL, qualitatively similar for the $x_{\text{SOL}} = 0$ and $x_{\text{SOL}} = 50$ cases. By plotting the flatness moment versus the skewness, presented in Fig. 8, it is seen that for both simulation cases there is a nearly parabolic relationship between these higher order moments. Such a parabolic relationship is predicted by the stochastic model describing

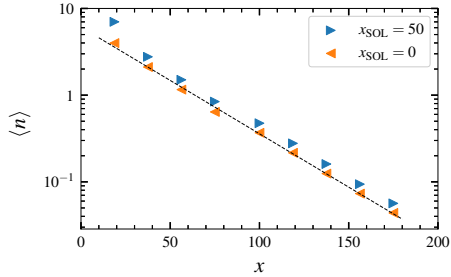


FIG. 4. Time-averaged electron density profile for the $x_{\text{SOL}} = 0$ and $x_{\text{SOL}} = 50$ cases. The broken line is the best fit of an exponential function with a scale length of 35.5.

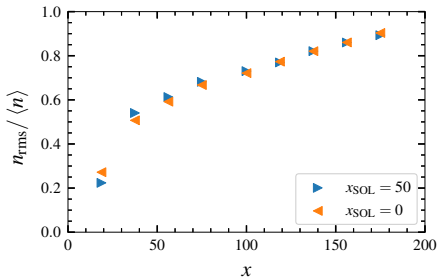


FIG. 5. The relative fluctuation level of the electron density at different positions in the SOL for the $x_{\text{SOL}} = 0$ and $x_{\text{SOL}} = 50$ cases.

the fluctuations as a super-position of uncorrelated pulses,^{43–46} which can be related to blob-like structures moving radially outwards in the SOL as seen in Fig. 2.

The PDFs for the normalized electron density fluctuations at different radial positions are presented in Figs. 9 and 10 for the $x_{\text{SOL}} = 0$ and $x_{\text{SOL}} = 50$ cases, respectively. The PDFs change from a narrow and nearly symmetric distribution in the edge/near SOL region to a distribution with an exponential tail for large fluctuation amplitudes in the far SOL. In Fig. 11 we further compare the PDFs of the electron density time series recorded in the far SOL at $x = 100$ for both simulation cases with a Gamma distribution with a shape parameter of 1.4. Such a Gamma distribution is predicted by the stochastic model describing the fluctuations as a super-position of uncorrelated exponential pulses. The Gamma distribution is clearly an excellent description of the PDF for the electron density fluctuations in the simulations. A similar change in the shape of the PDF radially

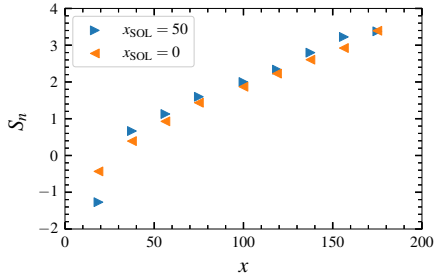


FIG. 6. Skewness of the electron density fluctuations at different radial positions for the $x_{\text{SOL}} = 0$ and $x_{\text{SOL}} = 50$ cases.

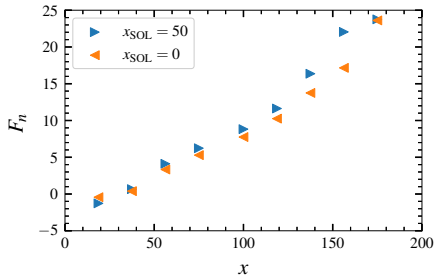


FIG. 7. Flatness of the electron density fluctuations at different radial positions for the $x_{\text{SOL}} = 0$ and $x_{\text{SOL}} = 50$ cases.

outwards in the SOL has also been reported from previous turbulence simulations.^{72–74}

IV. FLUCTUATION STATISTICS

In this section we present a detailed analysis of the electron density fluctuations recorded at $x = 100$. In order to reveal the typical shape of large-amplitude bursts in the time series, a conditional averaging method which allows for overlapping events is applied. This identifies a total of 3128 conditional events with peak amplitudes larger than 2.5 times the root mean square value above the mean for the $x_{\text{SOL}} = 50$ case and 1701 conditional events for the $x_{\text{SOL}} = 0$ case. The average burst structures are presented in Fig. 12 and shows an asymmetric shape with a fast rise and a slower decay. This is compared to an asymmetric, two-sided exponential function given by Eq. (8) with duration time $\tau_d = 300$ and asymmetry parameter $\lambda = 0.2$. The conditional burst shape is

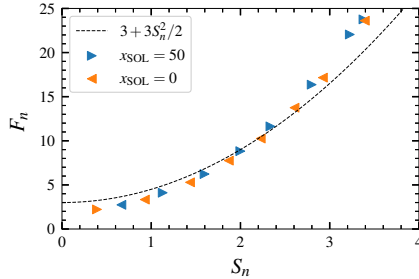


FIG. 8. Flatness plotted versus skewness for the electron density fluctuations in the SOL. The broken line shows the parabolic relationship $F_n = 3 + 3S_n^2/2$ for comparison.

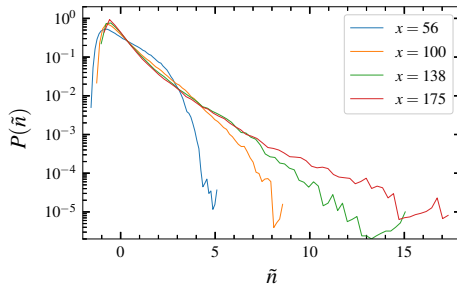


FIG. 9. Probability density functions of the normalized electron density recorded at different radial positions for the $x_{\text{SOL}} = 0$ case.

shown with semi-logarithmic axes in the inset in Fig. 12, showing that the decay of the conditional pulse shape is approximately exponential. However, the two-sided exponential function obviously fails to describe the smooth peak of the average burst shape in the simulations. As shown for short time lags in Fig. 12, this is better described using a skewed Lorentzian pulse as a fit function with duration 80 and skewness parameter 1 for the $x_{\text{SOL}} = 50$ case.^{87–90} The slightly elevated tails of the conditional burst shape is likely due to finite pulse overlap in the turbulence simulations.

The frequency power spectral density of the electron density fluctuations recorded at $x = 100$ is presented with semi-logarithmic axes in Fig. 13 for the $x_{\text{SOL}} = 50$ case. This shows an exponential decrease of power with frequency for high frequencies. This exponential fall off is attributed to the smooth peak of the large-amplitude bursts in the simulations. In agreement with the fit of a Lorentzian function to the peak of the conditionally averaged burst shape in Fig. 12, the power

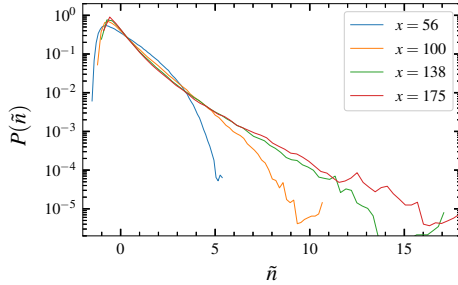


FIG. 10. Probability density functions of the normalized electron density recorded at different radial positions for the $x_{\text{SOL}} = 50$ case.

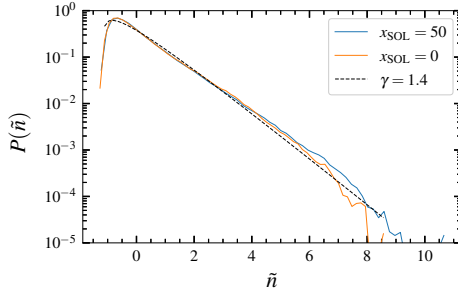


FIG. 11. Probability density functions of the normalized electron density recorded at $x = 100$ for both simulation cases compared to a Gamma distribution with shape parameter $\gamma = 1.4$ shown with the dashed black line.

spectral density decreases exponentially with a characteristic scale given by the duration of the Lorentzian-shaped peak.⁸⁹ The flattening of the power spectral density at low powers and high frequencies is due to the noise floor implied by round off errors in the computations.⁴⁹

The frequency power spectral density due to a super-position of uncorrelated exponential pulses is clearly not a good description of the simulation data for high frequencies. However, presenting the power spectrum with double-logarithmic axes shows that the spectrum given by Eq. (9) gives excellent agreement for high powers and low frequencies. This is clearly shown in Fig. 14 for the case $x_{\text{SOL}} = 50$. The exponential decay of the power at high frequencies is clearly due to the smooth peak of the large-amplitude bursts in the time series. This is consistent with the

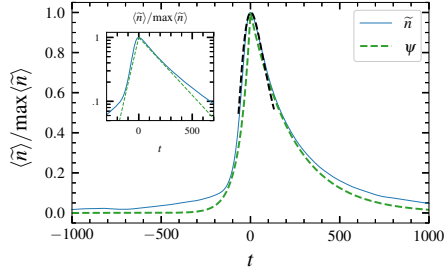


FIG. 12. Conditionally averaged burst shape at $x = 100$ of the $x_{\text{SOL}} = 50$ case (full blue line) compared to a two-sided exponential pulse (dashed green line), as well as a skewed Lorentzian pulse for short time lags (dashed black line). The conditional average is normalized by its peak amplitude.

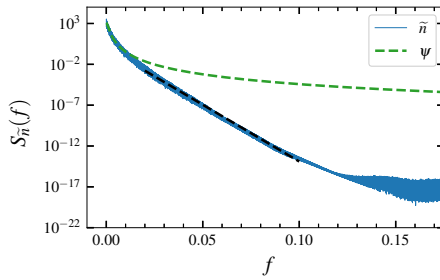


FIG. 13. Frequency power spectral density for the electron density fluctuations recorded at $x = 100$ for the $x_{\text{SOL}} = 50$ case (full line). This is compared to the predictions of a stochastic model describing the fluctuations as a super-position of uncorrelated, two-sided exponential pulses (dashed green line), as well as an exponential function for the high frequency part (dashed black line).

conditionally averaged burst shape presented in Fig. 12. Similar results for conditional averaging and frequency power spectra are found for the case $x_{\text{SOL}} = 0$ but with slightly different pulse parameters.

The conditionally averaged burst shape is presented in Fig. 15 for different radial positions in the SOL for the $x_{\text{SOL}} = 50$ case. Here it is seen that the burst shape in the far SOL region is the same for all radial positions, despite the fact that the relative fluctuation amplitude increases radially outwards. Accordingly, as predicted by the stochastic model, the frequency power spectral density has the same shape for all these different radial positions, as is shown in Figs. 16 and 17

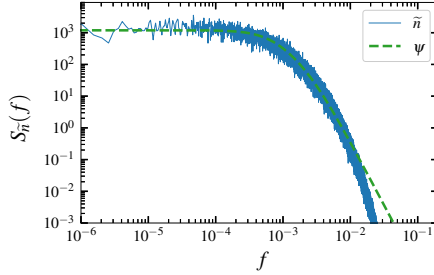


FIG. 14. Frequency power spectral density of the electron density fluctuations recorded at $x = 100$ for the $x_{\text{SOL}} = 50$ case (full blue line). This is compared to the predictions of a stochastic model describing the fluctuations as a super-position of uncorrelated, two-sided exponential pulses with duration time $\tau_d = 300$ and asymmetry parameter $\lambda = 0.2$ (dashed green line).

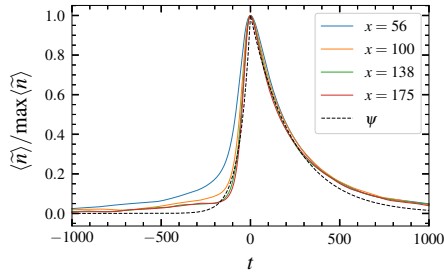


FIG. 15. Conditionally averaged burst shapes at different radial positions for the $x_{\text{SOL}} = 50$ case. The conditional averages are normalized by their peak amplitude.

for both the one- and two-region cases. The spectra are well described by that of a two-sided exponential pulse function, shown by the dashed black line in the figures.

Restricting the peak amplitude of conditional events in the electron density to be within a range of 2–4, 4–6 and 6–8 times the rms value, the appropriately scaled conditional burst shapes are presented in Fig. 18. This reveals that the average burst shape and duration do not depend on the burst amplitude and is again well described by a two-sided exponential function except for the smooth peak. This supports the assumption of fixed pulse duration in the stochastic model describing the fluctuations as a super-positions of pulses.

From the conditional averaging we further obtain the peak amplitudes of conditional events and

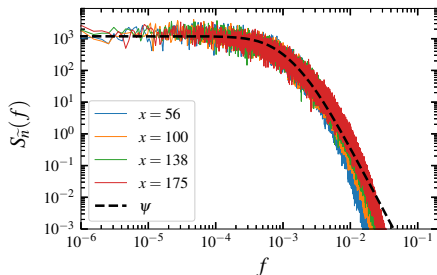


FIG. 16. Frequency power spectral densities of the electron density fluctuation recorded at different radial positions for the $x_{\text{SOL}} = 50$ model. The dashed line shows the spectrum due to a super-position of uncorrelated, two-sided exponential pulses with duration time τ_d .

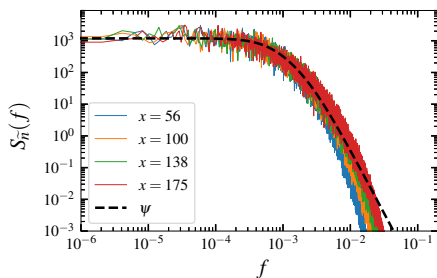


FIG. 17. Frequency power spectral densities of the electron density fluctuation recorded at different radial positions for the $x_{\text{SOL}} = 0$ model. The dashed line shows the spectrum due to a super-position of uncorrelated two-sided exponential pulses.

the waiting times between them. The PDFs of these are presented in Figs. 19 and 20, respectively. The distributions are similar for both simulation cases and are clearly well described by an exponential distribution as shown by the dashed black line in the plots. This is in agreement with the assumptions for the stochastic model presented in Sec. II. In particular, the exponential waiting time distribution supports the hypothesis that the events are uncorrelated and arrive according to a Poisson process.

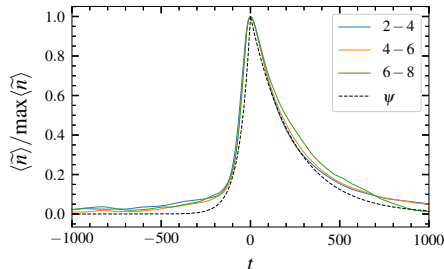


FIG. 18. Conditionally averaged burst shape at $x = 100$ of the $x_{\text{SOL}} = 50$ case for different conditional amplitude threshold intervals. The conditional averages are normalized by their peak amplitudes.

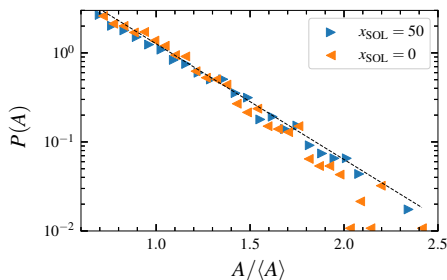


FIG. 19. Probability density functions of conditional burst amplitudes of the electron density time series recorded at $x = 100$.

V. DISCUSSION AND CONCLUSIONS

The abundant experimental evidence for universal statistical properties of fluctuations in the SOL of magnetically confined fusion plasmas sets high requirements for validation of turbulence simulation codes for the boundary region.^{54–56} In this context, we have examined the statistical properties of the electron density fluctuations in the SOL by numerical simulations of plasma turbulence in the two-dimensional plane perpendicular to the magnetic field. Two model cases have been considered, one describing resistive drift waves in the edge region and another including only the interchange instability due to unfavorable magnetic field curvature. For both cases, mushroom-shaped blob-like structures move radially outwards, resulting in large-amplitude fluctuations and high average particle densities in the SOL. The numerical simulations show that the time-averaged radial profile decreases exponentially with radial distance into the SOL with the same characteris-

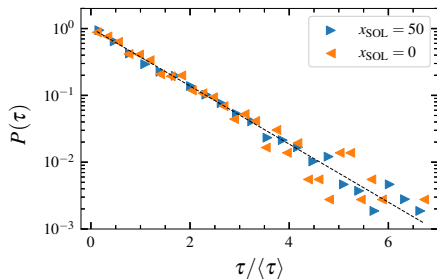


FIG. 20. Probability density functions of waiting times between consecutive large-amplitude burst in the electron density time series recorded at $x = 100$.

tic length scale for both simulation cases. Moreover, the fluctuation statistics in the SOL are the same for both cases. This is despite the different linear instability mechanisms driving the fluctuations in the edge/near SOL region in the two simulation cases. It appears that any drift-ordered instability mechanism will lead to formation of filament structures when coupled to a SOL region with unfavorable magnetic field curvature.

According to a stochastic model describing the profile as due to radial motion of filament structures, the profile scale length is given by the product of the radial filament velocity and the parallel transit time.^{46–48} This suggests that typical filament velocities are the same in both simulation cases. Future work will investigate the distribution of filament sizes and velocities by analysis of the velocity fluctuations and applying a blob tracking algorithm as described in Ref. 91.

The relative fluctuation level increases radially outwards, nearly reaching unity in the far SOL for the plasma parameters investigated here. Similarly, the skewness and flatness moments also increase into the SOL, and these higher order moments closely follow a quadratic dependence as predicted by the stochastic model describing the fluctuations as a super-position of uncorrelated pulses. The PDF of the electron density fluctuations changes from a nearly Gaussian distribution in the edge/near SOL region to a distribution with an exponential tail for large amplitudes in the far SOL. In the far SOL region, the PDFs are well described by a Gamma distribution with the shape parameter given by the ratio of the pulse duration and average waiting time. The increase of this intermittency parameter with radial distance into the SOL suggests that only the most coherent and large-amplitude blob structures are able to move through the entire SOL region before they disperse and break up due to secondary instabilities.

A conditional averaging analysis has revealed that the shape of large-amplitude bursts in single-point recordings in the far SOL is well described by a two-sided exponential pulse, as has previously been found in experimental measurements. However, the high resolution and smoothness of the solution from the numerical computations implies that the burst structure has a rounded peak as opposed to the break point in experimental measurements due to their much lower sampling rate and additional measurement noise. The smooth peak is well described by a skewed Lorentzian pulse function. This is further supported by the frequency power spectral density, which is well described by that of a two-sided exponential pulse for high powers and low frequencies. However, for low powers and high frequencies, the frequency power spectral density has an exponential decay which obviously can be attributed to the smooth, Lorentzian shaped peak of large-amplitude fluctuations in the numerical simulations. In experimental measurements, this exponential tail in the spectrum may readily be masked by low sampling rates, limiting the highest frequencies resolved, or by additive measurement noise, limiting the lowest power resolved.^{49,50}

In summary, it is here demonstrated that a simple but self-consistent model for turbulent fluctuations in the scrape-off layer reveals the same statistical properties of large-amplitude events as found in the experiments. This includes exponentially distributed pulse amplitudes and waiting times, the latter supporting the assumption of Poisson events.^{28–33,36–40} The simulation data also agree with predictions of the stochastic model, namely an exponential average profile, Gamma distributed fluctuation amplitudes and a frequency power spectral density determined by the average shape of large-amplitude bursts. It is concluded that the filtered Poisson process, describing the fluctuations in single-point recordings as a super-position of uncorrelated pulses with fixed duration, is an excellent description of the SOL plasma fluctuations in the turbulence simulations investigated here.^{43–53}

The simple turbulence model used in this study does not include finite ion temperature effects, X-point physics, parallel collisional conductivity in the scrape-off layer, or any effect of interactions with neutral particles. Numerous SOL turbulence models and codes are now being extended to include these features.^{92–100} The statistical framework with super-position of filaments can be used for analysis and interpretation of simulation results in these more advanced models, similar to what has been done here and previously for experimental measurements. As such, this work sets a new standard for validation of turbulence simulation codes.^{54–56}

ACKNOWLEDGEMENTS

This work was supported by the UiT Aurora Centre Program, UiT The Arctic University of Norway (2020). AT was supported by a Tromsø Science Foundation Starting Grant under grant number 19_SG_AT. GD acknowledges the generous hospitality of the Culham Centre for Fusion Energy (CCFE) where parts of this work were conducted. Two supercomputers provided by the Norwegian Metacenter for Computational Science (NOTUR) were used for the computational work, the Fram and Stallo clusters at the University of Tromsø under project nn9348k. The MARCONI supercomputer was used for parts of the computational work under the Project No. FUA34_SOLBOUT4. The storm2d project has been used as a template for the presented physical models. This work was funded in part by the RCUK Energy Programme (Grant number EP/T012250/1) and the EPSRC Centre for Doctoral Training in the Science and Technology of Fusion Energy (Grant number EP/L01663X/1), as well as an iCASE award from CCFE.

DATA AVAILABILITY

The data that support the findings of this study are available from the corresponding author upon reasonable request.

REFERENCES

- ¹R. A. Pitts, J. P. Coad, D. P. Coster, G. Federici, W. Fundamenski, J. Horacek, K. Krieger, A. Kukushkin, J. Likonen, G. F. Matthews, M. Rubel, J. D. Strachan, and JET-EFDA contributors, “Material erosion and migration in tokamaks,” *Plasma Physics and Controlled Fusion* **47**, B303 (2005).
- ²B. Lipschultz, X. Bonnin, G. Counsell, A. Kallenbach, A. Kukushkin, K. Krieger, A. Leonard, A. Loarte, R. Neu, R. Pitts, T. Rognlien, J. Roth, C. Skinner, J. Terry, E. Tsitrone, D. Whyte, S. Zweben, N. Asakura, D. Coster, R. Doerner, R. Dux, G. Federici, M. Fenstermacher, W. Fundamenski, P. Ghendrih, A. Herrmann, J. Hu, S. Krasheninnikov, G. Kirnev, A. Kreter, V. Kurnaev, B. LaBombard, S. Lisgo, T. Nakano, N. Ohno, H. Pacher, J. Paley, Y. Pan, G. Pautasso, V. Philipps, V. Rohde, D. Rudakov, P. Stangeby, S. Takamura, T. Tanabe, Y. Yang, and S. Zhu, “Plasma–surface interaction, scrape-off layer and divertor physics: implications for ITER,” *Nuclear Fusion* **47**, 1189 (2007).

- ³A. Loarte, B. Lipschultz, A. Kukushkin, G. Matthews, P. Stangeby, N. Asakura, G. Counsell, G. Federici, A. Kallenbach, K. Krieger, A. Mahdavi, V. Philipps, D. Reiter, J. Roth, J. Strachan, D. Whyte, R. Doerner, T. Eich, W. Fundamenski, A. Herrmann, M. Fenstermacher, P. Ghendrih, M. Groth, A. Kirschner, S. Konoshima, B. LaBombard, P. Lang, A. Leonard, P. Monier-Garbet, R. Neu, H. Pacher, B. Pegourie, R. Pitts, S. Takamura, J. Terry, E. Tsitrone, and the ITPA Scrape-off Layer and Divertor Physics Topical Group, “Chapter 4: Power and particle control,” *Nuclear Fusion* **47**, S203 (2007).
- ⁴S. Wiesen, D. Reiter, V. Kotov, M. Baelmans, W. Dekeyser, A. S. Kukushkin, S. W. Lisgo, R. A. Pitts, V. Rozhansky, G. Saibene, I. Veselova, and S. Voskoboynikov, “The new SOLPS-ITER code package,” *Journal of Nuclear Materials* **463**, 480 (2015).
- ⁵X. Bonnin, W. Dekeyser, R. Pitts, D. Coster, S. Voskoboynikov, and S. Wiesen, “Presentation of the new SOLPS-ITER code package for tokamak plasma edge modelling,” *Plasma and Fusion Research* **11**, 1403102 (2016).
- ⁶D. A. D’Ippolito, J. R. Myra, S. I. Krasheninnikov, G. Q. Yu, and A. Y. Pigarov, “Blob transport in the tokamak scrape-off-layer,” *Contributions to Plasma Physics* **44**, 205 (2004).
- ⁷S. I. Krasheninnikov, D. A. D’Ippolito, and J. R. Myra, “Recent theoretical progress in understanding coherent structures in edge and SOL turbulence,” *Journal of Plasma Physics* **74**, 679 (2008).
- ⁸O. E. Garcia, “Blob transport in the plasma edge: a review,” *Plasma and Fusion Research* **4**, 019 (2009).
- ⁹D. A. D’Ippolito, J. R. Myra, and S. J. Zweben, “Convective transport by intermittent blob-filaments: Comparison of theory and experiment,” *Physics of Plasmas* **18**, 060501 (2011).
- ¹⁰N. Asakura, Y. Koide, K. Itami, N. Hosogan, K. Shimizu, S. Tsuji-Iio, S. Sakurai, and A. Sakasai, “SOL plasma profiles under radiative and detached divertor conditions in JT-60U,” *Journal of Nuclear Materials* **241-243**, 559 (1997).
- ¹¹B. LaBombard, R. L. Boivin, M. Greenwald, J. Hughes, B. Lipschultz, D. Mossessian, C. S. Pitcher, J. L. Terry, S. J. Zweben, and Alcator Group, “Particle transport in the scrape-off layer and its relationship to discharge density limit in Alcator C-Mod,” *Physics of Plasmas* **8**, 2107 (2001).
- ¹²B. Lipschultz, B. LaBombard, C. S. Pitcher, and R. Boivin, “Investigation of the origin of neutrals in the main chamber of Alcator C-Mod,” *Plasma Physics and Controlled Fusion* **44**, 733 (2002).

- ¹³O. E. Garcia, J. Horacek, R. A. Pitts, A. H. Nielsen, W. Fundamenski, J. P. Graves, V. Naulin, and J. J. Rasmussen, “Interchange turbulence in the TCV scrape-off layer,” *Plasma Physics and Controlled Fusion* **48**, L1 (2005).
- ¹⁴D. L. Rudakov, J. A. Boedo, R. A. Moyer, P. C. Stangeby, J. G. Watkins, D. G. Whyte, L. Zeng, N. H. Brooks, R. P. Doerner, T. E. Evans, M. E. Fenstermacher, M. Groth, E. M. Hollmann, S. I. Krasheninnikov, C. J. Lasnier, A. W. Leonard, M. A. Mahdavi, G. R. McKee, A. G. McLean, A. Y. Pigarov, W. R. Wampler, G. Wang, W. P. West, and C. P. C. Wong, “Far SOL transport and main wall plasma interaction in DIII-D,” *Nuclear Fusion* **45**, 1589 (2005).
- ¹⁵B. LaBombard, J. W. Hughes, D. Mossessian, M. Greenwald, B. Lipschultz, J. L. Terry, and the Alcator C-Mod Team, “Evidence for electromagnetic fluid drift turbulence controlling the edge plasma state in the Alcator C-Mod tokamak,” *Nuclear Fusion* **45**, 1658 (2005).
- ¹⁶O. E. Garcia, R. A. Pitts, J. Horacek, A. H. Nielsen, W. Fundamenski, V. Naulin, and J. J. Rasmussen, “Turbulent transport in the TCV SOL,” *Journal of Nuclear Materials* **363–365**, 575 (2007).
- ¹⁷O. E. Garcia, J. Horacek, R. A. Pitts, A. H. Nielsen, W. Fundamenski, V. Naulin, and J. J. Rasmussen, “Fluctuations and transport in the TCV scrape-off layer,” *Nuclear Fusion* **47**, 667 (2007).
- ¹⁸O. E. Garcia, R. A. Pitts, J. Horacek, J. Madsen, V. Naulin, A. H. Nielsen, and J. J. Rasmussen, “Collisionality dependent transport in TCV SOL plasmas,” *Plasma Physics and Controlled Fusion* **49**, B47 (2007).
- ¹⁹D. Carralero, G. Birkenmeier, H. W. Müller, P. Manz, P. deMarne, S. H. Müller, F. Reimold, U. Stroth, M. Wischmeier, E. Wolfrum, and The ASDEX Upgrade Team, “An experimental investigation of the high density transition of the scrape-off layer transport in ASDEX Upgrade,” *Nuclear Fusion* **54**, 123005 (2014).
- ²⁰D. Carralero, H. W. Müller, M. Groth, M. Komm, J. Adamek, G. Birkenmeier, M. Brix, F. Janky, P. Hacek, S. Marsen, F. Reimold, C. Silva, U. Stroth, M. Wischmeier, E. Wolfrum, ASDEX Upgrade Team, COMPASS Team, and JET-EFDA Contributors, “Implications of high density operation on sol transport: A multimachine investigation,” *Journal of Nuclear Materials* **463**, 123 (2015).
- ²¹F. Militello, L. Garzotti, J. Harrison, J. T. Omotani, R. Scannell, S. Allan, A. Kirk, I. Lupelli, A. J. Thornton, and the MAST team, “Characterisation of the L-mode scrape off layer in MAST: decay lengths,” *Nuclear Fusion* **56**, 016006 (2016).

- ²²N. Vianello, C. Tsui, C. Theiler, S. Allan, J. Boedo, B. Labit, H. Reimerdes, K. Verhaegh, W. A. J. Vijvers, N. Walkden, S. Costea, J. Kovacic, C. Ionita, V. Naulin, A. H. Nielsen, J. J. Rasmussen, B. Schneider, R. Schrittwieser, M. Spolaore, D. Carralero, J. Madsen, B. Lipschultz, F. Militello, The TCV Team, and The EUROfusion MST1 Team, “Modification of SOL profiles and fluctuations with line-average density and divertor flux expansion in TCV,” *Nuclear Fusion* **57**, 116014 (2017).
- ²³N. Vianello, D. Carralero, C. K. Tsui, V. Naulin, M. Agostini, I. Cziegler, B. Labit, C. Theiler, E. Wolfrum, D. Aguiam, S. Allan, M. Bernert, J. Boedo, S. Costea, H. De Oliveira, O. Fevrier, J. Galdon-Quiroga, G. Grenfell, A. Hakola, C. Ionita, H. Isliker, A. Karpushov, J. Kovacic, B. Lipschultz, R. Maurizio, K. McClements, F. Militello, A. H. Nielsen, J. Olsen, J. J. Rasmussen, T. Ravensbergen, H. Reimerdes, B. Schneider, R. Schrittwieser, E. Seliunin, M. Spolaore, K. Verhaegh, J. Vicente, N. Walkden, W. Zhang, the ASDEX Upgrade Team, the TCV Team, and the EUROfusion MST1 Team, “Scrape-off layer transport and filament characteristics in high-density tokamak regimes,” *Nuclear Fusion* **60**, 016001 (2020).
- ²⁴P. C. Liewer, “Measurements of microturbulence in tokamaks and comparisons with theories of turbulence and anomalous transport,” *Nuclear Fusion* **25**, 543 (1985).
- ²⁵M. Endler, “Turbulent SOL transport in stellarators and tokamaks,” *Journal of Nuclear Materials* **266-269**, 84 (1999).
- ²⁶B. A. Carreras, “Plasma edge cross-field transport: experiment and theory,” *Journal of Nuclear Materials* **337**, 315 (2005).
- ²⁷S. J. Zweben, J. A. Boedo, O. Grulke, C. Hidalgo, B. LaBombard, R. J. Maqueda, P. Scarin, and J. L. Terry, “Edge turbulence measurements in toroidal fusion devices,” *Plasma Physics and Controlled Fusion* **49**, S1 (2007).
- ²⁸O. E. Garcia, I. Cziegler, R. Kube, B. LaBombard, and J. L. Terry, “Burst statistics in Alcator C-Mod SOL turbulence,” *Journal of Nuclear Materials* **438**, S180 (2013).
- ²⁹O. E. Garcia, S. M. Fritzner, R. Kube, I. Cziegler, B. LaBombard, and J. L. Terry, “Intermittent fluctuations in the Alcator C-Mod scrape-off layer,” *Physics of Plasmas* **20**, 055901 (2013).
- ³⁰O. E. Garcia, J. Horacek, and R. A. Pitts, “Intermittent fluctuations in the TCV scrape-off layer,” *Nuclear Fusion* **55**, 062002 (2015).
- ³¹A. Theodorsen, O. E. Garcia, J. Horacek, R. Kube, and R. A. Pitts, “Scrape-off layer turbulence in TCV: Evidence in support of stochastic modelling,” *Plasma Physics and Controlled Fusion* **58**, 044006 (2016).

- ³²O. E. Garcia, R. Kube, A. Theodorsen, J.-G. Bak, S.-H. Hong, H.-S. Kim, R. A. Pitts, and KSTAR Team, “SOL width and intermittent fluctuations in KSTAR,” *Nuclear Materials and Energy* **12**, 36 (2017).
- ³³A. Theodorsen, O. E. Garcia, R. Kube, B. LaBombard, and J. L. Terry, “Relationship between frequency power spectra and intermittent, large-amplitude bursts in the Alcator C-Mod scrape-off layer,” *Nuclear Fusion* **57**, 114004 (2017).
- ³⁴N. R. Walkden, A. Wynn, F. Militello, B. Lipschultz, G. Matthews, C. Guillemaut, J. Harrison, D. Moulton, and JET Contributors, “Statistical analysis of the ion flux to the JET outer wall,” *Nuclear Fusion* **57**, 036016 (2017).
- ³⁵N. R. Walkden, A. Wynn, F. Militello, B. Lipschultz, G. Matthews, C. Guillemaut, J. Harrison, D. Moulton, and J. Contributors, “Interpretation of scrape-off layer profile evolution and first-wall ion flux statistics on JET using a stochastic framework based on filamentary motion,” *Plasma Physics and Controlled Fusion* **59**, 085009 (2017).
- ³⁶R. Kube, O. E. Garcia, A. Theodorsen, D. Brunner, A. Q. Kuang, B. LaBombard, and J. L. Terry, “Intermittent electron density and temperature fluctuations and associated fluxes in the Alcator C-Mod scrape-off layer,” *Plasma Physics and Controlled Fusion* **60**, 065002 (2018).
- ³⁷O. E. Garcia, R. Kube, A. Theodorsen, B. LaBombard, and J. L. Terry, “Intermittent fluctuations in the Alcator C-Mod scrape-off layer for ohmic and high confinement mode plasmas,” *Physics of Plasmas* **25**, 056103 (2018).
- ³⁸A. Theodorsen, O. E. Garcia, R. Kube, B. LaBombard, and J. L. Terry, “Universality of Poisson-driven plasma fluctuations in the Alcator C-Mod scrape-off layer,” *Physics of Plasmas* **25**, 122309 (2018).
- ³⁹A. Bencze, M. Berta, A. Buzás, P. Hacek, J. Krbec, M. Szutyányi, and the COMPASS Team, “Characterization of edge and scrape-off layer fluctuations using the fast Li-BES system on compass,” *Plasma Physics and Controlled Fusion* **61**, 085014 (2019).
- ⁴⁰R. Kube, O. E. Garcia, A. Theodorsen, A. Q. Kuang, B. LaBombard, J. L. Terry, and D. Brunner, “Statistical properties of the plasma fluctuations and turbulent cross-field fluxes in the outboard mid-plane scrape-off layer of Alcator C-Mod,” *Nuclear Materials and Energy* **18**, 193 (2019).
- ⁴¹A. Kuang, B. LaBombard, D. Brunner, O. E. Garcia, R. Kube, and A. Theodorsen, “Plasma fluctuations in the scrape-off layer and at the divertor target in Alcator C-Mod and their relationship to divertor collisionality and density shoulder formation,” *Nuclear Materials and Energy*

19, 295 (2019).

- ⁴²R. Kube, A. Theodorsen, O. E. Garcia, D. Brunner, B. LaBombard, and J. L. Terry, “Comparison between mirror Langmuir probe and gas-puff imaging measurements of intermittent fluctuations in the Alcator C-Mod scrape-off layer,” *Journal of Plasma Physics* **86**, 905860519 (2020).
- ⁴³O. E. Garcia, “Stochastic modeling of intermittent scrape-off layer plasma fluctuations,” *Physical Review Letters* **108**, 265001 (2012).
- ⁴⁴R. Kube and O. E. Garcia, “Convergence of statistical moments of particle density time series in scrape-off layer plasmas,” *Physics of Plasmas* **22**, 012502 (2015).
- ⁴⁵A. Theodorsen and O. E. Garcia, “Level crossings, excess times, and transient plasma-wall interactions in fusion plasmas,” *Physics of Plasmas* **23**, 040702 (2016).
- ⁴⁶O. E. Garcia, R. Kube, A. Theodorsen, and H. L. Pécseli, “Stochastic modelling of intermittent fluctuations in the scrape-off layer: Correlations, distributions, level crossings, and moment estimation,” *Physics of Plasmas* **23**, 052308 (2016).
- ⁴⁷F. Militello and J. T. Omotani, “Scrape off layer profiles interpreted with filament dynamics,” *Nuclear Fusion* **56**, 104004 (2016).
- ⁴⁸F. Militello and J. T. Omotani, “On the relation between non-exponential scrape off layer profiles and the dynamics of filaments,” *Nuclear Fusion* **58**, 125004 (2016).
- ⁴⁹A. Theodorsen and O. E. Garcia, “Statistical properties of a filtered Poisson process with additive random noise: distributions, correlations and moment estimation,” *Physica Scripta* **92**, 054002 (2017).
- ⁵⁰O. E. Garcia and A. Theodorsen, “Auto-correlation function and frequency spectrum due to a super-position of uncorrelated exponential pulses,” *Physics of Plasmas* **24**, 032309 (2017).
- ⁵¹A. Theodorsen and O. E. Garcia, “Level crossings and excess times due to a superposition of uncorrelated exponential pulses,” *Physical Review E* **97**, 012110 (2018).
- ⁵²F. Militello, T. Farley, K. Mukhi, N. Walkden, and J. T. Omotani, “A two-dimensional statistical framework connecting thermodynamic profiles with filaments in the scrape off layer and application to experiments,” *Physics of Plasmas* **25**, 056112 (2018).
- ⁵³A. Theodorsen and O. E. Garcia, “Probability distribution functions for intermittent scrape-off layer plasma fluctuations,” *Plasma Physics and Controlled Fusion* **60**, 034006 (2018).
- ⁵⁴P. W. Terry, M. Greenwald, J.-N. Leboeuf, G. R. McKee, D. R. Mikkelsen, W. M. Nevins, D. E. Newman, D. P. Stotler, Task Group on Verification and Validation, U.S. Burning Plasma Orga-

- nization, and U.S. Transport Task Force, “Validation in fusion research: Towards guidelines and best practices,” *Physics of Plasmas* **15**, 062503 (2008).
- ⁵⁵M. Greenwald, “Verification and validation for magnetic fusion,” *Plasma Physics and Controlled Fusion* **17**, 058101 (2010).
- ⁵⁶C. Holland, “Validation metrics for turbulent plasma transport,” *Physics of Plasmas* **23**, 060901 (2016).
- ⁵⁷G. Decristoforo, A. Theodorsen, and O. E. Garcia, “Intermittent fluctuations due to Lorentzian pulses in turbulent thermal convection,” *Physics of Fluids* **32**, 085102 (2020).
- ⁵⁸O. Pogutse, W. Kerner, V. Gribkov, S. Bazdenkov, and M. Osipenko, “The resistive interchange convection in the edge of tokamak plasmas,” *Plasma Physics and Controlled Fusion* **36**, 1963 (1994).
- ⁵⁹H. Sugama and W. Horton, “L-H confinement mode dynamics in three-dimensional state space,” *Plasma Physics and Controlled Fusion* **37**, 345 (1995).
- ⁶⁰P. Beyer and K. H. Spatschek, “Center manifold theory for the dynamics of the L–H-transition,” *Physics of Plasmas* **3**, 995 (1996).
- ⁶¹W. Horton, G. Hu, and G. Laval, “Turbulent transport in mixed states of convective cells and sheared flows,” *Physics of Plasmas* **3**, 2912 (1996).
- ⁶²M. Berning and K. H. Spatschek, “Bifurcations and transport barriers in the resistive-g paradigm,” *Physical Review E* **62**, 1162 (2000).
- ⁶³O. E. Garcia, N. H. Bian, J.-V. Paulsen, S. Benkadda, and K. Rypdal, “Confinement and bursty transport in a flux-driven convection model with sheared flows,” *Plasma Physics and Controlled Fusion* **45**, 919 (2003).
- ⁶⁴O. E. Garcia and N. H. Bian, “Bursting and large-scale intermittency in turbulent convection with differential rotation,” *Physical Review E* **68**, 047301 (2003).
- ⁶⁵O. E. Garcia, N. H. Bian, V. Naulin, A. H. Nielsen, and J. J. Rasmussen, “Two-dimensional convection and interchange motions in fluids and magnetized plasmas,” *Physica Scripta* **T122**, 104 (2003).
- ⁶⁶F. Wilczynski, D. W. Hughes, S. V. Loo, W. Arter, and F. Militello, “Stability of scrape-off layer plasma: A modified Rayleigh–Bénard problem,” *Physics of Plasmas* **26**, 022510 (2019).
- ⁶⁷S. Benkadda, X. Garbet, and A. Verma, “Interchange instability turbulence model in edge tokamak plasma,” *Contributions to Plasma Physics* **34**, 247 (1994).

- ⁶⁸O. E. Garcia, “Two-field transport models for magnetized plasmas,” *Journal of Plasma Physics* **65**, 81 (2001).
- ⁶⁹Y. Sarazin and P. Ghendrih, “Intermittent particle transport in two-dimensional edge turbulence,” *Physics of Plasmas* **5**, 4214 (1998).
- ⁷⁰P. Ghendrih, Y. Sarazin, G. Attuel, S. Benkadda, P. Beyer, G. Falchetto, C. Figarella, X. Garbet, V. Grandgirard, and M. Ottaviani, “Theoretical analysis of the influence of external biasing on long range turbulent transport in the scrape-off layer,” *Nuclear Fusion* **43**, 1013 (2003).
- ⁷¹Y. Sarazin, P. Ghendrih, G. Attuel, C. Clément, X. Garbet, V. Grandgirard, M. Ottaviani, S. Benkadda, P. Beyer, N. Bian, and C. Figarella, “Theoretical understanding of turbulent transport in the SOL,” *Journal of Nuclear Materials* **313**, 796 (2003).
- ⁷²O. E. Garcia, V. Naulin, A. H. Nielsen, and J. J. Rasmussen, “Computations of intermittent transport in scrape-off layer plasmas,” *Physical Review Letters* **92**, 165003 (2004).
- ⁷³O. E. Garcia, V. Naulin, A. H. Nielsen, and J. J. Rasmussen, “Turbulence and intermittent transport at the boundary of magnetized plasmas,” *Physics of Plasmas* **12**, 062309 (2005).
- ⁷⁴O. E. Garcia, V. Naulin, A. H. Nielsen, and J. J. Rasmussen, “Turbulence simulations of blob formation and radial propagation in toroidally magnetized plasmas,” *Physica Scripta* **T122**, 89 (2006).
- ⁷⁵J. R. Myra, D. A. Russell, and D. A. D’Ippolito, “Transport of perpendicular edge momentum by drift-interchange turbulence and blobs,” *Physics of Plasmas* **15**, 032304 (2008).
- ⁷⁶D. A. Russell, J. R. Myra, and D. A. D’Ippolito, “Saturation mechanisms for edge turbulence,” *Physics of Plasmas* **16**, 122304 (2009).
- ⁷⁷J. R. Myra, W. M. Davis, D. A. D’Ippolito, B. LaBombard, D. A. Russell, J. L. Terry, and S. J. Zweben, “Edge sheared flows and the dynamics of blob-filaments,” *Nuclear Fusion* **53**, 073013 (2013).
- ⁷⁸N. Bisai, A. Das, S. Deshpande, R. Jha, P. Kaw, A. Sen, and R. Singh, “Simulation of plasma transport by coherent structures in scrape-off-layer tokamak plasmas,” *Physics of Plasmas* **11**, 4018 (2004).
- ⁷⁹N. Bisai, A. Das, S. Deshpande, R. Jha, P. Kaw, A. Sen, and R. Singh, “Edge and scrape-off layer tokamak plasma turbulence simulation using two-field fluid model,” *Physics of Plasmas* **12**, 072520 (2005).
- ⁸⁰N. Bisai, A. Das, S. Deshpande, R. Jha, P. Kaw, A. Sen, and R. Singh, “Formation of a density blob and its dynamics in the edge and the scrape-off layer of a tokamak plasma,” *Physics of*

Plasmas **12**, 102515 (2005).

- ⁸¹A. H. Nielsen, G. S. Xu, J. Madsen, V. Naulin, J. J. Rasmussen, and B. N. Wan, “Simulation of transition dynamics to high confinement in fusion plasmas,” *Physics Letters A* **379**, 3097 (2015).
- ⁸²A. H. Nielsen, J. J. Rasmussen, J. Madsen, G. S. Xu, V. Naulin, J. M. B. Olsen, M. Løiten, S. K. Hansen, N. Yan, L. Tophøj, and B. N. Wan, “Numerical simulations of blobs with ion dynamics,” *Plasma Physics and Controlled Fusion* **59**, 025012 (2017).
- ⁸³J. Olsen, A. H. Nielsen, J. J. Rasmussen, J. Madsen, T. Eich, B. Sieglin, and V. Naulin, “Scrape-off layer power fall-off length from turbulence simulations of ASDEX Upgrade L-mode,” *Plasma Physics and Controlled Fusion* **60**, 085018 (2018).
- ⁸⁴B. Dudson, M. Umansky, X. Xu, P. Snyder, and H. Wilson, “BOU++: A framework for parallel plasma fluid simulations,” *Computer Physics Communications* **180**, 1467 (2009).
- ⁸⁵F. Militello, B. Dudson, L. Easy, A. Kirk, and P. Naylor, “On the interaction of scrape off layer filaments,” *Plasma Physics and Controlled Fusion* **59**, 125013 (2017).
- ⁸⁶G. D. Byrne and A. C. Hindmarsh, “PVODE, an ODE solver for parallel computers,” *The International Journal of High Performance Computing Applications* **13**, 354 (1999).
- ⁸⁷J. E. Maggs and G. J. Morales, “Generality of deterministic chaos, exponential spectra, and Lorentzian pulses in magnetically confined plasmas,” *Physical Review Letters* **107**, 185003 (2011).
- ⁸⁸O. E. Garcia and A. Theodorsen, “Power law spectra and intermittent fluctuations due to uncorrelated Lorentzian pulses,” *Physics of Plasmas* **24**, 020704 (2017).
- ⁸⁹O. E. Garcia and A. Theodorsen, “Skewed Lorentzian pulses and exponential frequency power spectra,” *Physics of Plasmas* **25**, 014503 (2018).
- ⁹⁰O. E. Garcia and A. Theodorsen, “Intermittent fluctuations due to uncorrelated Lorentzian pulses,” *Physics of Plasmas* **25**, 014506 (2018).
- ⁹¹G. Decristoforo, F. Militello, T. Nicholas, J. Omotani, C. Marsden, N. Walkden, and O. E. Garcia, “Blob interactions in 2D scrape-off layer simulations,” *Physics of Plasmas* **27**, 122301 (2020).
- ⁹²F. D. Halpern, P. Ricci, S. Jolliet, J. Loizu, J. Morales, A. Masetto, F. Musil, F. Riva, T. M. Tran, and C. Wersal, “The GBS code for tokamak scrape-off layer simulations,” *Journal of Computational Physics* **315**, 388 (2016).

- ⁹³P. Tamain, H. Bufferand, G. Ciraolo, C. Colin, D. Galassi, P. Ghendrih, and F. Schwander, “The TOKAM3X code for edge turbulence fluid simulations of tokamak plasmas in versatile magnetic geometries,” *Journal of Computational Physics* **321**, 606 (2016).
- ⁹⁴B. D. Dudson and J. Leddy, “Hermes: global plasma edge fluid turbulence simulations,” *Plasma Physics and Controlled Fusion* **59**, 054010 (2017).
- ⁹⁵M. Held, M. Wiesenberger, R. Kube, and A. Kendl, “Non-Oberbeck–Boussinesq zonal flow generation,” *Nuclear Fusion* **58**, 104001 (2018).
- ⁹⁶M. Wiesenberger, L. Einkemmer, M. Held, A. Gutierrez-Milla, X. Sáez, and R. Iakymchuk, “Reproducibility, accuracy and performance of the FELTOR code and library on parallel computer architectures,” *Computer Physics Communications* **238**, 145 (2019).
- ⁹⁷A. Stegmeir, A. Ross, T. Body, M. Francisquez, W. Zholobenko, D. Coster, F. Jenko, B. N. Rogers, and K. S. Kang, “Global turbulence simulations of the tokamak edge region with GRILLIX,” *Physics of Plasmas* **26**, 052517 (2019).
- ⁹⁸D. R. Zhang, Y. P. Chen, X. Q. Xu, and T. Y. Xia, “Self-consistent simulation of transport and turbulence in tokamak edge plasma by coupling SOLPS-ITER and BOUT++,” *Physics of Plasmas* **26**, 012508 (2019).
- ⁹⁹D. A. Russell, J. R. Myra, and D. P. Stotler, “A reduced model of neutral-plasma interactions in the edge and scrape-off-layer: Verification comparisons with kinetic Monte Carlo simulations,” *Physics of Plasmas* **26**, 022304 (2019).
- ¹⁰⁰M. Giacomini and P. Ricci, “Investigation of turbulent transport regimes in the tokamak edge by using two-fluid simulations,” *Journal of Plasma Physics* **86**, 905860502 (2020).

Paper IV: Blob interactions in 2D scrape- off layer simulations

G. Decristoforo, F. Militello, T. Nicholas, J. Omotani, C. Marsden, N. Walkden
and O. E. Garcia,
Physics of Plasmas **27**, 122301 (2020),
doi:10.1063/5.0021314

Blob interactions in 2D scrape-off layer simulations

Cite as: Phys. Plasmas 27, 122301 (2020); <https://doi.org/10.1063/5.0021314>

Submitted: 10 July 2020 . Accepted: 26 October 2020 . Published Online: 01 December 2020

 G. Decristoforo,  F. Militello,  T. Nicholas,  J. Omotani,  C. Marsden,  N. Walkden, and  O. E. Garcia



View Online



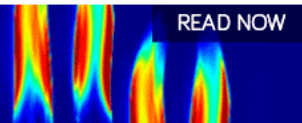
Export Citation



CrossMark

AIP Advances
Fluids and Plasmas Collection

READ NOW



Blob interactions in 2D scrape-off layer simulations

Cite as: Phys. Plasmas 27, 122301 (2020); doi: 10.1063/5.0021314

Submitted: 10 July 2020 · Accepted: 26 October 2020 ·

Published Online: 1 December 2020



View Online



Export Citation



CrossMark

G. Decristoforo,^{1,a)} F. Militello,² T. Nicholas,³ J. Omotani,² C. Marsden,⁴ N. Walkden,² and O. E. Garcia¹

AFFILIATIONS

¹Department of Physics and Technology, UiT The Arctic University of Norway, NO-9037 Tromsø, Norway

²CCFE, Culham Science Centre, Abingdon OX14 3DB, United Kingdom

³York Plasma Institute, Department of Physics, University of York, Heslington, York YO10 5DD, United Kingdom

⁴School of Physics and Astronomy, University of Birmingham, Edgbaston, Edgbaston Park Road, Birmingham B15 2TT, United Kingdom

^{a)}Author to whom correspondence should be addressed: gregor.decrstoforo@uit.no

ABSTRACT

Interaction of coherent structures known as blobs in the scrape-off layer of magnetically confined plasmas is investigated. Isolated and interacting seeded blobs, as well as full plasma turbulence, are studied by two-dimensional numerical simulations. The features of the blobs (position, size, amplitude) are determined with a blob tracking algorithm, which identifies them as coherent structures with amplitudes above a chosen particle density threshold, and their velocities are compared to a conventional center of mass approach. We find that the theoretical velocity-size scaling dependence for isolated blobs is correctly resolved by the blob tracking method. The benchmarked approach is then extended to a population of interacting plasma blobs with statistically distributed amplitudes, sizes, and initial positions for different levels of blob interaction. We observe a correlation between the level of blob interaction and the number of blobs deviating from size-velocity scaling laws of perfectly isolated blobs. This is found to be caused by the interaction of blobs with the electrostatic potential of one another, leading to higher average blob velocities. We introduce a model specific intermittency parameter, quantifying the degree of blob interaction. For interacting blobs, we estimate the deviation from the picture of perfectly isolated blobs as a function of the intermittency parameter. For full plasma turbulence simulations, we observe a strong correlation between the blob amplitudes, sizes, and velocities estimated by the blob tracking algorithm.

Published under license by AIP Publishing. <https://doi.org/10.1063/5.0021314>

I. INTRODUCTION

In tokamaks and other magnetically confined plasma experiments, particle transport in the plasma edge region is dominated by turbulence-driven coherent structures of high density and temperature called blobs or filaments. This can lead to enhanced erosion of the reactor walls and can contribute to the power loads to divertor targets.^{1–5} These structures have been observed in multiple plasma devices in all operation regimes using reciprocating or wall mounted Langmuir probes,^{6–12} fast visual cameras,^{3–5,13–16} and gas puff imaging.^{17–22}

In addition to experimental evidence, theoretical understanding of the underlying physical mechanism of blob propagation has been developed in the last 20 years.^{23–26} It is understood that the basic mechanism responsible for the radial transport of blobs arises due to grad-B and curvature drifts leading to a charge polarization in the plasma blob/filament. The resulting electric field gives rise to an $\mathbf{E} \times \mathbf{B}$ drift that propels the blob across the magnetic field. Since detailed physical models increase the analytical complexity significantly, the

scientific community relies on numerical simulations of isolated blobs and full turbulence simulations of the scrape-off layer. Numerical simulations in two dimensions^{27–36} and three dimensions^{37–45} have enhanced the understanding of the underlying mechanisms of blob and filament propagation in the scrape-off layer.

Most of these numerical simulations investigate idealized, isolated blobs modeled as positive amplitude and symmetrical Gaussian perturbations on a constant plasma background. This approach has provided an effective way of investigating the influence of specific physical effects, such as finite Larmor radius effects,⁴⁶ electromagnetic effects,⁴⁷ or parallel electron dynamics⁴⁸ on the blob velocity, coherence, and lifetime. Scaling laws describing the radial blob velocity dependence on its amplitudes and size^{29,30,34,35,49} have been developed, and different regimes determined by various physical parameters have been discovered.^{30,51}

Despite this progress, understanding how well these scaling laws describe blobs in fully turbulent scenarios where they interact with each other is non-trivial. Previous work has shown that single blobs in

close proximity do interact through the electric potential they generate.^{52,53} This analysis was performed on two spatially separated and seeded blobs on a constant plasma background and, therefore, does not address the complexity of a fully turbulent plasma environment. In our work, we expand the investigation by starting from isolated blob simulations and then extending our analysis to decreasingly intermittent systems, until we consider fully turbulent scrape-off layer plasma. The intermittency of such a system is a measure of the degree of blob overlap.^{54,55} To bridge these two extremes, we use a stochastic model of multiple randomly seeded blobs where blob amplitudes, sizes, initial positions, and the waiting times between consecutive blobs are randomly sampled from given distribution functions.

In order to track blobs in these intermittent and turbulent environments, we implement a tracking algorithm that provides specific blob parameters such as trajectory, velocity, size, and amplitude over the lifetime of individual blobs. Tracking algorithms using either simple threshold methods, defining every coherent structure above a chosen particle density threshold as a blob, or convolutional neural networks, have been presented and applied on two- and three-dimensional data.^{56–58} For our analysis, we choose the threshold method since it provides a simple and consistent definition for blobs in both the isolated and the fully turbulent cases. Since there are several ways of defining a blob, this has the advantage of being able to choose an exact and unbiased definition for blobs instead of using machine learning algorithms that require a test dataset. Note that our implementation of a blob tracking algorithm is only designed for numerical simulations where the time and spatial resolution can be chosen. Applying blob tracking techniques on experimental measurements with high speed imaging data using, for example, a watershed algorithm¹³ is complicated by the spatial and temporal resolution of the measurement techniques. The watershed algorithm is based on fitting two-dimensional Gaussians to local density maxima in order to extract the position, widths, and amplitudes of the fluctuations.

The structure of this publication is as follows: In Sec. II, we present the equations of the physical model that we use for our further analysis. In Sec. III, we present a detailed description of the implementation of the blob tracking algorithm and discuss all relevant parameters of this method. We apply this algorithm on isolated and seeded blob simulations in Sec. IV and compare the results to a conventional center of mass approach. In Sec. V, we extend this analysis to a model seeding multiple blobs randomly. We start with the case of identical amplitudes and starting positions for different levels of intermittency, extend this analysis to random initial positions, and finally to a model including random blob amplitudes. In all cases, we compare the results to the isolated blob simulations. In Sec. VI, we finally apply the blob tracking algorithm on scrape-off layer turbulence simulations and discuss the results in comparison to the previous approaches. A summary and discussion of our results are given in Sec. VII.

II. PHYSICAL MODEL

For our analysis, we choose a standard two-dimensional (2D), two-field fluid model derived from the Braginskii fluid equations.^{59–62} We assume for simplicity a quasi-neutral plasma, negligible electron inertia, isothermal electrons ($T_e = \text{constant}$), and cold ions ($T_i = 0$). Note that these assumptions for the electron and ion temperatures are taken for the sake of simplification, as experimental measurements of scrape-off layer plasmas often show high variations of T_e and

$T_i > T_e$.^{63–68} Nevertheless, this simplified model still captures the fundamental dynamics of the blobs and is therefore sufficient to study their interaction while keeping the number of free parameters of the model relatively low.

For our simulations, we use a simple slab geometry to model the plasma evolution in the two-dimensional plane perpendicular to the magnetic field, with x and y referring to the radial and the binormal/poloidal directions, respectively. The normalized electron particle continuity equation and vorticity equation are given by^{28,31,34,60–62}

$$\frac{dn}{dt} + g \left(\frac{\partial n}{\partial y} - n \frac{\partial \phi}{\partial y} \right) = D_{\perp} \nabla_{\perp}^2 n + F_n - \sigma(n - n_b) \exp(-\phi), \quad (1)$$

$$\frac{d\nabla_{\perp}^2 \phi}{dt} + \frac{g \partial n}{n \partial y} = \nu_{\perp} \nabla_{\perp}^4 \phi + \sigma[1 - \exp(-\phi)], \quad (2)$$

where n represents the electron plasma density and n_b the electron plasma density background. Moreover, ϕ is the electric potential, g is the effective gravity, i.e., interchange drive from magnetic curvature, F_n is the forcing or plasma source term, and D_{\perp} and ν_{\perp} are the collisional dissipative terms representing particle diffusivity and viscosity, respectively. The parameter σ describes the parallel loss rate of the system. The last term on the right hand side of both the particle continuity and electron drift vorticity equations results from modeling the parallel losses to the material surfaces. The forcing for the turbulence simulations is

$$F_n(x) = \frac{1}{w\sqrt{2\pi}} \exp\left(-\frac{1}{2} \frac{(x - \lambda)^2}{w^2}\right), \quad (3)$$

with w and λ providing the width and location of F_n . The source term represents the cross field transport from the core region, but its magnitude and shape chosen here are arbitrary, although convenient. For seeded blob simulations, F_n represents multiple blobs as

$$F_n(x, y, t) = \sum_{k=1}^K A_k \exp\left(-\frac{(x - x_k)^2 + (y - y_k)^2}{2\delta_{\perp k}^2}\right) \Delta(t - t_k), \quad (4)$$

where A_k represents the amplitudes, $\delta_{\perp k}$ the widths, x_k and y_k the initial positions, t_k the arrival time of the blobs, and Δ denotes the Dirac delta function.

In order to self-consistently describe order unity relative fluctuation levels, a term given by $\nabla \ln n \cdot d\nabla_{\perp}^2 \phi / dt$ should be added to the left hand side of Eq. (2). Moreover, the dependence on the electron density should be included in the collisional diffusion terms. However, this makes the numerical simulation code much more computer intensive and the simplified model given by Eqs. (1) and (2) has been used here. Further discussion on this topic, commonly referred to as the Boussinesq approximation, can be found in Ref. 36. Strictly, the presented model is derived to describe small density fluctuations and shows inconsistent blob velocity scaling for large amplitudes compared to a non-Boussinesq model. A discussion of this scaling correction is presented in Ref. 35. However, we do not expect this effect to have a significant influence on the qualitative results presented in this work.

The standard Bohm normalization is used for this model equivalent to that used in Refs. 41, 42, and 60–62 and is not discussed here for the sake of brevity. In addition, the advective derivative is given by $d/dt = \partial/\partial t + \mathbf{V}_E \cdot \nabla_{\perp}$, where $\mathbf{V}_E = -\nabla_{\perp} \phi \times \mathbf{B}/B^2$ is the $E \times B$

drift. We approximate \mathbf{B} to be constant for the $E \times B$ drift even though the effects of magnetic field curvature are considered in the effective gravity g . A discussion of this approximation can also be found in Ref. 35.

We apply periodic boundary conditions in the y -direction and zero gradient boundary conditions in the radial direction for both the density and vorticity fields. For the plasma potential, we choose fixed boundary conditions at the radial boundaries $\phi(x = 0) = \phi(x = L_x) = 0$. These boundary conditions are commonly used for numerical reasons,^{28,65} despite strictly speaking not being appropriate for scrape-off layer plasmas. The simulation domain is, however, big enough that the boundary conditions for the potential have no measurable effect on the dynamics.

The numerical model is implemented in the STORM code,⁵² which is based on BOUT++.^{69,70} The code uses a finite difference scheme in the x -direction and a spectral scheme in the y -direction, and time integration is performed by the PVODE solver.⁷¹ We choose a simulation domain size of $L_x = 150$ and $L_y = 100$ with a resolution of 256×256 grid points for all runs. The coefficients are representative of a medium sized machine with $g = 1.7 \times 10^{-3}$ and $\sigma = 1.8 \times 10^{-4}$. The parameters for the source term are $w = 7$ and $\lambda = 30$. For all presented simulations, the background density is set to $n_b = 1$. For single isolated blob simulations in Sec. IV, we choose $D_\perp = \nu_\perp = 2 \times 10^{-2}$, while for the remaining simulations of Secs. V and VI, we take $D_\perp = \nu_\perp = 5 \times 10^{-3}$. We choose higher diffusion coefficients for isolated blob simulations in Sec. IV since the blob coherence stays higher for higher diffusion coefficients and it is more straightforward to test the blob tracking algorithm.

III. BLOB TRACKING

The blob tracking algorithm is implemented in Python, employing the xarray library.⁷² Blobs are identified as positive amplitude fluctuations above a certain particle density threshold. The optimal choice of the thresholding technique depends on the problem at hand, and in the case of the isolated blob simulations presented in Sec. IV, we take a constant threshold n_{const} across the whole domain as the blob threshold n_{BT} . For Secs. V–VI, however, we add the binormal/poloidal- and time averaged profile to n_{const} , which takes the form,

$$n_{\text{BT}}(x) = n_{\text{const}} + \frac{1}{L_y} \int_0^{L_y} \int_{t_{\text{tr}}}^T dt [n(x, y, t) - n_b], \quad (5)$$

where T stands for the run time of the simulation and t_{tr} for the transient time before the simulation reaches a quasi-stationary state. This method is more robust for turbulence simulations due to the radially varying time-averaged profile.

We label the resulting coherent regions using the multi-dimensional image processing library `scipy.ndimage`. The output data of our simulations is stored as an `xarray` dataset where the simulation variables n , ϕ and the vorticity $\nabla_\perp^2 \phi$ are stored as a three-dimensional array, two dimensions for the spatial coordinates and one dimension for time. We then define a field with the same dimensionality as n with the value one in the regions where n exceeds n_{BT} and zero otherwise. Applying the function `scipy.ndimage.label` on this array returns a field where all coherent regions of ones are labeled from one to the maximum number of coherent structures in the data. We use this field of labels as the definition of blobs in the datasets.

Note that this implementation requires a relatively high temporal resolution of the output files since a blob is only labeled as one coherent structure over time if the blob spatially overlaps with itself in the next frame. The downside of this approach is the resulting large output files, which slows down the memory bound blob tracking algorithm. In addition, one has to consider the periodic boundary condition in the y -direction since the algorithm will label a blob traveling through the y -boundary of the domain as two different objects. For turbulence simulations in Sec. VI, the blob tracking algorithm is only applied in the domain region where $x > 0.4 L_x$ since we do not include the plasma source region in our analysis.

In order to determine the position and the velocity of the labeled blobs, we determine the center of mass of the blobs at each time step. For isolated blob simulations, the x -component of the center of mass is defined as

$$X_{\text{COM}}(t) = \frac{\int_0^{L_y} dy \int_0^{L_x} dx x [n(x, y, t) - n_b]}{\int_0^{L_y} dy \int_0^{L_x} dx [n(x, y, t) - n_b]}, \quad (6)$$

with the y -component defined analogously. For multiply seeded blobs and turbulence simulations, the blob tracking algorithm determines the x -component of the blob position by calculating the center of mass of the plasma region where the plasma density exceeds the threshold, which takes the form

$$X_{\text{BT}}(t) = \frac{\iint_{S_{\text{blob}}} dx dy x [n(x, y, t) - n_b]}{\iint_{S_{\text{blob}}} dx dy [n(x, y, t) - n_b]}, \quad (7)$$

where S_{blob} represents the region where the blob is detected. The algorithm determines the velocity by a finite difference scheme in time and requires therefore the blob being detected for at least two consecutive frames. If a structure is only detected for a single frame, the algorithm sets the velocity to zero. We estimate the blob size δ for each time step as

$$\delta = \left(\frac{1}{\pi} \iint_{S_{\text{blob}}} dx dy \right)^{1/2}. \quad (8)$$

Note that this definition is based on the assumption that the blob is circular so that $S_{\text{blob}} = \delta^2 \pi$. We choose this definition since it provides a consistent way to compare the detected sizes to seeded circular blobs even though the shape of blobs changes significantly over time. Since this estimate of the blob size varies from the input parameter for the width of seeded blobs δ_\perp , we distinguish between these two variables by dropping the perpendicular-sign for the size estimation from the blob tracking algorithm. Due to this definition, we observe a systematic mismatch between δ and δ_\perp when estimating the size of a seeded blob with our implementation of the algorithm. We further estimate the peak amplitude A of each blob as

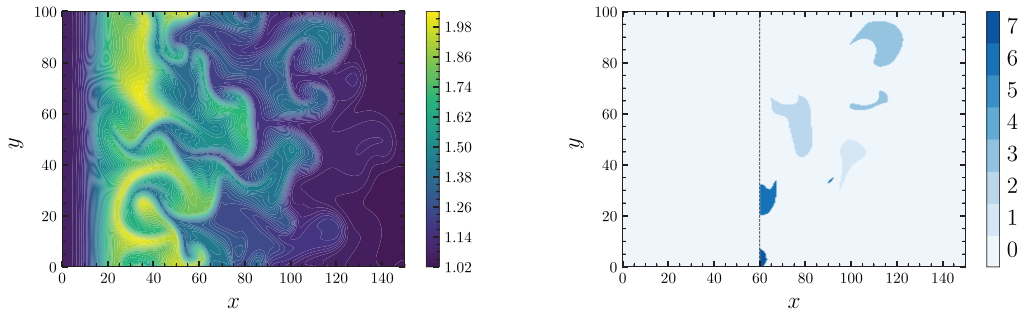


FIG. 1. Snapshots of plasma density n and associated blob labels of a turbulence simulation with parameters equivalent to Sec. II. Here, x refers to the radial and y to the poloidal/binormal coordinate. The colorbar on the right represents the labels of individual detected blobs with the label zero describing the background. The source region on the left side of the domain is excluded from the blob detection algorithm.

$$A = \max_{S_{\text{blob}}} (n(x, y, t) - n_b) \quad (9)$$

for each time step. We will use the here defined blob parameters for our statistical analysis for different forcings. We can then apply this method with the identical blob tracking parameters on isolated blobs, statistically seeded blobs and full scrape-off layer turbulence simulations in order to investigate how blob interaction is affected by the plasma intermittency, and its effect on the blob parameters.

An example of the blob tracking and labeling methods applied on a turbulence simulation is shown in Fig. 1. This figure shows the plasma density and the associated blobs detected by our algorithm. The background is labeled as zero and the individual blobs with ascending numbers.

IV. ISOLATED SEEDED BLOB SIMULATIONS

We begin the analysis by tracking single isolated blobs, seeded on a constant plasma background. We initialize the simulation with a symmetric Gaussian function as a blob as

$$n(x, y, t = 0) = n_b + A_0 \exp\left(-\frac{(x - x_0)^2 + (y - y_0)^2}{2\delta_{\perp}^2}\right), \quad (10)$$

where n_b represents the background density, A_0 the initial amplitude, δ_{\perp} the initial width, and x_0 and y_0 the initial position of the blob. We choose $x_0 = 0.25 L_x$ and $y_0 = 0.5 L_y$. The blob amplitude is set to be as large as the plasma background n_b , in this case $A_0 = n_b = 1$. We investigate how the blob velocity evolves over time by estimating the velocity with the blob tracking algorithm for three different thresholds. The results of this analysis are shown in Fig. 2 for a relatively small blob width of $\delta_{\perp} = 5$. The radial velocity is also determined by a conventional center of mass approach shown in Eq. (6).

The velocity estimates from the algorithm are strongly dependent on the threshold applied for the tracking. For a blob threshold of only one percent of its initial amplitude, we observe that the measured velocity remains very close to the center of mass approach for all widths investigated. This is not surprising since these two implementations are almost identical for low tracking thresholds. For higher blob thresholds, it is shown that the determined maximum radial velocity increases significantly, as the measured radial velocity for a threshold

of 40% of the initial blob amplitude more than doubles the center of mass results. This can be explained by the fact that for high thresholds, the algorithm only detects the densest parts of the blob that tends to propagate faster radially than their less dense regions. This has to be taken into account for further work when applying the blob tracking algorithm on more complex models than singular seeded blob simulations. In addition, it is shown that the detected lifetime of the blob for a higher threshold is lower. This can be simply explained by the fact that a narrower detected structure dissipates faster and its amplitude therefore falls below the threshold of the tracking algorithm. The precision of the blob tracking measurement also decreases with higher blob thresholds and smaller blobs. Intuitively, the blob tracking algorithm shows the best performance for wide blobs and low blob thresholds.

We further perform a parameter scan from $\delta_{\perp} = 2$ to $\delta_{\perp} = 30$ for the blob width. The results of this analysis are shown in Fig. 3. For all different methods of velocity measurements, we see that the size-velocity dependence follows the analytical predictions derived in previous work.^{11,34} The radial velocity of small blobs, which are in the

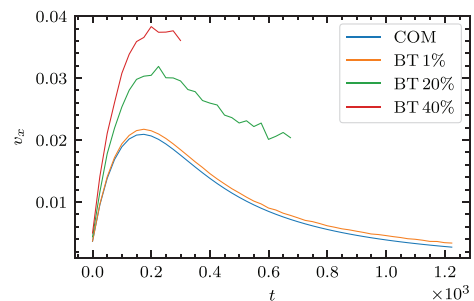


FIG. 2. Radial velocity of an isolated seeded blob width $\delta_{\perp} = 5$. The blue line refers to the center of mass approach. The other lines refer to the blob tracking algorithm using different percentages of its initial amplitude as the threshold. The radial velocity and the blob width are expressed in normalized units.

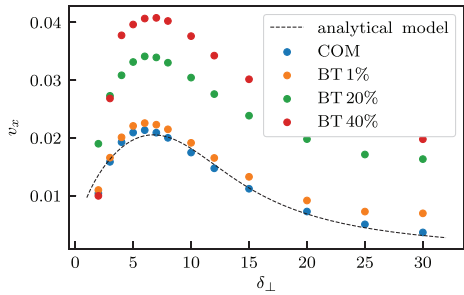


FIG. 3. The dependence of the maximum radial velocity of isolated seeded blobs on their widths compared to an analytical model. The blue dots refer to the center of mass approach, while the other dot colors correspond to the blob tracking algorithm that uses different percentages of the initial amplitude of the blob as a threshold.

so-called inertial limit, increases with the square root of its size. For large blobs, sheath currents dominate over polarization currents and the blob velocity is inversely proportional to the square of its size. These two limits are referred to as the inertial and sheath connected regimes, respectively.

For all applied blob thresholds, we observe that the scaling dependence is correctly resolved as is the case with the center of mass approach. We therefore conclude that these methods are consistent, which motivates extending our analysis to more complex forcings with multiple seeded blobs.

V. RANDOMLY SEEDED BLOB SIMULATIONS

The next step of our studies is a more complex model, in which blobs are seeded with random parameters, in particular, amplitude A_0 , width δ_{\perp} , initial poloidal/binormal launch positions x_0 and y_0 , and waiting time τ_w between the launch of consecutive blobs. This model is still artificial but provides valuable insight in blob interaction in a controlled environment. We start our analysis by only keeping waiting times and widths as random variables and then gradually adding the remaining free parameters to the model. In the most complex case, we sample the waiting times from an exponential distribution of the form,

$$P_{\tau_w} = \frac{1}{\langle \tau_w \rangle} \exp\left(-\frac{\tau_w}{\langle \tau_w \rangle}\right), \tag{11}$$

amplitudes from a truncated exponential distribution and the initial poloidal/binormal starting positions and the widths from a uniform distribution. Note that we choose a uniform distribution for the widths for illustration. Since we intend to compare the velocity-size dependency of detected blobs in this model to isolated blob studies, we choose to sample from a uniform distribution for the sizes to increase the number of large blobs. A snapshot of an example run of this model is presented in Fig. 4 showing the density field of three seeded blobs with different widths and amplitudes. The blob at approximately $y = 90$ propagates in an almost isolated way radially outward. The two blobs at approximately $y = 50$ show a strong interaction with each other and merge eventually into one coherent structure. A less intermittent case with numerous blobs is shown in Fig. 5 where individual

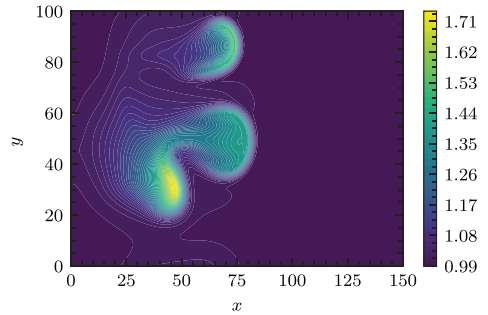


FIG. 4. Snapshot of plasma density n of a simulation of randomly seeded blobs with different amplitudes. The blob at approximately $y = 90$ propagates radially outward almost without interfering with other blobs. At approximately $y = 40$, we see two blobs merging into one coherent structure.

blobs interact strongly with each other, resulting in a turbulence-like density snapshot.

In the following analysis, we choose the same parameters for our blob tracking algorithm for all runs, in order to keep comparisons between different models consistent. In order to identify all structures present, one would choose a relatively low threshold for the blob tracking algorithm. Nevertheless, the threshold cannot be set too low in this model that simulates more than one blob since it would label several independent but spatially close structures as one blob. We subtract the time and y -averaged radial profile from the density and apply a blob threshold of 0.2 density units for the resulting fields. In addition, we rerun the blob tracking analysis on single isolated blobs from Sec. IV with these exact parameters to compare these two systems.

A. Single launch-point

We begin our analysis on randomly seeded blobs, keeping the blob amplitudes constant to $A_0 = 1$ and launching all blobs at $x_0 = 0.25 L_x$ and $y_0 = 0.5 L_y$, which leaves the waiting times and blob

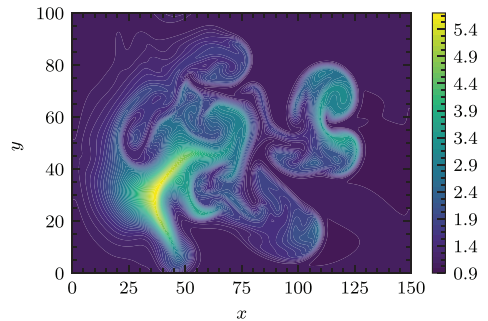


FIG. 5. Snapshot of plasma density n of a simulation of randomly seeded blobs with different amplitudes and low intermittency parameter. We observe strong interactions between individual seeded blobs similar to turbulence simulations.

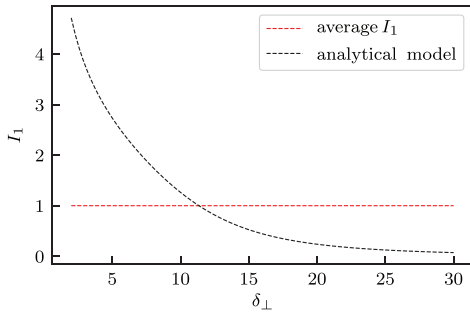


FIG. 6. Model specific intermittency parameter dependence on blob width and with fixed τ_w illustrated utilizing an analytical model for the radial velocity. This is compared to the average intermittency parameter for all δ_{\perp} .

widths as random variables. In order to quantify the interaction and overlap of individual blobs, we define a model specific intermittency parameter in the spirit of Ref. 54 as

$$I_1 = \frac{\langle v_x \rangle \langle \tau_w \rangle}{\langle \delta \rangle}, \quad (12)$$

where $\langle v_x \rangle$ represents the average radial velocity, $\langle \tau_w \rangle$ the average waiting time, and $\langle \delta \rangle$ the average width of a specific run. This model specific intermittency parameter is introduced in the spirit of previous work on stochastic modeling of intermittent fluctuations, analyzing time series,^{68,73–76} which defines the intermittency parameter as the ratio of the average duration time of one event above a chosen threshold and the average waiting time between two such consecutive events. From the definition I_1 is, strictly speaking, not constant but a function of δ of each individual blob. This effect is illustrated in Fig. 6, showing how the blob specific intermittency parameter deviates from the average value. Here, we calculate I_1 for constant $\langle \tau_w \rangle$ where $\langle v_x \rangle$ is given by the analytical solution for $v_x(\delta_{\perp})$ in Ref. 34. This has to be taken into consideration for the following investigation. Note that for the presented cases, we calculate $\langle v_x \rangle$ and $\langle \delta \rangle$ not from input parameters of the model but from the blob tracking of seeded blobs excluding structures that only are detected for one frame. We launch blobs for three different average waiting times, which refer to three different

states of intermittency. The results of the blob tracking algorithm for these three cases are presented in Fig. 7.

For the most intermittent case of $I_1 = 11.8$, where blobs are the most spatially separated, we see that the overwhelming majority of detected structures have parameters corresponding to isolated blobs. This implies that there is weak interaction between individual blobs. Some individually detected structures show a higher radial velocity than their isolated counterparts. This effect arises due to two closely separated blobs interacting with each other's electrostatic potential. Although this has been studied in some detail in previous work,⁵² we deliver an illustration of the physical mechanism in Fig. 8. We seed two identical blobs at different radial positions and apply the blob tracking algorithm to determine their radial velocity. The electrostatic potential created by the two separate blobs superposes and results in a stronger electric field, which increases the $\mathbf{E} \times \mathbf{B}$ drift that pulls the coherent blob structures radially outward. This effect can lead to the formation of so-called “blob trenches” in turbulence simulations. We estimate the radial velocity of the two blobs with the blob tracking algorithm and observe a clear increase in velocity for the trailing blob, shown in Fig. 9. The case of two blobs in the poloidal/binormal direction is also studied in Ref. 52, showing a decrease in the radial velocity compared to the isolated case. However, blobs in turbulent environments usually get diverted into the blob trenches by the electrostatic potential of previous blobs. We, therefore, observe significantly more cases of blobs in close radial than in poloidal/binormal proximity.

For $I_1 = 4.9$ and $I_1 = 1.8$ in Fig. 7, we observe an increasing number of blobs with a higher radial velocity than their isolated counterparts. Since the average waiting time decreases, individual blobs interact strongly through the potentials of nearby blobs and get accelerated radially outward. In addition, the blob tracking algorithm detects more smaller-sized coherent structures that usually have short lifetimes, often only one to two frames. Due to the increasing interactions and turbulent flow in this model, more of these small structures are detected by the algorithm, which can be classed as numerical artifacts.

B. Random launch-point

The next random variable of the investigated model added to our analysis is the poloidal/binormal launch position of the seeded blobs. We sample the launch position y_k from a uniform distribution $U(0.2L_y, 0.8L_y)$ to reduce the number of blobs propagating through the poloidal/binormal boundaries. The initial amplitudes remain a fixed parameter set to $A_0 = 1$. Seeding blobs from a random poloidal/

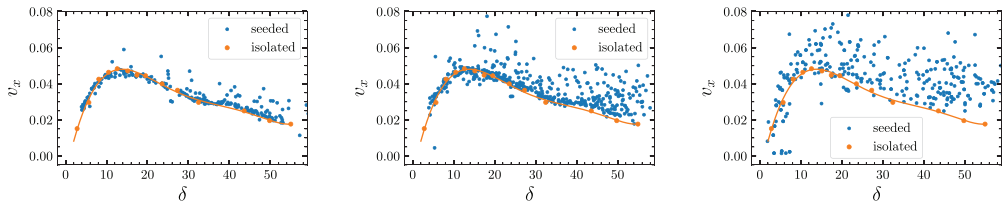


FIG. 7. Maximum radial velocity measured with the tracking algorithm of randomly seeded blobs with single launch position (blue dots) compared to isolated blobs (orange dots). The intermittency parameters for the displayed runs are approximately $I = 11.8$ (left), $I = 4.9$ (middle), and $I = 1.8$ (right). Blob widths are sampled from a uniform distribution with $\delta_{\perp} \in U(2, 30)$ and waiting times from an exponential distribution. The average waiting times for the displayed runs are $\langle \tau_w \rangle = 200$ (left), $\langle \tau_w \rangle = 75$ (middle), and $\langle \tau_w \rangle = 25$ (right).

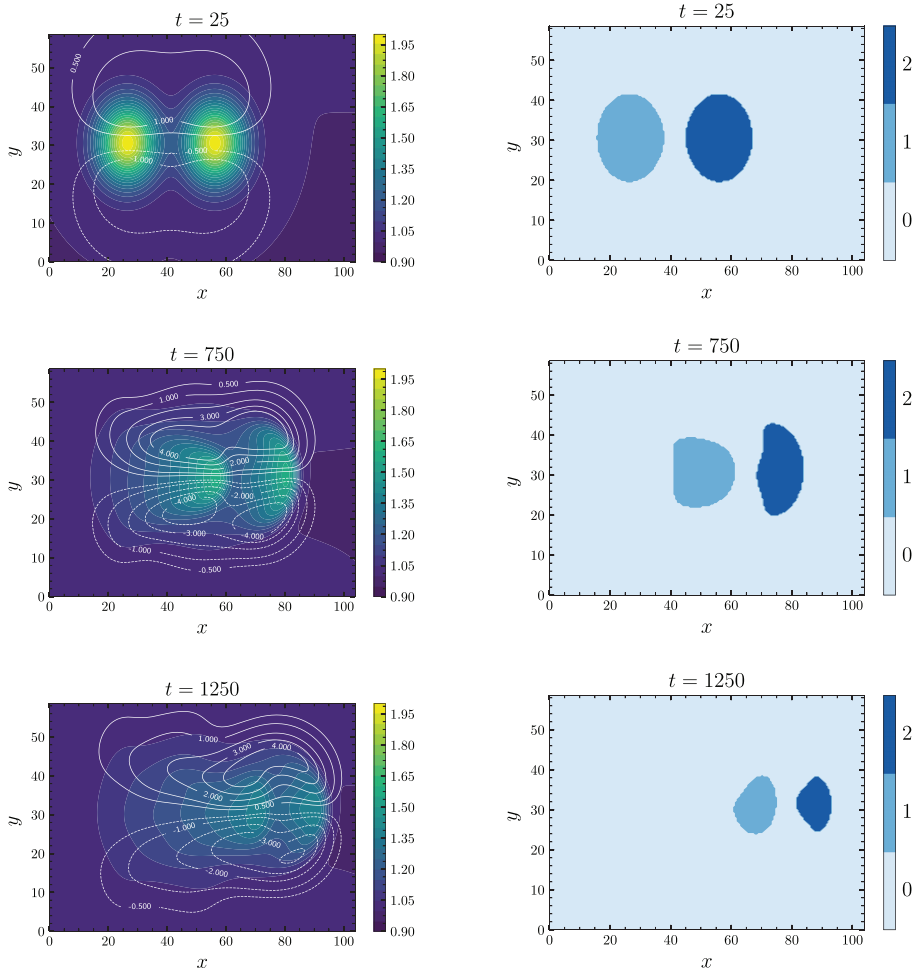


FIG. 8. Snapshot of the plasma density of two seeded identical blobs with their electrostatic potential indicated with white lines (left) and the associated blob labels, detected by the blob tracking algorithm at three different time steps (right). The label zero describes the background particle density. The interaction of the trailing blob by the electrostatic potential of the leading blob is illustrated.

binormal position increases the intermittency of the model and leads to more complex interactions between individual structures. We therefore multiply the expression for the intermittency parameter shown in Eq. (13) with $L_y/3\langle\delta\rangle$ resulting in

$$I_2 = \frac{\langle v_x \rangle \langle \tau_w \rangle L_y}{3\langle\delta\rangle^2} \tag{13}$$

to consider this extension of the model since $L_y/3$ is the average distance of two randomly chosen events from a uniform distribution

with length L_y . We run this model for three different intermittency parameters and present the results from the detected blobs in Fig. 10. As one might expect, most detected structures in the $I_2 = 7.6$ case follow the isolated blob line but show more spread around this line than in the single launch point model. In particular, many small blobs are detected by the blob tracking algorithm that show a significantly lower radial velocity than their isolated counterparts, with some blobs even showing a negative radial velocity. We provide an explanation for this effect in Fig. 11. It is shown that these small blobs deviating from the

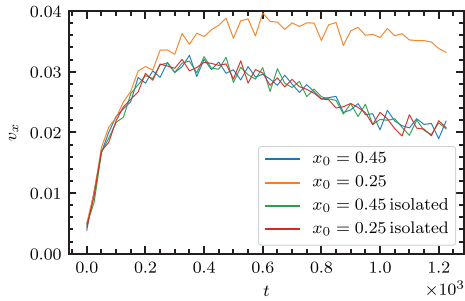


FIG. 9. Radial velocity of two seeded identical blobs at two different radial positions and their isolated counterparts. The blob, seeded at $x_0 = 0.25$, which is trailing the blob seeded at $x_0 = 0.45$, shows a significant increase in the radial velocity due to the electrostatic potential created by the leading blob.

theoretical predictions have a maximum amplitude significantly lower than $A = 1$ as the initially seeded blobs have. This indicates that these small structures result from the complex interaction of the seeded blobs. Since their amplitudes are significantly lower than the ones of their isolated counterparts, their radial velocity is also lower. For the cases of lower intermittency parameters, we observe again an increase in the average radial velocities and the spread. This remains consistent with the previous single launch point model and can be explained by the same blob-interaction mechanism.

We utilize the presented six runs to quantify the interaction of individual blobs for different intermittency parameters. For each model, we calculate the average deviation in radial velocity of the detected structures from the fit function of the isolated blobs. The result is shown in Fig. 12. The six data points are compared to a fit of the inverse of l times a constant. This clearly suggests that the intermittency of blobs in the scrape-off layer has a strong effect on their radial velocity and propagation.

C. Amplitude distribution

We add the final random variable of our model by seeding blobs with truncated exponentially distributed amplitudes since we only choose amplitudes with $0.5 < A_0 < 3$ in order to compare them more easily with isolated seeded blobs. We perform a parameter scan

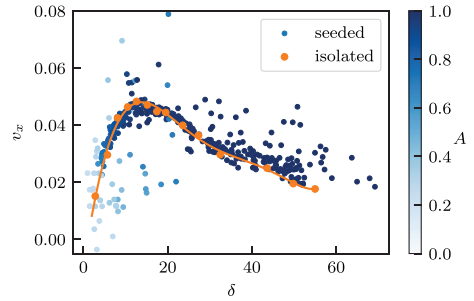


FIG. 11. Radial velocity and widths of detected blobs with an intermittency parameter of $l_2 = 7.6$ are compared to isolated blobs (orange dots). Blobs with a small maximum amplitude represent most small structures deviating from the scaling laws of isolated blobs.

for blob widths for isolated seeded blobs with amplitudes $A_0 = 0.5$ and $A_0 = 3$ in order to create reference values for the boundaries of our model. We then run our model for three different intermittency parameters and compare the results with the isolated blobs for different amplitudes. These results are shown in Fig. 13.

The results are consistent with our previous analysis. Most randomly seeded blobs lie in between the borders established by the isolated blobs. For small blobs, we observe again some data points with a lower radial velocity than in the isolated case, which can be explained by the same effect as in Sec. VB. For wider structures, we find some structures with higher velocities, which can again be explained by the electrostatic potential of interacting blobs. As expected, the average velocity is increasing for a decreasing intermittency parameter.

VI. TURBULENCE SIMULATIONS

After investigating randomly seeded blob models, we turn our attention to a simple self-consistent scrape-off layer model simulating plasma turbulence. Numerically, the model is equivalent to the seeded blob simulations but uses the term of Eq. (3) as a plasma source instead of Gaussian seeded blobs. The density profile in the simulation domain is built and balanced by the plasma source and the sheath dissipation included in the model. These are unstable due to bad curvature and interchange instability, which leads to coherent structures of plasma propagating outward radially due to the blob mechanism

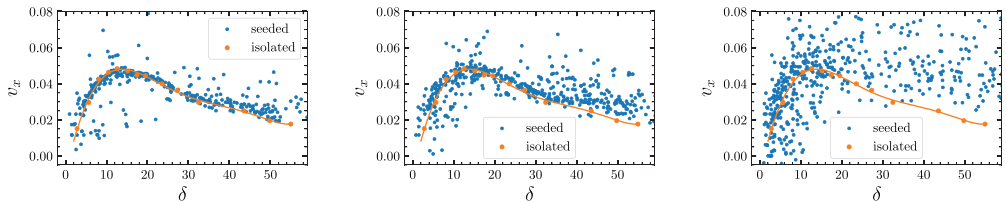


FIG. 10. Maximum radial velocity measured with the tracking algorithm of randomly seeded blobs with the random poloidal/binormal launch position (blue dots) compared to isolated blobs (orange dots). The intermittency parameters for the displayed runs are approximately $l_2 = 7.6$ (left), $l_2 = 2.5$ (middle), and $l_2 = 1.3$ (right). Widths are sampled from $\delta_x \in U(2, 30)$, initial poloidal/binormal positions from $y_0 \in U(0.2 \times L_y, 0.8 \times L_y)$, and waiting times from an exponential distribution. The average waiting times for the displayed runs are $\langle \tau_w \rangle = 120$ (left), $\langle \tau_w \rangle = 50$ (middle), and $\langle \tau_w \rangle = 13$ (right).

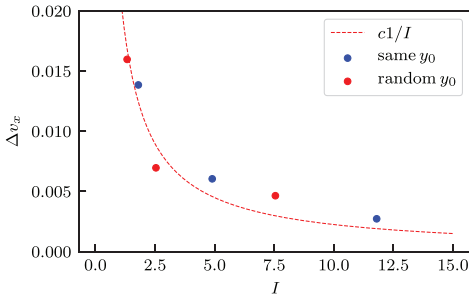


FIG. 12. Average deviation in the radial velocity of theoretical scaling law predictions measured in randomly seeded blob simulations for different intermittency parameters. The relationship between Δv_r and I is compared to a fit of the inverse of I times a constant.

discussed in Sec. I. These blob like structures vary in amplitude and width and can be detected and tracked by the tracking algorithm.

We exclude the source region for our blob tracking analysis and only consider coherent structures detected at $x > 0.4 L_x$ since this unphysical term only serves as a numerical term. In addition, we only include blobs with an initial center of mass of $0.25 L_y < y_{\text{init}} < 0.75 L_y$ in our statistical evaluation in order to exclude distorted tracked structures because of the periodic boundary conditions in the y -dimension. Even though it is straightforward to track blobs consistently that traverse the simulation border in this direction, our numerical implementation for this issue is computationally more expensive than running the simulation longer and only considering blobs in the central band of the domain. For such turbulence simulations, the tracking algorithm identifies numerous small structures that only appear for one frame. These structures represent approximately one third of the total number of detected blobs and are also excluded from our statistical analysis. The remaining parameters for the tracking algorithm stay the same as for the randomly seeded blob model. The determined radial velocities and sizes of the detected blobs in the turbulence simulation are shown as a 2D histogram in Fig. 14. We choose this type of plot since the illustrated 4542 blobs are too many to be shown distinctively in a scatterplot. The distribution of the sizes and amplitudes of the detected structures, as well as the joint probability

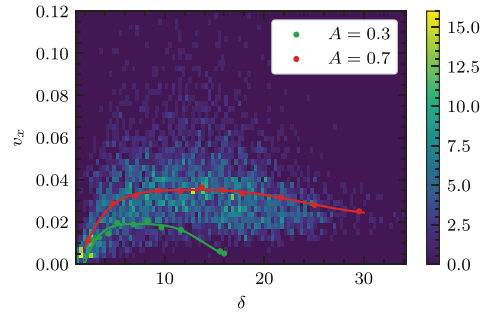


FIG. 14. Radial velocity of blobs detected in full turbulence simulations compared to isolated blobs with $A = 0.3$ and $A = 0.7$. Blobs only detected for one frame are excluded, as well as blobs close to the poloidal/binormal simulation boundary.

distribution functions (PDFs) of these two blob parameters, are shown in Fig. 15.

These measurements show that the amplitudes lie in between $A = 0.2$, which is equivalent to the threshold used for the blob tracking algorithm, and $A = 0.7$. Since blobs with an amplitude smaller than $A = 0.2$ are not detected and since many small blobs below $A = 0.4$ are dissipated too quickly to be detected, the shown PDF is not representative for all structures in the system. Taking these factors into account, the common assumption of blob amplitudes being exponentially distributed cannot be falsified by these measurements. The same is valid for the distribution of blob widths. Nevertheless, we observe a clear correlation between the amplitudes and widths as the correlation coefficient of these two parameters is $\rho = 0.85$. In order to compare the detected blobs with their isolated counterparts, we perform a parameter scan for blobs with the amplitudes $A_0 = 0.7$ and $A_0 = 0.3$ as the two edge values of the distribution. Since $A_0 = 0.2$ would be too small to be detected by the algorithm, we use $A_0 = 0.3$ as the lower border. These isolated blobs are shown together with their fit in Fig. 14. In this analysis, no blobs with a higher width than $\delta = 30$ appear; therefore, we rarely observe the decreasing radial velocity for bigger and denser blobs in our velocity–size scaling. Nevertheless, the dataset provides enough information to discuss the results in comparison to isolated blob simulations. As in the previous model of randomly seeded blobs with random amplitudes, we observe that the overwhelming majority

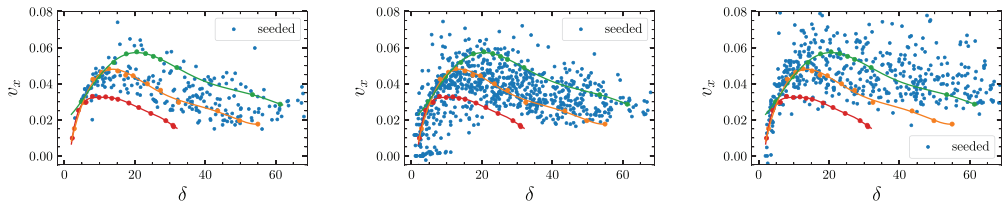


FIG. 13. Maximum radial velocity measured with the tracking algorithm of randomly seeded blobs with the random poloidal launch position and truncated exponentially distributed amplitudes (blue dots) compared to isolated blobs with $A_0 = 0.5$ (red dots), $A_0 = 1$ (orange dots), and $A_0 = 3$ (green dots). The intermittency parameters for the displayed runs are approximately $I = 10.3$ (left), $I = 7.9$ (middle), and $I = 1.7$ (right). The average waiting times for the displayed runs are $\langle \tau_w \rangle = 200$ (left), $\langle \tau_w \rangle = 75$ (middle), and $\langle \tau_w \rangle = 25$ (right).

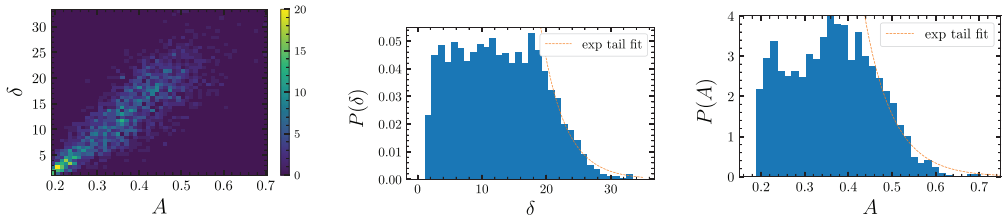


FIG. 15. 2D histogram showing the correlation of the maximum amplitudes and widths (left) resulting in a correlation coefficient of $\rho = 0.85$. Probability density functions of maximum width (middle) and amplitudes (right) of detected blobs in a fully turbulent simulation. The tail of the PDFs is compared to an exponential fit.

of detected blob structures lie in between the trends of the isolated blob simulations. As for the previous model, the algorithm detects a significant number of structures with a higher radial velocity than the isolated blobs. We explain these events again by the interaction of blobs with the electrostatic potential of one another. Due to these findings, we conclude that tracking blobs in a fully turbulent scenario shows very similar results to models of statistically seeded blobs. While the theoretical size–velocity scaling of isolated blobs gives a reasonable order of magnitude estimate, there is an order unity scatter due to strong interactions between blobs.

VII. DISCUSSION AND CONCLUSION

In this work, we investigated the interaction of blobs in the scrape-off layer for different models of varying complexity. In particular, we compared the relation between the radial velocity and the widths of the blobs with established scaling laws. We started with studying isolated blobs and extended our analysis on a model of randomly seeded blobs where the parameters are sampled from physically adequate PDFs. We studied this model for different levels of intermittency and applied the acquired knowledge on fully turbulent scrape-off layer plasma simulations.

In this process, we developed a blob tracking algorithm as a versatile tool to analyze and understand blob and plasma parameters in scrape-off layer plasma simulations. We publish our implementation on github under <https://github.com/gregordecristoforo/xblobs>. The current version of the algorithm can be applied on any 2D `xarray` dataset with a cartesian grid and constant spacing dx , dy and dt .⁷⁷ An extension of the algorithm to three dimensions is numerically easy to implement, but the 2D version of this algorithm can be valuable for analyzing blob propagation and turbulent transport, in a specific plane in three-dimensional plasma simulations. We will use this in the future to study how blob properties depend on specific physical effects or study the plasma transport in the scrape-off layer.

For isolated blob simulations, we find that the velocity-size scaling dependence is correctly resolved by the blob tracking method. For the case of non-isolated blobs, we observe a correlation between the level of blob interaction and the number of blobs deviating from size-velocity scaling laws of perfectly isolated blobs. Blobs show an increase in the radial velocity in cases of low intermittency for the randomly seeded blob model and turbulence model, compared to isolated and intermittent cases. We explain this observation by the interaction of blobs with the electrostatic potential of one another. The blob trajectories are influenced by the electrostatic potential, which gets diverted, leading to the creation of trenches in which blobs get accelerated by

the potential of ones in front of them. These findings are consistent with previous work studying the interaction of two seeded blobs.⁵² Additionally, we find a strong correlation between the blob amplitudes and sizes estimated by the blob tracking algorithm for full plasma turbulence simulations. For all studied forcings, we observe a systematic size–velocity relationship consistent with theoretical predictions from the model. This concludes that despite the significant interaction of blobs, they still follow established scaling laws and can therefore be regarded to the lowest order, as isolated structures propagating radially through the scrape-off layer. We thereby display the relevance of isolated seeded blob and filament simulations for complex turbulent models.

ACKNOWLEDGMENTS

This work was supported by the UiT Aurora Centre Program, UiT The Arctic University of Norway (2020). G.D. acknowledges the generous hospitality of the Culham Centre for Fusion Energy (CCFE) where this work was conducted. In addition, this work has been partially funded by the EPSRC Grant No. EP/T012250/1 and partially carried out within the framework of the EUROfusion Consortium and has received funding from the Euratom research and training programmes 2014–2018 and 2019–2020 under Grant Agreement No. 633053. The views and opinions expressed herein do not necessarily reflect those of the European Commission. The MARCONI supercomputer was used for parts of the computational work under the Project No. FUA34_SOLBOUT4.

DATA AVAILABILITY

The data that support the findings of this study are available from the corresponding author upon reasonable request.

REFERENCES

- G. Antar, S. Krasheninnikov, P. Devynck, R. Doerner, E. Hollmann, J. Boedo, S. Luckhardt, and R. Conn, "Experimental evidence of intermittent convection in the edge of magnetic confinement devices," *Phys. Rev. Lett.* **87**, 065001 (2001).
- G. Y. Antar, G. Counsell, Y. Yu, B. LaBombard, and P. Devynck, "Universality of intermittent convective transport in the scrape-off layer of magnetically confined devices," *Phys. Plasmas* **10**, 419–428 (2003).
- A. Kirk, N. B. Ayed, G. Counsell, B. Dudson, T. Eich, A. Herrmann, B. Koch, R. Martin, A. Meakins, S. Saarelma *et al.*, "Filament structures at the plasma edge on MAST," *Plasma Phys. Controlled Fusion* **48**, B433 (2006).
- B. Dudson, N. B. Ayed, A. Kirk, H. Wilson, G. Counsell, X. Xu, M. Umansky, P. Snyder, and B. Lloyd, "Experiments and simulation of edge turbulence and filaments in MAST," *Plasma Phys. Controlled Fusion* **50**, 124012 (2008).

- ⁵N. B. Ayed, A. Kirk, B. Dudson, S. Tallents, R. Vann, and H. Wilson, "Inter-ELM filaments and turbulent transport in the mega-amp spherical tokamak," *Plasma Phys. Controlled Fusion* **51**, 035016 (2009).
- ⁶J. A. Boedo, D. Rudakov, R. Moyer, S. Krasheninnikov, D. Whyte, G. McKee, G. Tynan, M. Schaffer, P. Stangeby, P. West *et al.*, "Transport by intermittent convection in the boundary of the DIII-D tokamak," *Phys. Plasmas* **8**, 4826–4833 (2001).
- ⁷D. Rudakov, J. Boedo, R. Moyer, S. Krasheninnikov, A. Leonard, M. Mahdavi, G. McKee, G. Porter, P. Stangeby, J. Watkins *et al.*, "Fluctuation-driven transport in the DIII-D boundary," *Plasma Phys. Controlled Fusion* **44**, 717 (2002).
- ⁸J. A. Boedo, D. L. Rudakov, R. A. Moyer, G. R. McKee, R. J. Colchin, M. J. Schaffer, P. Stangeby, W. West, S. L. Allen, T. E. Evans *et al.*, "Transport by intermittency in the boundary of the DIII-D tokamak," *Phys. Plasmas* **10**, 1670–1677 (2003).
- ⁹O. E. Garcia, J. Horacek, R. Pitts, A. H. Nielsen, W. Fundamenski, V. Naulin, and J. J. Rasmussen, "Fluctuations and transport in the TCV scrape-off layer," *Nucl. Fusion* **47**, 667 (2007).
- ¹⁰O. E. Garcia, R. Pitts, J. Horacek, J. Madsen, V. Naulin, A. H. Nielsen, and J. J. Rasmussen, "Collisionality dependent transport in TCV SOL plasmas," *Plasma Phys. Controlled Fusion* **49**, B47 (2007).
- ¹¹C. Theiler, I. Furno, P. Ricci, A. Fasoli, B. Labit, S. Müller, and G. Plyushchev, "Cross-field motion of plasma blobs in an open magnetic field line configuration," *Phys. Rev. Lett.* **103**, 065001 (2009).
- ¹²F. Militello, P. Tamain, W. Fundamenski, A. Kirk, V. Naulin, and A. H. Nielsen, "Experimental and numerical characterization of the turbulence in the scrape-off layer of MAST," *Plasma Phys. Controlled Fusion* **55**, 025005 (2013).
- ¹³T. Farley, F. Militello, N. Walkden, J. Harrison, S. Silburn, and J. Bradley, "Analysis of filament statistics in fast camera data on MAST," in APS Meeting Abstracts, 2017.
- ¹⁴N. Walkden, J. Harrison, S. Silburn, T. Farley, S. S. Henderson, A. Kirk, F. Militello, and A. Thornton, "Quiescence near the X-point of MAST measured by high speed visible imaging," *Nucl. Fusion* **57**, 126028 (2017).
- ¹⁵N. Walkden, F. Militello, J. Harrison, T. Farley, S. Silburn, and J. Young, "Identification of intermittent transport in the scrape-off layer of MAST through high speed imaging," *Nucl. Mater. Energy* **12**, 175–180 (2017).
- ¹⁶N. Walkden, B. Labit, H. Reimerdes, J. Harrison, T. Farley, P. Innocente, and F. Militello, "Fluctuation characteristics of the TCV snowflake divertor measured with high speed visible imaging," *Plasma Phys. Controlled Fusion* **60**, 115008 (2018).
- ¹⁷S. Zweben, D. Stotler, J. Terry, B. LaBombard, M. Greenwald, M. Muterspaugh, C. Pitcher, A. C. Group, K. Hallatschek, R. Maqueda *et al.*, "Edge turbulence imaging in the alcator C-Mod tokamak," *Phys. Plasmas* **9**, 1981–1989 (2002).
- ¹⁸J. Terry, S. Zweben, K. Hallatschek, B. LaBombard, R. Maqueda, B. Bai, C. Boswell, M. Greenwald, D. Kopon, W. Nevins *et al.*, "Observations of the turbulence in the scrape-off-layer of alcator C-Mod and comparisons with simulation," *Phys. Plasmas* **10**, 1739–1747 (2003).
- ¹⁹J. Myra, D. D'Ippolito, D. Stotler, S. Zweben, B. LeBlanc, J. Menard, R. Maqueda, and J. Boedo, "Blob birth and transport in the tokamak edge plasma: Analysis of imaging data," *Phys. Plasmas* **13**, 092509 (2006).
- ²⁰O. Grulke, J. Terry, B. LaBombard, and S. Zweben, "Radially propagating fluctuation structures in the scrape-off layer of alcator C-Mod," *Phys. Plasmas* **13**, 012306 (2006).
- ²¹S. Zweben, W. Davis, S. Kaye, J. Myra, R. Bell, B. LeBlanc, R. Maqueda, T. Munsat, S. Sabbagh, Y. Sechrest *et al.*, "Edge and SOL turbulence and blob variations over a large database in NSTX," *Nucl. Fusion* **55**, 093035 (2015).
- ²²S. Zweben, J. Myra, W. Davis, D. D'Ippolito, T. Gray, S. Kaye, B. LeBlanc, R. Maqueda, D. Russell, D. Stotler *et al.*, "Blob structure and motion in the edge and SOL of NSTX," *Plasma Phys. Controlled Fusion* **58**, 044007 (2016).
- ²³D. D'Ippolito, J. Myra, S. Krasheninnikov, G. Yu, and A. Y. Pigarov, "Blob transport in the tokamak scrape-off-layer," *Contrib. Plasma Phys.* **44**, 205–216 (2004).
- ²⁴D. D'Ippolito, J. Myra, and S. Zweben, "Convective transport by intermittent blob-filaments: Comparison of theory and experiment," *Phys. Plasmas* **18**, 060501 (2011).
- ²⁵S. Krasheninnikov, D. D'Ippolito, and J. Myra, "Recent theoretical progress in understanding coherent structures in edge and sol turbulence," *J. Plasma Phys.* **74**, 679–717 (2008).
- ²⁶O. E. Garcia, "Blob transport in the plasma edge: A review," *Plasma Fusion Res.* **4**, 019 (2009).
- ²⁷N. Bian, S. Benkadda, J.-V. Paulsen, and O. E. Garcia, "Blobs and front propagation in the scrape-off layer of magnetic confinement devices," *Phys. Plasmas* **10**, 671–676 (2003).
- ²⁸O. E. Garcia, V. Naulin, A. Nielsen, and J. J. Rasmussen, "Computations of intermittent transport in scrape-off layer plasmas," *Phys. Rev. Lett.* **92**, 165003 (2004).
- ²⁹O. E. Garcia, N. Bian, V. Naulin, A. Nielsen, and J. J. Rasmussen, "Mechanism and scaling for convection of isolated structures in nonuniformly magnetized plasmas," *Phys. Plasmas* **12**, 090701 (2005).
- ³⁰O. E. Garcia, N. Bian, and W. Fundamenski, "Radial interchange motions of plasma filaments," *Phys. Plasmas* **13**, 082309 (2006).
- ³¹D. Russell, J. Myra, and D. D'Ippolito, "Saturation mechanisms for edge turbulence," *Phys. Plasmas* **16**, 122304 (2009).
- ³²F. Militello, W. Fundamenski, V. Naulin, and A. H. Nielsen, "Simulations of edge and scrape off layer turbulence in mega ampere spherical tokamak plasmas," *Plasma Phys. Controlled Fusion* **54**, 095011 (2012).
- ³³F. Militello, V. Naulin, and A. H. Nielsen, "Numerical scalings of the decay lengths in the scrape-off layer," *Plasma Phys. Controlled Fusion* **55**, 074010 (2013).
- ³⁴R. Kube and O. E. Garcia, "Velocity scaling for filament motion in scrape-off layer plasmas," *Phys. Plasmas* **18**, 102314 (2011).
- ³⁵R. Kube, O. E. Garcia, and M. Wiesenberger, "Amplitude and size scaling for interchange motions of plasma filaments," *Phys. Plasmas* **23**, 122302 (2016).
- ³⁶M. Wiesenberger, M. Held, R. Kube, and O. E. Garcia, "Unified transport scaling laws for plasma blobs and depletions," *Phys. Plasmas* **24**, 064502 (2017).
- ³⁷J. R. Angus, M. V. Umansky, and S. I. Krasheninnikov, "Effect of drift waves on plasma blob dynamics," *Phys. Rev. Lett.* **108**, 215002 (2012).
- ³⁸N. Walkden, B. Dudson, and G. Fishpool, "Characterization of 3D filament dynamics in a MAST SOL flux tube geometry," *Plasma Phys. Controlled Fusion* **55**, 105005 (2013).
- ³⁹P. Ricci, F. Riva, C. Theiler, A. Fasoli, I. Furno, F. Halpern, and J. Loizu, "Approaching the investigation of plasma turbulence through a rigorous verification and validation procedure: A practical example," *Phys. Plasmas* **22**, 055704 (2015).
- ⁴⁰P. Tamain, H. Bufferand, G. Ciraolo, C. Colin, P. Ghendrih, F. Schwander, and E. Serre, "3D properties of edge turbulent transport in full-torus simulations and their impact on poloidal asymmetries," *Contrib. Plasma Phys.* **54**, 555–559 (2014).
- ⁴¹L. Easy, F. Militello, J. Omotani, B. Dudson, E. Havlíčková, P. Tamain, V. Naulin, and A. H. Nielsen, "Three dimensional simulations of plasma filaments in the scrape off layer: A comparison with models of reduced dimensionality," *Phys. Plasmas* **21**, 122515 (2014).
- ⁴²L. Easy, F. Militello, J. Omotani, N. Walkden, and B. Dudson, "Investigation of the effect of resistivity on scrape off layer filaments using three-dimensional simulations," *Phys. Plasmas* **23**, 012512 (2016).
- ⁴³F. Militello, N. Walkden, T. Farley, W. Gracias, J. Olsen, F. Riva, L. Easy, N. Fedorczak, I. Lupelli, J. Madsen *et al.*, "Multi-code analysis of scrape-off layer filament dynamics in MAST," *Plasma Phys. Controlled Fusion* **58**, 105002 (2016).
- ⁴⁴F. Riva, C. Colin, J. Denis, L. Easy, I. Furno, J. Madsen, F. Militello, V. Naulin, A. H. Nielsen, J. M. B. Olsen *et al.*, "Blob dynamics in the TORPEX experiment: A multi-code validation," *Plasma Phys. Controlled Fusion* **58**, 044005 (2016).
- ⁴⁵F. Riva, F. Militello, S. Elmore, J. T. Omotani, B. D. Dudson, and N. Walkden, "Three-dimensional plasma edge turbulence simulations of MAST and comparison with experimental measurements," *Plasma Phys. Controlled Fusion* **61**, 095013 (2019).
- ⁴⁶M. Wiesenberger, J. Madsen, and A. Kendl, "Radial convection of finite ion temperature, high amplitude plasma blobs," *Phys. Plasmas* **21**, 092301 (2014).
- ⁴⁷W. Lee, J. R. Angus, M. V. Umansky, and S. I. Krasheninnikov, "Electromagnetic effects on plasma blob-filament transport," *J. Nucl. Mater.* **463**, 765–768 (2015).
- ⁴⁸J. R. Angus, S. I. Krasheninnikov, and M. V. Umansky, "Effects of parallel electron dynamics on plasma blob transport," *Phys. Plasmas* **19**, 082312 (2012).

- ⁴⁹S. I. Krasheninnikov, "On scrape off layer plasma transport," *Phys. Lett. A* **283**, 368–370 (2001).
- ⁵⁰J. Myra, D. Russell, and D. D'Ippolito, "Collisionality and magnetic geometry effects on tokamak edge turbulent transport. I. A two-region model with application to blobs," *Phys. Plasmas* **13**, 112502 (2006).
- ⁵¹D. Russell, J. Myra, and D. D'Ippolito, "Collisionality and magnetic geometry effects on tokamak edge turbulent transport. II. Many-blob turbulence in the two-region model," *Phys. Plasmas* **14**, 102307 (2007).
- ⁵²F. Militello, B. Dudson, L. Easy, A. Kirk, and P. Naylor, "On the interaction of scrape off layer filaments," *Plasma Phys. Controlled Fusion* **59**, 125013 (2017).
- ⁵³A. Kendl, "Gyrofluid vortex interaction," *Plasma Phys. Controlled Fusion* **60**, 025017 (2018).
- ⁵⁴O. E. Garcia, "Stochastic modeling of intermittent scrape-off layer plasma fluctuations," *Phys. Rev. Lett.* **108**, 265001 (2012).
- ⁵⁵O. E. Garcia, S. M. Fritznier, R. Kube, I. Cziegler, B. LaBombard, and J. L. Terry, "Intermittent fluctuations in the Alcator C-Mod scrape-off layer," *Phys. Plasmas* **20**, 055901 (2013).
- ⁵⁶F. Nespoli, I. Furno, B. Labit, P. Ricci, F. Avino, F. Halpern, F. Musil, and F. Riva, "Blob properties in full-turbulence simulations of the TCV scrape-off layer," *Plasma Phys. Controlled Fusion* **59**, 055009 (2017).
- ⁵⁷F. Nespoli, P. Tamain, N. Fedorczak, G. Ciraolo, D. Galassi, R. Tatali, E. Serre, Y. Marandet, H. Bufferand, and P. Ghendrih, "3D structure and dynamics of filaments in turbulence simulations of WEST diverted plasmas," *Nucl. Fusion* **59**, 096006 (2019).
- ⁵⁸P. Paruta, C. Beadle, P. Ricci, and C. Theiler, "Blob velocity scaling in diverted tokamaks: A comparison between theory and simulation," *Phys. Plasmas* **26**, 032302 (2019).
- ⁵⁹D. D'Ippolito, J. Myra, and S. Krasheninnikov, "Cross-field blob transport in tokamak scrape-off-layer plasmas," *Phys. Plasmas* **9**, 222–233 (2002).
- ⁶⁰Y. Sarazin, P. Ghendrih, G. Attuel, C. Clément, X. Garbet, V. Grandgirard, M. Ottaviani, S. Benkadda, P. Beyer, N. Bian *et al.*, "Theoretical understanding of turbulent transport in the SOL," *J. Nucl. Mater.* **313–316**, 796–803 (2003).
- ⁶¹N. Bisai, A. Das, S. Deshpande, R. Jha, P. Kaw, A. Sen, and R. Singh, "Simulation of plasma transport by coherent structures in scrape-off-layer tokamak plasmas," *Phys. Plasmas* **11**, 4018–4024 (2004).
- ⁶²N. Bisai, A. Das, S. Deshpande, R. Jha, P. Kaw, A. Sen, and R. Singh, "Edge and scrape-off layer tokamak plasma turbulence simulation using two-field fluid model," *Phys. Plasmas* **12**, 072520 (2005).
- ⁶³M. Kočan, R. Pánek, J. Stöckel, M. Hron, J. Gunn, and R. Dejarnac, "Ion temperature measurements in the tokamak scrape-off layer," *J. Nucl. Mater.* **363–365**, 1436–1440 (2007).
- ⁶⁴M. Kočan, F. Gennrich, A. Kendl, H. Müller, and A. U. Team, "Ion temperature fluctuations in the ASDEX upgrade scrape-off layer," *Plasma Phys. Controlled Fusion* **54**, 085009 (2012).
- ⁶⁵O. E. Garcia, J. Horacek, R. Pitts, A. Nielsen, W. Fundamenski, J. Graves, V. Naulin, and J. J. Rasmussen, "Interchange turbulence in the TCV scrape-off layer," *Plasma Phys. Controlled Fusion* **48**, L1 (2005).
- ⁶⁶D. Rudakov, J. Boedo, R. Moyer, P. C. Stangeby, J. Watkins, D. Whyte, L. Zeng, N. Brooks, R. Doerner, T. Evans *et al.*, "Far SOL transport and main wall plasma interaction in DIII-D," *Nucl. Fusion* **45**, 1589 (2005).
- ⁶⁷J. Horacek, J. Adamek, H. Müller, J. Seidl, A. H. Nielsen, V. Rohde, F. Mehlmann, C. Ionita, E. Havlíčková *et al.*, "Interpretation of fast measurements of plasma potential, temperature and density in SOL of ASDEX upgrade," *Nucl. Fusion* **50**, 105001 (2010).
- ⁶⁸R. Kube, O. E. Garcia, A. Theodorsen, D. Brunner, A. Kuang, B. LaBombard, and J. L. Terry, "Intermittent electron density and temperature fluctuations and associated fluxes in the Alcator C-Mod scrape-off layer," *Plasma Phys. Controlled Fusion* **60**, 065002 (2018).
- ⁶⁹B. Dudson, M. Umansky, X. Xu, P. Snyder, and H. Wilson, "BOUT++: A framework for parallel plasma fluid simulations," *Comput. Phys. Commun.* **180**, 1467–1480 (2009).
- ⁷⁰B. Dudson, P. Hill, D. Dickinson, J. Parker, A. Allen, G. Breyianna, J. Brown, L. Easy, S. Farley, B. Friedman, E. Grinaker, O. Izcard, I. Joseph, M. Kim, M. Leconte, J. Leddy, M. Loiten, C. Ma, J. Madsen, D. Meyerson, P. Naylor, S. Myers, J. Omotani, T. Rhee, J. Sauppe, K. Savage, H. Seto, D. Schwörer, B. Shanahan, M. Thomas, S. Tiwari, M. Umansky, N. Walkden, L. Wang, Z. Wang, P. Xi, T. Xia, X. Xu, H. Zhang, A. Bokshi, H. Muhammed, and M. Estarellas (2019). BOUT++ v4.3.0 (Version 4.3.0). [Zenodo. http://doi.org/10.5281/zenodo.3518905](http://doi.org/10.5281/zenodo.3518905)
- ⁷¹G. D. Byrne and A. C. Hindmarsh, "PVOde, an ODE solver for parallel computers," *Int. J. High Perform. Comput. Appl.* **13**, 354–365 (1999).
- ⁷²S. Hoyer and J. Hamman, "xarray: ND labeled arrays and datasets in python," *J. Open Res. Software* **5**, 10 (2017).
- ⁷³O. E. Garcia, R. Kube, A. Theodorsen, and H. Pécseli, "Stochastic modelling of intermittent fluctuations in the scrape-off layer: Correlations, distributions, level crossings, and moment estimation," *Phys. Plasmas* **23**, 052308 (2016).
- ⁷⁴R. Kube, O. E. Garcia, A. Theodorsen, A. Kuang, B. LaBombard, J. L. Terry, and D. Brunner, "Statistical properties of the plasma fluctuations and turbulent cross-field fluxes in the outboard mid-plane scrape-off layer of Alcator C-Mod," *Nucl. Mater. Energy* **18**, 193–200 (2019).
- ⁷⁵A. Theodorsen, O. E. Garcia, J. Horacek, R. Kube, and R. Pitts, "Scrape-off layer turbulence in TCV: Evidence in support of stochastic modelling," *Plasma Phys. Controlled Fusion* **58**, 044006 (2016).
- ⁷⁶O. E. Garcia, R. Kube, A. Theodorsen, J.-G. Bak, S.-H. Hong, H.-S. Kim, and R. Pitts, "Sol width and intermittent fluctuations in KSTAR," *Nucl. Mater. Energy* **12**, 36–43 (2017).
- ⁷⁷G. Decristoforo and T. Nicholas, "xblobs v1.0.0," (2020). [Zenodo. http://doi.org/10.5281/zenodo.4091041](http://doi.org/10.5281/zenodo.4091041)